Stony Brook University

A Journey Toward the Center of the Earth – Iron/Light-Element Alloys at Extreme Conditions and Their Implications for the Earth's Core

A Dissertation Presented

by

Matthew Louis Whitaker

to

The Graduate School

in Partial Fulfillment of the

Requirements

for the Degree of

Doctor of Philosophy

in

Geosciences

Stony Brook University

August 2009

Stony Brook University

The Graduate School

Matthew Louis Whitaker

We, the dissertation committee for the above candidate for the

Doctor of Philosophy degree, hereby recommend

acceptance of this dissertation.

Dr. Baosheng Li – Dissertation Advisor
Research Professor, Mineral Physics Institute

Dr. William E. Holt – Chairperson of Defense
Professor, Department of Geosciences

Dr. Donald J. Weidner – Director of Mineral Physics Institute
Distinguished Professor, Department of Geosciences

Dr. Michael T. Vaughan
Research Associate Professor, Mineral Physics Institute

Dr. Thomas S. Duffy
Professor of Geosciences, Princeton University

This dissertation is accepted by the Graduate School

Lawrence Martin
Dean of the Graduate School

Abstract of the Dissertation

A Journey Toward the Center of the Earth – Iron/Light-Element Alloys at Extreme Conditions and Their Implications for the Earth's Core

by

Matthew Louis Whitaker

Doctor of Philosophy

in

Geosciences

Stony Brook University

2009

Understanding the composition of the Earth's core is integral to answering many questions in the Earth Sciences, including the mechanisms and timing of core formation and the conditions under which the core formed, and also has important implications for the composition of the Earth's mantle. Because of the remote nature of the core, seismic profiles of the Earth's interior must be relied upon to determine the velocity and density structure of the deep Earth, and these profiles must then be compared with experimental data on candidate core phases at extreme conditions. The work presented in this dissertation was designed to study the physical properties of several iron/light-element alloy (ILEA) compounds at high pressures and temperatures in order to quantify their behavior under extreme conditions. Four such materials (Fe_3P, FeS_2, FeS and ε-FeSi) were studied in this investigation using a combination of synchrotron-based static compression experiments in Diamond Anvil Cells (DAC) and combined ultrasonic interferometry and synchrotron X-radiation in a Multi-Anvil Cell (MAC). The results of these two different types of experiments were remarkably similar, showing much better agreement than has ever before been seen between MAC and DAC experiments on these types of materials. The results of these experiments have provided an important benchmark for future studies on these materials and have resolved some of the controversy regarding the physical properties of these phases under extreme conditions.

The results of the ultrasonic experiments were extrapolated to pressures and temperatures relevant to the Earth's inner core, and a compositional-density-velocity model was constructed for the solid portion of the core. This model was then compared with existing cosmochemical and experimental data, as well as element partitioning studies, to form a more comprehensive model of the Earth's inner and outer cores. Previous models of core composition have been conducted under the assumption that Birch's Law, which states that acoustic velocity is solely a function of density, is valid for Fe and ILEA phases have thus far been unable to account for all aspects of the PREM model. By treating the existing data on pure Fe differently than previous studies and accounting for the fact that iron does not seem to follow Birch's Law, a model accounting

for all aspects of PREM in the inner core, including the shear velocities, has been generated. This model, designed to account for experimentally observed deviations from Birch's Law, yields an inner core model containing 4.0-5.2 wt. % Si and ~0.1 wt. % O, corresponding to 4.8-6.12 wt. % Si and 5.3 wt. % O in the liquid outer core. This model satisfies geochemical constraints on the composition of the core as well as the density deficits observed in seismic profiles.

To Rich and Gramz
The two that couldn't make it.
For everything.

Somehow, Someday

The telephone rang, I knew something was wrong.
The voice on the other line told me you were gone.

I guess it's true what they say, every dog has his day, and everything must die.
Now I'm standing here, with the answers unclear, and I am wondering why.

I don't know exactly what makes up the human soul but I hope it's forever…

Even in my memories of my early days
I can't recall a time I didn't know your face.

It pains me that you're gone, but your memory lives on, and you are finally free.
Whether near or far, I only hope that you are, watching over me.

This feeling starts to rise, and when I close my eyes, I can see you there,
Smiling back at me, just the way you used to be, and I just can't despair.

You're all alone in God's hands now.
I hope you can hear me somehow…

This feeling starts to rise, and when I close my eyes, I can see you there,
Smiling back at me, just the way you used to be, and I just can't despair.
All the times we shared, and to know you really cared, meant the world to me.
As you're looking down, I just hope that you're proud, of the man you see.

I'll miss you more than words can say.
We will meet again… Someday…
I miss you…

- Matthew L. Whitaker

Table of Contents

List of Figures

List of Tables

Acknowledgements

First and foremost, I have to give all the thanks in the world to my advisor, Dr. Baosheng Li. Not only has he been an excellent advisor and a world-class scientist, but he has also been a great friend. His guidance during these last two and a half years has been an amazing gift and without him this work would never have gotten off the ground. There are not many people that are capable of seeing a student through a Ph.D. in two years, but his skills as a scientist and his talents as a teacher have done just that, and for all he has done I will be eternally grateful.

I also would like to thank the other members of my defense committee for their time and assistance during this difficult process. I am grateful to Tom Duffy for driving in from New Jersey at an ungodly hour of the morning to make it for the defense itself, as well as for insightful discussions over the last two years. I thank Mike Vaughan for his insights into the experimental side of things, and also for dealing with my many scheduling issues when it came to beamtime over the last couple of years. Thanks to Bill Holt for offering his unique insight into the many things I have worked on since I arrived at Stony Brook, and for being a good friend during some difficult times. I am also grateful to Don Weidner for always taking time out of his day to sit down and discuss ideas and problems with me, and for offering his considerable insights to the questions addressed in this dissertation.

I am very grateful to the other members of the Ultrasonics Group at Stony Brook. Qiong Liu has always been available for discussions and has offered her opinions freely. Wei Liu has offered her assistance every step of the way in this work, from teaching me how to use the presses for synthesis experiments, to helping train me for the synchrotron experiments, to walking me through the processing of the experimental data. I would not have been able to work through all of this without her help. Bob Liebermann has also lent his immense insight into the work presented here and helped shape it into what it is.

I am indebted to Wendy Panero, Daniel Reaman, Sara Whitaker, Cathy Tarabrella, Lauren Borkowski, and John Parise for allowing use of their facilities and training me to prepare and load samples for the diamond anvil cell experiments. Thanks also go to: Carey Koleda, for sample preparation assistance and cell assembly fabrication; Ken Baldwin, for technical support; Bill Huebsch, for computer and electronics support; Ben Vitale, for electronics support on the presses in the High Pressure Lab. I would also like to extend my gratitude to the beamline scientists I worked with during these experiments for their guidance and assistance; Liping Wang from X17B2 and Zhiqiang Chen and Sanjit Ghose from X17C.

Thank you to Boris Kiefer, Lars Ehm, Jianzhong Zhang, Andy Campbell, Jackie Li, Jim Tyburczy, Owen Evans, Evan Abrams, Taku Tsuchiya, Kanani Lee, Sebastien Merkel, James Badro, Guillaume Fiquet, Oliver Tschauner, Wendy Mao, Stacey Cochiara, Norimasa Nishiyama, and Tetsuo Irifune for insightful discussions. Special thanks also go out to the last two of those individuals for giving me a job after I graduate! I would be remiss if I did not thank Brian Phillips, Scott McLennan, Rich Reeder, Gil Hanson, and Donald Lindsley for everything they have done for me while I have been here at Stony Brook. I would also like to thank Loretta Budd from the Geosciences Main Office, Emily Vance from the COMPRES office and Samantha Lin from the MPI office for all of the support they have given over the last couple of years.

I have to give special thanks to my mother, Margaret Dugan, for everything she has done for me over the last 29 years of my life. We never had much, but she always made sure I was able to do the things I really wanted to do. She's definitely one of my heroes. I also give a shout out to my sister Valerie for being generally awesome and always there for a good pep talk. I would also like to give a quick acknowledgment to my step-dad and grandmother, to whom this dissertation is dedicated, for knowing long before I did what path my life would take and watching me begin that journey, even though they couldn't see it through to the end.

I offer my eternal gratitude and undying love to my wife, Sara Whitaker, for everything over this last year and a half. I thank her for the support she has offered during the most difficult periods of this work, and for giving me the motivation I needed to see it through to the end. She was always available not just for moral support, but scientific discussion and assistance as well. It's definitely cool having a scientist for a wife. She has been present in every facet of my life and has had a positive effect on it since she first appeared. Most of all, I am extremely grateful for her patience with me during this difficult time. I cannot say enough words of praise and thanks for her. I love You, Sara.

In closing, I would like to thank ex-wives, ex-advisors, and less-than-stellar drivers for showing me the true meaning of darkness and putting me on the path toward the light. Finally, I would like to thank myself, without whom none of this would have been possible.

This research was supported by NSF grants EAR00135550 and EAR0635860 to Baosheng Li. Use of the National Synchrotron Light Source, Brookhaven National Laboratory, was supported by the U.S. Department of Energy, Office of Science, Office of Basic Energy Sciences, under Contract No. DE-AC02-98CH10886. Use of the X17C and X17B2 beamlines was supported by COMPRES, the Consortium for Materials Properties Research in Earth Sciences under NSF Cooperative Agreement EAR 01-35554 and by the Mineral Physics Institute, Stony Brook University.

CHAPTER 1. INTRODUCTION

1.1 – Scientific Background

The composition of the Earth's core has been a long standing question in the field of the Earth Sciences (i.e., McDonough and Sun, 1995) since its discovery over a century ago (Oldham, 1906). Our ability to determine the structure and composition of the deep interior of the Earth is limited because we lack the capability of direct observation. Therefore, we have to rely on the tools we have available, most notably seismology and mineral physics, to make interpretations about what is present in the deep Earth interior.

Seismic waves generated by large earthquakes can propagate through the various regions of the Earth's interior, and inversions of these data have led to a distribution of density, compressibility, and velocity profiles for the Earth's interior. Compilation and analysis of a large population of seismic data gave rise to the Preliminary Reference Earth Model (PREM) of Dziewonski and Anderson (1981, see Figure 1.1.1). While these profiles give us information on the density and velocity structure of the Earth's interior, they do not give any compositional information. In order to determine what the composition of the various regions of the Earth's interior may be, the physical properties of materials under conditions of high pressure and temperature must be investigated, and then these data obtained via mineral physics studies must be compared to the seismic profiles of the Earth's interior. PREM has been one of the most widely accepted seismic models used to represent the interior structure of the Earth, and therefore will also be used as the basis for comparison throughout this dissertation.

It has long been accepted that the core of the Earth, as well as those of other terrestrial planetary bodies, is predominantly made up of metallic iron (or an iron-nickel alloy) based on three major observations (Jeanloz, 1990). First, the magnetic field of the Earth is the result of a dynamo mechanism, which requires a liquid metallic region inside the Earth (i.e., Jacobs, 1987); this observation was entirely consistent with seismic observations indicating a liquid region in the deep interior of the Earth (i.e., Oldham, 1906). Second, the measured densities and sound velocities in iron at high pressures and temperatures are similar to those found in seismic studies of the Earth's core (Birch, 1964; Brown and McQueen, 1986; Jeanloz, 1979; McQueen and Marsh, 1966). Third, Fe is the most abundant element, by a wide margin, that possesses seismic properties similar to those of the Earth's core (i.e., Anders and Ebihara, 1982). In addition to these observations, the Earth's core was also shown to have a layered structure based on seismological data (Dziewonski and Gilbert, 1971), with a metallic liquid outer core and a solid metallic inner core.

Though iron has been determined to be the predominant constituent of both the Earth's outer and inner cores, several studies have shown that metallic Fe alone is too dense to be the sole element in the Earth's core; particularly the solid inner core (i.e., Jephcoat and Olson, 1987; Mao et al., 1998). These studies and others suggest that there must be some amount of one or more light elements in the core. In order to assess which

elements might be present within the core of the Earth, and in what possible proportions, the physical properties of various iron-light element alloys (ILEAs) under extreme conditions must be ascertained and compared against the information gained from seismic studies on the Earth's interior.

There have been many previous investigations aimed at studying several of these materials at high temperatures and pressures in hopes of determining which elements are most likely to be present in the inner core. Based on these previous studies, several different elements have been suggested as being possible constituents of the Earth's inner core. For example, silicon has been suggested as a strong possibility for a light-element constituent of the Earth's core (i.e., Badro et al., 2007; Georg et al., 2007). A recent study on several different iron-bearing phases (Badro et al., 2007) came to the conclusion that the inner core contains 2.3 wt. % Si and a trace amount of O, which accounts for the density and velocity differences between those observed for the solid inner core and pure metallic iron-nickel. There is also strong geochemical and isotopic evidence that the Earth's core contains some amount of silicon (Georg et al., 2007).

Sulfur has also been extensively investigated as a possible core constituent, and has met with mixed results. Element partitioning seems to suggest that S is the most likely light element to be incorporated into the core during its formation (i.e., Li and Agee, 2001). Some experimental studies have indicated that the presence of a significant amount of S in the core is unlikely with respect to other possible light elements (i.e., Badro et al., 2007), while other experiments have suggested that the Earth's inner core does contain a significant amount of S (i.e., Li et al., 2001). Previous work has also suggested that the deviations in density and seismic velocities from pure iron observed in the inner core can be accounted for by having S present in the inner core in addition to another light element (Dreibus and Palme, 1996).

Phosphorous is another element that has been suggested as a possible light-element constituent of the Earth's core. Little experimental work has been done to constrain the properties of iron phosphide phases under extreme conditions (i.e., Scott et al., 2007; Scott et al., 2008), however the ubiquitous presence of minerals like barringerite (Fe_2P) and schreibersite (Fe_3P) in iron meteorites suggests that P strongly partitions into the metallic Fe phase under conditions of planetary core formation.

In addition to these three light elements, others have also been suggested as possible elements within the core, including oxygen, carbon, and hydrogen (Badro et al., 2007; Gao et al., 2008; Hirao et al., 2004; Knittle and Jeanloz, 1991; Scott et al., 2001; Yagi and Hishinuma, 1995). However, the work presented in this dissertation will focus on only the first three elements discussed here: Si, S, and P.

This study was designed to use multiple experimental mineral physics techniques to determine the physical properties of iron silicide, iron sulfide, and iron phosphide compounds under extreme conditions of pressure and temperature in order to expand our understanding of these materials and help to constrain the possible light elements present in the Earth's core. Four compounds were chosen as starting materials for this work based on either the scarcity or controversy of available data: ε-FeSi, FeS, FeS_2, and Fe_3P.

1.2 – Sample Materials

Fe_3P adopts a tetragonal structure in space group $I\bar{4}$ under ambient conditions (Fasiska and Zwell, 1967). Some work has been conducted previously on the

thermodynamics, thermal expansion, and hyperfine interactions of this material (Fasiska and Zwell, 1967; Vorobyev and Yelsukov, 1998; Zaitsev et al., 1995), but the experimental phase relations are not yet well understood. High pressure studies of this material have been extremely limited (Scott et al., 2007; Scott et al., 2008), and to date there is a scarcity of available data on the physical properties of schreibersite at high pressure. This work set out to add to the database of information available regarding the physical properties of this material under extreme conditions.

FeS_2 occurs in a cubic structure in space group *Pa*3 at room P and T (Merkel et al., 2002). Previous studies have characterized the many differences between samples and examined the thermal expansion of pyrite (Chrystal, 1965; Smith, 1942), and there have been several studies conducted at high pressure (both static and dynamic) to determine the Raman spectra, electronic structure, elasticity, and equation-of-state of pyrite (Ahrens and Jeanloz, 1987; Blanchard et al., 2005; Kleppe and Jephcoat, 2004; Le Page and Rodgers, 2005; Merkel et al., 2002; Sithole et al., 2003). In addition, low-pressure studies have determined the single-crystal elastic constants of pyrite (Prasad and Wooster, 1956; Simmons and Birch, 1963). There is some inconsistency between the results of these previous studies, and there has not yet been any data made available on the shear properties of polycrystalline samples of pyrite, which was the impetus for investigating this material in this study.

At room temperature and pressure, FeS exists in a hexagonal structure with a $P\bar{6}2c$ space group (King and Prewitt, 1982). This material is the most complex out of the four chosen for this study, as it undergoes several phase transitions within the pressure and temperature space investigated (Figure 1.1.2). Upon compression at room temperature, the FeS-I troilite phase transforms to an orthorhombic (space group *Pnma*) FeS-II phase, and then to a monoclinic (space group $P2_1/a$) FeS-III phase (King and Prewitt, 1982; Marshall et al., 2000; Martin et al., 2001; Nelmes et al., 1999). With increasing temperature, these phases transform to a hexagonal NiAs superstructured FeS-IV phase, then to a hexagonal NiAs-type FeS-V phase (Fei et al., 2000; Kusaba et al., 1997; Kusaba et al., 1998; Urakawa et al., 2002; Urakawa et al., 2004). Two additional phases of FeS have recently been experimentally discovered as well (Ohfuji et al., 2007; Ono and Kikegawa, 2006; Sata et al., 2008), but they are found at pressures significantly greater than those achieved in this work. In spite of all of the aforementioned studies on FeS, there is still considerable debate on the elastic properties of the different phases, and a complete lack of information on the shear properties of phases I-V, which this study seeks to rectify.

Under ambient conditions, FeSi occurs in the ε-FeSi form, which has a cubic (B20) structure belonging to space group $P2_13$. This material has an unusual characteristic in that the coordination numbers of both silicon and iron are seven (Pauling and Soldate, 1948), and has a structure similar to the NaCl structure, but with the silicon and iron atoms displaced along the [111] directions (Knittle and Williams, 1995). Many studies have been conducted on this material, yet considerable debate still exists over the behavior and physical properties of ε-FeSi under extreme conditions (Guyot et al., 1997; Knittle and Williams, 1995; Lin et al., 2003a; Sarrao et al., 1994; Wood et al., 1995); in particular, there is a lack of information on the shear properties of fersilicite. The work on ε-FeSi presented in this dissertation was aimed at filling in some of the gaps in the

available data on this material, and to attempt to lay to rest some of the controversy regarding this material's properties under extreme conditions.

There have been previous investigations into the physical properties of the four materials chosen for this study. However, these previous investigations have either given controversial results, or have not provided much of the information necessary to be able to draw comparisons to seismic profiles of the Earth's core. For example, prior to this work, there existed no reported data on the bulk shear properties of these materials, which is an important piece of information for comparison to the Earth's interior.

In the work presented in this dissertation, the properties of these materials were investigated in two different types of experiments: 1) *in situ* studies at high pressures (and temperatures) using a combination of synchrotron X-ray diffraction, X-radiographic imaging, and ultrasonic interferometry in multi-anvil apparatus (i.e., Li et al., 2004), and 2) *in situ* static compression experiments conducted at ambient temperature in Diamond Anvil Cells using synchrotron X-ray diffraction (i.e., Lin et al., 2003a). The ultrasonic experiments, while limited to lower pressures than obtained in some previous studies, allows for the direct measurement of acoustic velocities in a sample as a function of temperature and pressure; information which has thus far not been made available for any of these materials. Experiments were also conducted in Diamond Anvil Cells in an attempt to reconcile the results obtained in these two different types of experiments, which traditionally have been quite different for these materials. The work presented in this dissertation is aimed at resolving some of the existing controversy regarding these materials and providing new data that will lead to a greater understanding of how these materials behave under extreme conditions of temperature and pressure.

Details regarding the synthesis of sample materials used in this dissertation will be presented in Chapter 2. Chapter 3 provides the details and results of the Diamond Anvil Cell experiments on these four sample materials. The experimental details and results of the combined ultrasonic and X-ray experiments will be presented in Chapter 4. Comparisons between the sample materials and their implications for the composition of the Earth's core are found in Chapter 5, along with conclusions based on the results of all of the work presented in this dissertation.

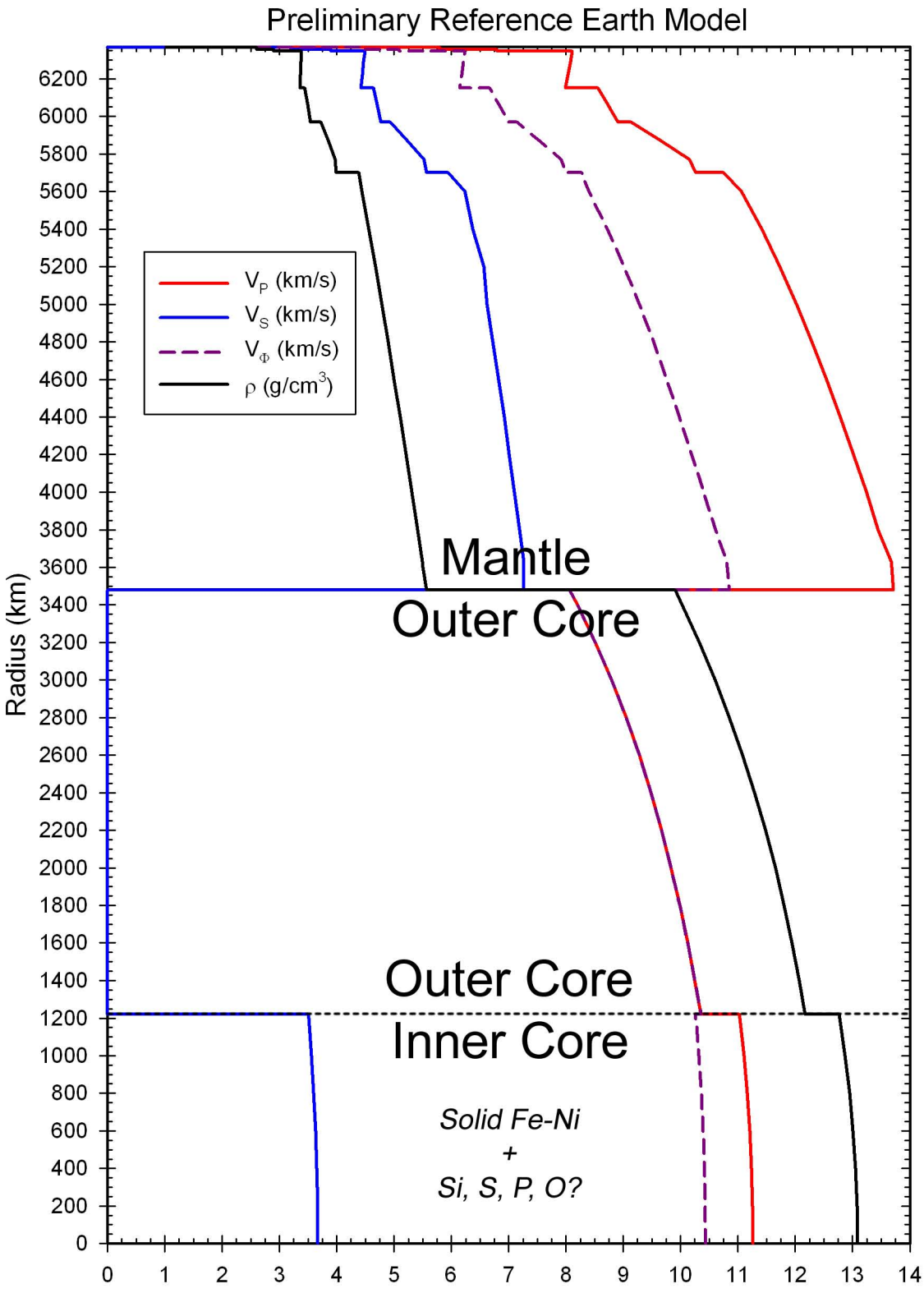

Figure 1.1.1. Preliminary Reference Earth Model (PREM) of Dziewonsky and Anderson (1981) showing variation in density and acoustic velocities with depth in the Earth.

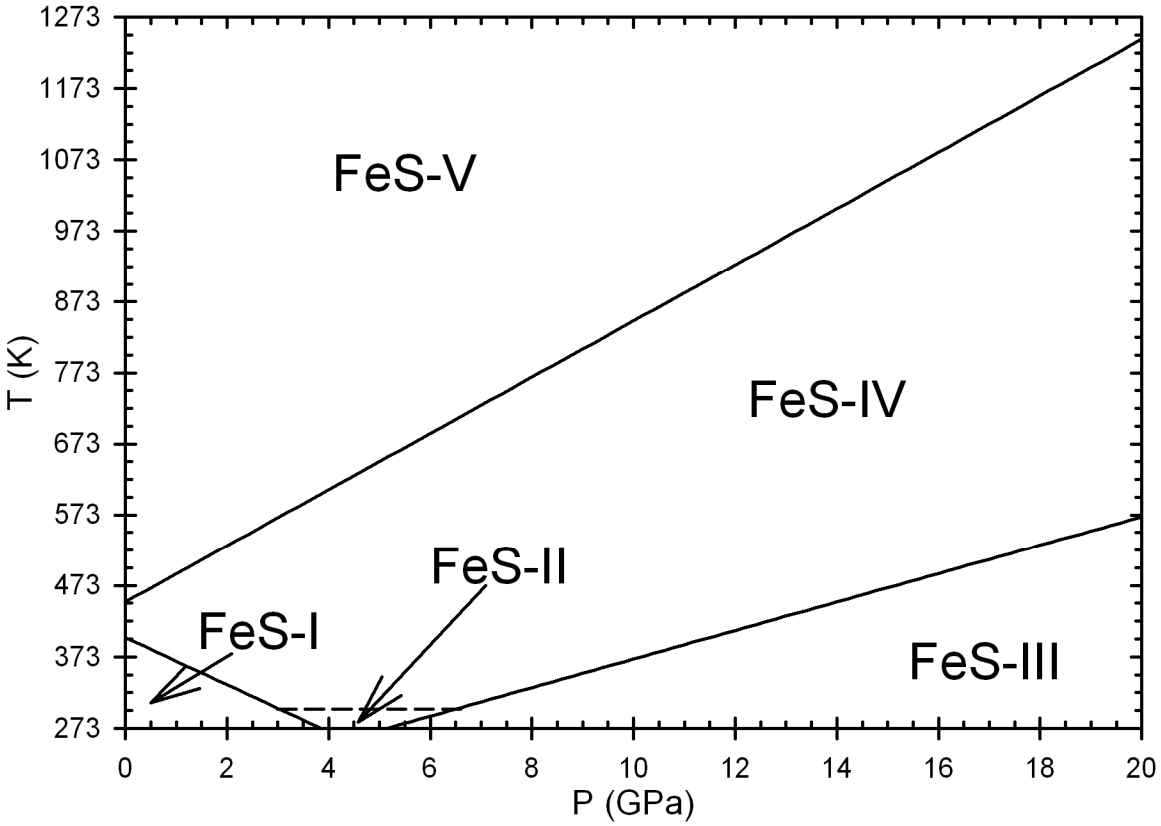

Figure 1.1.2. P-T phase diagram of FeS (troilite) to 20 GPa and 1273 K showing transition conditions (from Urakawa et al., 2004) between FeS-I (hexagonal), FeS-II (orthorhombic), FeS-III (monoclinic), FeS-IV (hexagonal), and FeS-V (hexagonal).

CHAPTER 2. SYNTHESIS TECHNIQUES AND SAMPLE DETAILS

The four samples investigated in this work were obtained in powdered form, and as such did not need to undergo a batch synthesis from some other starting materials. These powders were characterized using X-ray powder diffraction to verify their composition before any experiments were carried out. For the experiments to be conducted in the Diamond Anvil Cells, this powdered material was sufficient for use as the sample (with the exception of the FeS powder, as will be discussed later). However, for the experiments involving ultrasonic interferometry, a powdered sample would not be of sufficient quality to allow efficient transfer of acoustic energy. Therefore, hot-pressing experiments needed to be conducted on each of the powdered materials to form dense polycrystalline aggregates that would then be suitable for use as samples in the *in situ* ultrasonic experiments.

2.1 – Synthesis Techniques

The methods for hot-pressing powdered material in a multi-anvil apparatus in order to fabricate low-porosity polycrystalline aggregates have been well developed (Gwanmesia et al., 1993; Gwanmesia et al., 1990). Two different multi-anvil apparatuses were used in this work to synthesize aggregate samples for ultrasonic studies. The first is a 1000-ton uniaxial split-cylinder apparatus (USCA-1000) known as the Kennedy Press (Figure 2.1.1), and the second is the newly-refurbished Sumitomo Press (Figure 2.1.2), which is a 2000-ton uniaxial split-cylinder apparatus (USCA-2000). Both of these presses are Kawai-type apparatuses that utilize compression in the vertical direction to transfer pressure from the six-sided experimental housing through the anvils to the cell assembly at the center of the experimental setup.

The anvils used in these synthesis experiments are tungsten carbide (WC) cubes with truncated corners (Figure 2.1.3a). These cubes are then arranged such that the truncated corners come together to form an octahedral cavity at the center, which is where the cell assembly is placed. All of the synthesis experiments conducted for this work were carried out using the 14/8 cell assembly, which means the truncated corners of the cubic anvils measured 8 mm in length, and the length of the edges of the octahedral cell assemblies measured 14 mm. These cell assemblies were obtained from Kurt Leinenweber at Arizona State University through the COMPRES (COnsortium for Materials Properties Research in Earth Sciences) Multi-Anvil Cell Assembly Initiative (Figure 2.1.3a,b).

The powdered materials were more coarse-grained than desired for fabrication of a dense polycrystalline aggregate, so each of the starting powders were hand ground in an agate mortar for 30 minutes; this resulted in an average grain size of less than 5 microns. This fine powder was then packed tightly into a gold capsule and dried in an oven at 150°C for 2 hours to drive off any adsorbed moisture. Visual inspection, SEM analysis, and X-ray diffraction indicate that no appreciable amount of oxidation of the sample

materials occurred during this drying procedure. After drying, the capsule was pressure-sealed and placed into the cell assembly, a schematic of which is shown in Figure 2.1.4.

The anvils are then prepared for the experiment; during this process, four of the anvils have the necessary parts attached to them, while the other four are left clean (Figure 2.1.5). First, the insulating paper is krazy glued to the cube faces surrounding the truncation that is the intended anvil face. Next, the pyrophyllite gaskets are affixed to the exposed cube faces near the truncation with Duco cement. The first cube has 3 short gaskets, the second has 2 short and 1 long, the third has 1 short and two long, and the fourth has 3 long gaskets. The short gaskets are centered on the cube face, while the long gaskets have their long ends hanging off to the left (see Figure 2.1.5). Pieces of balsa wood are then attached to the insulating paper with Duco cement to provide stabilization of the cube assembly.

Once the glue and cement has dried, the first and second cubes are arranged with two of the clean cubes to form a cup into which the octahedral cell assembly is placed (Figure 2.1.6a). The remaining cubes are then arranged on top of these first four such that the gaskets make a complete octahedral enclosure around the cell. Resin squares are then affixed to the outside of the cube assembly to hold all of the pieces in place and insulate the cube assembly from the press; slits are cut in two of the resin sheets so copper strips can be attached, connecting the anvils that are in contact with the furnace portion of the cell assembly (Figure 2.1.6b). This allows electricity to pass through the cell assembly only in the direction required for the resistive heating to take place.

For an experiment in the Kennedy Press, the complete cube assembly is then placed inside the press (Figure 2.1.7a), the top guideblocks are put in place (Figure 2.1.7b), and the jacketed lid is placed on top to enclose the sample chamber (Figure 2.1.7c). The module is then slid into place, and pressure is advanced by the ram below. A similar procedure is followed for an experiment in the Sumitomo Press, except the top guideblocks are already in place, and the bottom half of the press simply slides into place and is advanced to meet the top half.

The sample is then compressed slowly at room temperature to the desired pressure of the experiment via the computer control system, which then maintains the target pressure throughout the duration of the experiment. Once at the target pressure, the sample is then slowly heated to the desired temperature for the hot-pressing experiment, where it is held for a predetermined amount of time (usually ~1 hour). After the “cooking” period is complete, one of two things are done; either the sample is slowly brought straight down to room temperature and then slowly decompressed to room pressure (quench), or the sample is cooled in steps during decompression (step). Once the experiment returned to ambient pressure, the press is opened and the cube assembly can then be removed (Figure 2.1.7d). The cubes are then carefully opened to access the cell assembly inside (Figure 2.1.7e). Figures 2.1.7e) and f) show very clearly the deformation of the gaskets and the cell assembly during the experiment. The cell assembly is then broken apart to access the capsule inside, which is then cut open to retrieve the newly hot-pressed sample inside.

2.2 – Sample Details

The resulting sintered cylindrical samples were analyzed at beamline X17B2 at the National Synchrotron Light Source (NSLS) at Brookhaven National Laboratory (BNL) to check for heterogeneity in grain size and/or composition. The samples were then

analyzed with SEM to double check grain size and homogeneity in composition, and the density of the aggregate was measured via the Archimedes method. Samples that passed all of these quality checks were then prepared for the ultrasonic experiments. The hot-pressed cylinders are approximately 3 mm in diameter and 2.5-3 mm in length, which are then cored down to 2 mm in diameter and polished down to a more appropriate length (~0.5-1 mm). Polished cylinders of each of the four sample materials examined in this study were prepared for the synchrotron-based ultrasonic experiments. The results of the synthesis experiments conducted in this study are summarized in Table 2.1.

2.2.1 – Fe_3P, Schreibersite. The starting Fe_3P material used throughout this work was purchased in powdered form from Alfa Aesar (99.5% pure). X-ray powder diffraction conducted on this powder confirmed that it was pure, homogeneous schreibersite. This is in contrast to previous studies, which have found their starting material, also purchased from Alfa Aesar, to be a mixture of Fe_3P and Fe_2P (Scott et al., 2007; Scott et al., 2008). The finely-ground Fe_3P powder was hot-pressed in the Kennedy Press at 7 GPa and 700°C for 65 minutes, after which it was quenched to room T and decompressed over 15 hours. This pressure was chosen to remain below the anomalous change in compressibility found in Scott et al. (2007). The recovered cylindrical sample (K0826) was 98.6% of the theoretical density. Figure 2.2.1 shows an SEM (Scanning Electron Microscope) image of this sample. The surface had been polished, so grain size must be estimated based on the presence of the divots in the surface, which yields an estimate of ~10 μm. EDS (Energy Dispersive Spectrum) spectra collected from multiple points were nearly identical, which combined with the uniform brightness of the image indicates compositional homogeneity of the sample.

2.2.2 – FeS_2, Pyrite. The pyrite starting material used in this work was purchased from Alfa Aesar in powdered form (99.9% pure) packed under an argon atmosphere. This powder was significantly more hygroscopic than the other used in this study, and tended to react with moisture and oxygen from the air to form sulfate; as such the material was kept in a dessicator at all times when not actively being used. X-ray powder diffraction on the sample confirmed that the starting material was pure homogeneous pyrite.

Three different samples of FeS_2 were synthesized for this study because of problems experienced in the ultrasonic experiments. The first sample (K0827) was synthesized in the Kennedy Press at 10 GPa and 1000°C for 70 minutes, after which it was quenched to room T and decompressed over 15 hours. The recovered sample was 97.3% of the theoretical density. The second pyrite sample (K0846) was synthesized in the Kennedy Press at 11 GPa and 900°C for 68 minutes, after which it was ramped down to 350°C while it was decompressed to ~3 GPa, then to 150°C while it decompressed to ~1.5 GPa, then quenched to room T as it decompressed to ambient pressure. The recovered sample was 98.8% of the theoretical density. Figure 2.2.2 shows an SEM image of sample K0846. There appears to be a bimodal grain size distribution, with the larger grains averaging 2-5 μm, and the smaller grains averaging 250-500 nm; triple junctions can be seen in several grain boundaries in this image, indicating low porosity and a good sintering. EDS spectra of all analyzed points contained no impurities and were nearly identical to one another.

The third pyrite sample (S4020) was synthesized in the Sumitomo Press at 10 GPa and 900°C for 1 hour, after which it was quenched to room T and decompressed over 18 hours. The recovered sample was 99.2% of the theoretical density. Figure 2.2.3 shows an

SEM image of the S4020 sample. It should be noted that a different type of detector was used in this image than in the others shown in this dissertation to accentuate the grain boundaries. The bimodal grain size distribution appears here again, with the larger grains averaging 2-3 μm, and the smaller averaging around half a micron. Triple junctions are again visible in several locations. The EDS spectra collected in several areas were identical to each other, and remarkably similar to those from the K0846 pyrite sample; again there was no evidence of any impurities.

2.2.3 – FeS, Troilite. Though the FeS powder, purchased from Alfa Aesar, was tested to be 99.9% pure on a metals basis, X-ray powder diffraction showed that the material was actually 6 different iron sulfide phases (~80 % of which was pure troilite), whose bulk chemistry added up to a stoichiometric FeS. In order to attain a pure FeS sample for use in later experiments, the powder needed to react at high temperature and pressure during the hot-pressing process to form a homogeneous sample.

A hot-pressing of the "FeS" powder was therefore conducted to create a suitable starting material for the diamond anvil cell (DAC) experiments to be discussed in Chapter 3. These experiments use such a minute amount of powdered sample as the starting material that using the unreacted powder could yield disastrous results. This sample (K0851) was fabricated in the Kennedy Press at 11 GPa and 1000°C (FeS-V field) for 61 minutes, after which it was quenched to room T and decompressed over 12 hours. This sample was then ground into a fine powder for use in the DAC experiments; X-ray powder diffraction confirmed that the reaction went to completion, and the sample had converted to pure homogeneous FeS. Figure 2.2.4 shows an SEM image of the troilite sample K0851. This broken surface shows that the largest grains are ~10 μm, while the average size is ~5 μm, and the smaller grains averaging around 1 μm. Triple junctions are seen throughout the image. The EDS spectra collected throughout the sample indicated it was homogeneous in composition.

The troilite sample for the ultrasonic experiment (K0852) was synthesized in the Kennedy Press at 7 GPa and 700°C (in the stability field of FeS-V) for 75 minutes to allow the powder to react completely and form pure FeS, after which the temperature was ramped down to 400°C while the sample was decompressed to ~4 GPa, then ramped down to 150°C during decompression to ~2 GPa, and finally quenched to room T as the sample was decompressed to ambient conditions. X-Ray diffraction of the recovered sample confirmed that the reaction did take place, and the resulting sample was pure FeS-I. The recovered cylindrical sample was found to be 98.7% of the theoretical density.

2.2.4 – ε-FeSi, Fersilicite. The starting FeSi material used throughout this work was purchased in powdered form from Alfa Aesar (99.9% pure). X-ray powder diffraction conducted on this starting material revealed that the powder was pure, homogeneous ε-FeSi in composition. The starting ε-FeSi powder was hot-pressed in the Kennedy Press at 7 GPa and 700°C for exactly 1 hour, and then quenched to room T and decompressed over 13 hours. The recovered sample (K0825) was 97.9% of the theoretical density. Figure 2.2.5 shows an SEM image of the ε-FeSi sample K0825 after the ultrasonic experiment. The dark spots are areas where crystals had been plucked from the surface during polishing. The surface of this sample had been polished, so grain size can only be estimated by the imperfections in the polished surface, which suggest that the average grain size is ~5-10 μm. All EDS spectra collected throughout the sample gave identical peak positions and intensities, verifying that the sample is homogenous in composition.

Figure 2.1.1. The Kennedy Press (USCA-1000): 1000-ton uniaxial split-cylinder apparatus. a) Front view, showing computer and manual pressure controls and gauges. b) Rear view showing Walker module of the split-cylinder.

Figure 2.1.2. The Sumitomo Press (USCA-2000): 2000-ton uniaxial split-cylinder apparatus. a) Front view, showing computer controls, catwalk, and press. b) View downward into the base of the press showing where the cubic anvil assembly goes during the experiment.

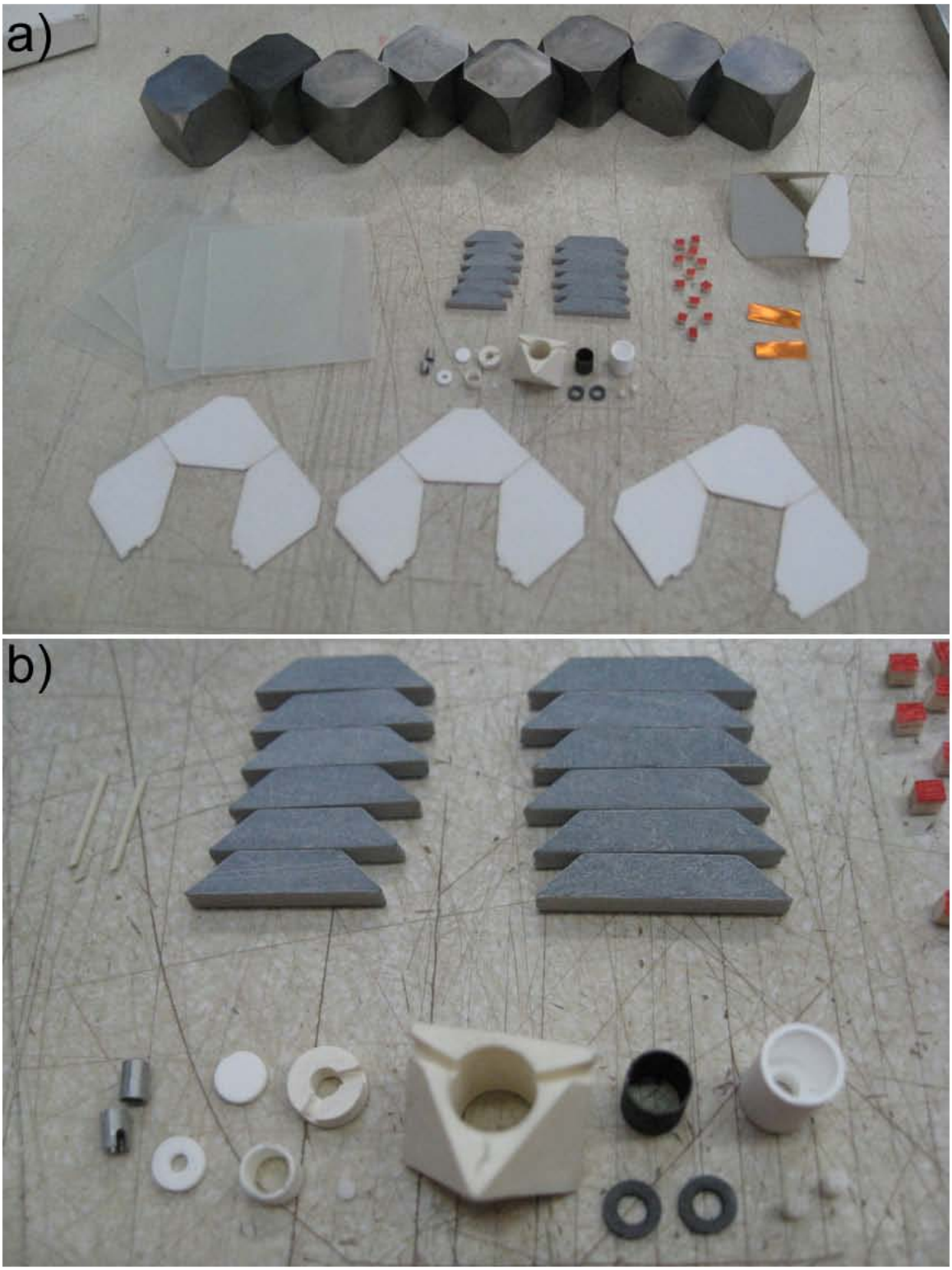

Figure 2.1.3 – The 14/8 cube and cell assembly parts. a) WC anvils shown along top edge of photograph, resin sheets at left, and insulating paper along bottom. Insulating paper folded into shape shown at right, with conducting copper strips below. Cell assembly parts in center. b) Pyrophyllite gaskets shown at top, red strips of balsa wood at right. Individual parts of cell assembly labeled in schematic in Figure 2.1.4 for comparison.

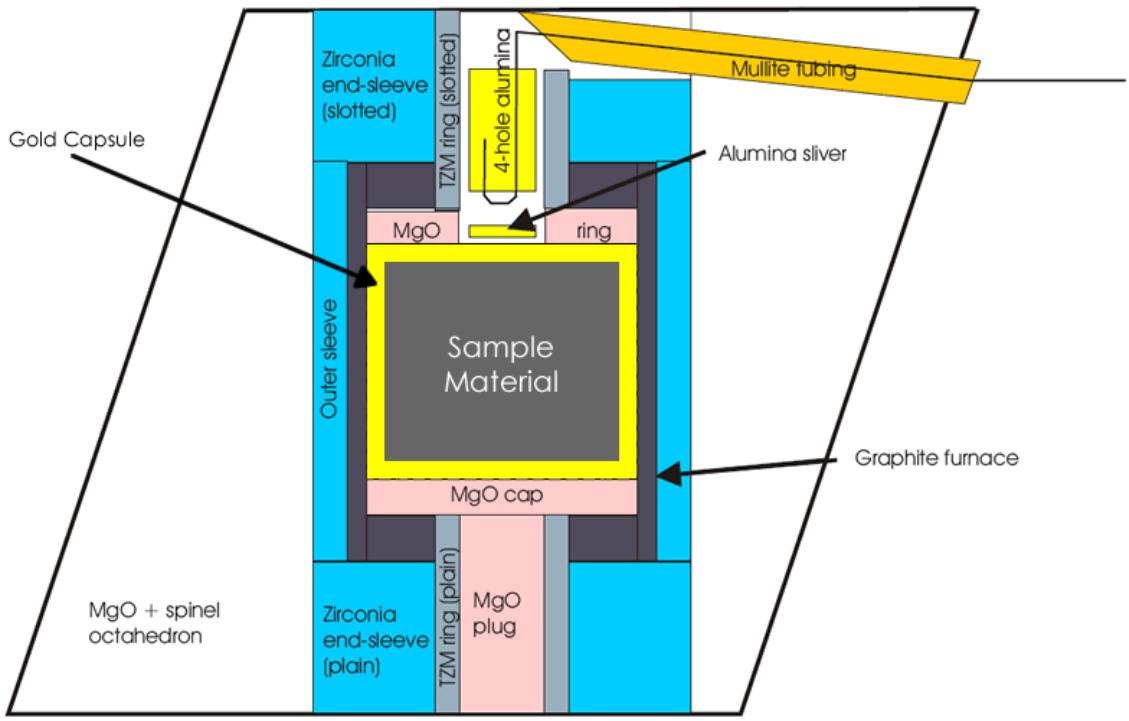

Figure 2.1.4. Schematic of the standard COMPRES 14/8 cell assembly (modified after original diagram by Kurt Leinenweber). Diagram shows how all of the pieces pictured in Figure 2.1.3b) fit together in an experiment.

Figure 2.1.5. Photograph of cubes with insulating paper, pyrophyllite gaskets, and balsa wood strip glued in place. Note that the cube on the left has 3 short gaskets, the second has 2 short and 1 long, the thirds has 1 short and 2 long, and the fourth has 3 long gaskets, and that the extra length of the long gaskets always hangs off to the left.

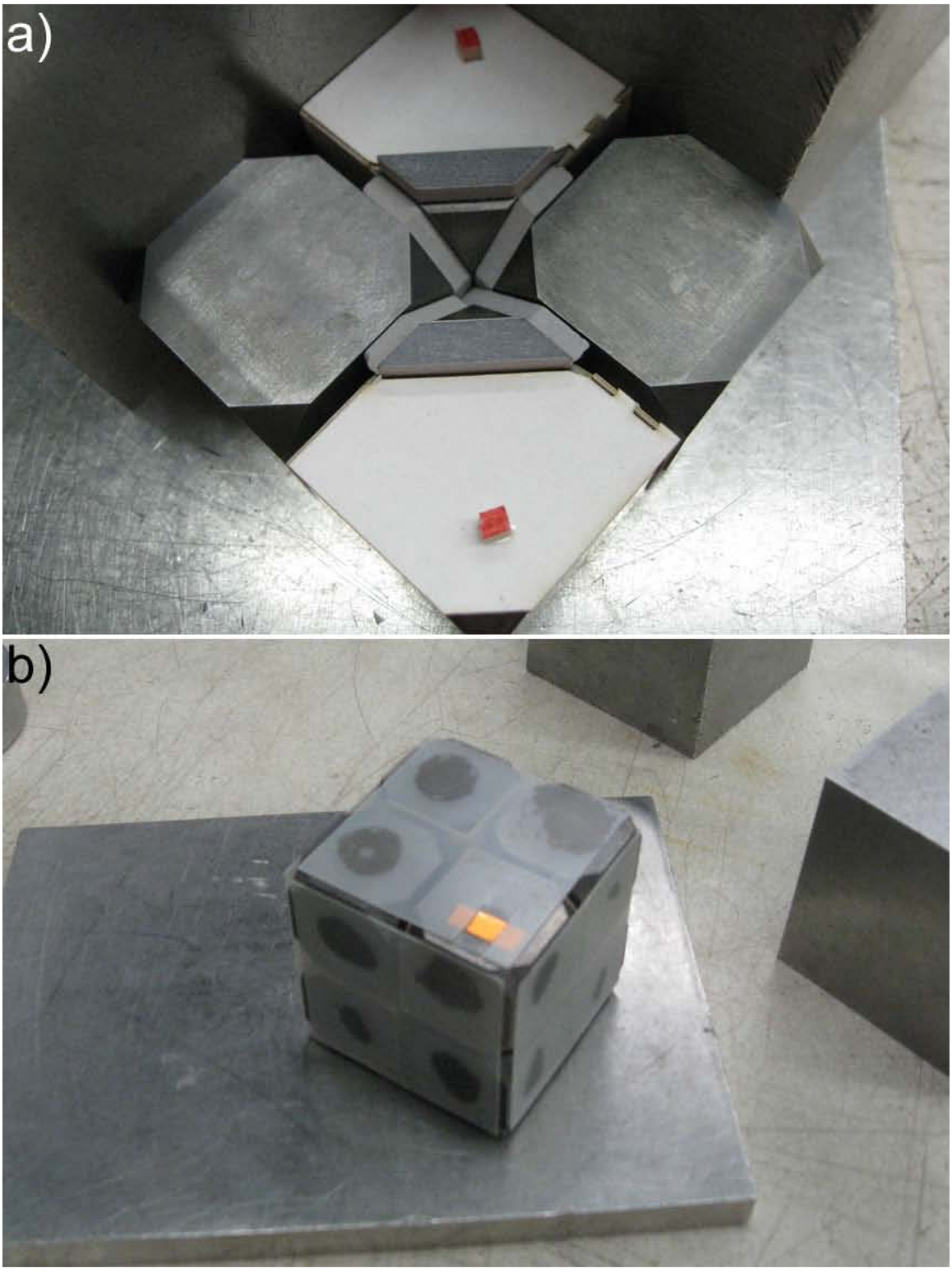

Figure 2.1.6. a) Photograph showing how cubes are assembled such that the pyrophyllite gaskets form a cup for the octahedral cell assembly to be placed into. b) Photograph of all cubes assembled and held in place by the resin sheets. Note the copper strip on the top that allows electrical contact only to the cubes that are in contact with the furnace assembly, while all other anvils are insulated by the resin sheets.

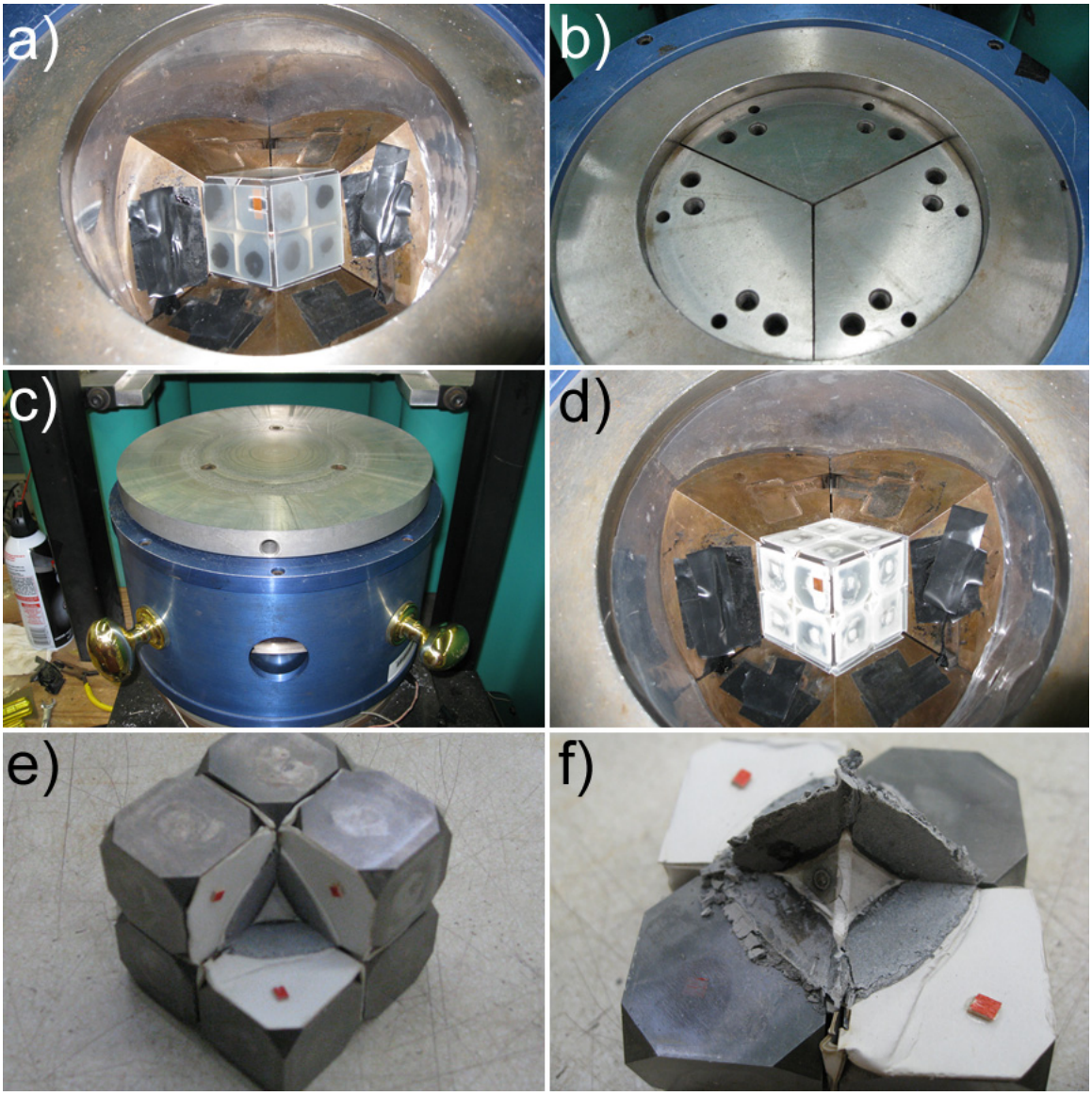

Figure 2.1.7. Before and after the experiment. a) Photograph of cube assembly placed inside the Walker module. b) The guideblocks have been put in place. c) The jacketed lid is placed on top of the guideblocks, then the module is slid into the press. d) Photograph of the cube assembly after the synthesis experiment. e) Resin sheets removed, and one cube removed to expose the cell assembly inside. f) All four top cubes removed to show run products. Note the deformation of the phyrophyllite gaskets and the flattening of the balsa wood pieces.

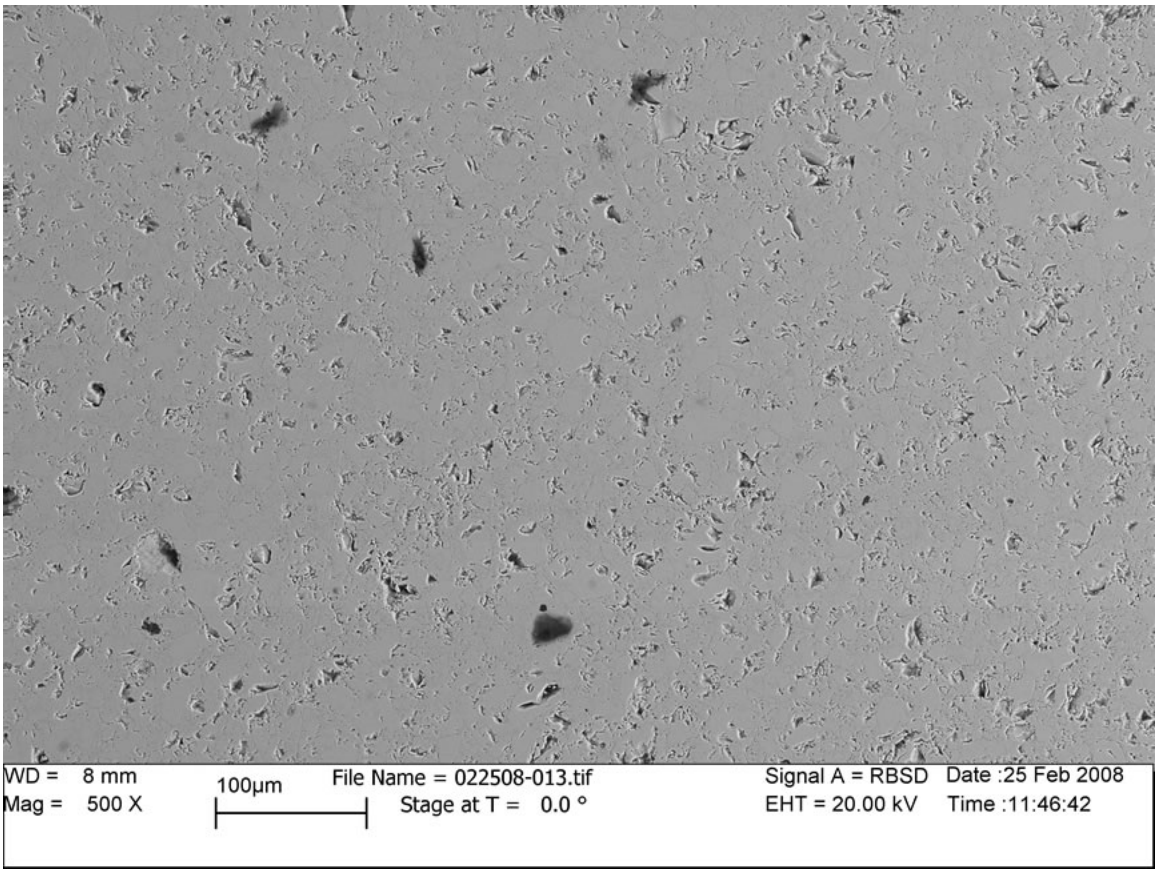

Figure 2.2.1. Scanning Electron Microscope image of polished surface of schreibersite (Fe_3P) sample K0826.

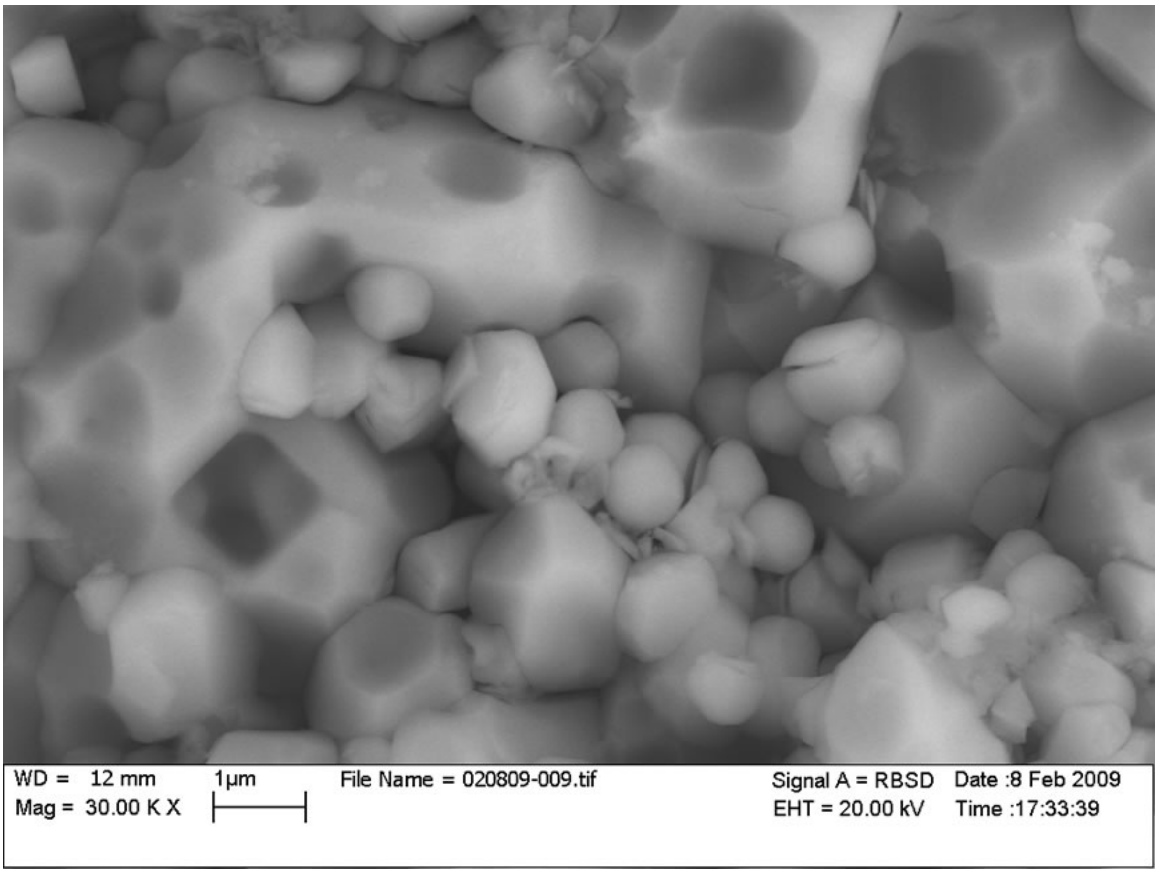

Figure 2.2.2. Scanning Electron Microscope image of rough surface of second pyrite (FeS_2) sample K0846.

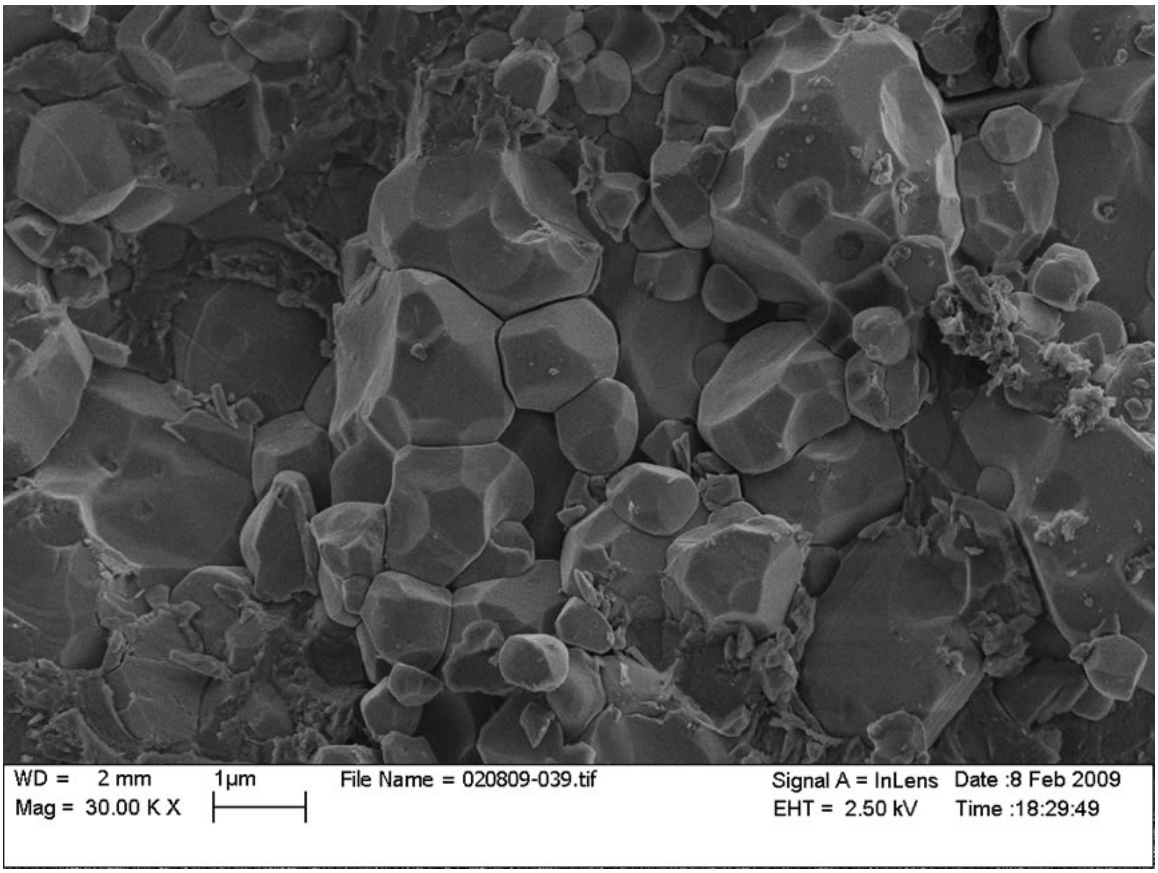

Figure 2.2.3. Scanning Electron Microscope image of rough surface of the third pyrite (FeS_2) sample S4020.

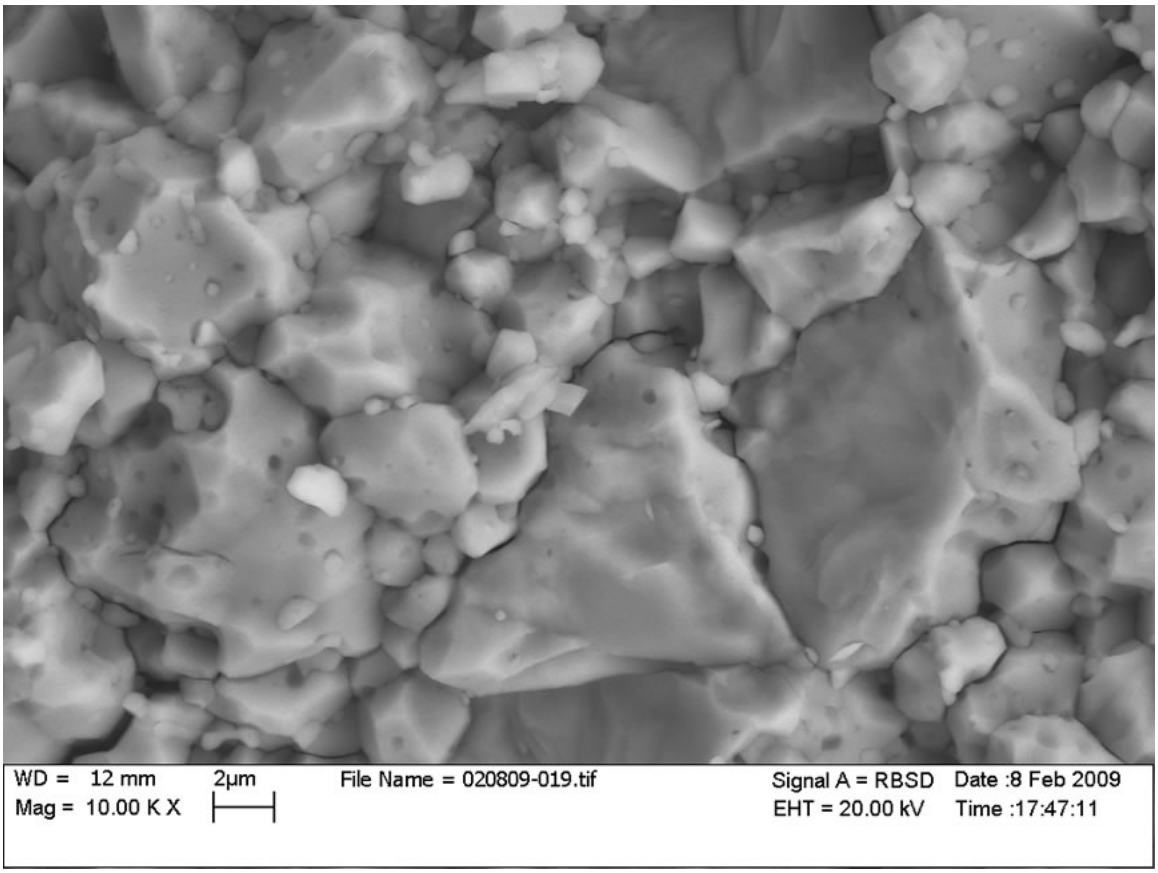

Figure 2.2.4. Scanning Electron Microscope image of rough surface of the troilite (FeS) sample K0851.

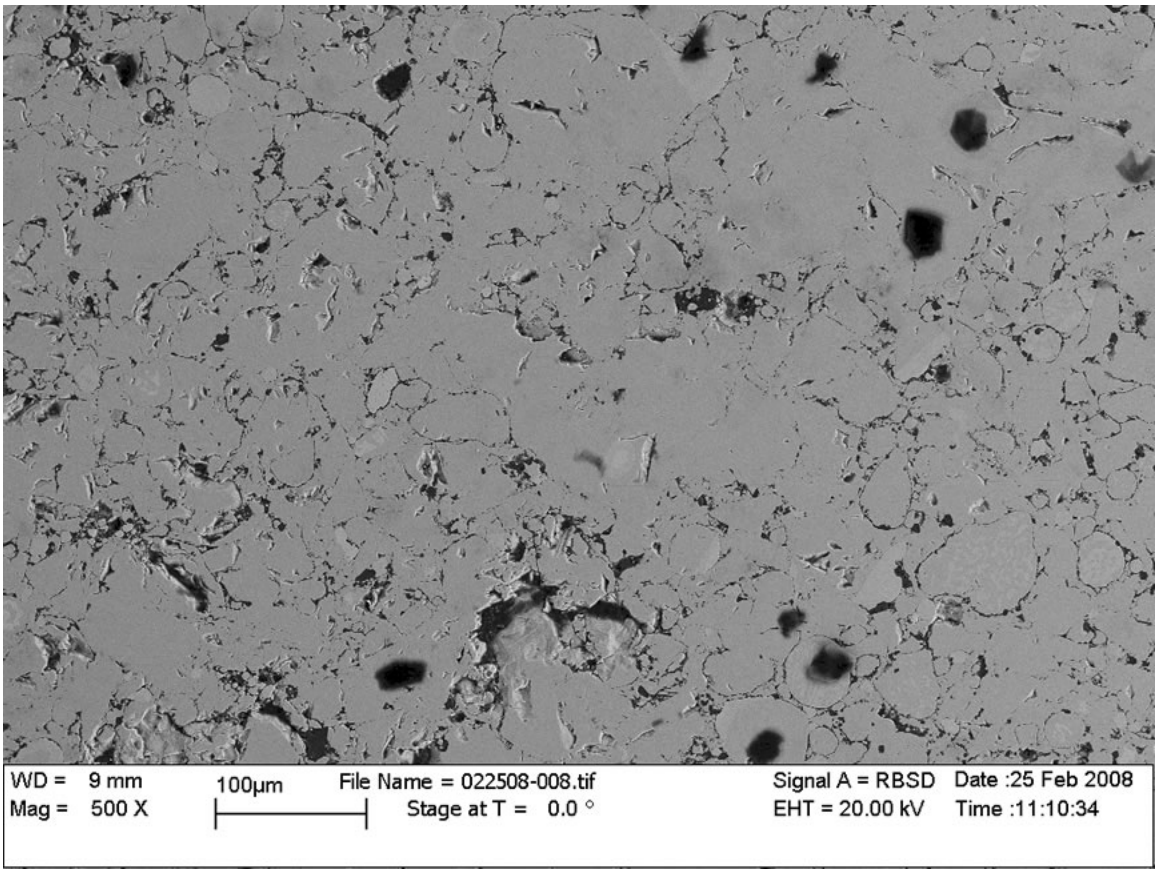

Figure 2.2.5. Scanning Electron Microscope image of polished surface of fersilicite (ε-FeSi) sample K0825.

Table 2.1. Results of synthesis experiments

Date	Sample	ID	P (GPa)	T (°C)	Time (min)	Type	V_0 (Å^3)	ρ (g/cm^3)	% Density	SEM	Comments
4/23/2007	FeS	K0808	7	700	75	Quench	361.26	4.849	97.2%	Yes	Ultrasonics unsuccessful
9/17/2007	ε-FeSi	K0825	7	700	65	Quench	90.45	6.171	97.9%	Fig. 2.2.5	Ultrasonics in Chapter 4
1/16/2008	Fe_3P	K0826	7	700	65	Quench	368.90	7.149	98.6%	Fig. 2.2.1	Discussed in Chapter 3
2/5/2008	FeS_2	K0827	10	1000	60	Quench	158.75	5.020	97.3%	No	X-ray only; Chapter 4
8/24/2008	Fe_3P	K0844	14	1000	-	-	-	-	-	No	Run Failed
8/27/2008	Fe_3P	K0845	11	1000	60	Step	369.10	-	-	Yes	Sample incorporated Au
10/23/2008	FeS_2	K0846	11	900	68	Step	158.78	5.019	98.8%	Fig. 2.2.2	X-ray only; Chapter 4
10/23/2008	$Fe_{0.91}Si_{0.09}$	K0847	11	1000	66	Step	-	-	-	-	Sample not sintered
1/23/2009	FeS	K0848	11	1000	77	Step	-	-	-	No	Sample not sintered
1/28/2009	FeS	K-	-	-	-	-	-	-	-	No	Run Failed
1/31/2009	FeS	K0851	11	1000	61	Quench	361.94	4.840	-	Fig. 2.2.4	DAC in Chapter 3
2/2/2009	FeS_2	K-	-	-	-	-	-	-	-	No	Run Failed
2/5/2009	FeS_2	S4020	10	900	60	Quench	159.01	5.012	99.2%	Fig. 2.2.3	Ultrasonics in Chapter 4
2/6/2009	FeS	S-	10	1000	75	Quench	-	-	-	No	Sample not sintered
2/12/2009	FeS	K0852	11	1000	75	Step	362.07	4.838	98.7%	No	Ultrasonics in Chapter 4

Run ID starting with K conducted in Kennedy Press, run ID starting with S conducted in Sumitomo. Step details given in sample description in text.

CHAPTER 3. P-V EQUATION OF STATE STUDIES

Understanding how a material behaves under pressure is of utmost importance in unraveling the mystery of the interior of the Earth. Both static and dynamic compression experiments are commonly employed to study materials at high pressures relevant to the deep interior of the Earth. Dynamic compression experiments, commonly referred to as shockwave experiments, are capable of achieving very high pressures for very short periods of time by striking the sample with a shot from either a laser or a physical explosion. These experiments have the drawback of not having any control over the temperature of the sample, and the limited time period for which the sample remains at high pressure and temperature. Static compression experiments, on the other hand, can maintain the same conditions of P and T for significantly longer periods of time (hours plus), though it is difficult to obtain pressures as high as those in shockwave experiments.

Static compression experiments conducted at room temperature are commonly employed to examine the behavior of a material under compression. These experiments essentially are designed to determine the volume (or density) of a material as a function of pressure. These data can then be fit to an equation of state that describes the material's physical properties under pressure. Static compression experiments are commonly conducted using Multi-Anvil Apparatus and Diamond Anvil Cells. The work presented in this chapter will focus primarily on Diamond Anvil Cells, but also includes the results of one experiment conducted in a Multi-Anvil Apparatus.

3.1 – Experimental Procedure

Diamond Anvil Cells (DACs) have become increasingly popular for high pressure studies in the Earth Sciences over the last couple of decades because of their portability (see Figure 3.1.1) and their compatibility with synchrotron radiation experiments (i.e., Mao and Hemley, 1996). The diamond anvils in these cells are transparent, thus allowing synchrotron radiation to pass through and access the sample *in situ* while at pressure. DACs are commonly used in conjunction with synchrotron X-rays and Infrared radiation to study different materials at high pressures.

The main components of a DAC are two diamond anvils uniaxially compressing a gasket, usually made of some type of hard metal, i.e., rhenium or stainless steel (Figure 3.1.2). The pressure attainable in a DAC experiment is determined by the size of the culet on the diamond face. The amount of force applied by the cell is constant regardless of the diamond size, so the smaller the area of the working face, the greater the pressure applied to the gasket and sample chamber.

The diamond anvils are affixed to WC seats using an epoxy resin; these seats have apertures allowing the passage of X-rays into and out of the cell. These seats are then installed in the cell, and the diamonds are aligned both laterally and rotationally to ensure that they are perfectly parallel and uniformly compressing the gasket. Once the diamonds have been aligned, the gasket is put in place and pre-indented. This indentation serves to

strengthen the gasket material in the area that will be compressed by the culet, and forms a seal that will keep the sample and pressure medium contained during the experiment.

Once the gasket is indented, a hole is then drilled in the center of the indentation to form the sample chamber. A variety of methods are used to make these holes, including using a micro-awl to physically punch a hole through the gasket and using a laser to drill the hole through the center of the indentation. Most commonly, however, an EDM (electrical discharge machining) machine is used to drill the holes in the gaskets. The EDM drills its hole by repeatedly discharging current rapidly between a thin "drill bit" electrode and the gasket through a dielectric liquid medium, thereby removing the material in small increments until the hole is drilled completely through the gasket.

Two important things that must be taken into consideration when indenting and drilling the gasket are the thickness and diameter of the sample chamber. The thicker the gasket is in the indented area, the greater potential there is for deformation of the gasket material during the experiment. Also, it is important that the diameter of the gasket hole be significantly smaller than the size of the culet face to ensure that the entire sample chamber remains sealed between the diamonds during the experiment.

A variety of solids, liquids, and gases have been used in DAC experiments as pressure-transmitting media. The pressure medium is meant to uniformly distribute the pressure throughout the sample chamber. It is important that the pressure medium be strong enough to prevent the gasket hole from closing over with increasing pressure, but soft enough to provide a hydrostatic (or as close to it as possible) pressure environment for the sample to minimize the effects of deviatoric stress in the sample chamber.

The experiments presented here were conducted using diamonds with 300 μm culets and stainless steel gaskets that were 250 μm thick. The gaskets were indented to a thickness of ~50-90 μm and drilled using an EDM machine; the gasket holes were 120-150 μm in diameter. The pressure medium used in these experiments was Methanol-Ethanol-Water 16:3:1 (MEW), with the exception of the experiment on FeS_2, which utilized Methanol-Ethanol 4:1 (M-E) to prevent reaction of the sample material with water. These liquid pressure media are known to behave hydrostatically until their freezing points, at which point they behave quasi-hydrostatically. MEW freezes between 13-15 GPa, while M-E freezes between 10-12 GPa; the pressure ranges explored in these experiments were purposely kept predominantly within the range where these pressure media remained liquid and hydrostatic.

Once indented and drilled, the gasket wass seated on the lower diamond in the same orientation in which it was indented, and the cell was closed around it to make it flush with the diamond culet. The sample powder was then loaded into the sample chamber using a fine needle. Since the materials studied in this work were all Fe-rich and opaque, the sample chamber was not packed tightly with the sample powder. Too much sample presented two problems during the experiment. First, since iron is very absorbing to X-rays, the amount of time necessary to collect a good diffraction pattern became excessively long (>30 minutes) with a full chamber of sample. Second, with the material being so opaque, it makes it difficult to see the sample chamber for focusing both within the beam and for pressure measurement.

A balance was therefore struck where a significant enough amount of sample was loaded into the sample chamber to allow for good diffraction patterns to be collected in a reasonable amount of time (10-20 minutes), yet some light still passed through the

sample chamber to make it easier to find and focus during the experiment. After the sample had been loaded, one or two chips of ruby were added to the sample chamber for pressure measurement using an Ar laser (Figure 3.1.2). The pressure medium was added last, and then the cell was closed and brought to pressure (usually ~1-2 GPa) to prevent the pressure medium from escaping or evaporating.

Once the DAC was loaded and closed, it was ready for the synchrotron-based experiment. These experiments were conducted at beamline X17C of the National Synchrotron Light Source (NSLS) at Brookhaven National Laboratory (BNL). The cell was mounted in a jig that is fitted to the sample stage, which can translate in three directions and rotate in the beam path. The cell is then optically aligned using a microscope so that the sample is centered in the beam vertically and horizontally. The sample chamber is brought into focus and the position of the stage noted, then the back of the diamond is brought into focus and its position noted; the difference in position between these two points, multiplied by the refractive index of diamond, gives the thickness of the diamond. The sample position is then adjusted by this amount to ensure that it is optimally centered in the beam path (x-direction) at the proper sample-to-detector distance. The optimized sample-to-detector distance is determined by the experimental set-up in the hutch, and is measured using an external CeO_2 standard.

As shown in Figure 3.1.2, the X-ray beam enters through one diamond, diffracts off the sample material, and exits through the opposite diamond. The X-ray beam used in these experiments was monochromatic with a wavelength of 0.4066Å and was about 20x20μm. After centering in the x-direction as described above, the sample chamber was centered horizontally (y-direction) and vertically (z-direction) in the beam path using a photodiode by measuring the intensity of X-ray transmission through the cell. Once centered, test patterns were collected in several different places within the sample chamber to determine where the best diffraction was found. If possible, the diffraction patterns were collected close to the location of a ruby grain so the pressure measurement would be as accurate as possible. An example of an X-ray diffraction pattern collected by the image plate detector is shown in Figure 3.1.3.

The pressure in the sample chamber was measured using the ruby fluorescence method. The ruby grains in the sample chamber fluoresce when excited by an Argon laser, and the wavelength of the fluorescence is pressure-dependent and has been well-calibrated (Mao et al., 1978). The pressure was measured both before and after the X-ray diffraction pattern was collected to mark any changes that might have occurred during that time. If more than one ruby grain was available in the sample chamber, they were all analyzed and checked for consistency. In all cases when more than one grain was present, the sample chamber was under hydrostatic conditions within the precision of the measurement.

Once the pressure measurement and X-ray diffraction patterns have been taken, the pressure is then increased by tightening the screws (Figure 3.1.1). It is important that this be done very carefully, usually no more than 1/16 of a turn at a time, to prevent large jumps in pressure. After tightening, the cell is allowed to sit for a few minutes, and then the pressure is measured again. After measuring the pressure, the sample is re-centered in the beam, and the X-ray diffraction pattern is collected, after which the pressure is measured again, and pressure can be increased again. These steps are repeated until the maximum desired pressure of the experiment is obtained. When possible, data were

collected during decompression in the same manner. At the end of the experiment, the cell was opened completely and a final diffraction pattern collected of the sample at zero pressure for reference. The dataset collected in each experiment was then analyzed to determine the behavior of each material at high pressure.

3.2 – Data Processing and Analysis

The raw X-ray diffraction patterns were imported into Fit2D as images (Hammersley et al., 1996), and then integrated to give standard 2θ vs. Intensity diffraction patterns (chi plots) that can then be refined to determine the unit cell volume (see Figures 3.2.1-3.2.4). These chi plots were then imported into Igor, which is a program commonly used for DAC data analysis that allows the use of user-created functions. These data were then converted to d-spacing plots, and each individual peak was fit to a Gaussian function to determine it's d-spacing and full width at half maximum (FWHM). Standard JCPDS files for each material were used as references to index the peaks in the pattern. Once all the peaks had been fit and indexed, the unit cell volume was refined. This process was repeated for every diffraction pattern in a given experiment.

The experiments conducted in the DAC provided information on the unit cell volume of these materials as a function of pressure. These data can then be fit to some P-V equation of state to determine the isothermal bulk modulus at zero pressure (K_{0T}) and it's first pressure derivative ($\partial K_{0T}/\partial P = K_{0T}'$). For example, one of the most commonly used equations of state in the Earth Sciences is the third-order Birch-Murnaghan EoS (Birch, 1947; Birch, 1952):

$$P(V,T) = \frac{3}{2} K_{0T} \left[\left(\frac{V_{0T}}{V} \right)^{7/3} - \left(\frac{V_{0T}}{V} \right)^{5/3} \right] \times \left\{ 1 + \frac{3}{4} \left(K'_{0T} - 4 \right) \left[\left(\frac{V_{0T}}{V} \right)^{2/3} - 1 \right] \right\} \quad (3.1)$$

Where V_{0T} is the unit cell volume of the material at ambient conditions, and V is the volume measured at high pressure. This is the EoS that will be used in this work.

The volumes obtained from the unit cell refinements were paired with their pressure measurements (and their uncertainties) to fit for the K_{0T} and K'_{0T} using equation 3.1. The refinements and fitting were all carried out using user functions written to process this type of data in Igor. The results of these P-V experiments on each of the four starting materials are presented in the next section.

3.3 – Results and Discussion

3.3.1 – Fe_3P. X-ray diffraction patterns collected throughout the experiment indicate that no first-order phase transition occurred over the range of pressures explored (Figure 3.2.1). The sample maintained the same tetragonal structure, and no less than 10 diffraction lines were used in the unit cell refinement for each data point. Unit cell volumes and lattice parameters from these refinements for each pressure point are given in Table 3.1. Molar volumes are also given, along with sample density, which is calculated using the theoretical density and the refined unit cell volumes. The unit cell volume at ambient pressure (V_0) was measured to be 369.22(59) $Å^3$.

Experiments on this material conducted in the multi-anvil apparatus met with several difficulties, and therefore a complete ultrasonic dataset was not able to be obtained.

However, X-ray diffraction patterns were collected as a function of pressure during compression at room temperature, and these data are of good quality. Therefore, the data from the multi-anvil experiment are presented here in Table 3.2. An example of the X-ray diffraction patterns collected at both low and high pressure is shown in Figure 3.3.1. The experimental procedure for synchrotron experiments in the multi-anvil apparatus will be discussed in the following chapter of this dissertation.

Figure 3.3.2 shows the change in unit cell volume with pressure for both the DAC and multi-anvil experiments on Fe_3P. The data from Scott et al. (2007) are plotted as open symbols in the background as reference. Results of fitting these data to the 3rd order Birch-Murnaghan (BM-3) equation (Eq. 3.1) are listed on the diagram. Curves plotted behind data represent the calculated compression curves using the parameters obtained from the fitting. Blue circles and curves represent data from the DAC experiment (green circles are data collected during decompression), and red circles and curves are from the multi-anvil cell (MAC) experiment. Diffraction patterns from both the DAC and MAC experiments indicated that the sample did not undergo any first-order phase transition over the range of pressures explored, consistent with previous studies showing that the known phase transition occurs upon laser heating at pressures above 20 GPa (Scott et al., 2007; Scott et al., 2008).

The data from the DAC and MAC experiments show very good agreement with one another up to ~8 GPa, where both datasets show what may be a possible inflection point in the compression curves, but no change in crystal structure. This change in compressibility was noted in the previous static compression study on this material (Scott et al., 2007). Above 8 GPa, the DAC data seem to follow the Scott et al. (2007) data more closely, while the MAC data follow the lower edge of the scatter in their data. This change in compressibility has been attributed to a possible change in electronic spin-state configuration (Scott et al., 2007), similar to that observed in both Fe_3C (Lin et al., 2004b) and Fe_3S (Lin et al., 2004a), which was reinforced by examining changes in the c/a ratio with pressure.

Figure 3.3.3 shows the variation in c/a ratio with pressure, and the data of Scott et al. (2007) is shown in the background as reference. The change in slope of the c/a ratio that Scott et al observed at pressures above 8 GPa was used to argue that this change in compressibility was real. However, in Figure 3.3.3 it is clear that only the data points collected in the quasi-hydrostatic NaCl pressure medium begin to slope upward, while the slope of the data collected in the hydrostatic MEW pressure medium remains largely constant until the highest pressure point, which was about the freezing point of MEW and was no longer hydrostatic. Moreover, the data from the MAC experiment presented here (red circles) falls along a more or less continuous trend with Scott et al.'s NaCl data (the line labeled Quasi-hydrostatic in Figure 3.3.3), and the DAC data presented here (blue circles), which also had MEW as a pressure medium, matches their MEW trend very well (the line labeled Hydrostatic in Figure 3.3.3). Note that the green circles were data collected during decompression, and the hydrostaticity of the system during those measurements is in question, which may explain the much larger degree of scatter. If the difference in slope is in fact caused by the hydrostaticity of the experiment as Figure 3.3.3 seems to suggest, then the c/a ratio does not indicate the need for any change in compressibility at ~8 GPa as was previously suggested. While this possible change in compressibility could be explained by a second-order phase transition, further study is

required to determine what might cause this feature, and whether or not this change in compressibility is real or just an artifact of fitting the data.

Table 3.3 presents a comparison of the results of these static compression studies on Fe_3P with those obtained in previous work. A BM-3 fit of the entire dataset from the DAC experiment with V_0 fixed at 369.2(6) $Å^3$ yields a zero-pressure isothermal bulk modulus (K_{0T}) of 132.6(44) GPa, and a first pressure derivative ($\partial K_{0T}/\partial P = K_{0T}'$) of 14.5(15). A BM-3 fit of the full MAC dataset with V_0 fixed at 368.9(5) $Å^3$ results in a K_{0T} of 137.6(45) GPa, and a K_{0T}' of 10.6(13). Scott et al (2007) similarly noted an anomalously high K_{0T}' in their study as well (8.5), though they did not specify the value they obtained for K_{0T} by fitting the entire dataset. Figure 3.3.2 shows that the compression curves calculated using these parameters are a decent fit at the lowest and highest pressures explored, however they do not reproduce as well the observed compression behavior at the intermediate pressures.

To alleviate the problem caused by the possible change in compressibility in trying to fit the entire dataset for each experiment, data collected up to 8 GPa were BM-3 fit separately from data collected above 8 GPa. Keeping V_0 fixed as before, the data from the DAC experiment collected up to 8 GPa gave a K_{0T} of 156.8(11) GPa, and a K_{0T}' of 5.3(3), while the equivalent data from the MAC experiment yielded a K_{0T} of 153.3(9) GPa, and a K_{0T}' of 5.3(2). These results show very strong agreement between the two different experiments conducted using two different techniques, and also strong agreement with the results of Scott et al (2007). It is important to note that in that study, K_{0T}' was fixed at 4, resulting in a K_{0T} of 159(1) GPa. Refitting of the data collected in Scott et al (2007) by allowing K_{0T}' to vary along with K_{0T} and fixing V_0 at their value of 369.2(6) $Å^3$, a K_{0T} of 155.7(44) GPa, and a K_{0T}' of 5.4(16) are obtained; these results are in very strong agreement with the results of both the DAC and MAC experiments.

A separate BM-3 fit was conducted for the data collected above 8 GPa in each experiment. In these fits, V_0, K_{0T}, and K_{0T}' were all allowed to vary. The fit of the high pressure data from the DAC experiment yielded a V_0 of 365.5(2) $Å^3$, a K_{0T} of 196.9(24) GPa, and a K_{0T}' of 7.7(5). The same fit for the MAC experiment gave a V_0 of 365.8(<1) $Å^3$, a K_{0T} of 178.1(<1) GPa, and a K_{0T}' of 8.0(<1). There was no such fitting done in Scott et al (2007), and attempts at fitting their data collected at above 8 GPa fail to converge, presumably due to the large amount of scatter in their dataset and being unable to fix any of the fitted parameters. At present, there is not sufficient data of high enough resolution to definitively state that the possible change in compressibility is real or to begin determining what its cause may be.

3.3.2 – FeS_2. X-ray diffraction patterns collected throughout the experiment showed no signs of any phase transition occurring throughout the range of pressure explored (Figure 3.2.2). This is consistent with previous studies which saw no phase transition in pyrite to pressures above 50 GPa (i.e., Merkel et al., 2002). The WC seat used in this experiment on the detector side of the cell had a very small 4θ aperture, which resulted in a very narrow range of d-spacings to pass through and be collected on the image plate. As such, there were only two peaks that were consistently found in all patterns and used for indexing and cell refinement. Since pyrite is cubic, there were still more measurements than parameters to be refined, so the unit cell volumes obtained from these refinements are robust. Refined unit cell volumes and lattice parameters are given with measured pressures in Table 3.4. Molar volumes and sample densities are also given.

The unit cell volume at ambient pressure (V_0) was found to be 159.14(5) $Å^3$. The change in unit cell volume of pyrite with pressure is shown in Figure 3.3.4. Results of the BM-3 fit of these data are shown on the diagram. Curves plotted behind data represent the calculated compression curves using the parameters obtained from the fitting. The blue circles and curve represent data from this study, and the gray circles plotted as reference are from Merkel et al (2002). Only two data points from the Merkel et al (2002) study are within the range of pressures explored in this study, but within mutual uncertainties the data and the calculated compression curves agree reasonably well.

Table 3.5 presents a comparison of the results of this static compression study on FeS_2 with those obtained in previous studies. A BM-3 fit of the entire dataset from the DAC experiment (minus the highest pressure data point, which was collected above the freezing point of M-E) with V_0 fixed at 159.14(5) $Å^3$ yields a K_{0T} of 143.1(10) GPa and K_{0T}' of 5.0(2). While the V_0 obtained in this study is very slightly larger than those used in previous studies, the K_{0T} and K_{0T}' fall within the range of values from previous experimental investigations (133.5-162 GPa and 4.7-5.73 respectively). The bulk modulus obtained from a shockwave study on pyrite (Ahrens and Jeanloz, 1987) is significantly higher than those obtained in static compression studies (162 vs. ~140), even taking into account the adiabatic to isothermal conversion.

The K_{0T} obtained in this study compares very well with those obtained from previous linear compression (148 GPa, Bridgman, 1949), diffuse X-ray (143.3 GPa, Prasad and Wooster, 1956), and ultrasonic (145.9 GPa, Simmons and Birch, 1963) studies. The bulk modulus matches the one obtained in the diffuse X-ray study almost exactly, and is very close to that obtained in the ultrasonic study. It is important to note, however, that none of these aforementioned studies offered any information about K_{0T}', so only the data on K_{0T} can be directly compared. Merkel et al (2002) obtained a lower bulk modulus (133.5 GPa) and a higher pressure derivative (5.73) than this study, despite both investigations being conducted in diamond anvil cells. In part this discrepancy arises from the slightly different values for V0 and the difference in pressure range explored in the two studies. Also, as K_{0T} and K_{0T}' are directly related such that an increase in one will bring about a decrease in the other, the difference between the two sets of results is not as great as it first appears.

The bulk modulus and its first pressure derivative as obtained by first-principles calculations exhibit a marked discrepancy from those obtained experimentally. The K_0 values obtained via these calculations above the upper limit of the range found in static experiments (150 to 176 GPa vs. 133.5 to 148 GPa), and the K_{0T}' is below the range observed experimentally (4.56 to 4.65 vs. 5.0 to 5.73). This discrepancy is commonly seen, especially in iron minerals, and is caused both by the assumptions that need to be taken in order to conduct these types of calculations, and the fact that such calculations are most commonly conducted at 0 K, while experimental results most commonly have a reference temperature of ~300 K. Theoretical calculations can give a wealth of information about a material's behavior under high pressures, but often do not exactly reproduce the experimental observations of compressibility and elasticity.

3.3.3 – FeS. Over the pressure range explored during this experiment, the FeS sample underwent two distinct phase transitions (Figure 3.2.3). At ambient conditions, the sample was in the hexagonal FeS-I (troilite) phase, which persisted up to 3 GPa. The sample then transformed to the orthorhombic FeS-II phase, on which data was collected

from 4 to 6.6 GPa. The high pressure monoclinic FeS-III phase was observed from 7.9 to 11.6 GPa. For FeS-I, 9-12 diffraction peaks were indexed and used in the cell refinement, 8-9 were used for FeS-II, and 19-24 were used for FeS-III, Refined unit cell volumes and lattice parameters of all three phases are given as a function of pressure in Table 3.6, along with molar volumes and sample densities.

The phase transition from FeS-I to FeS-II occurs between 3 and 4 GPa, which is consistent with the reported pressure of the phase transformation from previous studies (King and Prewitt, 1982; Kusaba et al., 1997; Martin et al., 2001; Nelmes et al., 1999). None of the diffraction patterns collected indicated coexisting phases. The volume change across this phase boundary was ~2.8%, which is comparable to that found in the aforementioned investigations. FeS-II persisted through 6.6 GPa, and had converted to FeS-III by 7.9 GPa, which again was consistent with the pressure range for the phase transition found in previous studies; no diffraction patterns gave any indication of coexisting phases. The volume change across this phase transition was ~5.5%, which is slightly lower than but consistent with those found in previous studies (~6-9%, King and Prewitt, 1982; Kusaba et al., 1997; Martin et al., 2001; Nelmes et al., 1999).

The change in unit cell volume of FeS with pressure is shown in Figure 3.3.5. Results of the BM-3 fit of these data are shown on the diagram. Curves plotted behind data represent the calculated compression curves using the parameters obtained from the fitting. The blue circles and solid curve represent data for FeS-I, the blue upward triangles and long dashed curve represent data for FeS-II, and FeS-III is represented by the blue downward triangles and short dashed curve. Data from previous studies were present only in graphical format and not tabulated, so they could not accurately be shown here for reference.

Table 3.7 presents a comparison of the results of this static compression study on all three phases of FeS with those obtained in previous studies. For FeS-I, V_0 was found to be 361.9(3) $Å^3$ (18.16(2) cm^3/mol). This V_0 falls within the range used in previous studies, and is nearly identical to that of King and Prewitt (1982). A BM-3 fit of the entire FeS-I dataset with a fixed V_0 yields a K_{0T} of 89.2(6) GPa and K_{0T}' of -4.2(3).

While a negative value for K_{0T}' is extremely rare, every previous study on this material that did not fix this parameter at a value of 4 also obtained a negative K_{0T}' from their fitting (King and Prewitt, 1982; Martin et al., 2001). A negative K_{0T}' would imply that the material becomes more compressible with increasing pressure, which is counterintuitive. It is possible that this phenomenon may actually be caused by second-order phase transition that leads to an increased compressibility; there may be an instability in the structure of troilite as it approaches the phase transition to the higher-pressure FeS-II phase. This instability may allow for an increase in the compressibility of the structure in preparation for the large volume collapse that occurs during the transition from FeS-I to FeS-II. Unfortunately this mechanism cannot be distinguished from a true negative K_{0T}' within the resolution of this experiment.

The bulk modulus from this study is slightly higher than but within mutual uncertainties of those from previous experimental studies (73(3)-82(7) GPa), and within the broad range of values obtained from theoretical calculations (75.6-257 GPa). The studies that obtained anomalously high values for the bulk modulus suffer not only from the problems discussed in section 3.3.2, but also from fixing their K_{0T}' at a value of 4,

which artificially drives up the value of K_{0T} because of the negative slope of the compression curve.

Since FeS-II does not exist under ambient conditions, the V_0 of this phase was also obtained from the BM-3 fit, and was found to be 121.80(34) $Å^3$ (18.34(5) cm^3/mol). This is ~1% larger than the V_0 of the FeS-I troilite phase, and is slightly smaller than the value obtained by King and Prewitt (1982). The BM-3 fitting of the FeS-II dataset yielded a K_{0T} of 35.8(20) GPa and K_{0T}' of 4.4(4). These values are very similar to, and within mutual uncertainties of, the results of King and Prewitt (1982). The results of Kusaba et al (1997) are different than those obtained here, but in that study K_{0T}' was fixed at a value of 4. The K_{0T} and K_{0T}' obtained by theoretical calculations are again significantly different from those obtained in all experimental studies (Kobayashi et al., 2005; Martin et al., 2001). The large differences in V_0, K_{0T}, and K_{0T}' between the results of the experimental studies and those of Martin et al (2001) may be due in part to a difference in reference pressure, but the paper is unclear on this point.

The BM-3 fitting of the FeS-III dataset gave a V_0 of 333.541(4) $Å^3$ (16.738(1) cm^3/mol), a K_{0T} of 47.777(3) GPa and K_{0T}' of 5.898(9). This V_0 is ~8% smaller than that of the FeS-I phase, and significantly larger than the V_0 used in previous studies (Kusaba et al., 1997; Martin et al., 2001); however, it is unclear whether the reference pressure was brought back to 0 GPa as was done in this study. The bulk modulus obtained in this study is similar to that obtained by Kusaba et al (1997), but their value of K_{0T}' was fixed at 4, so a direct comparison of that parameter cannot be drawn. Once again, a large discrepancy exists between the experimental data and the results of theoretical calculations. This may in part be caused by a possible difference in reference pressure, but is again largely caused by the assumptions incorporated into the calculations.

3.3.4 – ε-FeSi. X-ray diffraction patterns collected throughout the experiment showed no signs of any phase transition occurring throughout the range of pressure explored (Figure 3.2.4). This is consistent with previous experimental and theoretical studies which have suggested that a phase transition from the B20 to B2 structure may occur somewhere between 30 and 40 GPa (Caracas and Wentzcovitch, 2004; Ono et al., 2007). At least five diffraction peaks were consistently found in all patterns and used for indexing and cell refinement. Refined unit cell volumes and lattice parameters are given with measured pressures in Table 3.8, as are molar volumes and sample densities.

Figure 3.3.6 shows the change in unit cell volume of fersilicite with pressure. The unit cell volume at ambient pressure (V_0) was measured to be 90.40(3) $Å^3$. With V_0 fixed at this value, a BM-3 fit of this dataset yields a K_{0T} of 169.4(64) GPa and K_{0T}' of 6.7(14), as shown on the diagram. Black stars represent the data reported in Knittle and Williams (1995), dark gray X's are the data of Lin et al (2003a) , light gray triangles are from Wood et al (1995), and the light gray crosses represent the data of Guyot et al (1997). The first two of these studies were conducted in Diamond Anvil Cells, while the latter two were conducted in a Multi-Anvil Cell. Curves plotted behind data represent the calculated compression curves using the fitted parameters. This diagram shows the considerable differences between results of previous studies conducted on this material.

Table 3.9 presents a comparison of the results of this study with those of previous studies on ε-FeSi. The bulk modulus obtained from this study is significantly lower than those reported in studies based on first-principles calculations, which is also true of nearly all other experimental studies on this material. Previously reported experimental

values for the isothermal bulk modulus of ε-FeSi range from 160 to 209; the result of this work falls near the lower end of this range. The K_{T0}' obtained from this study, however, is higher than those of previous studies (range of 3.5 to 4.75).

The previous studies which have fitted for K_{T0} and K_{T0}' simultaneously (Knittle and Williams, 1995; Lin et al., 2003a) both have lower values of K_{T0}' and significantly higher values for K_{T0}. An increase in one of these parameters in the fitting will lead to a decrease of the other. Using the dataset from this study, if the value of K_{T0} to be equal to those given by the previous studies, the resulting K_{T0}' decreases significantly, even becoming negative when using the K_{T0} of Knittle and Williams (1995). Fixing K_{T0}' to be equal to those of previous studies results in a significant increase in K_{T0}. Taking this exchange into account, the results of this study agree fairly well with those of Lin et al (2003a) and extremely well with those of Guyot et al (1997).

A comparison between samples and the results of these experiments will be presented and discussed in Chapter 5 of this dissertation.

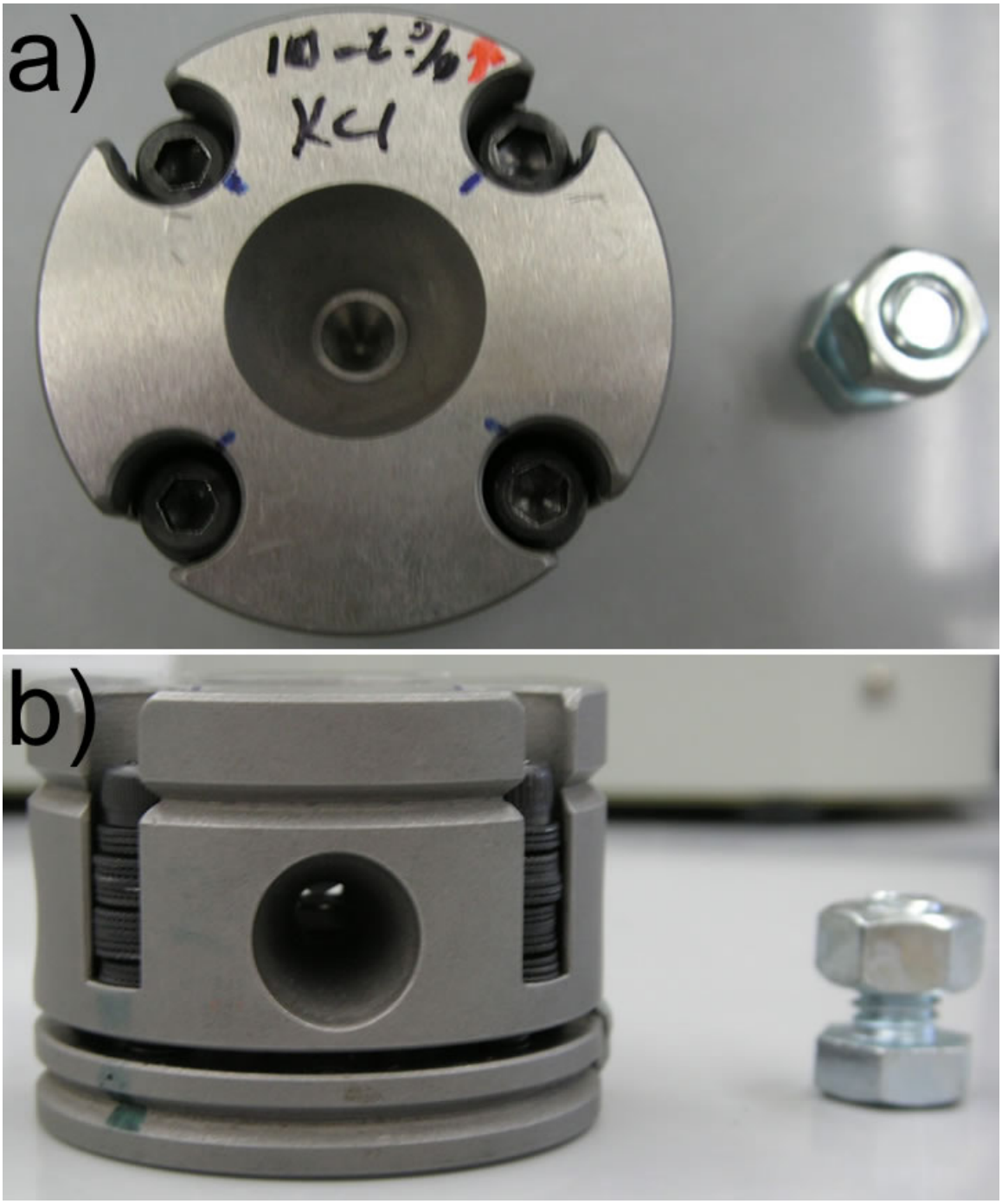

Figure 3.1.1. Photographs of the symmetric Diamond Anvil Cell (DAC). a) Top view of the DAC with quarter-inch nut for scale. Two of the hex screws are left-hand threaded, two are standard right-hand threaded. The WC backing plate in the middle of the cell has a wide-angle aperture to allow for maximum diffraction collection through the diamond anvil. b) Side view of the DAC. The opening in the side permits a view of the diamonds coming together on the gasket. The washers on the screws facilitate the transfer of pressure to the sample.

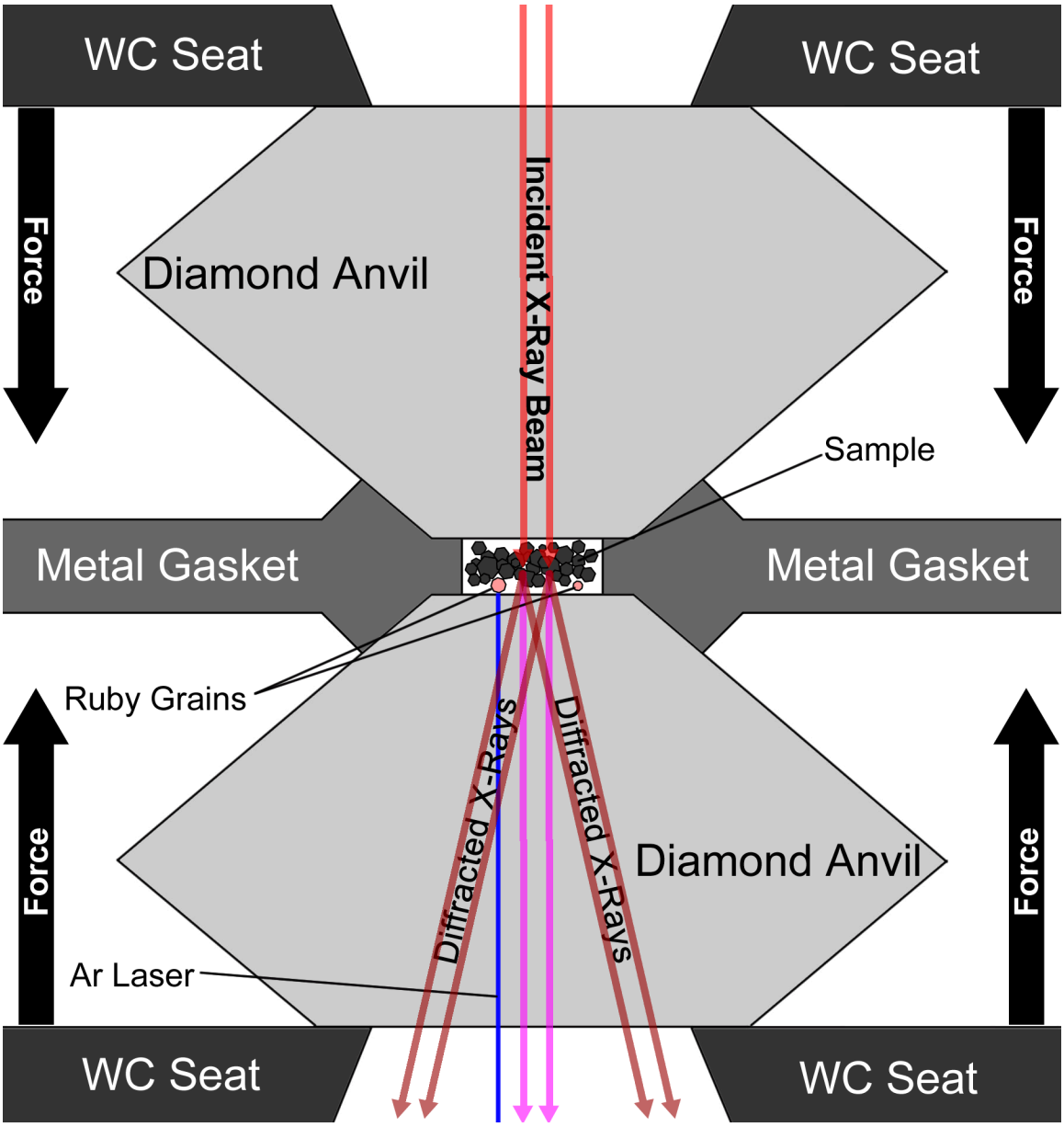

Figure 3.1.2. Schematic diagram of Diamond Anvil Cell experiment. Force is applied uniaxially by squeezing the diamonds together around the gasket, thereby increasing pressure on the sample chamber. Sample material, ruby grains, and pressure medium are loaded in the gasket hole/sample chamber. Pressure is measured by ruby fluorescence using an Ar laser through the diamond. Monochromatic X-ray beam enters through the diamond, and diffracted X-rays from the sample are collected on an imaging plate through the opposite diamond.

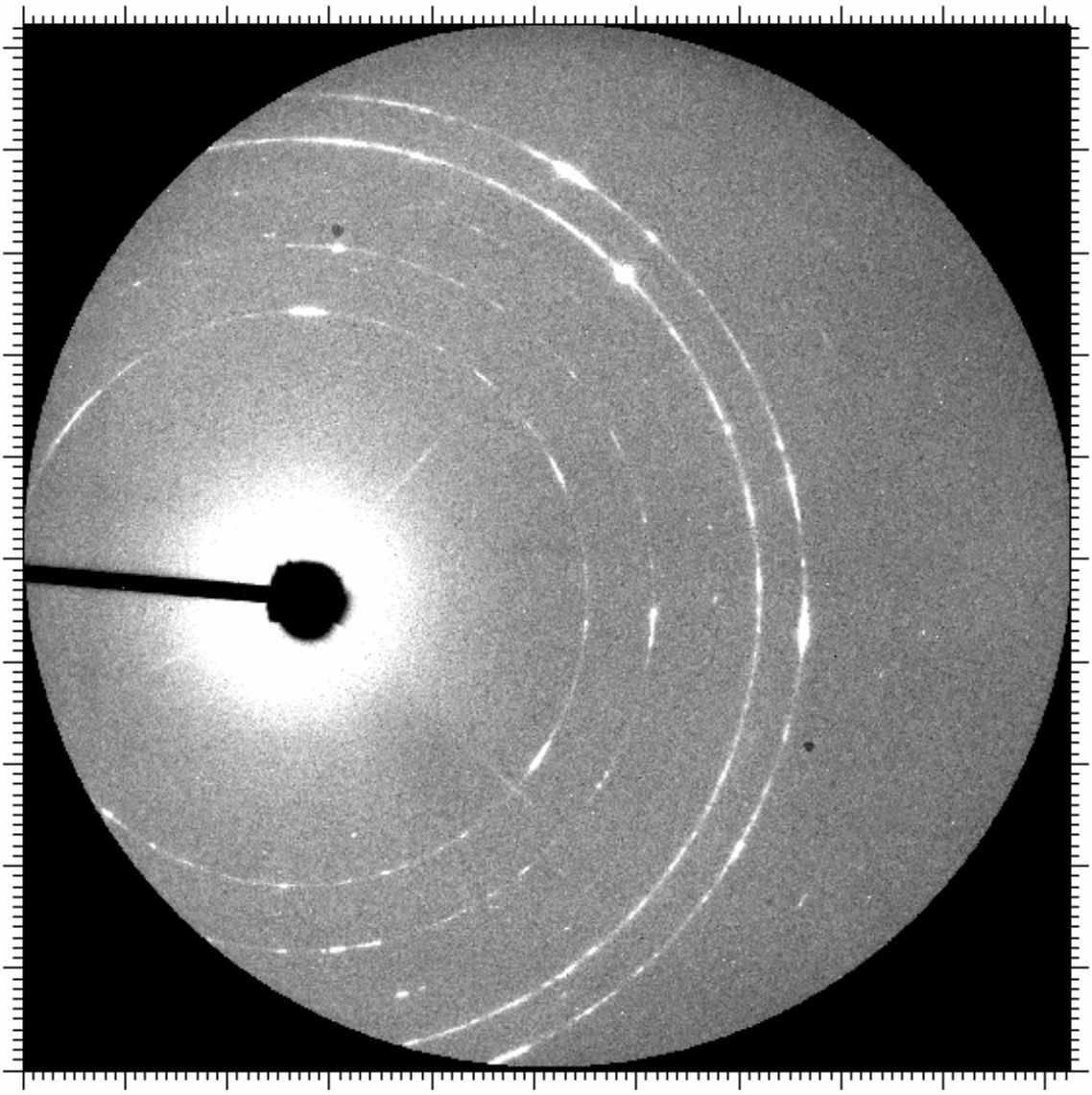

Figure 3.1.3. Example of an X-ray diffraction pattern collected by imaging plate detector at beamline X17C of the NSLS; this pattern is of ε-FeSi at 0 GPa. The black arm and round mass are the image of the beamstop, designed to prevent the majority of the intense X-ray beam from flooding the detector, though the bright halo around the stop shows that some of the corona of the beam still gets through. The Bragg rings collected in this 2-D image can then be integrated to get a standard 1-D diffraction pattern.

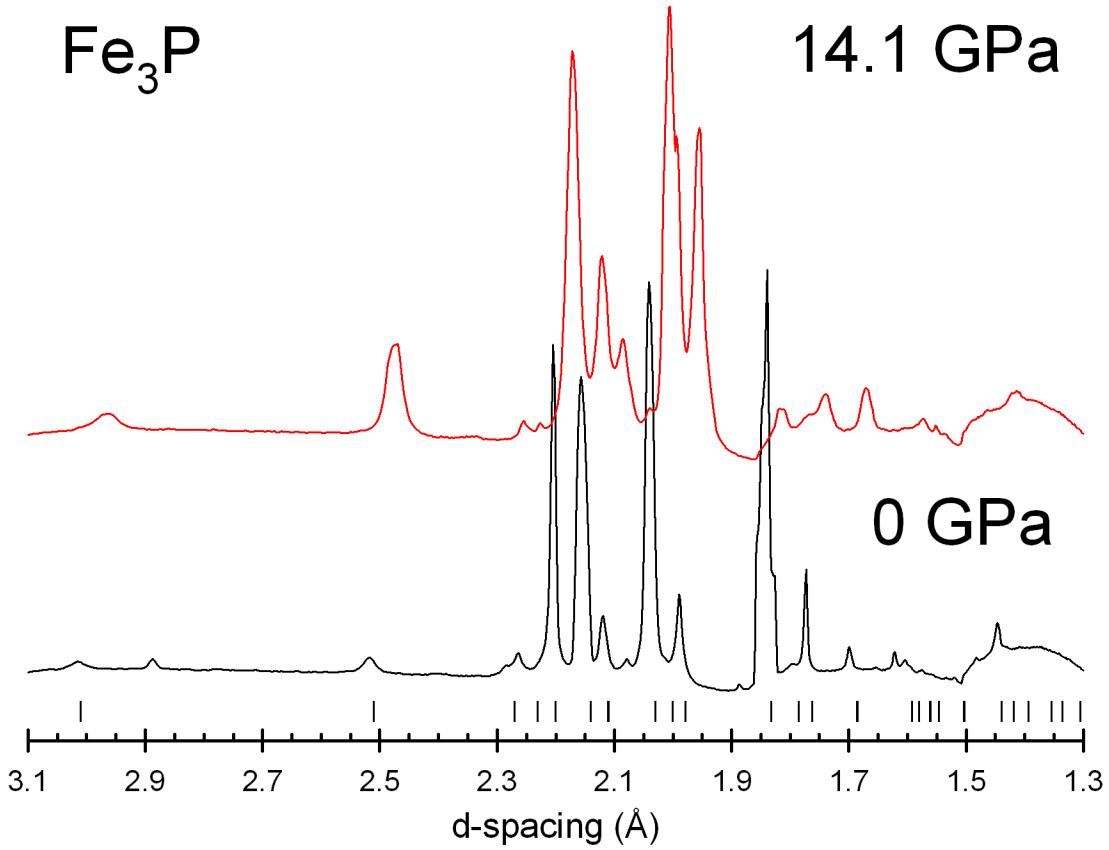

Figure 3.2.1. X-ray diffraction patterns of Fe_3P sample in the Diamond Anvil Cell at 0 GPa and 14.1 GPa. Vertical lines below diffraction pattern indicate peak positions in the standard powder diffraction file that were used to index the pattern. Unmarked peaks are consistent with parasitic scattering from the gasket and ruby pressure marker.

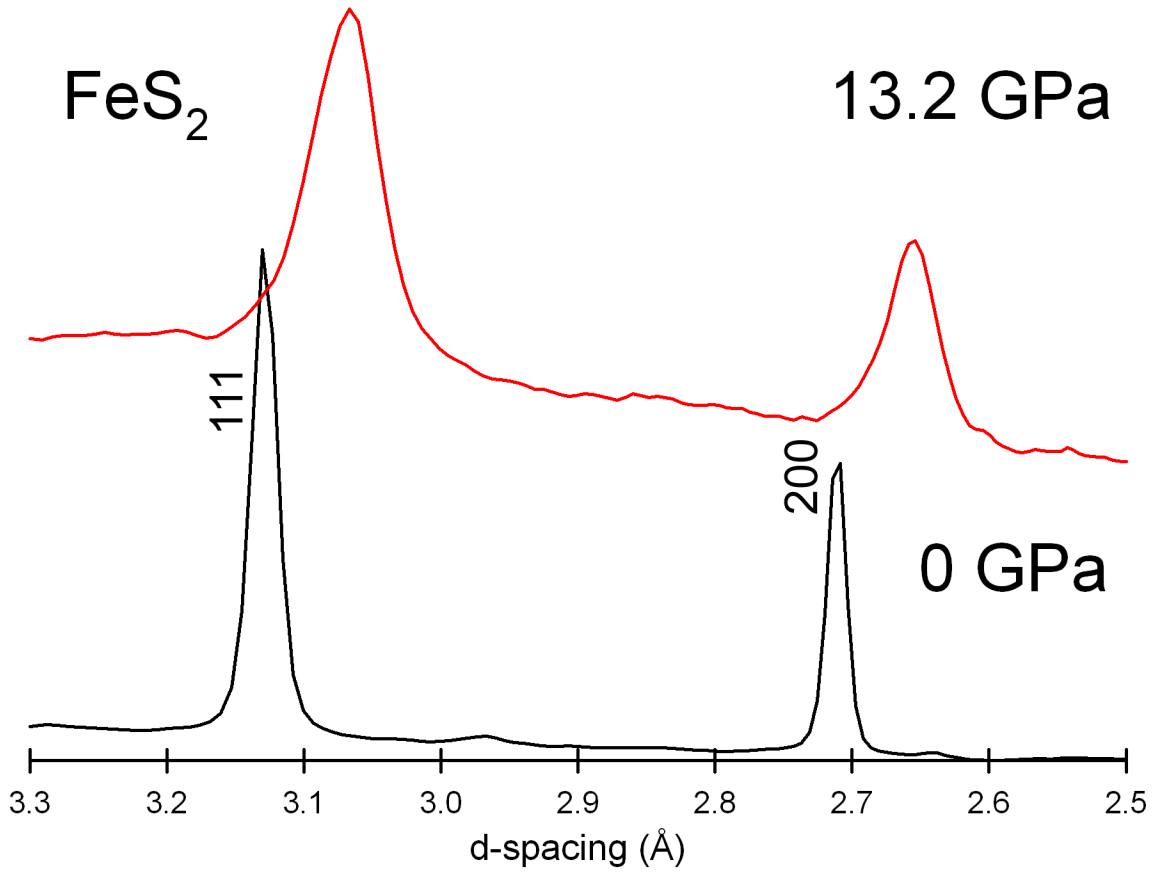

Figure 3.2.2. X-ray diffraction patterns of FeS_2 sample in the Diamond Anvil Cell at 0 GPa and 13.2 GPa. Peaks are labeled with their *hkl* values. Significant peak broadening can be seen in the highest-pressure pattern; this is caused by deviatoric stress on the sample. This pattern was collected above the pressure at which the M-E pressure medium froze. Patterns collected at pressures below the freezing point of the M-E displayed little to no broadening.

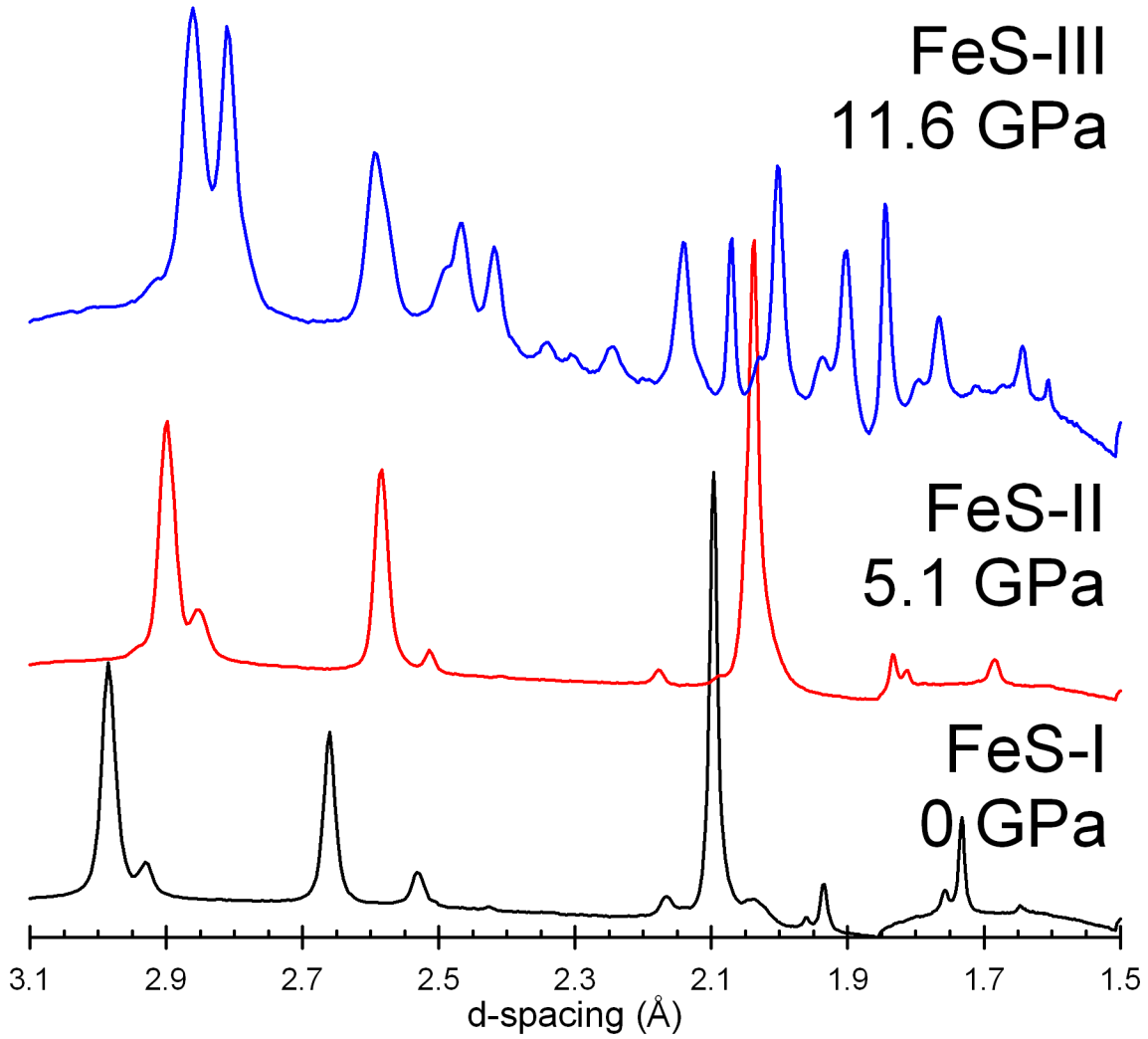

Figure 3.2.3. X-ray diffraction patterns of FeS sample in the Diamond Anvil Cell at 0 GPa (FeS-I, hexagonal), 5.1 GPa (FeS-II, orthorhombic), and 13.2 GPa (FeS-III, monoclinic).

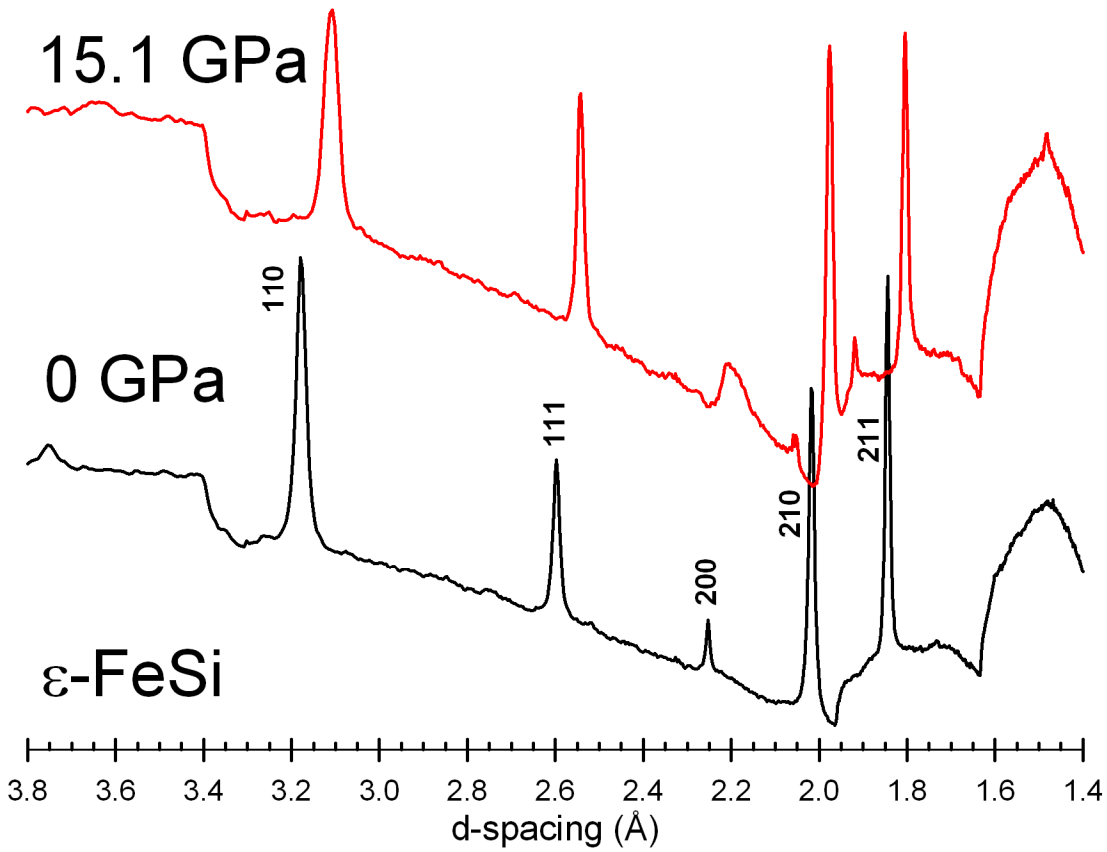

Figure 3.2.4. X-ray diffraction patterns of ε-FeSi sample in the Diamond Anvil Cell at 0 GPa and 15.1 GPa. Some minor broadening of the 110 and 200 peaks in the 15.1 GPa pattern may be caused by some stress on the sample at this highest pressure. The large broadening of the 200 peak and the other small peaks present in the high pressure pattern are consistent with diffraction from the ruby pressure calibrant and minor overlap with the stainless steel gasket.

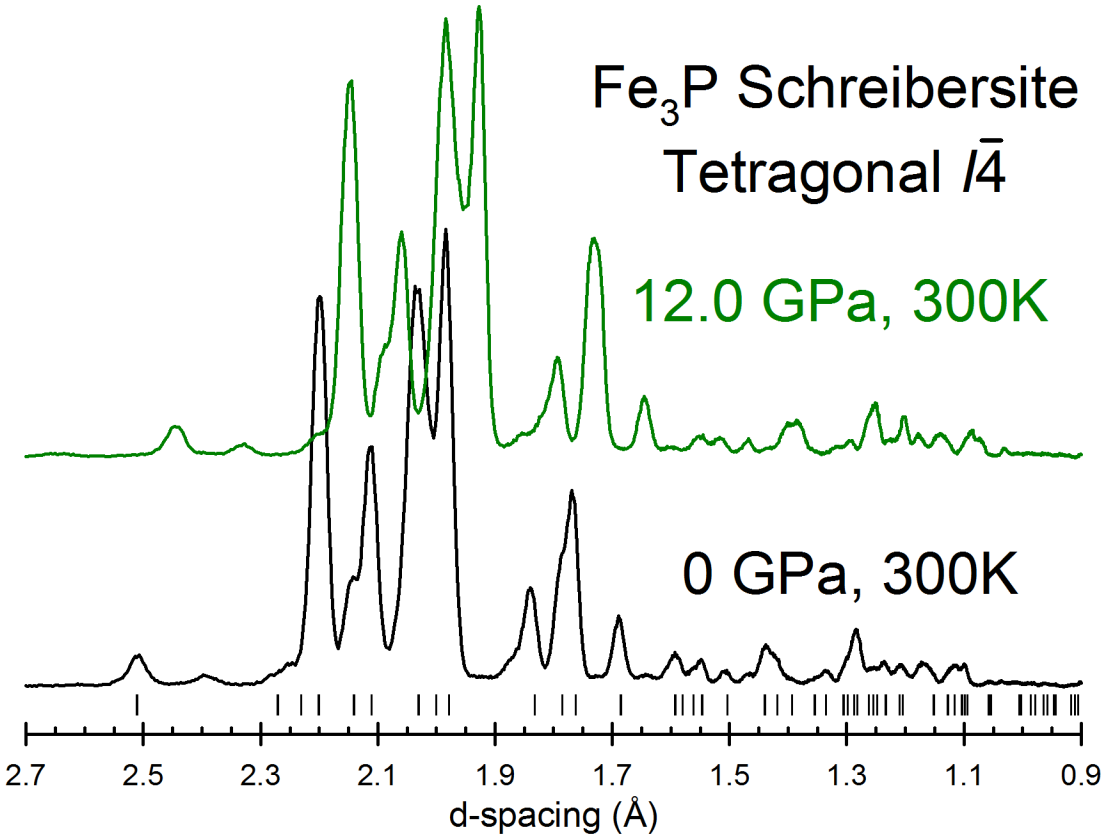

Figure 3.3.1. X-ray diffraction patterns of Fe_3P sample in the multi-anvil experiment at 0 GPa and 12.0 GPa. Vertical lines below diffraction pattern indicate peak positions in the standard powder diffraction file that were used to index the pattern. Unmarked peaks are the result of parasitic scattering from the surrounding material in the cell assembly.

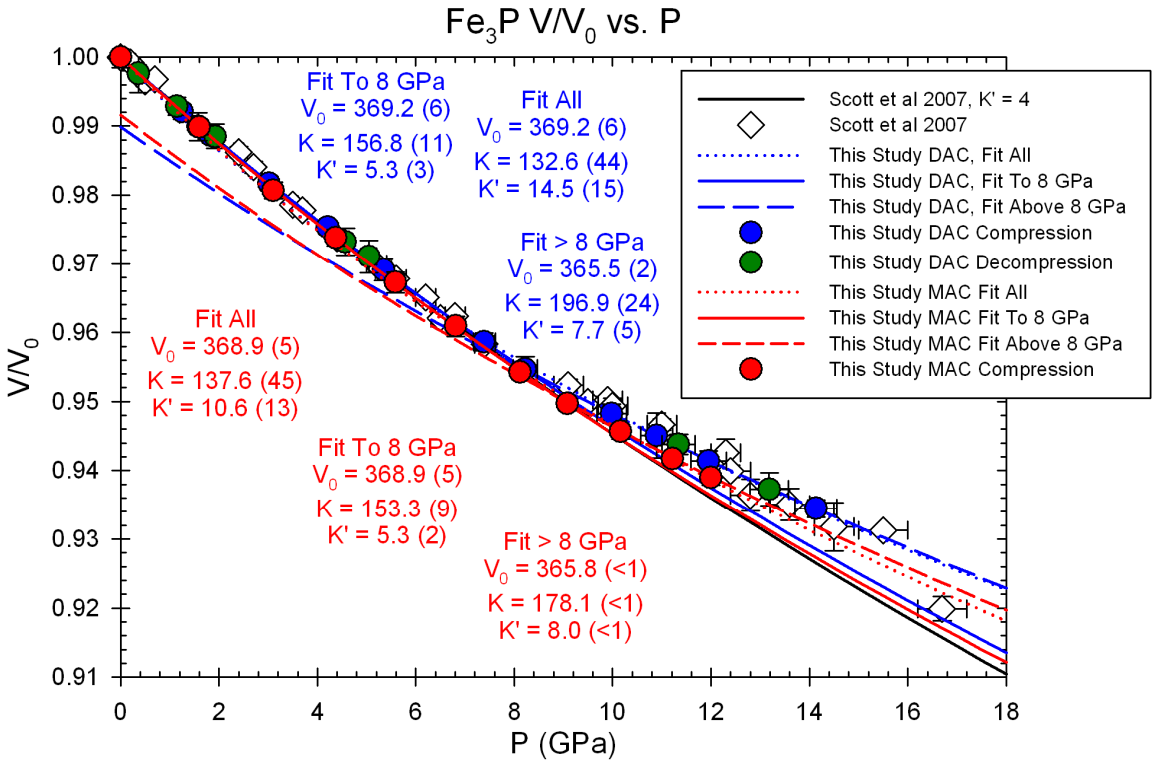

Figure 3.3.2. Volume change vs. pressure for the DAC and MAC experiments on Fe_3P. Reference data plotted in background from Scott et al (2007). Parameters obtained from third-order Birch-Murnaghan fits are shown on diagram. Both experiments exhibited a possible change in the slope of the compression curve at ~8 GPa, which is consistent with the results of Scott et al (2007).

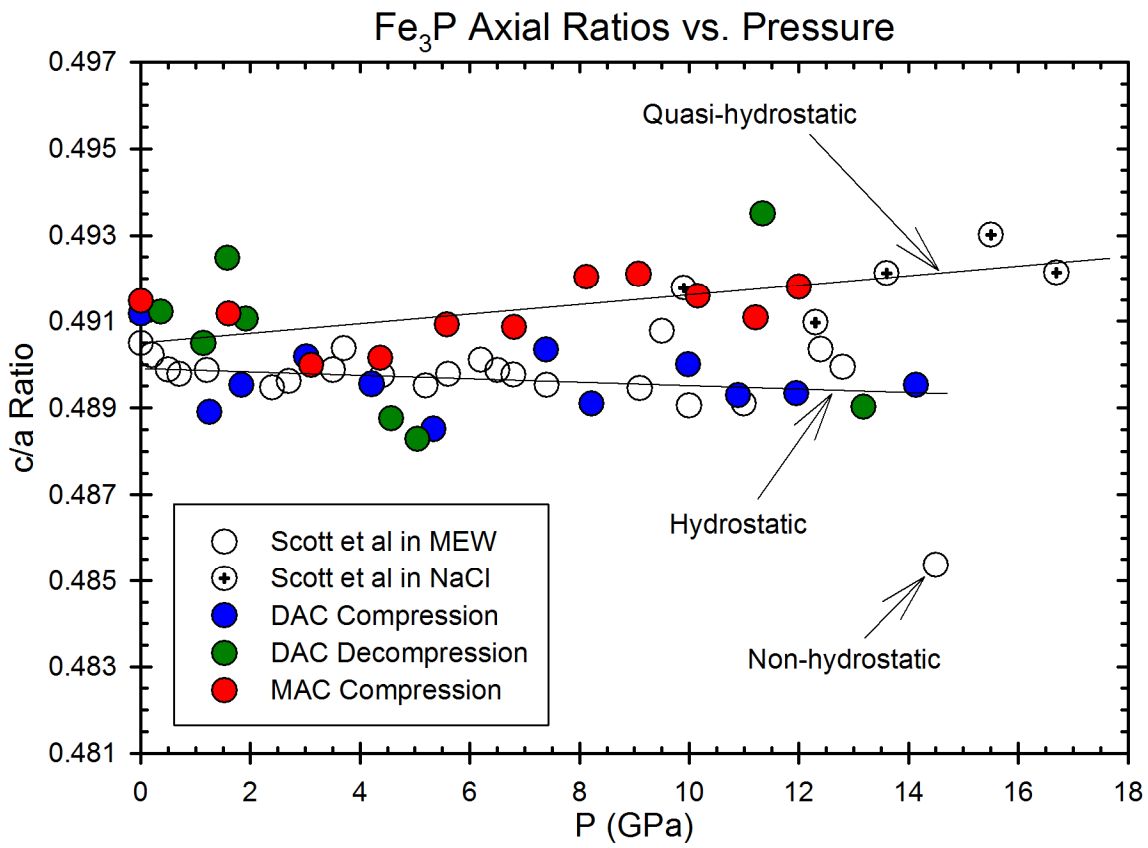

Figure 3.3.3. Variation in c/a ratio in Fe3P with pressure. Data from Scott et al (2007) shown for reference.

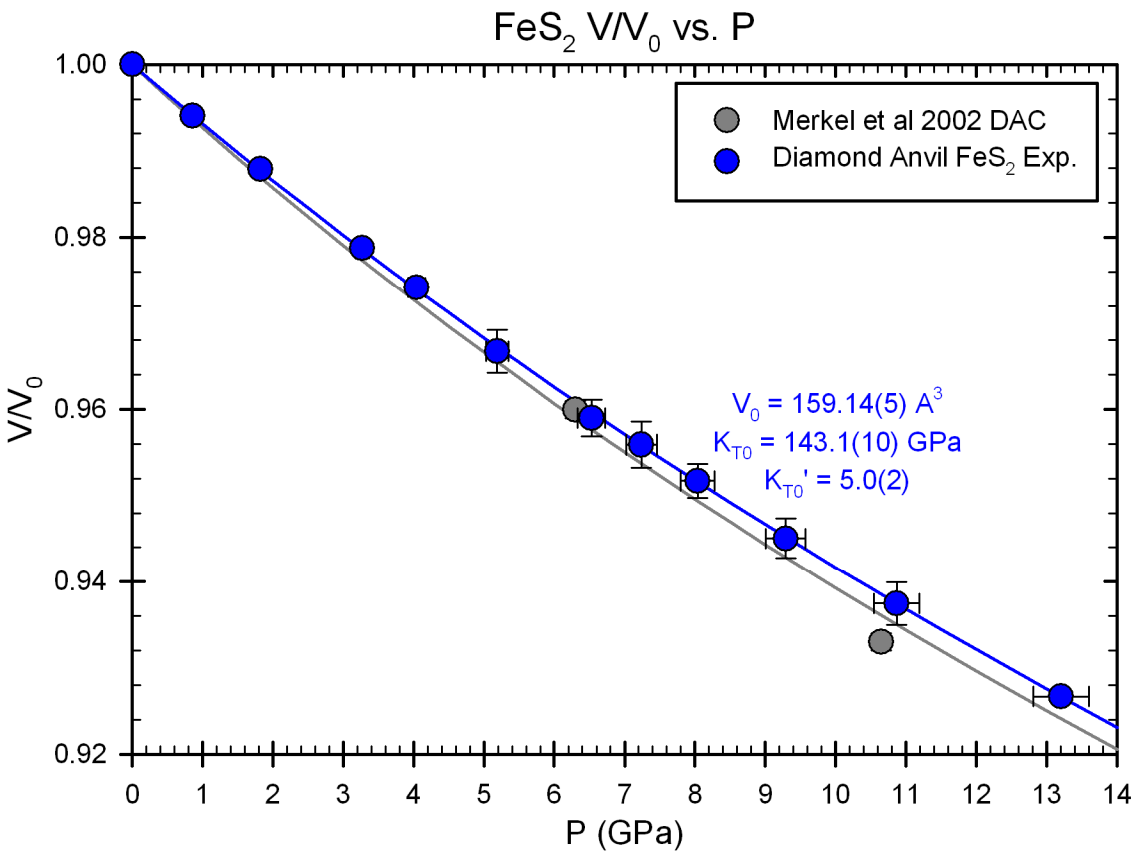

Figure 3.3.4. Volume change vs. pressure for the DAC experiment on FeS_2. Reference data plotted in background from Merkel et al (2002). Parameters obtained from third-order Birch-Murnaghan fits are shown on diagram.

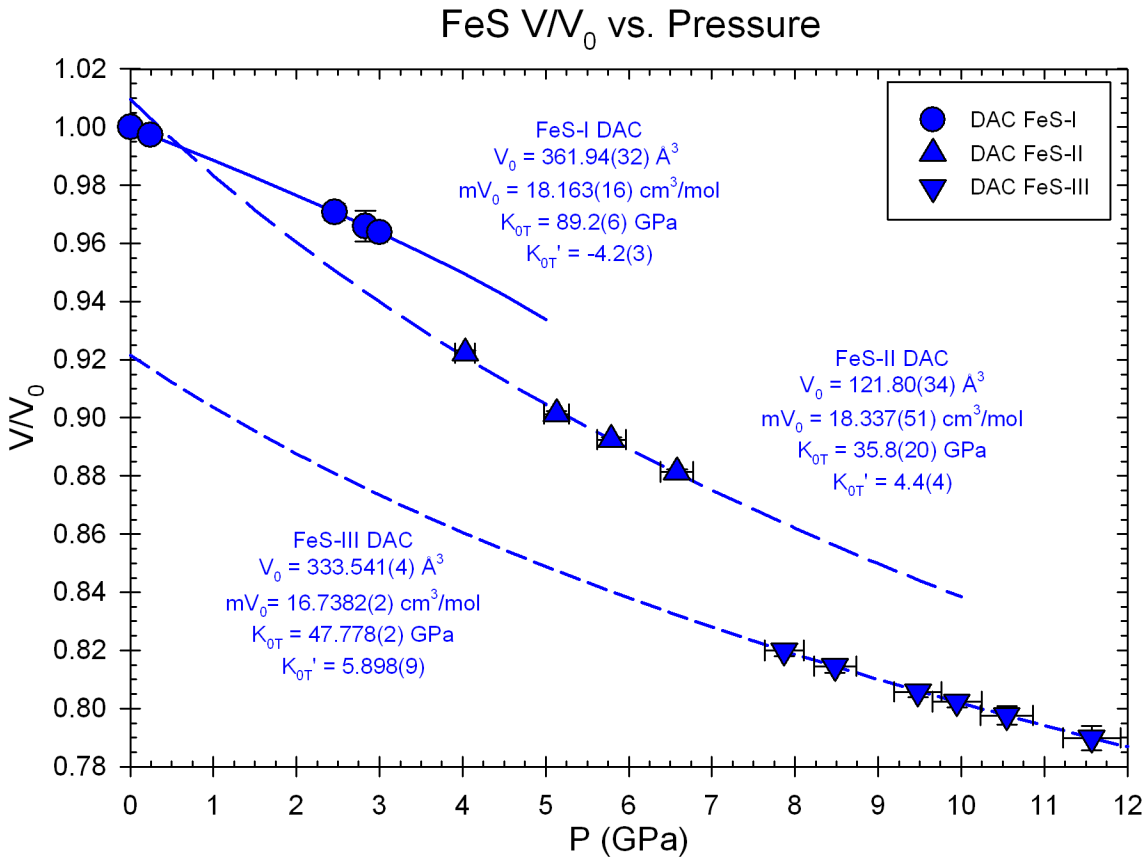

Figure 3.3.5. Volume change vs. pressure for the DAC experiment on FeS. Reference data are unavailable due to a lack of data tables in previous studies. Parameters obtained from third-order Birch-Murnaghan fits of each of the three phases observed during the experiment are shown on diagram.

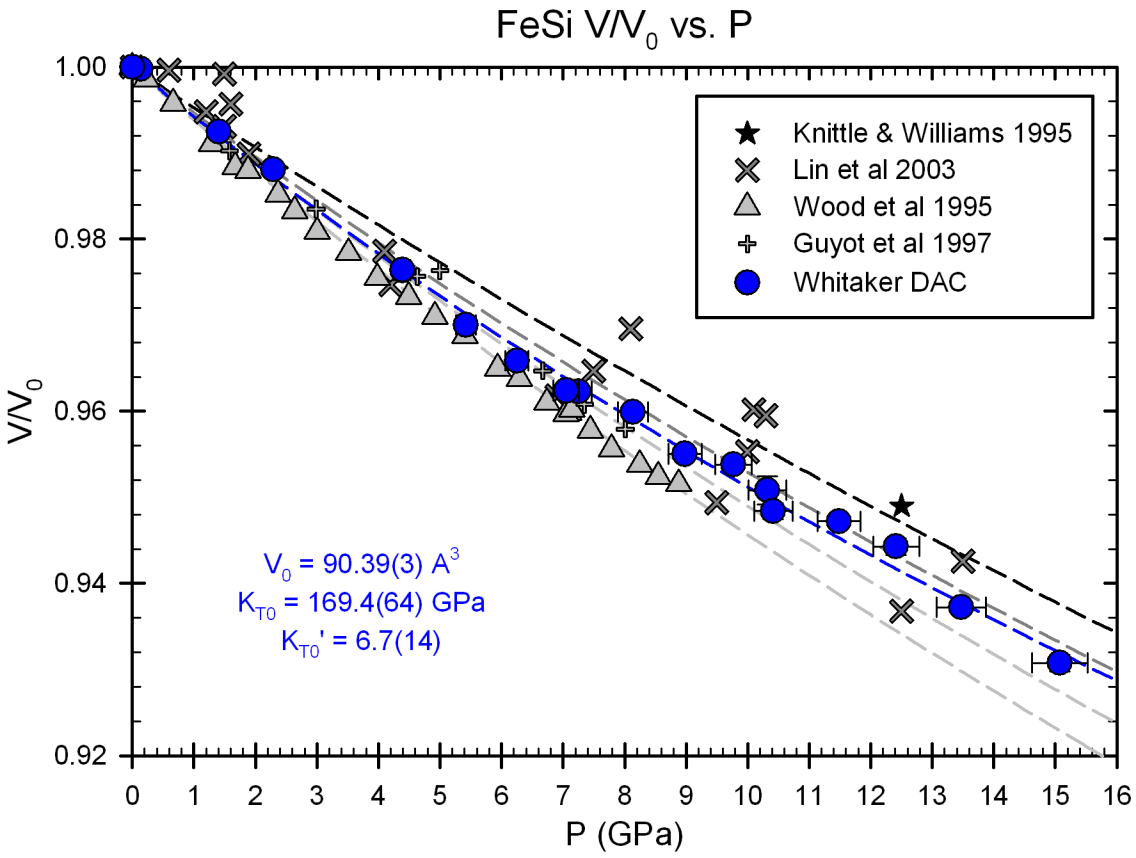

Figure 3.3.6. Volume change vs. pressure for the DAC experiment on ε-FeSi. Reference data plotted in background from Knittle & Willams (1995), Lin et al (2003), Wood et al (1995), and Guyot et al (1997). First two references were experiments in diamond anvil cells, the second two were conducted in multi-anvil apparatuses. Parameters obtained from third-order Birch-Murnaghan fits are shown on diagram.

Table 3.1. Experimental results of static compression experiment on Fe_3P in Diamond Anvil Cell

P (GPa)	σ P (GPa)	a (Å)	σ a (Å)	c (Å)	σ c (Å)	V (Å^3)	σ V (Å^3)	V_m (cm^3 mol^{-1})	σ V_m (cm^3 mol^{-1})	V/V_0	σ V/V_0	ρ (g cm^{-3})
0.00	0.00	9.0925	0.0051	4.4660	0.0050	369.218	0.586	27.793	0.044	1.0000	0.0016	7.143
1.25	0.04	9.0824	0.0036	4.4404	0.0034	366.287	0.404	27.572	0.030	0.9921	0.0011	7.200
1.83	0.05	9.0681	0.0029	4.4391	0.0022	365.028	0.293	27.477	0.022	0.9887	0.0008	7.225
3.02	0.09	9.0429	0.0035	4.4326	0.0028	362.473	0.367	27.285	0.028	0.9817	0.0010	7.276
4.21	0.13	9.0270	0.0037	4.4192	0.0026	360.104	0.366	27.107	0.028	0.9753	0.0010	7.323
5.34	0.16	9.0142	0.0051	4.4036	0.0049	357.813	0.573	26.934	0.043	0.9691	0.0016	7.370
7.39	0.22	8.9704	0.0040	4.3986	0.0044	353.942	0.474	26.643	0.036	0.9586	0.0013	7.451
8.22	0.25	8.9658	0.0050	4.3852	0.0064	352.499	0.647	26.534	0.049	0.9547	0.0018	7.481
9.98	0.30	8.9400	0.0048	4.3806	0.0040	350.114	0.496	26.355	0.037	0.9483	0.0013	7.532
10.89	0.33	8.9344	0.0106	4.3715	0.0156	348.946	1.190	26.267	0.090	0.9451	0.0032	7.558
11.95	0.36	8.9225	0.0056	4.3661	0.0034	347.585	0.534	26.164	0.040	0.9414	0.0014	7.587
14.13	0.42	8.8994	0.0049	4.3565	0.0037	345.027	0.478	25.972	0.036	0.9345	0.0013	7.643
13.18	0.40	8.9113	0.0095	4.3578	0.0061	346.062	0.883	26.050	0.066	0.9373	0.0024	7.621
11.34	0.34	8.9049	0.0043	4.3946	0.0053	348.475	0.541	26.231	0.041	0.9438	0.0015	7.568
5.05	0.15	9.0217	0.0014	4.4051	0.0106	358.533	0.873	26.989	0.066	0.9711	0.0024	7.355
4.57	0.14	9.0254	0.0017	4.4113	0.0086	359.335	0.713	27.049	0.054	0.9732	0.0019	7.339
1.92	0.06	9.0582	0.0052	4.4481	0.0060	364.977	0.646	27.474	0.049	0.9885	0.0018	7.226
1.58	0.05	9.0538	0.0054	4.4588	0.0076	365.497	0.758	27.513	0.057	0.9899	0.0021	7.215
1.14	0.03	9.0751	0.0043	4.4513	0.0040	366.592	0.478	27.595	0.036	0.9929	0.0013	7.194
0.36	0.01	9.0891	0.0077	4.4647	0.0097	368.341	1.017	27.727	0.077	0.9976	0.0028	7.160

Table 3.2. Experimental results of static compression experiment on Fe_3P in Multi-Anvil Cell

P (GPa)	σ P (GPa)	a (Å)	σ a (Å)	c (Å)	σ c (Å)	V (Å^3)	σ V (Å^3)	V_m (cm^3 mol^{-1})	σ V_m (cm^3 mol^{-1})	V/V_0	σ V/V_0	ρ (g cm^{-3})
0.000	0.000	9.0880	0.0046	4.4665	0.0039	368.897	0.462	27.769	0.035	1.0000	0.0015	7.149
1.596	0.016	9.0589	0.0043	4.4495	0.0043	365.146	0.394	27.486	0.030	0.9898	0.0011	7.222
3.104	0.031	9.0383	0.0052	4.4286	0.0050	361.772	0.448	27.232	0.034	0.9807	0.0012	7.290
4.371	0.044	9.0160	0.0051	4.4192	0.0049	359.234	0.435	27.041	0.033	0.9738	0.0012	7.341
5.582	0.056	8.9911	0.0070	4.4140	0.0039	356.829	0.553	26.860	0.042	0.9673	0.0015	7.391
6.809	0.068	8.9717	0.0063	4.4039	0.0061	354.479	0.535	26.683	0.040	0.9609	0.0015	7.440
8.125	0.081	8.9439	0.0036	4.4007	0.0033	352.022	0.302	26.498	0.023	0.9543	0.0008	7.492
9.076	0.091	8.9292	0.0044	4.3941	0.0040	350.346	0.365	26.372	0.027	0.9497	0.0010	7.527
10.162	0.102	8.9195	0.0041	4.3848	0.0039	348.848	0.398	26.260	0.030	0.9457	0.0011	7.560
11.213	0.112	8.9104	0.0038	4.3758	0.0038	347.416	0.341	26.152	0.026	0.9418	0.0009	7.591
11.997	0.120	8.8972	0.0047	4.3757	0.0044	346.384	0.391	26.074	0.029	0.9390	0.0011	7.613

Table 3.3. Comparison of static compression of Fe_3P with previous studies

Ref.	Method	P Range (GPa)	V_0 (Å^3)	K_{T0} (GPa)	K_{T0}'
1	XRD-DAC	0-14	369.2(6)	132.6(44)	14.5(15)
1	XRD-DAC	0-8	369.2(6)	156.8(11)	5.3(3)
1	XRD-DAC	8-14.0	365.5(2)	196.9(24)	7.7(5)
1	XRD-MAC	0-12.0	368.9(5)	137.6(45)	10.6(13)
1	XRD-MAC	0-8	368.9(5)	153.3(9)	5.3(2)
1	XRD-MAC	9-12.0	365.8(<1)	178.1(<1)	8.0(<1)
2	XRD-DAC	0-17	369.5(1)	-	8.5
2	XRD-DAC	0-8	369.5(1)	159(1)	4 (fixed)

1. This Study; 2. Scott et al (2007)

XRD = X-Ray Diffraction; MAC = Multi-Anvil Cell; DAC = Diamond Anvil Cell

Table 3.4. Experimental results of static compression experiment on FeS_2 in Diamond Anvil Cell

P (GPa)	σ P (GPa)	a (Å)	σ a (Å)	V (Å^3)	σ V (Å^3)	V_m (cm^3 mol^{-1})	σ V_m (cm^3 mol^{-1})	V/V_0	σ V/V_0	ρ (g cm^{-3})
0.00	0.00	5.4191	0.0005	159.137	0.046	23.958	0.007	1.0000	0.0003	5.008
0.86	0.03	5.4083	0.0004	158.190	0.039	23.816	0.006	0.9940	0.0002	5.038
1.82	0.05	5.3971	0.0003	157.211	0.022	23.668	0.003	0.9879	0.0001	5.069
3.27	0.10	5.3804	0.0001	155.752	0.011	23.448	0.002	0.9787	0.0001	5.117
4.04	0.12	5.3720	0.0014	155.030	0.122	23.340	0.018	0.9742	0.0008	5.140
5.19	0.16	5.3583	0.0044	153.843	0.382	23.161	0.058	0.9667	0.0025	5.180
6.53	0.20	5.3440	0.0038	152.613	0.322	22.976	0.048	0.9590	0.0021	5.222
7.24	0.22	5.3383	0.0048	152.124	0.413	22.902	0.062	0.9559	0.0027	5.239
8.04	0.24	5.3305	0.0035	151.458	0.299	22.802	0.045	0.9517	0.0020	5.262
9.29	0.28	5.3179	0.0041	150.393	0.347	22.642	0.052	0.9451	0.0023	5.299
10.87	0.33	5.3037	0.0044	149.186	0.367	22.460	0.055	0.9375	0.0025	5.342
13.21	0.40	5.2832	0.0000	147.466	0.004	22.201	0.001	0.9267	0.0000	5.404

Table 3.5. Comparison of static compression of FeS_2 with previous studies

Ref.	Method	P Range (GPa)	V_0 (Å^3)	K_{T0} (GPa)	K_{T0}'
1	XRD-DAC	13.2	159.14(5)	143.1(10)	5.0(2)
2	Linear Compression	0.3	-	148	-
3	Diffuse X-Ray	0	158.34	143.3	-
4*	Ultrasonic	0	158.87	145.9	-
5*	Shockwave	180	-	162(9)	4.7(3)
6	Radial XRD in DAC	50	159.04	133.5(52)	5.73(58)
7	Calculation	Calc. 44 GPa	157.33	154.5	-
8	Calculation	Calc. 150 GPa	158.87	176.21	4.65
9	Calculation	Calc. 135 GPa	159.035	150	4.56

1. This Study; 2. Bridgman (1949); 3. Prasad & Wooster (1956); 4. Simmons & Birch (1963); 5. Ahrens & Jeanloz (1987); 6. Merkel et al (2002); 7. Sithole et al (2003); 8. Blanchard et al (2005); 9. LePage & Rodgers (2005)

XRD = X-Ray Diffraction; DAC = Diamond Anvil Cell; *Adiabatic values

Table 3.6. Experimental results of static compression experiment on FeS in Diamond Anvil Cell

FeS-I (Hexagonal)

P (GPa)	σ P (GPa)	a (Å)	σ a (Å)	b (Å)	σ b (Å)	c (Å)	σ c (Å)	β (°)	σ β (°)	V (Å^3)	σ V (Å^3)	V_m (cm^3 mol^{-1})	σ V_m (cm^3 mol^{-1})	V/V_0	σ V/V_0	ρ (g cm^{-3})
0.00	0.00	5.9712	0.0017	5.9712	0.0017	11.7215	0.0081	120.0000	0.0000	361.939	0.323	18.163	0.016	1.0000	0.0009	4.840
0.24	0.01	5.9678	0.0012	5.9678	0.0012	11.7029	0.0056	120.0000	0.0000	360.947	0.226	18.114	0.011	0.9973	0.0006	4.853
2.46	0.07	5.9312	0.0042	5.9312	0.0042	11.5334	0.0284	120.0000	0.0000	351.376	0.997	17.633	0.050	0.9708	0.0028	4.985
2.83	0.08	5.9010	0.0127	5.9010	0.0127	11.5937	0.0356	120.0000	0.0000	349.620	1.848	17.545	0.093	0.9660	0.0053	5.011
3.00	0.09	5.8912	0.0007	5.8912	0.0007	11.6058	0.0174	120.0000	0.0000	348.832	0.531	17.506	0.027	0.9638	0.0015	5.022

FeS-II (Orthorhombic)

P (GPa)	σ P (GPa)	a (Å)	σ a (Å)	b (Å)	σ b (Å)	c (Å)	σ c (Å)	β (°)	σ β (°)	V (Å^3)	σ V (Å^3)	V_m (cm^3 mol^{-1})	σ V_m (cm^3 mol^{-1})	V/V_0	σ V/V_0	ρ (g cm^{-3})
4.03	0.12	5.7222	0.0031	3.3587	0.0024	5.7895	0.0040	90.0000	0.0000	111.269	0.108	16.752	0.016	0.9223	0.0010	5.248
5.13	0.15	5.6767	0.0031	3.3354	0.0024	5.7427	0.0039	90.0000	0.0000	108.733	0.105	16.370	0.016	0.9013	0.0010	5.370
5.79	0.17	5.6589	0.0027	3.3266	0.0021	5.7197	0.0034	90.0000	0.0000	107.673	0.092	16.210	0.014	0.8925	0.0009	5.423
6.58	0.20	5.6341	0.0031	3.3141	0.0026	5.6948	0.0032	90.0000	0.0000	106.333	0.099	16.008	0.015	0.8814	0.0009	5.492

FeS-III (monoclinic)

P (GPa)	σ P (GPa)	a (Å)	σ a (Å)	b (Å)	σ b (Å)	c (Å)	σ c (Å)	β (°)	σ β (°)	V (Å^3)	σ V (Å^3)	V_m (cm^3 mol^{-1})	σ V_m (cm^3 mol^{-1})	V/V_0	σ V/V_0	ρ (g cm^{-3})
7.87	0.24	8.1178	0.0058	5.6663	0.0085	6.4637	0.0059	93.4509	0.0657	296.774	0.561	14.893	0.028	0.8200	0.0019	5.903
8.48	0.25	8.1043	0.0066	5.6501	0.0098	6.4493	0.0067	93.3832	0.0579	294.798	0.643	14.794	0.032	0.8145	0.0022	5.942
9.48	0.28	8.0695	0.0061	5.6221	0.0082	6.4391	0.0064	93.3473	0.0664	291.629	0.561	14.635	0.028	0.8057	0.0019	6.007
9.95	0.30	8.0432	0.0070	5.6256	0.0065	6.4281	0.0093	93.1465	0.0854	290.417	0.594	14.574	0.030	0.8024	0.0020	6.032
10.55	0.32	8.0272	0.0139	5.6001	0.0040	6.4316	0.0165	93.0885	0.1400	288.703	0.919	14.488	0.046	0.7977	0.0032	6.068
11.57	0.35	7.9916	0.0161	5.5876	0.0085	6.4127	0.0210	93.2510	0.1537	285.891	1.190	14.347	0.060	0.7899	0.0042	6.127

Table 3.7. Comparison of elastic properties of FeS with previous studies

FeS-I						
Ref.	Method	P Range (GPa)	Fit Conditions	V_0 (cm^3 mol^{-1})	K_{T0} (GPa)	K_{T0}'
1	XRD-DAC	3	0 GPa, 300K	18.163(16)	89.2(6)	-4.2(3)
2	XRD-DAC	3.4	0 GPa, 300K	18.162(54)	82(7)	-5(4)
3	XRD-MAC	3	0 GPa, 300K	18.191(20)	73(3)	4 (fixed)
4	Calculation	Calc. ~5 GPa	0 GPa, 300K	17.500(12)	75.6(7)	-0.9(2)
5	Calculation	Calc. 0-2.3 GPa	0 GPa, 17K	18.181	257(4)	4 (fixed)
5	Calculation	Calc. 2.3-5 GPa	0 GPa, 17K	18.181	109(3)	4 (fixed)
FeS-II						
Ref.	Method	P Range (GPa)	Fit Conditions	V_0 (cm^3 mol^{-1})	K_{T0} (GPa)	K_{T0}'
1	XRD-DAC	4 - 6.6	0 GPa, 300K	18.337(52)	35.8(20)	4.4(4)
2	XRD-DAC	3.6 - 6.4	0 GPa, 300K	18.44(4)	35(4)	5(2)
3	XRD-MAC	3.0 - 7.0	? GPa, 300K	-	44(3)	4 (fixed)
4	Calculation	Calc. 0-9 GPa	-	16.765(6)	76.8(3)	2.20(9)
5	Calculation	Calc. 5-7 GPa	? GPa, 17K	-	67(5)	4 (fixed)
FeS-III						
Ref.	Method	P Range (GPa)	Fit Conditions	V_0 (cm^3 mol^{-1})	K_{T0} (GPa)	K_{T0}'
1	XRD-DAC	7.9 - 11.6	0 GPa, 300K	16.738(1)	47.777(3)	5.898(9)
3	XRD-MAC	7 - 14.5	10.3 GPa, 300K	14.555	49(2)	4 (fixed)
4	Calculation	Calc. 0-25 GPa	-	14.844(18)	157.7(8)	4.72(3)
5	Calculation	Calc. 8-28 GPa	? GPa, 17K	-	153(3)	4 (fixed)

1. This Study; 2. King & Prewitt (1982); 3. Kusaba et al (1997); 4. Martin et al (2001); 5. Kobayashi et al (2005)

XRD = X-Ray Diffraction; MAC = Multi-Anvil Cell; DAC = Diamond Anvil Cell

Table 3.8. Experimental results of static compression experiment on ε-FeSi in Diamond Anvil Cell

P (GPa)	σ P (GPa)	a (Å)	σ a (Å)	V (Å^3)	σ V (Å^3)	V_m (cm^3 mol^{-1})	σ V_m (cm^3 mol^{-1})	V/V_0	σ V/V_0	ρ (g cm^{-3})
0.00	0.00	4.4880	0.0005	90.395	0.030	13.609	0.005	1.0000	0.0003	6.167
1.41	0.04	4.4767	0.0005	89.715	0.028	13.507	0.004	0.9925	0.0003	6.214
4.39	0.13	4.4523	0.0006	88.256	0.038	13.287	0.006	0.9763	0.0004	6.317
6.25	0.19	4.4363	0.0007	87.310	0.042	13.145	0.006	0.9659	0.0005	6.385
7.25	0.22	4.4308	0.0003	86.987	0.016	13.096	0.002	0.9623	0.0002	6.409
8.14	0.24	4.4271	0.0006	86.769	0.035	13.063	0.005	0.9599	0.0004	6.425
9.77	0.29	4.4178	0.0007	86.220	0.041	12.980	0.006	0.9538	0.0005	6.466
10.32	0.31	4.4131	0.0024	85.949	0.140	12.940	0.021	0.9508	0.0016	6.486
11.48	0.34	4.4076	0.0009	85.626	0.055	12.891	0.008	0.9472	0.0006	6.511
12.41	0.37	4.4030	0.0014	85.358	0.080	12.851	0.012	0.9443	0.0009	6.531
13.47	0.40	4.3920	0.0011	84.720	0.063	12.755	0.010	0.9372	0.0007	6.580
15.08	0.45	4.3819	0.0014	84.138	0.080	12.667	0.012	0.9308	0.0010	6.626
10.42	0.31	4.4094	0.0013	85.732	0.078	12.907	0.012	0.9484	0.0009	6.503
8.98	0.27	4.4197	0.0009	86.332	0.054	12.997	0.008	0.9551	0.0006	6.458
7.05	0.21	4.4310	0.0009	86.996	0.050	13.097	0.008	0.9624	0.0006	6.408
5.42	0.16	4.4427	0.0013	87.688	0.077	13.201	0.012	0.9701	0.0009	6.358
2.29	0.07	4.4701	0.0005	89.318	0.030	13.447	0.005	0.9881	0.0003	6.242
0.14	0.00	4.4876	0.0009	90.375	0.055	13.606	0.008	0.9998	0.0006	6.169

Table 3.9. Comparison of static compression of ε-FeSi with previous studies

Ref.	Method	P Range (GPa)	V_0 (Å^3)	K_{T0} (GPa)	K_{T0}'
1	XRD-DAC	15	90.40(3)	169.4(64)	6.7(14)
2*	Resonant Ultrasonics	0	-	173	-
3	XRD-DAC	50	89.015	209	3.5
4	Neutron	9	90.21(2)	160	4 (fixed)
5	XRD-DAC	8.25	90.39(4)	172	4 (fixed)
6	XRD-DAC	50.7	90.193	184.7	4.75
7	Calculation	Calculated	88.896	227	3.9
8	Calculation (LDA)	Calculated	84.09	255	4.143
8	Calculation (GGA)	Calculated	90.174	221	4.175

1. This Study; 2. Sarrao et al (1994); 3. Knittle & Williams (1995); 4. Wood et al (1995); 5. Guyot et al (1997); 6. Lin et al (2003); 7. Vocadlo et al (1999); 8. Caracas & Wentzcovitch (2004)
XRD = X-Ray Diffraction; DAC = Diamond Anvil Cell; *Adiabatic values

CHAPTER 4. P-V-T-V_P-V_S EQUATION OF STATE STUDIES

Static compression experiments and P-V equation of state studies can be very useful in understanding how a material behaves under pressure. While these types of studies can determine the compressibility and density of a material, and how those properties change with pressure, there are still many questions that remain unaddressed by these experiments. In order to determine the elasticity of a material, not only must the bulk modulus be determined, but the shear properties must also be measured. Over the last several years, *in situ* high pressure experiments have been developed using a combination of synchrotron X-rays and ultrasonic interferometry in multi-anvil apparatus that allow for making these types of measurements. These experiments, much like the previously discussed static compression experiments, also measure the volume of a material at high pressure, in addition to using ultrasonics to measure acoustic wave speeds in the sample, thereby determining its elastic properties.

The experimental results presented in Chapter 3, while useful, only provide information about the density and compressibility of each of those materials under pressure. Previous studies have used this information to try to place constraints on possible compositions of the Earth's core. However, one major drawback to these approaches is the lack of information regarding the shear properties of these materials. Utilization of ultrasonic interferometry in conjunction with synchrotron X-rays allows for the direct measurement of both the compressional and shear velocities of these materials as a function of pressure and temperature, yielding a more complete dataset that can then be used to compare to seismic profiles of the Earth's core.

4.1 – Experimental Procedure

Ultrasonic interferometry utilizes a piezoelectric transducer that both sends and receives acoustic waves. The transducer generates a pulse that travels through the experimental assembly, is reflected at different interfaces within the assembly, and is then recorded by the same transducer. The time delay between the pulse generation and the recording of the return pulse is the two-way travel time of that acoustic wave. These travel times can then be used to determine seismic wave speeds which, when combined with the volume data obtained from synchrotron X-ray diffraction, gives a direct measurement of the elastic bulk and shear moduli of the material. While these experiments in the multi-anvil press are more limited than the diamond anvil cell in terms of pressure generation, they are capable of generating a wealth of useful information not easily attainable any other way.

The samples for these experiments were synthesized and prepared as described in Chapter 2 of this dissertation. The *in situ* ultrasonic experiments were conducted in the DIA-type SAM85 press installed at beamline X17B2 at the NSLS. A DIA-type multi-anvil press consists of 6 anvils coming together in a cubic arrangement (Figure 4.1.1 a). Anvils are attached to the top and bottom of the press itself, and then the four anvils in

the horizontal plane have tapered back blocks (Figure 4.1.1 b). Force is applied vertically by the hydraulic ram in the press which causes the six anvils to uniformly apply pressure to the cell assembly (Figure 4.1.1 c).

A schematic of the cell assembly used in these experiments is shown in Figure 4.1.2. The Boron-Epoxy cube was made of a 4:1 mixture ground in acetone for approximately 30 minutes, and then allowed to dry for 1 hour to ensure evaporation of the acetone. The B-E mixture was then pressed into a mold at a pressure of ~850-950 P.S.I. The finished cube was then placed in an oven at 150°C for 30 minutes to cure. Holes were then drilled into opposite edges of the cube to facilitate the use of thermocouples in the experiment. The alumina sleeve, graphite furnace, MgO plug, and BN sleeve were then put in place, and holes were hand-drilled through these layers to allow the thermocouple to be in direct contact with the sample during the experiment to ensure that the temperature reading is as accurate as possible. Though Figure 4.1.2 only shows a single thermocouple, the cell assembly actually has two thermocouples coming in opposite edges of the cube as shown in Figure 4.1.3.

The thermocouples were then glued into place using zirconia cement, after which the BN disc was loaded into the BN sleeve. The NaCl:BN powder mixture was then loaded into the BN cup, followed by the sample and the alumina buffer rod. 1μm-thick discs of gold foil were placed between the sample and salt, and between the buffer rod and sample, and then a square of gold foil was glued across the cell face and buffer rod to hold the cell together. These layers of gold foil served two major purposes; first, to enhance the mechanical coupling between the surfaces and second to act as markers in the X-radiographic images collected during the experiment.

The BN capsule and the NaCl:BN powder (10:1 wt. %) mixture provide a pseudohydrostatic environment for the sample. NaCl also serves as a pressure marker during the experiment. To ensure that there was a minimal loss of acoustic energy at the interfaces between materials, all surfaces along the acoustic travel path were polished with 1μm diamond paste to be perfectly flat and parallel within 0.05°; this includes the WC anvil on which the transducer was mounted, and both sides of the alumina buffer rod and sample.

A schematic of the experimental setup is shown in Figure 4.1.4. Unlike the monochromatic X-rays used in the previously discussed DAC experiments, these experiments utilized white beam, which were polychromatic X-rays with a large energy range. The incident X-ray beam was collimated to a size of 0.1 mm × 0.1 mm. Pressure was controlled and maintained by the press. At each desired set of P-T conditions, an X-radiographic image of the sample was taken, ultrasonic data were collected, and an energy dispersive X-ray diffraction pattern for both the NaCl pressure calibrant and the sample were collected.

The ultrasonic measurements were conducted using a dual-mode $LiNbO_3$ transducer (10° Y-cut) that was capable of generating and receiving frequencies from 20 to 70 MHz, which allows us to determine the travel times of both P and S waves simultaneously, with a standard deviation of ~0.2 ns and ~0.4 ns respectively. At least 1000 acquisitions were averaged to maximize the signal-to-noise ratio. We use the transfer function method (Li et al., 2002) to record the acoustic response of the cell assembly in the frequency range of 20-70MHz; we then extract the monochromatic waveform data from these measurements and use the pulse echo overlap (PEO) technique to determine the two-way travel times of

P and S waves going through the sample. An example of the ultrasonic signal in ε-FeSi for P waves at 60 MHz is shown in Figure 4.1.4 b). For more information on the ultrasonic measurements and how they are processed, see (Li et al., 2002; Li et al., 2004).

The CCD camera in the experimental setup was used to record snapshot X-radiographic images of the cell assembly. In these images, the sample region can be identified by the contrasting brightness due to the difference in the X-ray absorption coefficients (Figure 4.1.5). This provides a direct means of determining the length of the sample during the experiment, and the precision of this direct image measurement of sample length has been shown to be 0.2-0.4% (Li et al., 2004). By determining the length of the sample in pixels at the end of the experiment when the press is opened, and then measuring the absolute length of the sample after the experiment, the pixel to length ratio can be calibrated, and thereby the absolute length of the sample at all P-T conditions can be determined. Figure 4.1.5 shows X-radiographic images of the ε-FeSi sample, and shows clearly the change in sample length during compression. From the lengths and travel times, the P and S wave velocities in the sample at all conditions can then be directly obtained.

4.2 – Data Processing and Analysis

The raw X-ray diffraction patterns were analyzed using Plot85, which is a program written by Ken Baldwin at Stony Brook University that is designed to process X-ray diffraction data collected at X17B2. Standard powder diffraction files for each material were used as references to index the peaks in the pattern. Plot85 was used to fit and index individual peaks in the X-ray diffraction patterns, carry out the unit cell refinements, and calculate the pressure based on the diffraction pattern of the NaCl standard.

The X-radiographic images were processed using a program called UImage written by Baosheng Li at Stony Brook University. This program gave the brightness of the image as a function of vertical pixel number, which was then used to determine the length of the sample in pixels; the pixel-to-length ratio was then applied to each of these pixel length measurements to determine the absolute length of the sample.

The ultrasonic data was processed using the PEO-TDS program, also written by Baosheng Li. This program imports the full ultrasonic signal, and then allows for the extraction of a single frequency from the 20-70 MHz dataset that was collected. The Pulse-Echo Overlap (PEO) technique was then used on the monochromatic waveform to overlay the buffer rod signal with the sample signal. The time offset observed when an exact match is found is the two-way travel time of the acoustic wave through the sample.

This entire process was repeated for every set of conditions in a given experiment. The unit cell volumes obtained from the cell refinements were used to calculate the theoretical density of the material. The sample lengths and the two-way travel times of the acoustic waves give the P and S wave velocities in the sample. The shear ($G = \rho V_S^2$) and adiabatic bulk ($K_S = \rho V_P^2 - 4G/3$) moduli at high pressures and temperatures are obtained directly from the densities and acoustic velocities. The density (ρ) and velocity (V_P, V_S) data are simultaneously fit to the third-order finite strain equations (i.e., Davies and Dziewonski, 1975):

$$\rho V_P^2 = (1-2\varepsilon)^{5/2}(L_1 + L_2\varepsilon) \tag{4.1}$$

$$\rho V_S^2 = (1-2\varepsilon)^{5/2}(M_1 + M_2\varepsilon) \tag{4.2}$$

where the volume strain on the sample (ε) is given by

$$\varepsilon = \frac{1-(V_0/V)^{2/3}}{2}. \tag{4.3}$$

The adiabatic bulk and shear moduli and their isothermal pressure derivatives [$K_{S(0,300)}$; $K_{S(0,300)}' = (\partial K_{S(0,300)}/\partial P)_T$; $G_{(0,300)}$; $G_{(0,300)}' = (\partial G_{(0,300)}/\partial P)_T$] are related to the fitting coefficients through the following equations:

$$M_1 = G \tag{4.4}$$

$$M_2 = 5G - 3K_S G' \tag{4.5}$$

$$L_1 = K_S + \frac{4G}{3} \tag{4.6}$$

$$L_2 = 5L_1 - 3K_S\left(K_S' + \frac{4G'}{3}\right) \tag{4.7}$$

In order to more directly compare the adiabatic results obtained from this fitting with the results of previous studies, which are predominantly isothermal, these data can be converted to isothermal values using the relationship $K_S/K_T = (1 + \alpha\gamma T)$, where α is the thermal expansion coefficient and γ is the Grüneisen parameter. The pressure on the sample is then calculated directly using the 3rd-order Birch-Murnaghan equation introduced in Chapter 3:

$$P(V,T) = \frac{3}{2}K_{0T}\left[\left(\frac{V_{0T}}{V}\right)^{7/3} - \left(\frac{V_{0T}}{V}\right)^{5/3}\right]\times\left\{1+\frac{3}{4}(K'_{0T}-4)\left[\left(\frac{V_{0T}}{V}\right)^{2/3}-1\right]\right\} \tag{3.1}$$

The pressures calculated in this manner are presented in the data tables for the room temperature experiments in the following sections, and are used in the figures and discussion that follow.

The temperature derivatives of the elastic moduli [$(\partial K_{S(0,300)}/\partial T)_P$; $(\partial G_{(0,300)}/\partial T)_P$] were obtained by fitting all of the data at high temperature and high pressure. To do this, the entire dataset was fitted to equations (4.1)-(4.7) along individual isentropes, assuming the pressure at each data point was raised along an adiabatic path from zero pressure with different foot temperatures; in this way, we account for the fact that the acoustic response of the sample is measured adiabatically, while the experiment is conducted isothermally. The adiabatic foot temperature (T_0) for each data point, and the thermoelastic properties at zero pressure and T_0, are related to their values at zero pressure and room temperature via the following equations:

$$\left(\frac{\partial T}{\partial P}\right)_S = \frac{\gamma_{(0,T0)} T_0}{K_S} \tag{4.8}$$

$$\rho_{0,T_0} = \rho_{0,300} \mathrm{e}^{-\int \alpha dT_0} \tag{4.9}$$

$$K_{S(0,T_0)} = K_{S(0,300)} + (T_0 - 300)\left(\frac{\partial K_S}{\partial T}\right)_P \tag{4.10}$$

$$G_{(0,T_0)} = G_{(0,300)} + (T_0 - 300)\left(\frac{\partial G}{\partial T}\right)_P \tag{4.11}$$

$$K'_{SS(0,T_0)} = \left(K'_{S(0,300)} + (T_0 - 300)\left(\frac{\partial^2 K_S}{\partial P \partial T}\right)_P\right) + \left(\frac{\partial K_S}{\partial T}\right)_P \left(\frac{\gamma T_0}{K_S}\right) \tag{4.12}$$

$$G'_{S(0,T_0)} = \left(G'_{S(0,300)} + (T_0 - 300)\left(\frac{\partial^2 G_S}{\partial P \partial T}\right)_P\right) + \left(\frac{\partial G}{\partial T}\right)_P \left(\frac{\gamma T_0}{K_S}\right) \tag{4.13}$$

where α is the thermal expansion coefficient ($\alpha = a + bT + cT^2$). More details about the data analysis procedures can be found elsewhere (i.e., Li and Zhang, 2005; Liu et al., 2005). In conducting all of these calculations, the assumptions that $\rho\gamma$ = constant and that the cross-derivatives [$(\partial^2 K_S/\partial P \partial T)_P$ and $(\partial^2 G/\partial P \partial T)_P$] are equal to zero are employed. The pressure on the sample can then be concurrently calculated from these fitted elastic parameters (Eq. 4.14), without relying on an external pressure standard.

$$P = -(1 - 2\varepsilon)^{5/2}\left(3K_{S(0,T_0)}\varepsilon + \left(\frac{\left(36K_{S(0,T_0)} - 9K_{S(0,T_0)}K'_{SS(0,T_0)}\right)\varepsilon^2}{2}\right)\right) \tag{4.14}$$

The pressures calculated in this manner are given in the data tables for experiments conducted at high pressures and temperatures, and are used in discussions and figures that follow. All of these fittings were conducted both in Microsoft Excel and SigmaPlot to check for consistency and to allow for the determination of uncertainties in the fitted parameters. The results of these ultrasonic experiments at both ambient and high temperatures are presented in the following sections.

4.3 – FeS_2, Pyrite

The sample was slowly brought up to the maximum load of 60 tons at room T, stopping every six tons along the way to collect data. After the data at the peak pressure were collected, heating of the sample resulted in a catastrophic blowout of the anvils in the press, ending the experiment. Thus, no data were able to be collected at high temperature or during decompression. The 2θ angle was calibrated at 6.693° for this

experiment. X-ray diffraction was collected for 120 seconds on the NaCl standard, and for 180 seconds on the pyrite sample.

All of the experimental data for this experiment are given in Table 4.1, along with the X-ray diffraction results of two previous experiments on pyrite that were unsuccessful in obtaining usable ultrasonic signals. The X-ray diffraction patterns collected during all three of these experiments indicated that pyrite does not undergo any phase transitions up in the pressure range explored (Figure 4.3.1). This is consistent with the results obtained in the DAC experiment in this investigation, and all previous studies on this material (Ahrens and Jeanloz, 1987; Blanchard et al., 2005; Bridgman, 1949; Le Page and Rodgers, 2005; Merkel et al., 2002; Prasad and Wooster, 1956; Simmons and Birch, 1963; Sithole et al., 2003). Depending on the pressure, and interference from Pb fluorescence peaks, a total of 12-15 diffraction lines were used in the refinement to determine the unit-cell volume of FeS_2, with a relative standard deviation less than 0.05%. The unit-cell volumes obtained from the refinements (using the space group *Pa*3) exhibit a smooth trend of decreasing volume with increasing pressure (Figure 4.3.2). Values obtained for the unit-cell volume at ambient conditions (V_0) are shown in Table 4.2, along with those obtained in previous studies. The V_0 obtained in each of these three MAC experiments fall right within the range of those obtained in previous studies.

The changes in unit-cell volume with pressure of the MAC experiments are compared with the data from the DAC experiment and the results of Merkel et al (2002) in Figure 4.3.2. Results of BM-3 fits of the P-V data for each experiment are shown on the diagram. The data from the MAC experiments are in very good agreement with one another, though the K' value obtained for the ultrasonic experiment (6.0) is slightly higher than those obtained in the experiments with only X-ray data (5.3). This is likely caused by the slight difference in pressure obtained using the NaCl standard (MAC 1 & 2) vs. that obtained via direct calculation in the ultrasonic experiment. These data are also in good agreement with the results of Merkel et al (2002) within the pressure range explored. The results of the DAC experiment presented in Chapter 3 of this dissertation also agree well with the MAC data. This agreement is much closer than is usually observed between data collected in MAC and DAC experiments.

Figure 4.3.3 part a) shows the variation of P and S wave velocities as a function of pressure, and part b) shows the change in derived elastic moduli with pressure. X-ray diffraction patterns of the sample indicate no discernable increase in the X-ray diffraction peak widths (FWHM), which implies low deviatoric stress level on the sample. By fitting all of the experimental ultrasonic and X-ray data, we obtain the following parameters for FeS_2: K_{S0} = 138.9 (7) GPa, G_0 = 112.3 (3) GPa, K_{S0}' = 6.0 (1), G_0' = 3.0 (<1). Adiabatic results were converted to isothermal values using the relationship $K_S/K_T = (1 + \alpha\gamma T) \approx 1.01$, where the thermal expansion coefficient $\alpha(300K) = 2.57 \times 10^{-5}$ K^{-1} (Skinner, 1966), and the Grüneisen parameter $\gamma = 1.30$ (Blanchard et al., 2005). The pressure on the sample was then calculated directly using Equation 3.1.

Table 4.2 presents a comparison of the results of this study with those of previous studies on FeS_2. The V_0, K_{0T} and K_{0T}' for the two X-ray-only MAC experiments fall within the range of values from previous experimental investigations (158.34-159.04 $Å^3$, 133.5-162 GPa and 4.7-5.73 respectively), while the K' obtained in the ultrasonic experiment is slightly higher than this range. The bulk modulus obtained from a shockwave study on pyrite (Ahrens and Jeanloz, 1987) is significantly higher than those

obtained in static compression studies (162 vs. ~140), even taking into account the adiabatic to isothermal conversion.

The K_{0T} obtained in these experiments are slightly slower than those obtained from previous linear compression (148 GPa, Bridgman, 1949), diffuse X-ray (143.3 GPa, Prasad and Wooster, 1956), and ultrasonic (145.9 GPa, Simmons and Birch, 1963) studies. It is important to note, however, that none of these aforementioned studies offered any information about K_{0T}', so only the data on K_{0T} can be directly compared. The results of these MAC experiments are in very good agreement with the results of Merkel et al (2002) despite being conducted in different experimental apparatus.

The G_0 obtained from the ultrasonic experiment is lower than those obtained from taking the Voight-Reuss-Hill average (VRH) of the elastic constant data obtained via diffuse X-ray diffraction and ambient pressure ultrasonic studies (Prasad and Wooster, 1956; Simmons and Birch, 1963). While the VRH is a good approximation of the shear modulus of a material, the shear modulus is a bulk property and is directly measured in this ultrasonic experiment rather than calculated from single-crystal elastic constants. Also, these previous studies contain no information on G_0'. This study fits the data to determine not only the shear modulus and its pressure derivative, but the bulk modulus and its pressure derivative as well, leading to a more complete data set. In addition, the results are not subject to the effects of pressure calibration using an outside standard; these factors lead to very robust and internally consistent results.

The elastic bulk and shear modulus and their first pressure derivatives as obtained by first-principles calculations exhibit a marked discrepancy from those obtained experimentally. The K_0 values obtained via these calculations above the upper limit of the range found in static experiments (150 to 176 GPa vs. 133.5 to 148 GPa), and the K_{0T}' is below the range observed experimentally (4.56 to 4.65 vs. 5.0 to 6.0). The G_0 obtained via first-principles is slightly higher than the VRH averages discussed previously, and significantly higher than that obtained in this investigation, and the G_0' obtained via calculations is significantly lower than that obtained ultrasonically (Le Page and Rodgers, 2005). It should be noted that much like the trade-off between K_0 and K_0', an increase in G_0 leads to a decrease in G_0' during the fitting process, and vice versa. If the dataset presented here is fit with either G_0 or G_0' fixed to the values presented in Le Page and Rodgers (2005), the fitting results match those presented in that study much more closely, though there is still a discrepancy. These types of discrepancies are commonly seen, especially in iron minerals, and are caused both by the assumptions that need to be taken in order to conduct these types of calculations, and the fact that such calculations are most commonly conducted at 0 K, while experimental results most commonly have a reference temperature of ~300 K.

The results of this study have provided some much needed information on the shear properties of this material. The results presented here provide some important new insights into this phase, and provide some new constraints for refining models and calculations involving FeS_2 and its physical properties under extreme conditions by making available the first data on the shear modulus of this phase and its first pressure derivative. This study presents the first complete experimental dataset on the elastic bulk and shear moduli and their first pressure derivatives for this material and provides an important benchmark for future studies on this material.

4.4 – FeS, Troilite

4.4.1. – Ambient Temperature. The sample was slowly brought up to the maximum load of 60 tons at room T, stopping every three tons along the way to collect data in an attempt to get good coverage during compression because of the expected phase transitions. It was necessary to collect as much data as possible during compression because the transition to FeS-II phase has been shown to not happen when cooling from high temperature, so it is only found upon compression. Also, after heating and the relaxation of the cell assembly, the pressure has dropped below the stability field of FeS-III. Therefore, great care was taken to collect as much data as possible on these two phases. The 2θ angle was calibrated at 6.696° for this experiment. All of the data collected in this room T experiment are given in Tables 4.3-4.4. Diffraction was collected for 120 seconds on the NaCl standard, and for 180 seconds on the troilite sample.

In this experiment, problems with long tails in the ultrasonic P-wave signal rendered the data unusable. The S-wave data, however, were very robust, as were the X-ray data. Therefore, in order to process this dataset, a different approach had to be taken in order to fit the data to the finite strain equations and determine that properties of this material. When a complete dataset is collected, there is redundancy in the data, which is why the pressure can be directly calculated, rendering the NaCl pressure unnecessary. However, in this case, there is a lack of reliable P-wave data, so the pressure measured via NaCl is now a necessary portion of the dataset. The pressure and volume data obtained via X-ray diffraction were BM-3 fit to Equation 3.1 to determine K_{0T} and K_{0T}' for all three phases, as well as V_0 for FeS-II and FeS-III which do not exist at ambient conditions. These isothermal parameters were then converted to adiabatic parameters via the following equations:

$$K_S = K_T(1+\alpha\gamma T) \tag{4.15}$$

$$(\partial K_{0T}/\partial T)_P = \frac{(\partial K_{0S}/\partial T)_P}{(1+\alpha\gamma T)} - \frac{K_{0S}}{(1+\alpha\gamma T)^2}[\alpha\gamma + (\partial\alpha/\partial T)\gamma T] \tag{4.16}$$

$$(\partial K_{0T}/\partial P)_T = (1+\alpha\gamma T)^{-1}\left[(\partial K_{0s}/\partial P)_T - \frac{\gamma T}{K_{0T}}(\partial K_{0T}/\partial T)_P\right] \tag{4.17}$$

where $(\partial\alpha/\partial T)$ is the b parameter in the thermal expansivity term. An $\alpha(300K) = 1.41 \times 10^{-4}$ K^{-1} was used for FeS-I (Tenailleau et al., 2005), and since no thermal expansivity data are available for FeS-II or FeS-III, this value was used for those two phases as well. A $\gamma = 0.6$ was used for FeS-I (Hofmeister and Mao, 2003), and $\gamma = 1.54$ was used for FeS-III (Brown et al., 1984). No γ was available for FeS-II, so $\gamma = 1.07$, the average of these two, was used. Since there are no data available for the $(\partial K/\partial T)$ of FeS-I, FeS-II, or FeS-III, due largely to the narrow temperature range in which they are stable, the assumption the $K_{0T}' = K_{0S}'$ was made.

The adiabatic bulk modulus and its first pressure derivative were then fixed during the fitting of the dataset to Equations 4.1-4.7 to obtain G_0 and G_0'. Instead of minimizing against the residuals of P- and S-wave velocities as is normally done, this fitting was minimized against S-wave velocities and calculated pressure. From these fitted results, P-

wave velocities could then be calculated for each data point. The V_P presented in Table 4.4, and the K_S calculated from them, were obtained in this manner.

The X-ray diffraction patterns collected during compression at room T showed that both phase transitions expected to occur in this pressure range did in fact take place (Figure 4.4.1). FeS-IV and FeS-V will be discussed in the next section. Depending on the pressure, and interference from Pb fluorescence peaks, a total of 9-11 diffraction lines were used in the refinement to determine the unit-cell volume of FeS-I, 7-9 were used for FeS-II, and 8-10 were used for FeS-III, all with a relative standard deviation less than 0.05%. The unit-cell volumes obtained from the refinements exhibit a smooth trend of decreasing volume with increasing pressure (Figure 4.4.2). The jumps in volume that occur at the phase transitions can be clearly seen. In this experiment, FeS-I and FeS-II coexisted at 4.3 GPa, and FeS-II and FeS-III coexisted at a pressure of 6.8 GPa. The unit-cell volumes of both phases were refined at these pressures. The results of the BM-3 fits of each of these datasets are shown on the diagram.

A value of 362.07 (35) $Å^3$ was obtained for the unit-cell volume at ambient conditions (V_0) of FeS-I, which is within the range of those found in previous studies on this material (see Table 4.5). Since FeS-II and FeS-III do not exist at ambient conditions, the V_0 for these phases had to be obtained through the BM-3 fitting. This yielded a V_0 of 123.24 (1) $Å^3$ for FeS-II and 333.8940 (1) $Å^3$ for FeS-III. The V_0 obtained for FeS-II is slightly higher than that found in previous DAC studies (King and Prewitt, 1982, this work), and significantly higher than that obtained from first-principles calculations (Martin et al., 2001). The V_0 obtained here for FeS-III is very similar to that obtained in the DAC experiment reported in Chapter 3, but significantly higher than previous experimental and theoretical studies (Kusaba et al., 1997; Martin et al., 2001). This may be due in large part to a different choice of reference pressure; the papers are unclear on the matter. X-ray diffraction patterns of the sample indicate no discernable increase in the X-ray diffraction peak widths (FWHM), implying low deviatoric stress on the sample.

By taking the parameters obtained from the BM-3 fitting of the P-V data, converting them to adiabatic values using Equations 4.15-4.17, and fixing them in the fitting of the ultrasonic data from the cold compression portion of the experiment, the following parameters are obtained for FeS-I: K_{S0} = 83.2 GPa, G_0 = 39.6 (4) GPa, K_{S0}' = -4.3, G_0' = 1.1 (2). For FeS-II: K_{S0} = 32.13 GPa, G_0 = 44.5 (3) GPa, K_{S0}' = 4.78, G_0' = 1.1 (2). For FeS-III: K_{S0} = 51.553 GPa, G_0 = 43.9 (3) GPa, K_{S0}' = 5.239, G_0' = 1.3 (2). Pressures obtained via X-ray diffraction of the NaCl standard were used in these fittings as discussed above, and are used in all subsequent diagrams and discussion. Figure 4.4.3 part a) shows the variation of P and S wave velocities as a function of pressure, and part b) shows the change in derived elastic moduli with pressure. P wave velocities and bulk moduli were calculated from the fitted parameters as discussed above.

The sample existed in the FeS-I phase from ambient pressure to 4.3 GPa, which is slightly higher than previous experimental studies found the transition to take place (~3.5 GPa, King and Prewitt, 1982; Kusaba et al., 1997), but lower than that found in theoretical studies (~5 GPa, Kobayashi et al., 2005; Martin et al., 2001). However, in this experiment, FeS-I and FeS-II were found to be coexisting at this pressure, with FeS-II being the dominant phase in the diffraction pattern. This suggests that FeS-I was only present residually and the phase transition had simply not gone to completion. The volume change across this phase boundary was ~2.3%, which is slightly lower that found

in previous investigations. FeS-II was found to exist between 4.3 and 6.8 GPa, where it was found to coexist with FeS-III. This agrees very well with the transition pressure found in previous studies (see Table 4.5). The volume change across this phase transition was ~5.7%, which is slightly lower than but consistent with those found in previous studies (~6-9%, King and Prewitt, 1982; Kusaba et al., 1997; Martin et al., 2001; Nelmes et al., 1999). FeS-III was found to persist from 6.8 GPa to the highest pressure obtained in the experiment (10.4 GPa), in agreement with previous studies.

Table 4.5 presents a comparison of the results of this static compression study on these three phases of FeS with those obtained in previous studies. The bulk modulus obtained for FeS-I is within the range of those found in previous studies. A negative value for K_0', while rare, but is consistent with the results of the DAC experiment, and the results of every previous study on this material that did not fix this parameter at a value of 4 (King and Prewitt, 1982; Martin et al., 2001). Instead of a steady increase in compressibility that would be represented by a negative K_{0T}', this phenomenon may actually be caused by second-order phase transition that leads to an increased compressibility; unfortunately this mechanism cannot be distinguished from a true negative K_{0T}' within the resolution of this experiment. The theoretical studies that obtained anomalously high values for the bulk modulus suffer not only from the problems brought about by the required assumptions and 0 K temperature, but also from fixing their K_{0T}' at a value of 4, which artificially drives up the value of K_{0T} because of the negative slope of the compression curve. This study presents the first available data on the shear modulus and its first pressure derivative for this phase.

The bulk modulus obtained for FeS-II is lower than that obtained in the DAC experiment and those found in previous studies. This may in part be caused by the slightly higher pressure at which this phase was found in this experiment. The K_0' obtained via this study is within the range found in previous experiments. These parameters as obtained by theoretical calculations are again significantly different from those obtained in all experimental studies (Kobayashi et al., 2005; Martin et al., 2001). The large differences in V_0, K_{0T}, and K_{0T}' between the results of the experimental studies and those of Martin et al (2001) may be due in part to a difference in reference pressure, but the paper is unclear on this point. This study again presents the first available data on the shear modulus and its first pressure derivative for this phase.

The bulk modulus obtained for FeS-III in this study is similar to that obtained by Kusaba et al (1997), but their value of K_{0T}' was fixed at 4, so a direct comparison of that parameter cannot be drawn. Again, the results of the MAC and DAC experiments conducted in this study are in remarkably good agreement, as they are for the other phases of FeS. Once again, a large discrepancy exists between the experimental data and the results of theoretical calculations. This may in part be caused by a possible difference in reference pressure, but is again largely caused by the assumptions incorporated into the calculations. Once again, this study presents the first available data on the shear modulus and its first pressure derivative for this phase.

The results of this study have helped to quantify the physical properties of FeS under high pressure, and have provided some much needed information on the shear properties all three room T phases of this material. The results presented here provide important new insights into physical properties of FeS-I, FeS-II, and FeS-III under extreme conditions by making available the first data on the shear moduli of these phases and

their first pressure derivatives. Experimental data on the high temperature phases of FeS are presented next, and offer a more complete picture of this complex material.

4.4.2. – High Temperature. The sample was first compressed to the maximum load of 60 tons while at room T, after which the sample was heated to the maximum temperature of 1073 K; this resulted in a pressure decrease from 10.4 GPa to 8.3 GPa as the cell assembly relaxed and flowed at high T. Data were collected at this maximum temperature, and in 200 K intervals on the way down to room T, after which five additional heating and cooling cycles were conducted at about a 1.0 GPa interval in pressure to provide a dense coverage in P-T space. The 2θ angle was calibrated at 6.696° for this experiment. All of the data collected in this experiment are given in Tables 4.6-4.7. X-ray diffraction was collected for 120 seconds on the NaCl standard, and for 180 seconds on the FeS sample.

As mentioned in the previous section, the ultrasonic P wave signal in this experiment was unusable, but the S-wave and X-ray data were very robust. Therefore, in order to process this dataset, the pressure, volume, and temperature data obtained via X-ray diffraction were fit to the high temperature Birch-Murnaghan (HTBM) to determine $V_{0,300}$, $K_{T(0,300)}$, $K_{T(0,300)}'$, and $(\partial K_{(0,300)}/\partial T)_P$ for FeS-IV and FeS-V; the two high temperature phases found in this experiment. The HTBM is as follows:

$$P(V,T) = \frac{3}{2} K_{T(0,T)} \left[\left(\frac{V_{0,T}}{V} \right)^{7/3} - \left(\frac{V_{0,T}}{V} \right)^{5/3} \right] \times \left\{ 1 + \frac{3}{4} \left(K'_{T(0,T)} - 4 \right) \left[\left(\frac{V_{0,T}}{V} \right)^{2/3} - 1 \right] \right\} \tag{4.18}$$

$$K_{T(0,T)} = K_{T(0,300)} + (T - 300) \left(\frac{\partial K_T}{\partial T} \right)_P \tag{4.19}$$

$$V_{0,T} = V_{0,300} e^{\int \alpha dT} \tag{4.20}$$

with the assumption that $K'_{T(0,T)} = K_{T(0,300)}'$.

Figure 4.4.4 a) shows the molar volume vs. pressure for this experiment. FeS-IV is represented by squares, and the compression curves based on the PVT fit to the HTBM are shown as solid lines, while FeS-V is represented by diamonds and dashed lines. The star shows the one data point where FeS-IV and FeS-V were found to coexist, and the circle represents the lone data point collected for FeS-I on decompression. FeS-IV persists metastably to well within the stability field of FeS-I in this experiment, likely caused by the hysteresis effect in the phase transition. Symbols are color-coded by their temperature. The results of the HTBM fits for both phases are shown on the diagram. Figure 4.4.5 shows the c/a ratio in FeS-IV and FeS-V as a function of pressure and temperature. A general trend of decreasing c/a ratio toward ideal close-packed values with increasing temperature can be observed within the range of pressures and temperatures explored, indicating a greater linear thermal expansion along the a-axis. The contour lines shown are the isopleths showing the c/a ratio of the fundamental NiAs unit cell given in Urakawa et al. (2004). The data presented here follow those contour lines exactly, with the exception of the lowest-pressure FeS-IV data point, which exists metastably and is therefore not important.

These isothermal parameters obtained from the HTBM fits were then converted to adiabatic values via Equations 4.15-4.17 and held fixed in the high temperature finite strain fitting to obtain $G_{(0,300)}$, $G_{(0,300)}'$ and $(\partial G_{(0,300)}/\partial T)_P$. The thermal expansivity data available for both FeS-IV and FeS-V (Urakawa et al., 2004) were insufficient to explain the dataset obtained in this experiment, so the PVT data was used to determine α for these two phases as well. An $\alpha(300K) = 2.16 \times 10^{-4}$ K^{-1} was obtained for FeS-IV, and an $\alpha(300K) = 1.42 \times 10^{-4}$ K^{-1} was obtained for FeS-V. It should be noted that these values are much closer to the $\alpha(300K) = 1.41 \times 10^{-4}$ K^{-1} that has been observed for FeS-I (Tenailleau et al., 2005) than the values presented in Urakawa et al (2004). A $\gamma = 1.174$ was used for FeS-V (Anderson and Ahrens, 1996), and since no γ was available for FeS-IV, this same value was used. Figure 4.4.4 b) shows the acoustic velocities in FeS-IV and FeS-V as a function of pressure. The same coding scheme is used as in Figure 4.4.4 a). As discussed in Section 4.4.1, the P-wave velocities and adiabatic bulk moduli are calculated based on the fitted parameters. A diagram showing the derived elastic moduli is not included here because the values for K_S and G for these two materials are so similar that they plot nearly on top of one another, making the diagram cluttered and unclear.

Using the finite-strain approach, a fit of the entire FeS-IV dataset given in Table 4.7 gives the adiabatic zero-pressure bulk and shear moduli and their first pressure and temperature derivatives: K_{S0}=39.96 GPa, G_0=40.8 (3) GPa, K_{S0}'=1.772, G_0'=1.82 (1), $(\partial K_{S0}/\partial T)_P$=–0.0090 GPa K^{-1}, $(\partial G_0/\partial T)_P$=–0.0259 (8) GPa K^{-1}. The following parameters were obtained for FeS-V: K_{S0}=35.09 GPa, G_0=38.1 (2) GPa, K_{S0}'=2.412, G_0'=2.13 (2), $(\partial K_{S0}/\partial T)_P$=–0.0023 GPa K^{-1}, $(\partial G_0/\partial T)_P$=–0.0199 (9) GPa K^{-1}. The values of $(\partial K_0/\partial T)_P$ are quite low compared to most materials, but they are only just slightly outside the range of mutual uncertainties of those previously obtained for these materials (Urakawa et al., 2004). All previous experimental studies on both phases have fixed K_{0T}' at a value of 4, so they cannot be directly compared to the results obtained here (see Table 4.8). The values obtained for K_0 are lower than those obtained previously; however, this study fits all of the data back to 0 GPa and 300 K, which was not done in the other investigations (Kusaba et al., 1998; Urakawa et al., 2004). The first results on the shear modulus and its first pressure and temperature derivatives available for both FeS-IV and FeS-V are made available here.

This study presents the first complete set of elastic moduli and their first pressure and temperature derivatives of the two high temperature phases of FeS. The results presented here will allow the refining of existing models and calculations involving FeS-IV and FeS-V by providing new constraints on their behavior at high pressure and temperature. The implications of the data presented here on all five phases of FeS for the Earth's core will be discussed in Chapter 5.

4.5 – ε-FeSi, Fersilicite

4.5.1. – Ambient Temperature. The results of this experiment have been published previously (Whitaker et al., 2008). X-ray diffraction patterns of the samples were collected at a series of points while under ambient conditions by changing their position in the beam laterally and vertically; the diffracted X-rays were collected by four detectors (two aligned vertically and two horizontally) positioned at $\chi = 0°$, 90°, 180°, and 270°. Figure 4.5.1 shows an example of the diffraction patterns collected in this manner for the ε-FeSi sample. The diffraction patterns recorded by the horizontal (3 & 4 in Fig. 4.5.1)

and vertical detectors (1 & 2 in Fig. 4.5.1) were virtually identical for each point analyzed, and all points analyzed in a given sample gave similar diffraction patterns; this indicates that there was no detectable preferred orientation of the grains in the samples.

The sample was slowly brought up to the maximum load of 60 tons at room T, stopping every five tons along the way to collect data. After the data at the peak pressure were collected, the sample was heated to a temperature of 1000°C to relax any stress accumulated in the cell assembly during compression. Data were again collected after cooling to room T, after which the pressure was decreased systematically, and data were collected during this decompression process. After each decompression step, the sample was heated again to release any possible extensional stress acting on the system; data were collected both before and after this heating and showed good agreement between the two, which indicates the effect of extensional stress on the system during decompression was nominally insignificant. The 2θ angle was calibrated at 6.495° for this experiment.

All of the experimental data for this experiment are given in Table 4.9. The X-ray diffraction patterns collected during the experiment showed that the sample remained in the cubic B20 structure right up to 12 GPa, the highest pressure achieved in this study (Figure 4.5.2). Depending on the pressure, and interference from Pb fluorescence peaks, a total of 10-13 diffraction lines were used in the refinement to determine the unit-cell volume of the ε-FeSi, with a relative standard deviation less than 0.05%. Small peaks appearing in these diffraction patterns that are not labeled were either sample peaks not used for cell refinement or parasitic diffraction peaks from the surrounding material in the cell assembly.

The unit-cell volumes obtained from the refinements (using the space group $P2_13$) exhibit a smooth trend of decreasing volume with increasing pressure (Figure 4.5.3). A value of 90.45 (3) $Å^3$ was obtained for the unit-cell volume at ambient conditions (V_0), which is slightly higher than, but comparable with, those found in previous studies on this material (see Table 4.10).

By fitting all of the data from the cold compression portion of the experiment, we obtain the following parameters for ε-FeSi: K_{S0} = 165.3 (17) GPa, G_0 = 113.1 (8) GPa, K_{S0}' = 6.0 (3), G_0' = 2.7 (1). Fitting the data from the post-heating decompression portion of the experiment yields slightly different results: K_{S0} = 169.3 (8) GPa, G_0 = 116.3 (4) GPa, K_{S0}' = 6.5 (3), G_0' = 3.0 (1). Adiabatic results were converted to isothermal values using the relationship $K_S/K_T = (1 + \alpha\gamma T) \approx 1.03$, where the thermal expansion coefficient $\alpha(300K) = 4.85 \times 10^{-5}\ K^{-1}$, and the Grüneisen parameter $\gamma = 2.33$ (Vocadlo et al., 2002). The pressure on the sample was calculated directly using Equation 3.1.

The iron silicide sample remained in the cubic B20 structure throughout the range of conditions explored in this experiment. First-principles calculations indicate that the transition from the B20 phase to a CsCl (B2) structure should occur anywhere from ~13 GPa (Al-Sharif et al., 2001; Vocadlo et al., 1999) to pressures as high as 30-40 GPa (Caracas and Wentzcovitch, 2004). Previous experimental investigations that have been conducted both in similar pressure ranges as this study (≤ 12 GPa), as well as to pressures above those at which the predicted phase transition occurs, have also shown no sign of the B20 to B2 phase transition (Badro et al., 2007; Guyot et al., 1997; Knittle and Williams, 1995; Lin et al., 2003a; Wood et al., 1995; Wood et al., 1996). The first observation of the B2 structure of FeSi was not transformed from ε-FeSi, but rather

synthesized from pure Fe and Si, with a slight excess of Fe in the system, at 24 GPa (Dobson et al., 2003; Dobson et al., 2002). A recent study finally observed the transition from the B20 to B2 structure somewhere between 25 and 35 GPa (Ono et al., 2007). This study, however, saw no such phase transition, as was expected.

The change in unit-cell volume with pressure is compared with the data from previous studies in Figure 4.5.3. The data from this study are in excellent agreement with the results of (Guyot et al., 1997), and a good match with the results of (Wood et al., 1995). The data from (Lin et al., 2003a) show a lot of scatter in the results, but a similar trend is observed in all of these data sets. It should be noted that the data presented in (Lin et al., 2003a) are results of experiments conducted in diamond anvil cells, while the other two studies and this study were conducted in a multi-anvil apparatus. The results of the DAC experiment presented in Chapter 3 of this dissertation follow a very similar trend to those collected in this experiment; the two experiments show much closer agreement, in fact, than is usually seen between MAC and DAC experiments. The data along compression and decompression from this study are essentially indistinguishable, suggesting that the deviatoric stress on the sample during cold compression is negligible. The trends followed by the compression and decompression portions of the experiment, however, are slightly different from one another, particularly with increasing pressure, reaching ~0.1% at 12GPa, though they are considered in agreement within the current experimental uncertainties.

Figure 4.5.4 shows the variation of P and S wave velocities as a function of density along compression and those obtained during decompression, and Figure 4.5.5 displays the change in derived elastic moduli with pressure. It is noted that there is slight offset in the values between data collected during cold compression and those collected during decompression after heating. As shown in Figure 4.5.3, the deviatoric stress that built up in the system during cold compression appears to be insignificant. Examination of the X-ray diffraction patterns of the sample indicates no discernable increase in the X-ray diffraction peak widths (FWHM), which also implies low stress level on the sample (quantifying the stress on the sample is impossible at present due to the lack of data on elastic constants at high pressures). We therefore attribute the difference between the two data sets largely (if not all) to the further closure of porosity of high aspect ratios within the sample upon heating to 1000°C at peak pressure. This interpretation is supported by density measurements conducted on the bulk sample before and after the current experiment using the Archimedes method. Before the NSLS experiment, the sample density was 97.9% of the theoretical density of ε-FeSi, while after the experiment it increased to 99.1%. If this deviation from the theoretical density is taken into account, the data from both compression and decompression shown in Figure 4.5.4 would lie virtually on top of each other.

It should be noted here that a change in texture after heating the sample, if any, could also bring about changes in the observed acoustic velocities. However, in this experiment, the X-ray diffraction patterns of the sample taken both before and after heating were extremely similar in both peak position and relative intensities, which indicates that the sample did not undergo any detectable changes in grain size or orientation because of the heating. In addition, SEM images of the sample taken before and after this experiment showed no discernable differences in grain size, which indicates that little grain growth occurred.

It is further noted that at any given pressure, the difference in elastic moduli between the two datasets is on the order of ~2%, and for a given density the difference in acoustic wave velocities are ~2%. This suggests that the pressure dependences obtained during compression and decompression are very similar, which is also in support for an porosity-closure origin rather than effect of stress or texture. Since the decompression data were collected under conditions that were deviatoric-stress-free within the detectability of the current experimental set-up, the zero-pressure elastic moduli and their pressure derivatives calculated by fitting these data are chosen as the preferred ones for this material.

Table 4.10 presents a comparison of the results of this study with those of previous studies on ε-FeSi. The bulk modulus obtained from this study is significantly lower than those reported in studies based on first-principles calculations; this is true of nearly all other experimental studies on this material as well. The previously reported experimental isothermal bulk modulus for ε-FeSi ranges from 160 to 209 GPa; the result obtained in this study of 164.4 GPa falls at the lower end of this range. The K_{T0}' obtained from this study (6.5), however, is higher than those of previous studies (range of 3.5 to 4.75). The G_0 obtained here agrees extremely well with the estimate based on the graphical data of (Sarrao et al., 1994); this study did not present any data on the pressure derivatives of the elastic moduli. The results presented here are the first direct measurements on the shear properties of ε-FeSi, and the first complete set of data pertaining to both elastic moduli and their first pressure derivatives.

At first glance, the G_0' obtained for this material may seem abnormally high, especially when compared to the normal suite of mantle minerals. The value obtained in this study (3.0) is quite similar to the highest value for MgO obtained in previous studies (2.2-2.9, see (Li et al., 2006)). However, when comparing these data with the results obtained from cold compression which spans nearly twice of the pressure range as that in decompression, the resulting G_0' and K_{S0}' are lowered to $G_0' = 2.7$ (1) and $K_{S0}' = 6.0$ (3), respectively. However, if the cold compression data are fit only over the same pressure range as the decompression data, the resulting first pressure derivatives of the elastic moduli are nearly identical to those found from the decompression data. The current data seem to suggest that there may be a relatively strong component of second pressure derivative for K and G, however because of the difference in acoustic velocities brought about by the collapse in porosity in the sample at high pressure and temperature, this cannot be determined for certain. The pressure range needs to be further expanded to verify these observations.

It is important to note that the previous studies which have fitted their data to solve for both K_{T0} and K_{T0}' simultaneously (Knittle and Williams, 1995; Lin et al., 2003a) both have lower values of K_{T0}', and also obtained significantly higher values for K_{T0}. An increase in one of these parameters will lead to a decrease of the other in the fitting. If we fix our results for the shear properties, and set the value of K_{T0} to be equal to those given by the previous studies, our K_{T0}' decreases significantly (even becoming negative when using the K_{T0} of 209 given by (Knittle and Williams, 1995)). If we set our K_{T0}' to be equal to those given in previous studies, then we see an increase in our value for K_{T0}. The results of this study agree fairly well with those of (Lin et al., 2003a) and extremely well with those of (Guyot et al., 1997). This study fits the data to determine not only the bulk modulus and its pressure derivative, but the shear modulus and its pressure derivative as

well, leading to a more complete data set. In addition, the results are not subject to the effects of pressure calibration using an outside standard; these factors lead to very robust and internally consistent results.

The results of this study have helped to clarify some of the debate regarding the physical properties of ε-FeSi under high pressure, and have provided some much needed information on the shear properties of this material. The results presented here provide some important new insights into this phase, and provide some new constraints for refining models and calculations involving ε-FeSi and its physical properties under extreme conditions by making available the first data on the shear modulus of this phase and its first pressure derivative. In order to more fully investigate the properties of fersilicite, and its likelihood as a possible constituent of planetary cores, the temperature dependence of its physical properties must be obtained. These data are presented next, and offer a more complete dataset for this important material.

4.5.2. – High Temperature. The results of this experiment have also been published previously (Whitaker et al., 2009). The sample was first compressed to the maximum load of 60 tons while at room T, after which it was heated to the maximum temperature of 1273 K; this resulted in a pressure decrease from 12 GPa to 8 GPa as the cell assembly relaxed and flowed at high T. Data were collected at this maximum temperature, and in 200 K intervals on the way down to room T, after which seven additional heating and cooling cycles were conducted at about a 0.5-1.0 GPa interval in pressure to provide a dense coverage in P-T space. The 2θ angle was calibrated at 6.495° for this experiment. All of the data collected in this experiment are given in Table 4.11.

The X-ray diffraction patterns of the sample collected throughout the experiment indicated that the sample remained in the cubic B20 structure over all P-T conditions explored. The cell refinements were conducted using the $P2_13$ space group. A total of 9-13 diffraction lines were used in the cell refinement of the ε-FeSi diffraction patterns, depending on the peak intensities, pressure, and interference from fluorescence peaks. Unit cell volumes obtained via cell refinement are shown in Figure 4.5.6, and have a relative standard deviation of less than 0.05%. The unit-cell volume at ambient conditions (V_0) was found to be 90.45(3) $Å^3$, which is slightly higher but comparable with those of previous studies (see Table 4.12). The density of the sample at each set of P-T conditions is derived using the calculated theoretical density and the unit-cell volumes obtained from the cell refinement.

In addition to monitoring the sample structure and cell volume throughout the experiment, the X-ray diffraction patterns also suggest that there was minimal deviatoric stress acting on the sample during the experiment, as the peaks did not show any significant signs of broadening (FWHM). The diffraction patterns throughout the experiment suggest there were little to no discernable changes in grain size or orientation during the experiment; this is reaffirmed by SEM images taken both before and after the experiment which show no difference in grain size.

The compressional and shear wave velocities obtained from all eight heating/cooling cycles during the experiment are shown in Figure 4.5.7. As this figure shows, the data agree quite well with the values obtained from the fitting of this dataset over the entire range of conditions explored. Figure 4.5.8 shows the elastic moduli determined for each set of pressure and temperature conditions during the experiment. These data also largely agree with the values obtained from the fitting of the entire dataset. The acoustic

velocities and the elastic moduli all show a steady increase with increasing pressure at a constant temperature, and a decrease in value with temperature at a given pressure, as is expected.

Using the finite-strain approach, a fit of the entire dataset given in Table 4.11 gives the adiabatic zero-pressure bulk and shear moduli and their first pressure and temperature derivatives: K_{S0}=168.9 (7) GPa, G_0=116.5 (3) GPa, K_{S0}'=6.6 (2), G_0'=2.9 (1), $(\partial K_{S0}/\partial T)_P$=–0.023 (1) GPa K^{-1}, $(\partial G_0/\partial T)_P$=–0.030 (1) GPa K^{-1}. There is very good agreement between the elastic properties obtained via fitting of the entire dataset, and those obtained using only the room temperature dataset presented previously. It should be noted that in the current fitting, pressure is not included in the fitting procedure, and therefore the elastic moduli and their pressure derivatives obtained via this method are not dependent upon pressure measurements taken during the experiment or upon the pressure standard chosen and/or the accuracy of the pressure scale used.

Table 4.12 presents a comparison of the thermoelastic properties of ε-FeSi obtained from this study with those of previous experimental and theoretical studies on this material. The first thing to note in this table is that this study reports the first data on the temperature dependence of the elastic moduli, and a complete set of thermodynamically internally consistent elastic properties and their pressure and temperature derivatives.

The bulk modulus of this material determined via first-principles calculations are all significantly higher than that obtained from this study. This difference may arise from two main sources: the necessary assumptions used in order to conduct such calculations, and the fact that such calculations are most often conducted at 0 K, while the thermoelastic properties from this study are all determined at a reference temperature of 300 K. To accurately compare the adiabatic bulk modulus from this study with those of previous experimental studies, which are isothermal values, the relationship $K_S/K_T = (1 + \alpha\gamma T) \approx 1.03$ was used to convert our K_{S0} to K_{T0}, which yielded a value of 164.2 GPa. This falls at the lower end of the range of previously reported values of K_{T0} for ε-FeSi, which spanned from 160 to 209 GPa. The K_{T0}' obtained from this study is higher than those found in all previous studies, which ranged from 3.5 to 4.75. The first temperature derivative of the adiabatic bulk modulus obtained in this study (–0.023 (1) GPa K^{-1}), when converted to an isothermal value (–0.039 (1) GPa K^{-1}) compares very well with the value of –0.043 GPa K^{-1} obtained by Guyot et al. (1997). Our shear modulus is in excellent agreement with the data from the previous resonant ultrasound study, and there are no existing data on the temperature dependence of the elastic shear modulus against which to compare.

The differences between the elastic properties determined in previous studies versus those obtained in this study arise from several sources. Most of the previous experimental studies (with the exception of the resonant ultrasound study conducted only at ambient pressure) were static compression studies, which used a secondary pressure standard as a measure of pressure, and either X-rays or neutrons to determine the cell volume of the material at that pressure. These pressure and volume data were then fit to an equation of state to determine K_{T0} and K_{T0}'. This means the parameters obtained from this fitting are heavily dependent upon the accuracy of the pressure measurement. In addition, by fixing the value of one of these parameters, you can dramatically change the other, as in the fitting procedure K_{T0} and K_{T0}' are strongly correlated with each other as well as with the volume at zero pressure. For instance, the compression curve (V/V_0 vs. P) derived using

the equation of state parameters (K_{T0}, K_{T0}' and V_0) of Lin et al. (2003) are found to be in agreement within 0.3% with that obtained from the current study up to their highest pressure (50.7 GPa), but the apparent values of K_{T0} and K_{T0}' differ from the current study as much as 12% and 28% respectively (Table 4.12, see also Whitaker et al., 2008). The advantage of the study reported here over the previously reported studies is two-fold. First, at each set of pressure and temperature conditions, we are directly measuring the bulk and shear modulus, rather than have to rely on fitting of volume data alone, and this leads to a more reliable and complete dataset. Second, the results obtained using these techniques are not dependent upon any external pressure calibration based on a standard. These two factors combine to give an inherently robust and internally consistent dataset that cannot be obtained using individual X-ray diffraction or acoustic methods.

This study has helped to further resolve some existing controversy regarding the elastic properties of ε-FeSi by providing the first complete set of thermodynamically internally consistent elastic moduli and their first pressure and temperature derivatives. The results presented here will allow the refining of existing models and calculations involving this phase by providing new constraints on its behavior at high pressure and temperature. The data presented here, along with studies currently underway on other iron silicide alloys, will be of great help in determining the possible presence of Si in the Earth's core.

The results of the experiments presented in this Chapter have provided a much-needed benchmark for future studies on these materials and have helped to ameliorate some of the controversy regarding the physical properties of these important mineral phases. The implications of all the experiments presented in this Chapter will be discussed in the following Chapter of this dissertation.

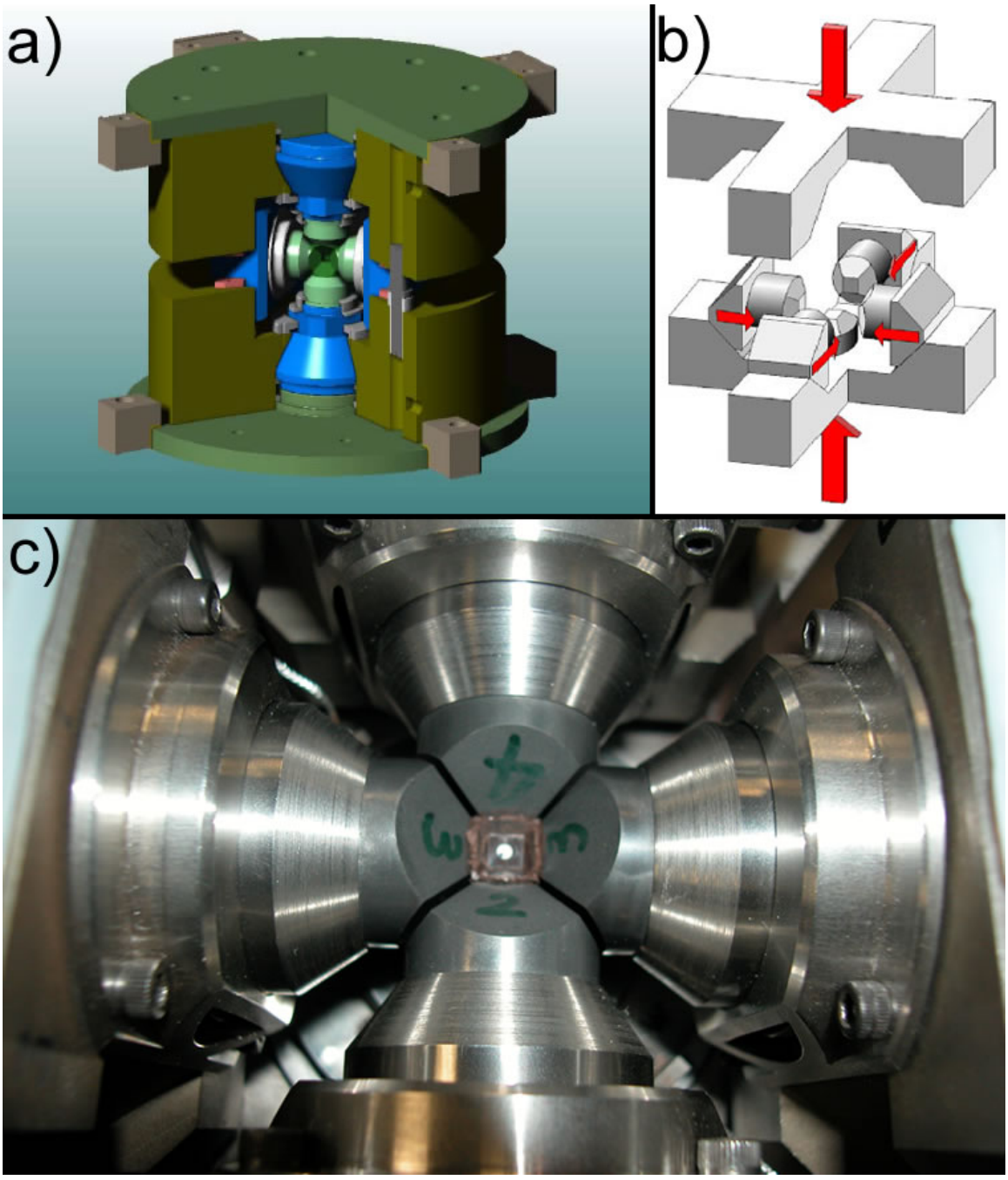

Figure 4.1.1. DIA-type apparatus. a) Schematic drawing of DIA apparatus showing how anvils are brought together around a cubic cavity in the center. b) Schematic showing the tapered backs of the anvil guideblocks and how force is applied during the experiment. c) Photograph showing how the four anvils in the horizontal plane come together around the cell assembly. Images courtesy of COMPRES Image Library.

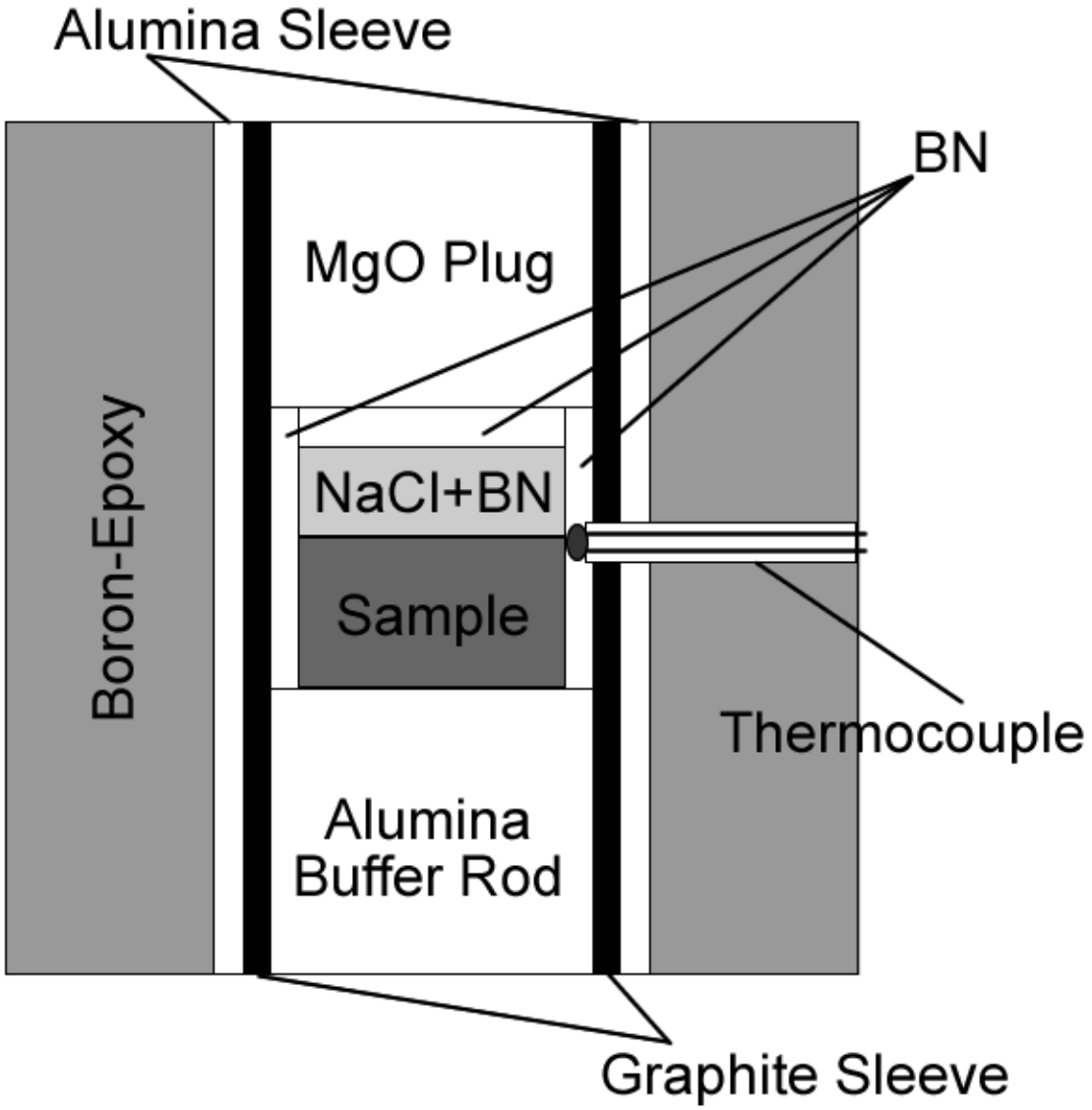

Figure 4.1.2. Schematic of the cell assembly used in the synchrotron-based ultrasonic experiments. The NaCl + BN is a powdered mixture in 10:1 proportions; the NaCl powder serves as a pressure marker, and the addition of BN to NaCl is to prevent significant grain growth of NaCl during heating. A 1μm-thick disc of Au foil is placed above and below the sample and at the bottom of the buffer rod to smooth all contact surfaces.

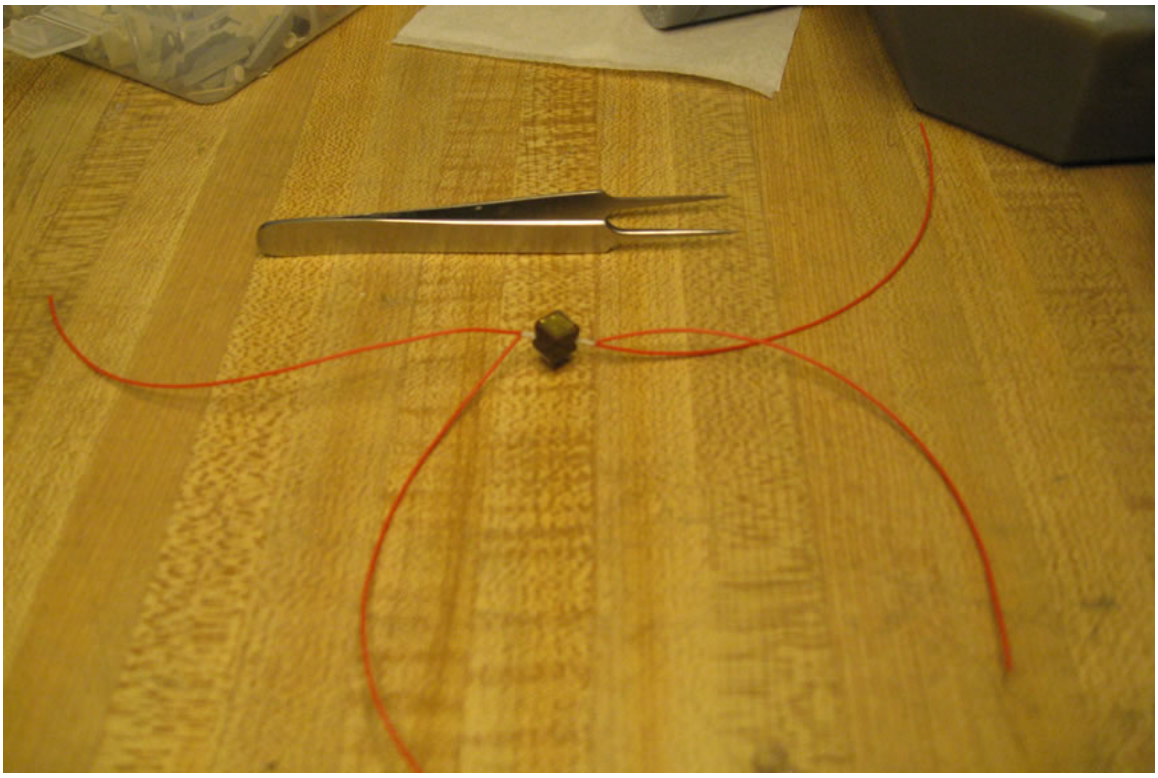

Figure 4.1.3. Photograph of assembled ultrasonic cell showing square of Au foil affixed to the end of the cell over the buffer rod and the two thermocouples protruding from opposite edges of the cube.

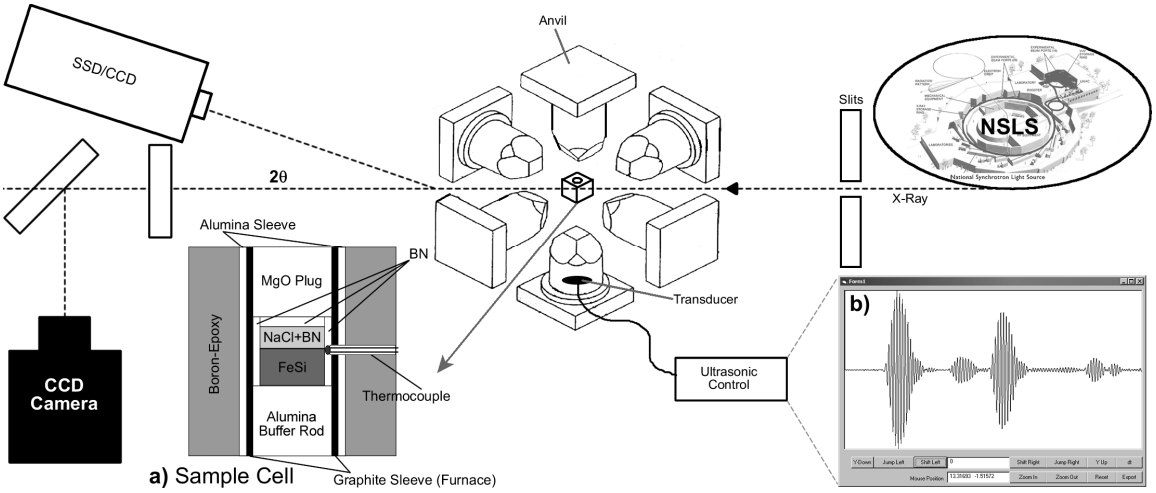

Figure 4.1.4. Outline of the experimental DIA-type SAM85 setup at beamline X17B2 at the NSLS. a) Cell Assembly as shown in Figure 4.1.2. b) Ultrasonic Interferometer – Ultrasonic measurements allowing for the simultaneous collection of both P and S Wave data were conducted using a dual-mode transducer capable of generating frequencies from 20 to 70 MHz. The ultrasonic signal shown here illustrates the P-wave signal collected at Room T at 15 tons of oil pressure during initial cold compression. First pulse is anvil/buffer rod interface, second is buffer rod/sample interface, third is sample/salt interface. More information on this experimental setup can be found in (Li et al., 2004).

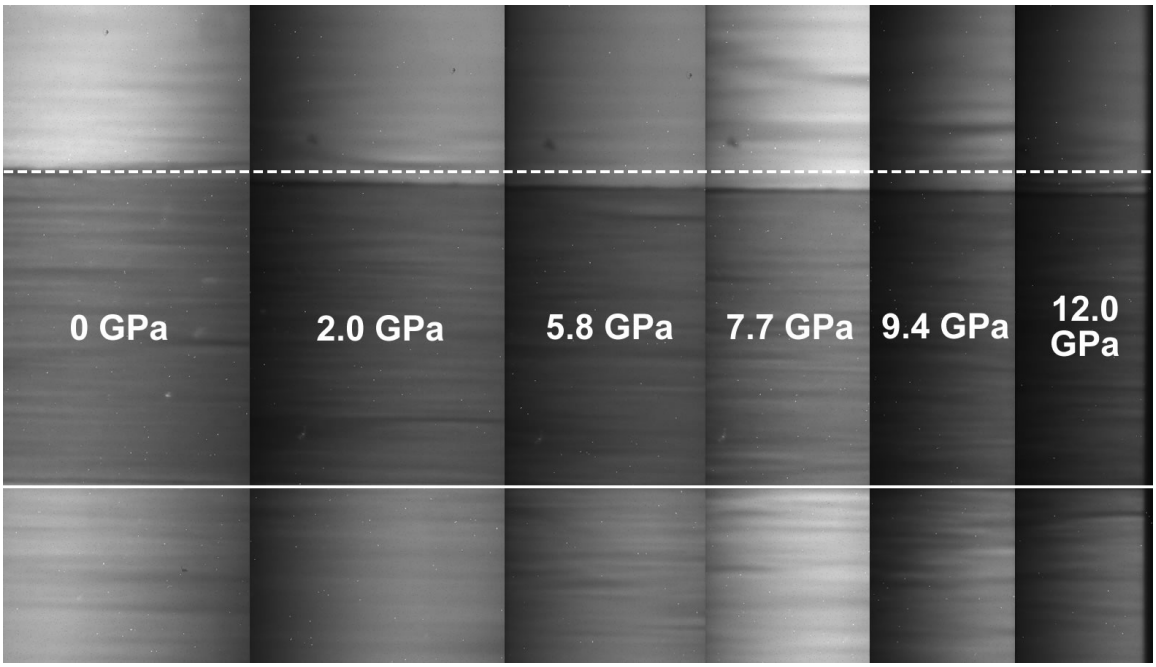

Figure 4.1.5. X-radiographic imaging of the ε-FeSi sample during cold compression. Pressure is listed for each image. Bottom of sample in images have been aligned to the same line, and the dashed line shows top of sample at beginning of experiment. Change in sample length is evident as pressure increases.

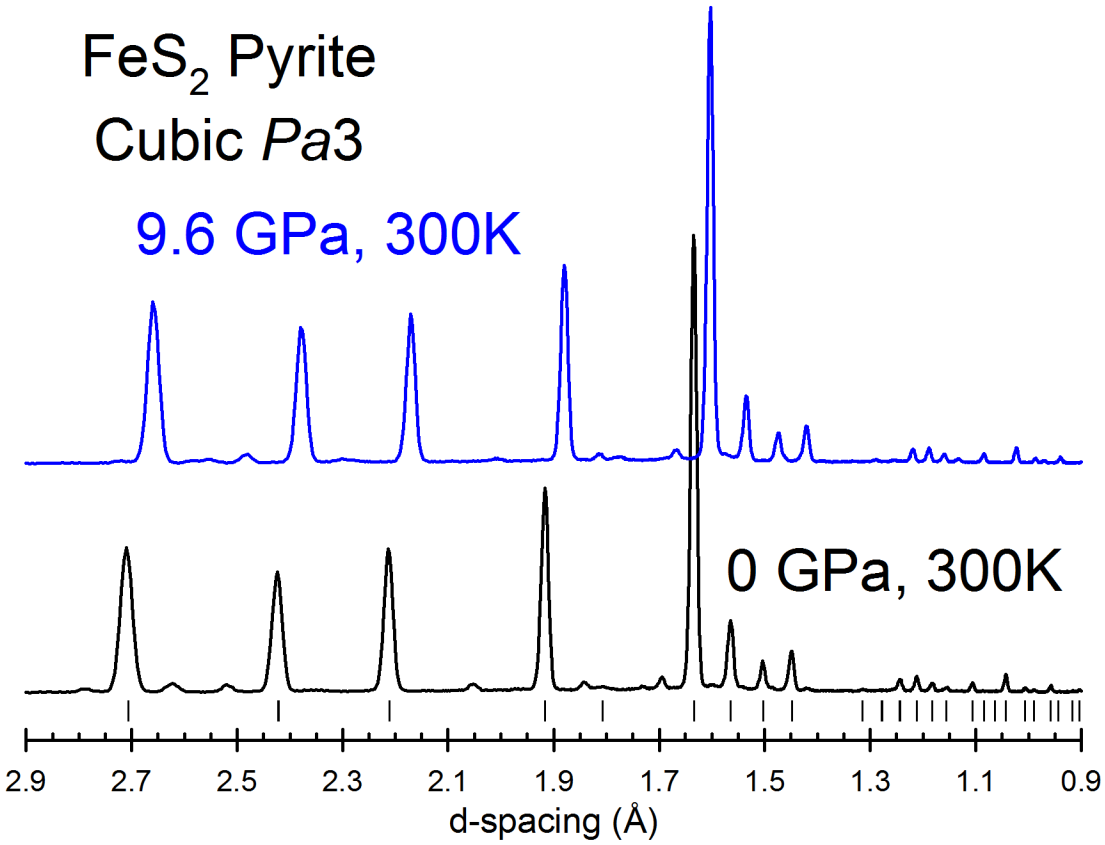

Figure 4.3.1. X-ray diffraction patterns of FeS_2 sample used in ultrasonic experiment in the Multi-Anvil Cell at 0 GPa and 9.6 GPa. Vertical lines below diffraction pattern indicate peak positions in the standard powder diffraction file that were used to index the pattern. Unmarked peaks are the result of parasitic scattering from the surrounding material in the cell assembly.

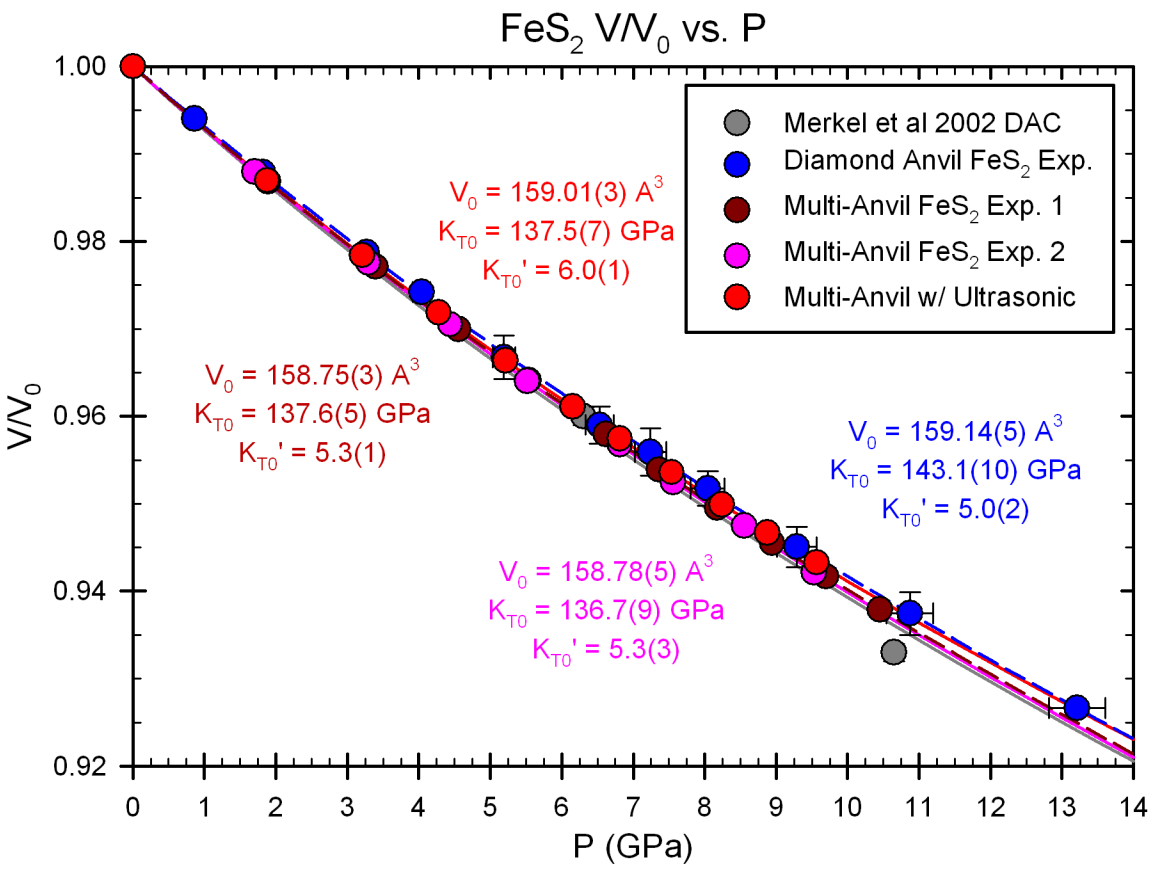

Figure 4.3.2. Volume change vs. pressure for the ultrasonic experiment on FeS_2. Also plotted are results from two compression experiments that were unsuccessful in obtaining ultrasonic data and the results of the DAC study discussed in Chapter 3. Reference data plotted in background from Merkel et al (2002). Parameters obtained from third-order Birch-Murnaghan fits to Equation 3.1 are shown on diagram for each dataset.

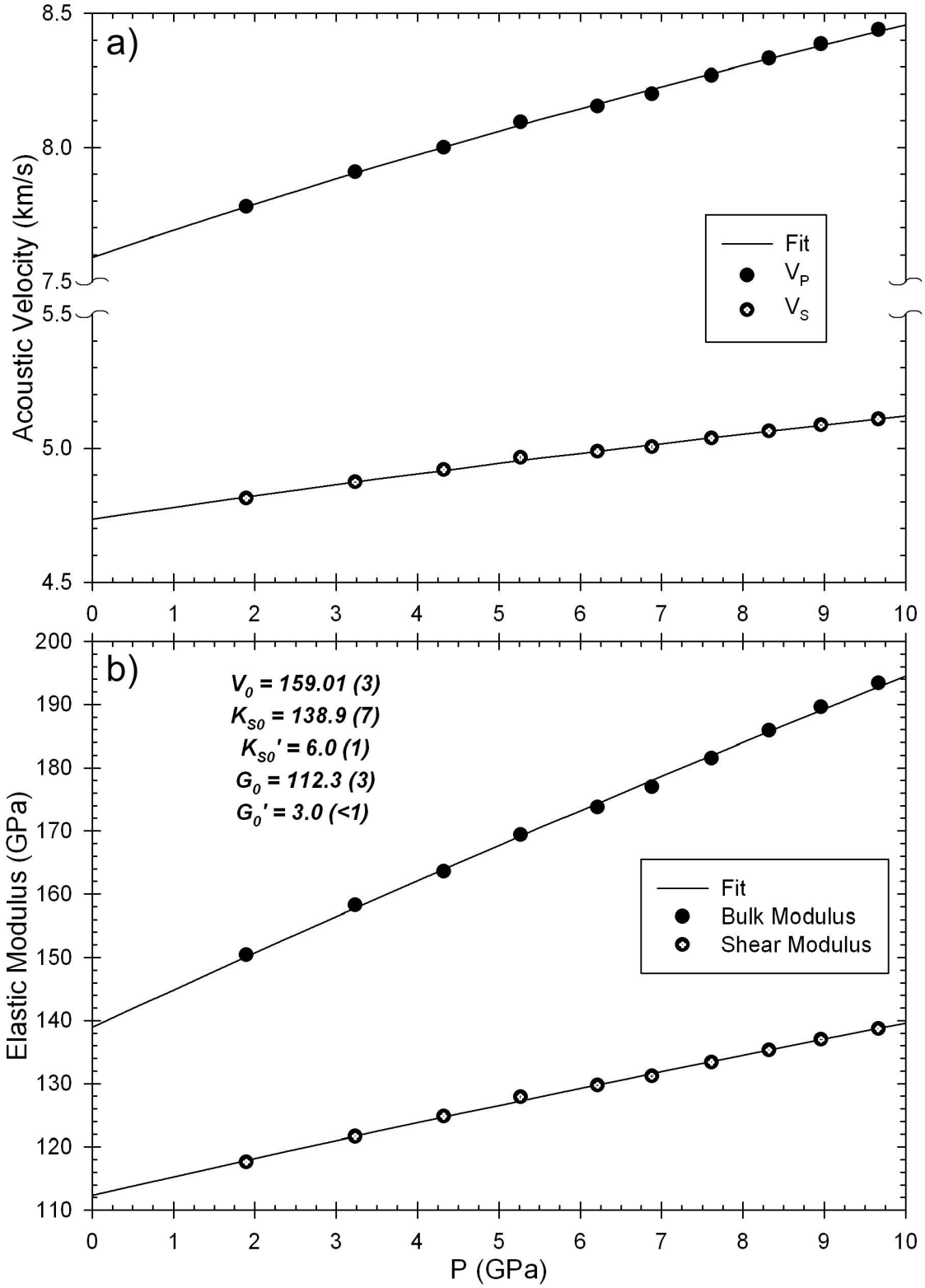

Figure 4.3.3. a) Acoustic velocities in FeS_2 vs. Pressure. Black circles represent P wave velocities; circles with crosshairs represent S wave data. b) Elastic Modulus of FeS_2 vs. Pressure. Black circles are adiabatic bulk modulus; circles with crosshairs represent shear modulus. Fitting results are shown on b). Lines are curves from these fitted parameters.

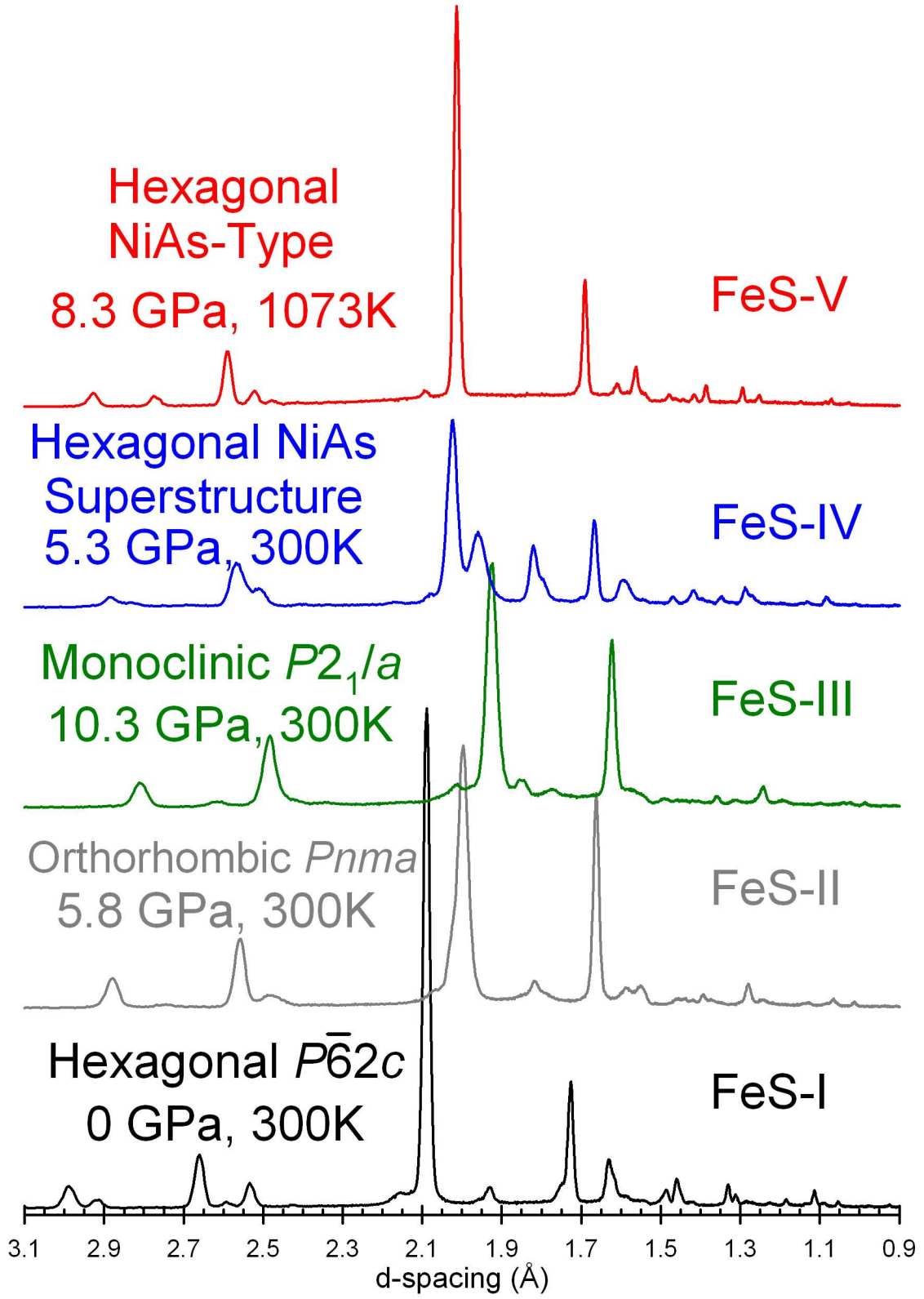

Figure 4.4.1. X-ray diffraction patterns of FeS sample used in ultrasonic experiment in the Multi-Anvil Cell. All five phases shown in Figure 1.1.2 were found.

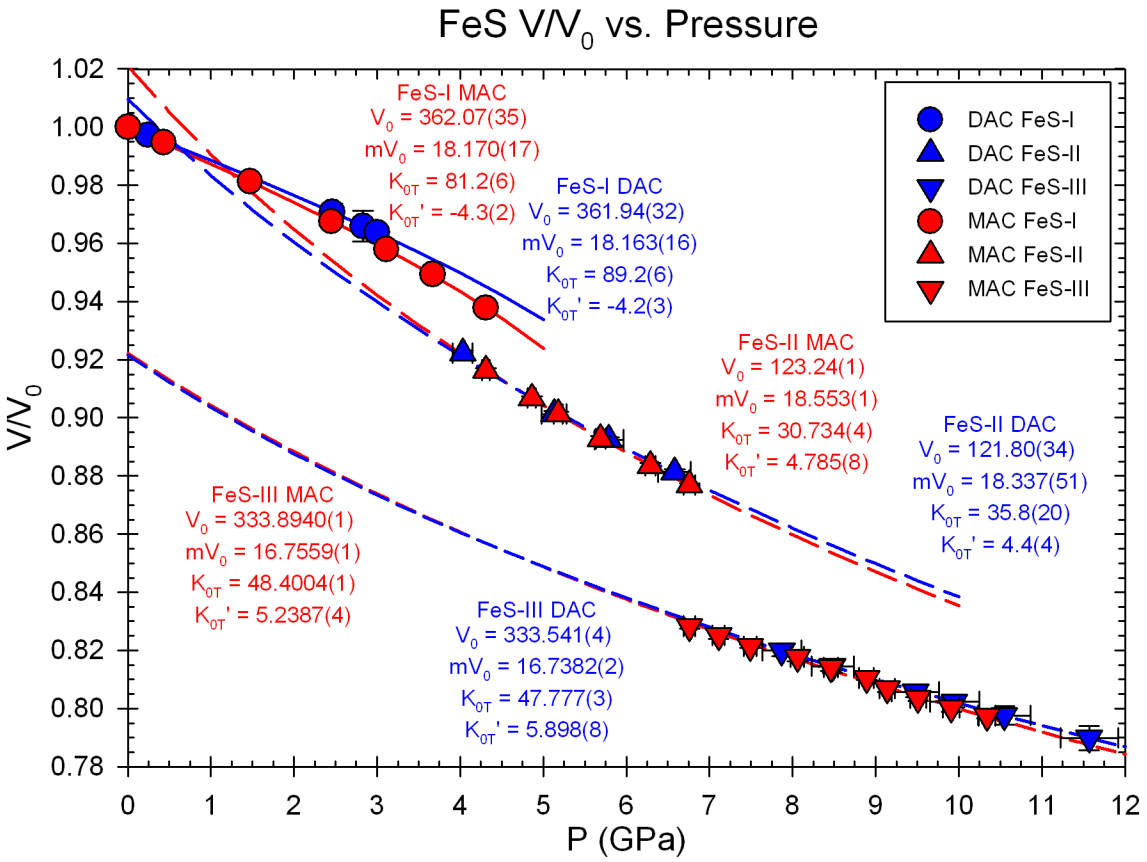

Figure 4.4.2. Volume change vs. pressure for the room temperature ultrasonic experiment on FeS. Red circles are FeS-I, red upward triangles are FeS-II, and red downward triangles are FeS-III. Data from DAC experiment discussed in Chapter 3 shown in blue as reference. Parameters obtained from third-order Birch-Murnaghan fits of each of the three phases observed during the experiment are shown on diagram. Curves are calculated compression curved based on these fits for each phase.

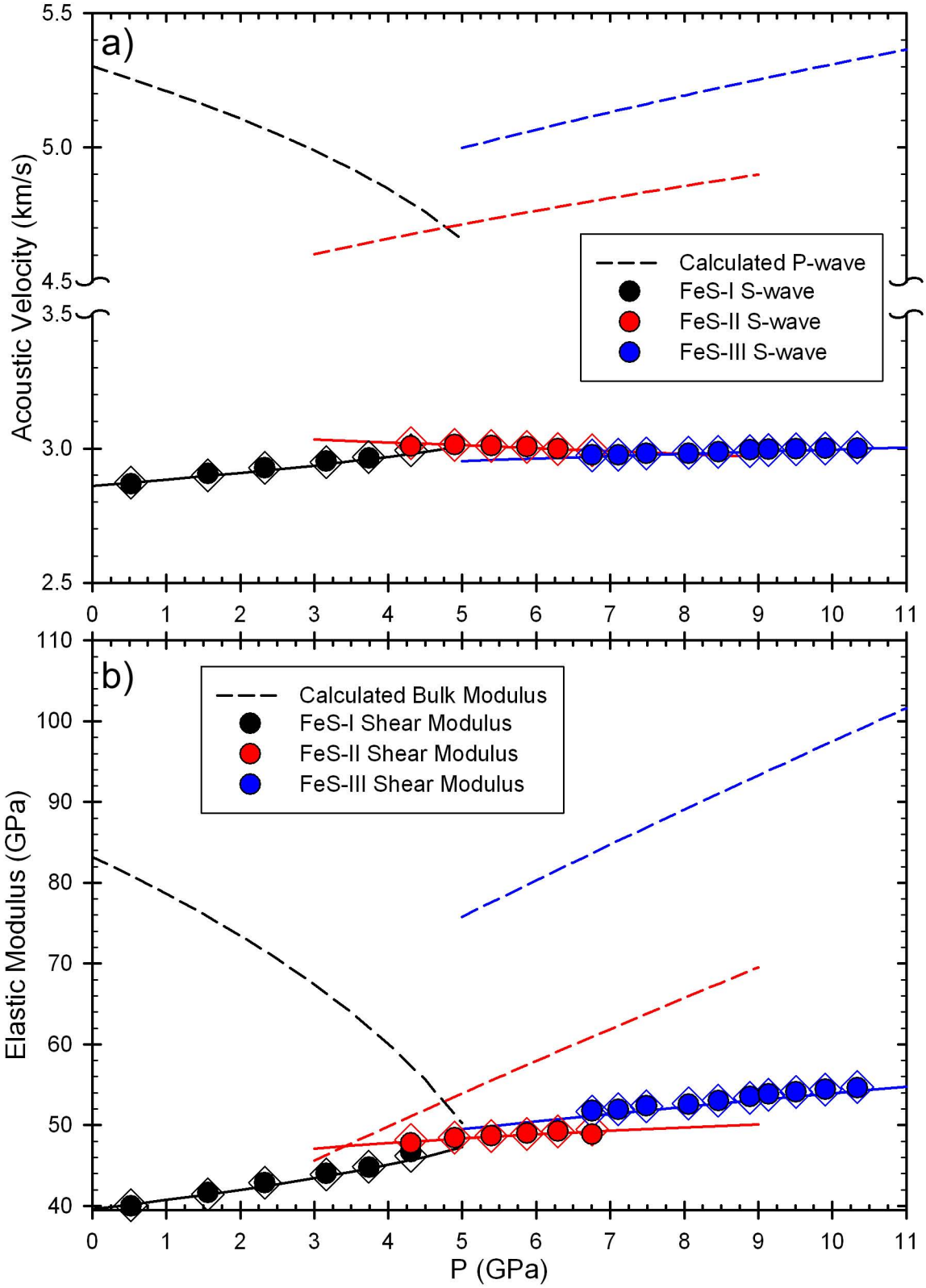

Figure 4.4.3. a) Acoustic velocities in FeS vs. Pressure. b) Elastic Modulus of FeS vs. Pressure. Circles represent measured velocities, diamonds and dashed lines are calculated values. Black symbols and curves are FeS-I, red are for FeS-II, and blue are FeS-III.

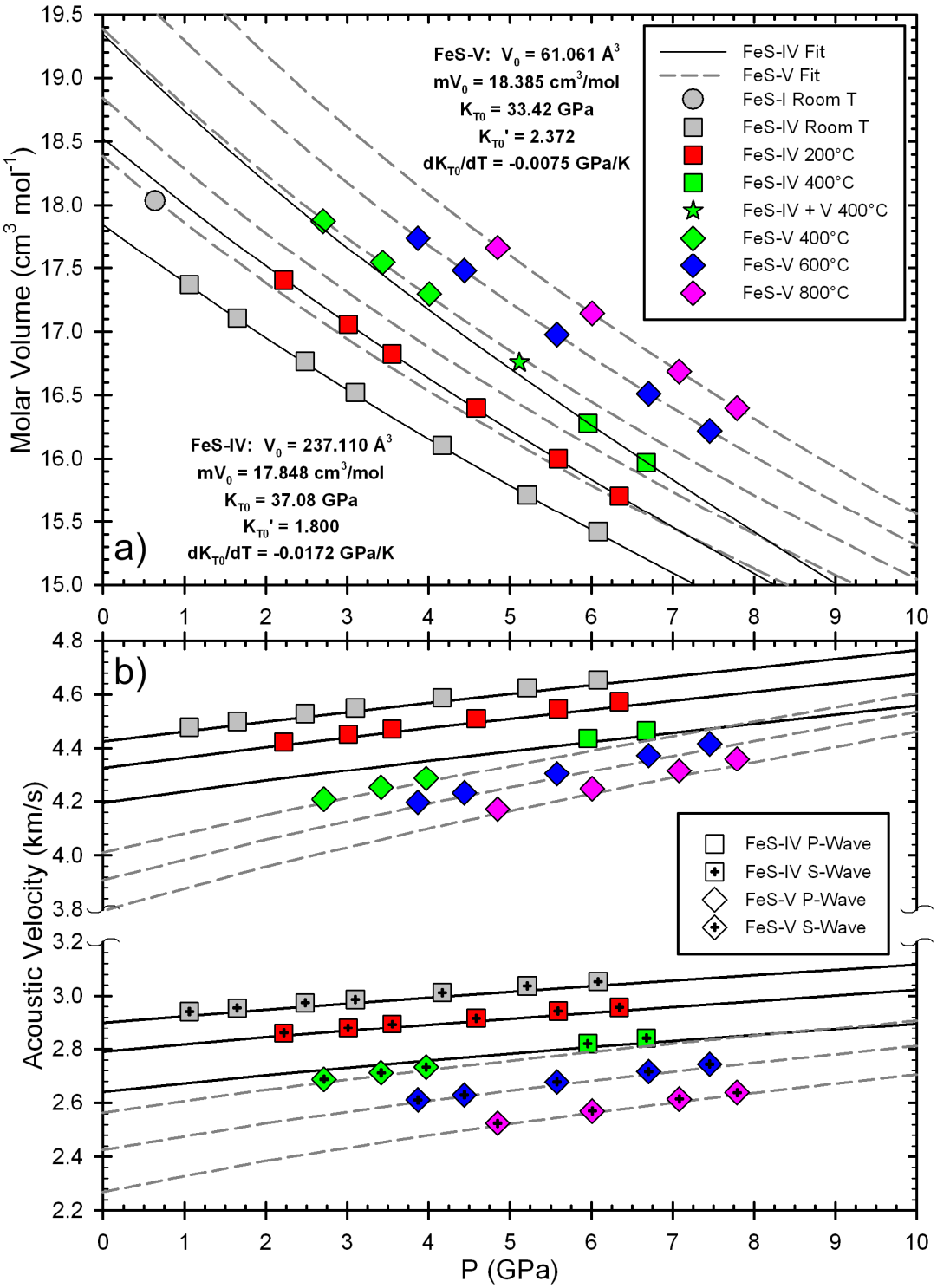

Figure 4.4.4. a) Molar volume vs. pressure for the high T ultrasonic experiment on FeS. Squares represent FeS-IV, and diamonds represent FeS-V; symbols temperature-coded as in legend. Parameters obtained from high-temperature third-order Birch-Murnaghan fits are shown on diagram. Calculated compression curves based on these fits are shown. b) Acoustic velocities vs. pressure. Open symbols are P-wave velocities, symbols with crosshairs are S-wave velocities. Coding of symbols is the same as in a).

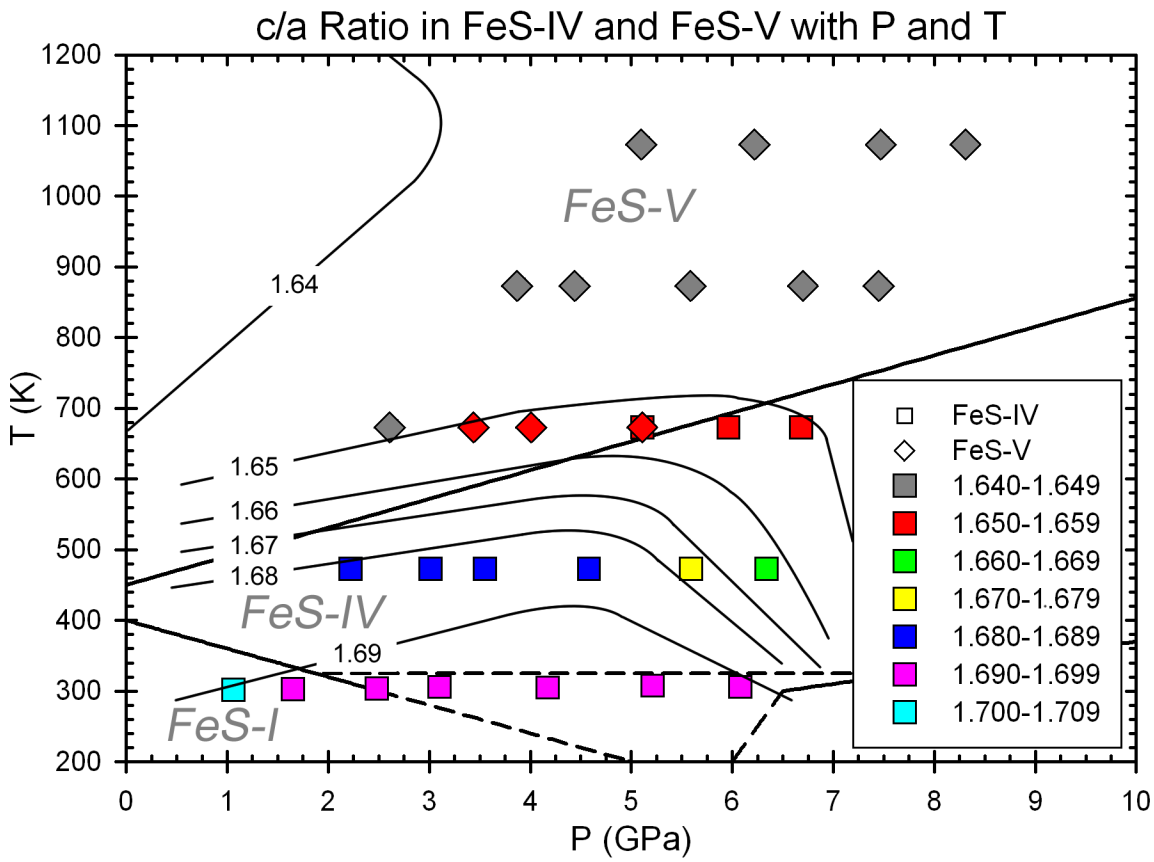

Figure 4.4.5. Plot of c/a ratio in FeS-IV and FeS-V as a function of pressure and temperature. Squares represent FeS-IV and diamonds represent FeS-V, with data points color coded as in the legend. Contour lines are the isopleths showing the c/a ratio of the fundamental NiAs unit cell given in Urakawa et al. (2004). Phase boundaries from Urakawa et al. (2004) are shown as reference.

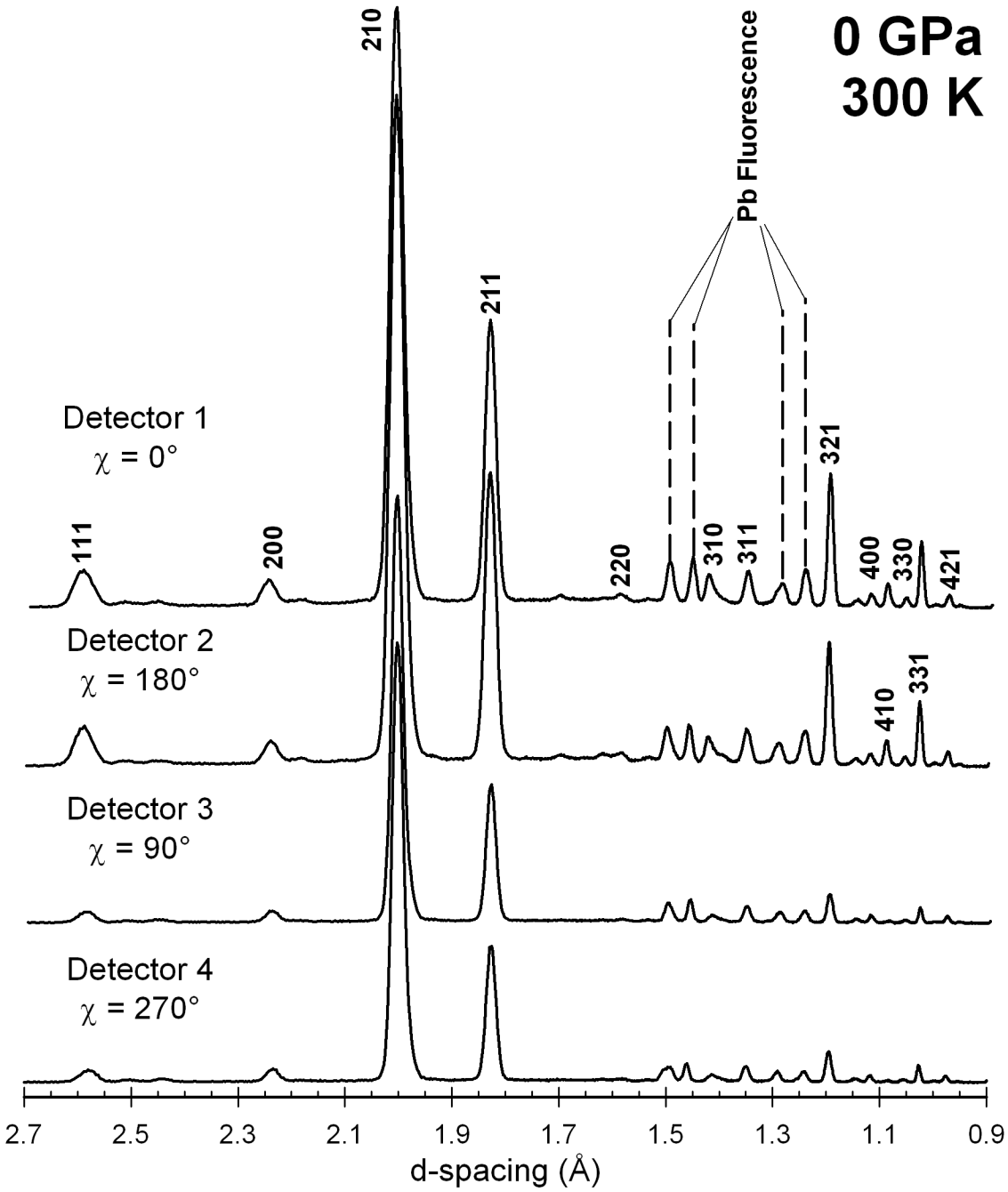

Figure 4.5.1. X-ray diffraction patterns of the ε-FeSi sample taken by each of the four detectors at ambient pressure and temperature. Orientation of the detector is shown for each pattern. Intensities normalized to highest peak intensity (Detector 2) for comparison between patterns. Slight shifts in peak position between detectors are caused by differences in calibration angle for each detector. Peaks are labeled with their *hkl* values, and Pb fluorescence peaks are shown for reference. Only peaks used in cell refinement are labeled.

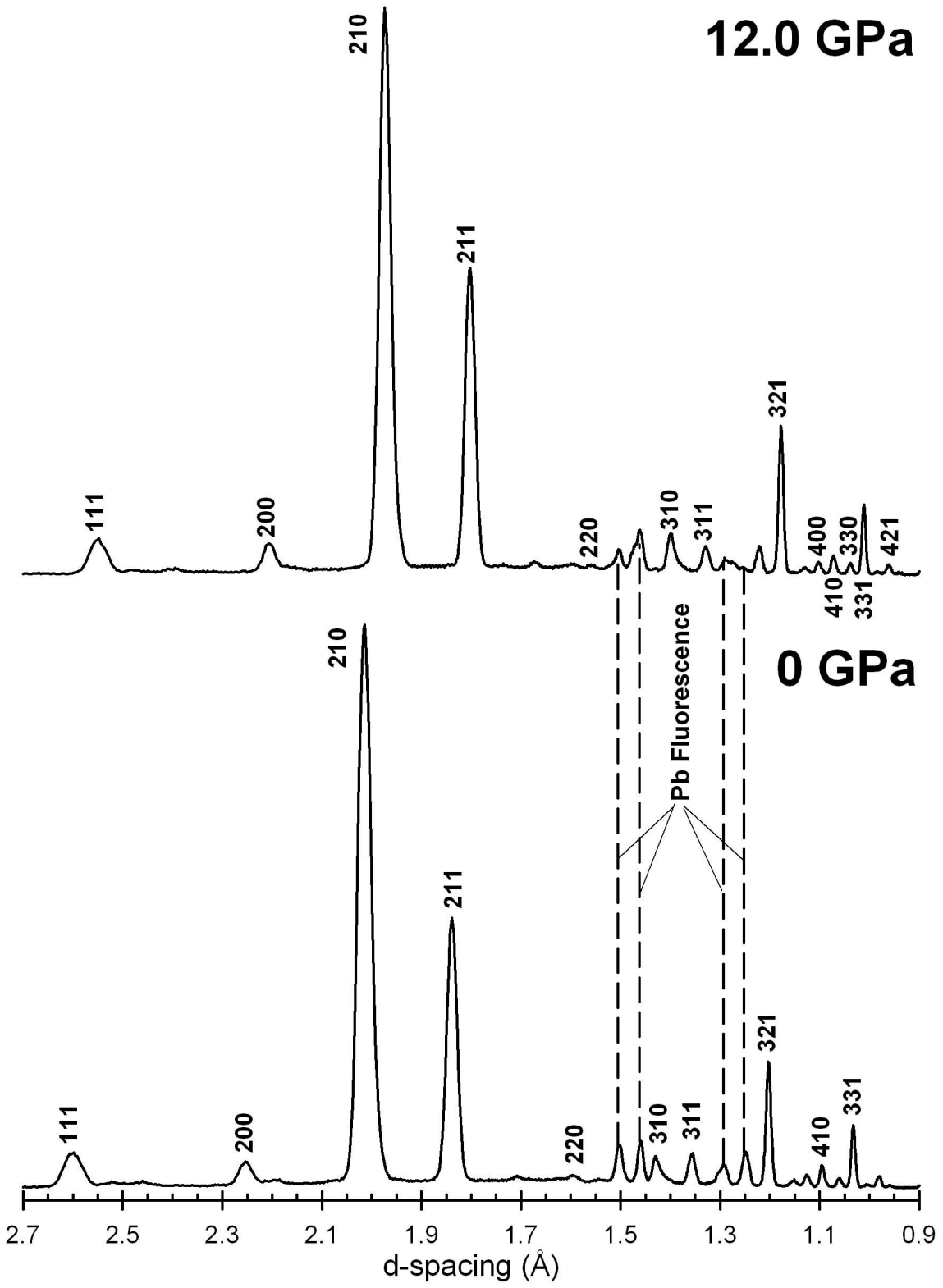

Figure 4.5.2. X-ray diffraction patterns of the ε-FeSi sample taken at ambient pressure (bottom) and 12.0 GPa (top) at room T. Peaks are labeled with their hkl values, and Pb fluorescence peaks are shown for reference. Sample clearly remains ε-FeSi throughout experiment. Only peaks used in cell refinement are labeled.

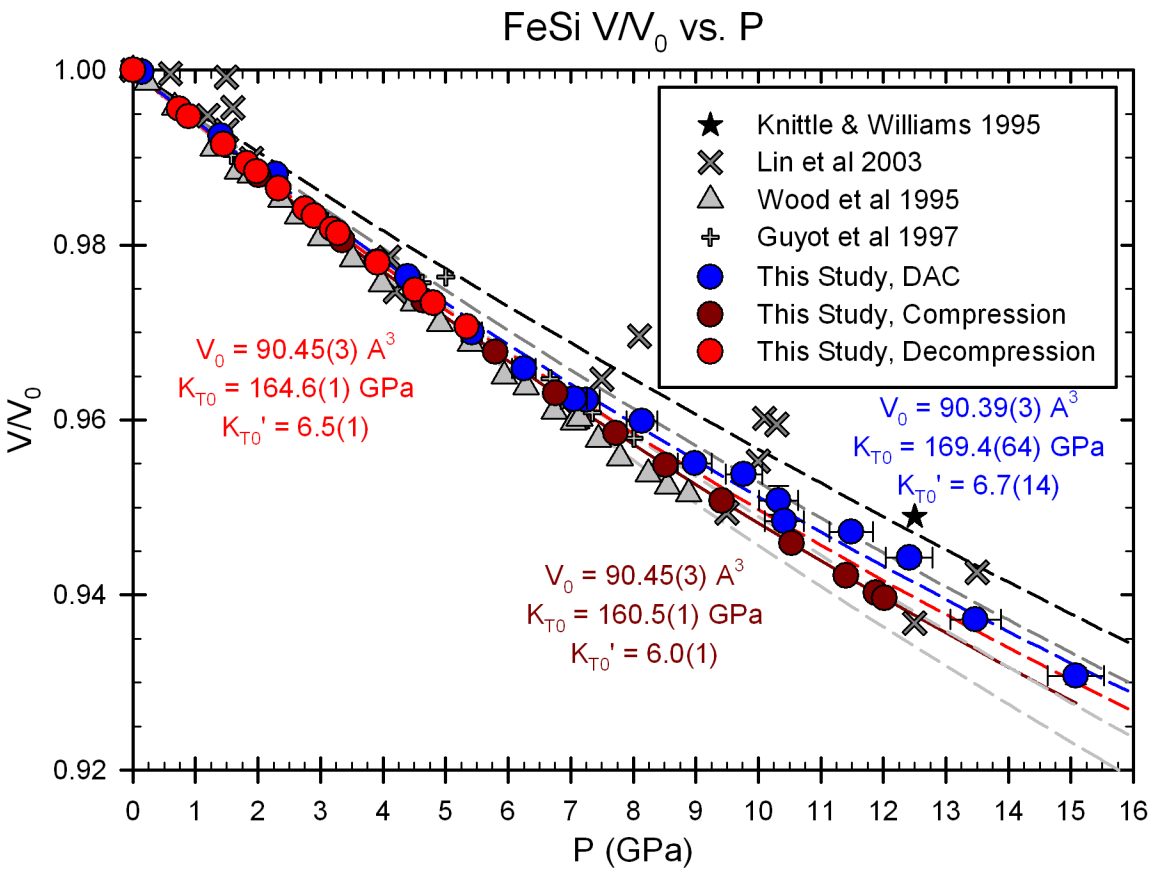

Figure 4.5.3. Variation of unit-cell volumes of ε-FeSi with pressure compared with previous studies. Black stars are the results of Knittle and Williams (1995), dark gray X's are the results of Lin et al. (2003), gray triangles are the data of Wood et al (1995), and gray crosses are data from Guyot et al. (1997). Dark red circles are data collected in this study during cold compression, red circles are data collected during decompression after heating. Dashed lines represent curves for each set of data BM-3 fitted to Equation 3.1 for comparison with other data sets.

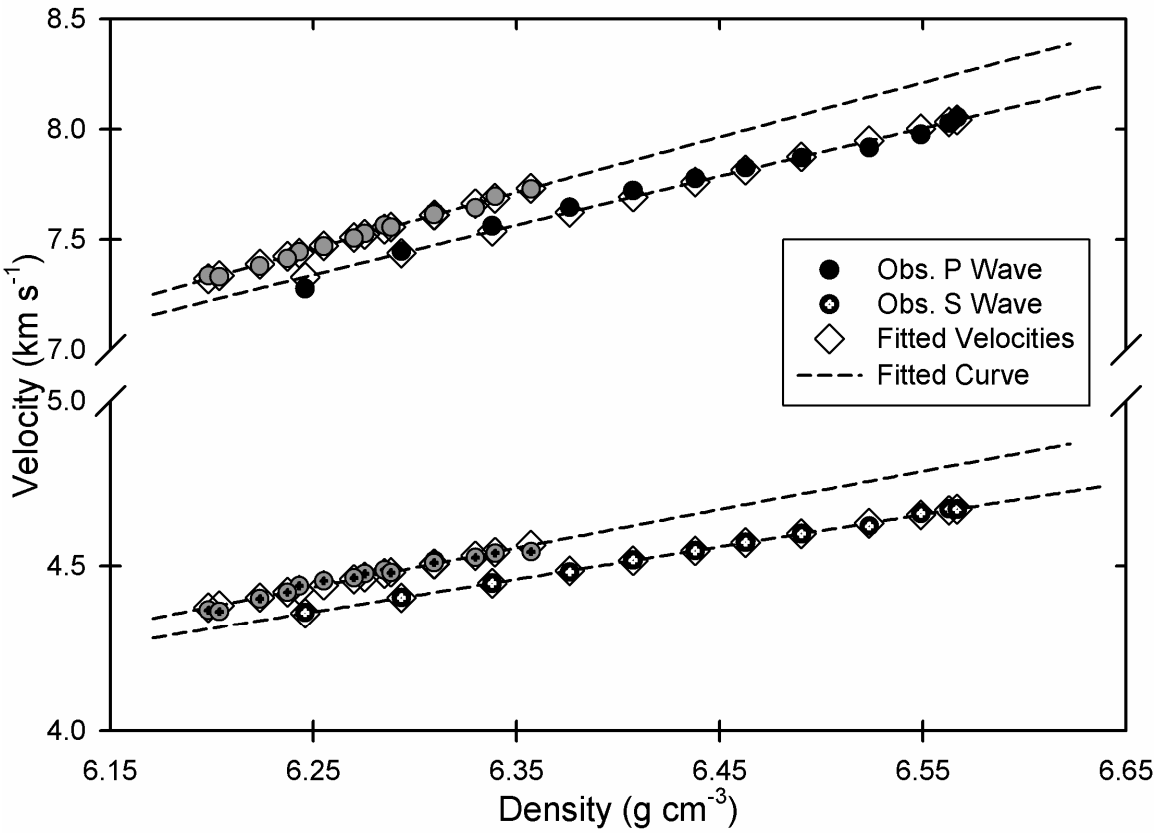

Figure 4.5.4. Variation of elastic compressional (V_P) and shear (V_S) wave velocities for ε-FeSi as a function of density from the ultrasonic measurements and X-ray data to 12.0 GPa. Solid circles are observed P wave velocities, and the circles with crosshairs represent observed S wave velocities. Black symbols are data collected during cold compression; gray symbols are data collected during decompression after heating. Open diamonds are the velocities obtained from the finite-strain fitting of the elastic moduli data; dashed lines are fitted curves based on this finite-strain fitting of each data set.

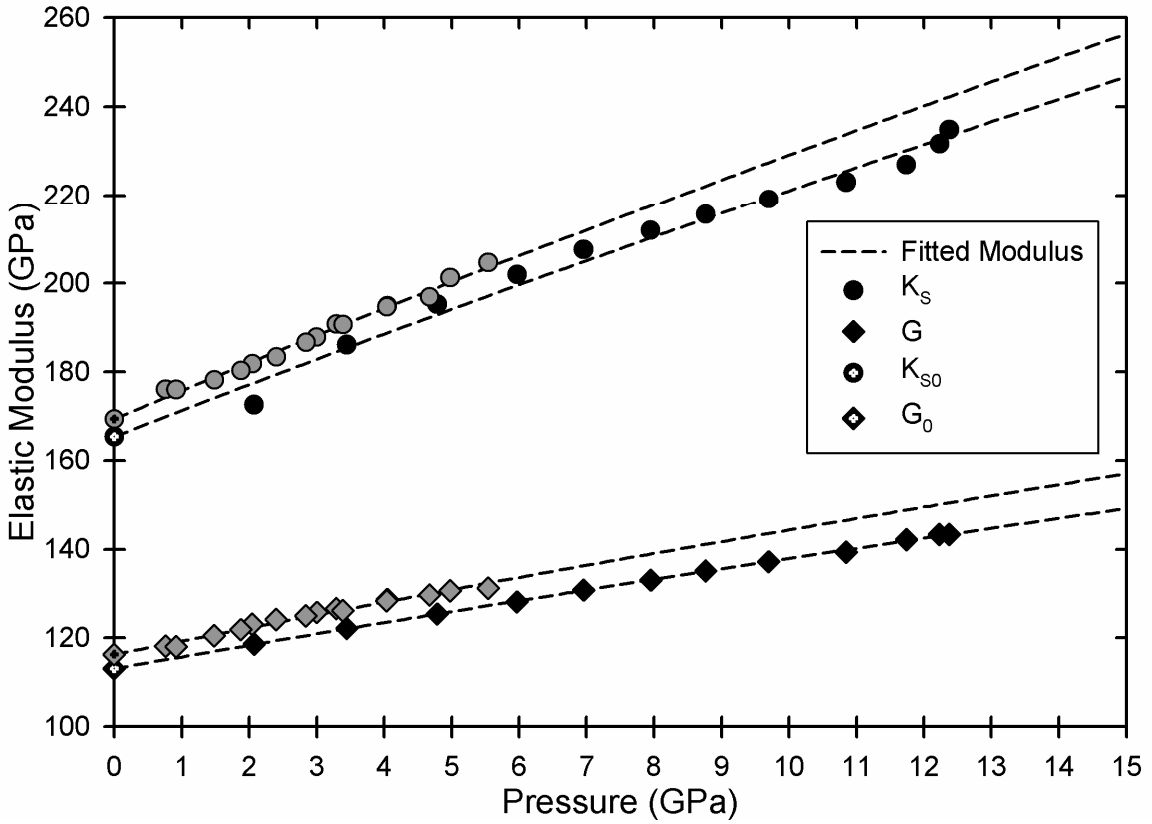

Figure 4.5.5. Variation of experimental measurements of elastic bulk (K_S) and shear (G) moduli as a function of pressure. Circles are adiabatic bulk modulus measurements, diamonds are shear modulus values. Black symbols represent data collected during cold compression, gray symbols are those data collected during decompression after heating. Symbols with crosshairs are the zero-pressure values obtained from the finite-strain fitting of each data set. Pressures in this figure calculated adiabatically, which accounts for slight shift from isothermal values.

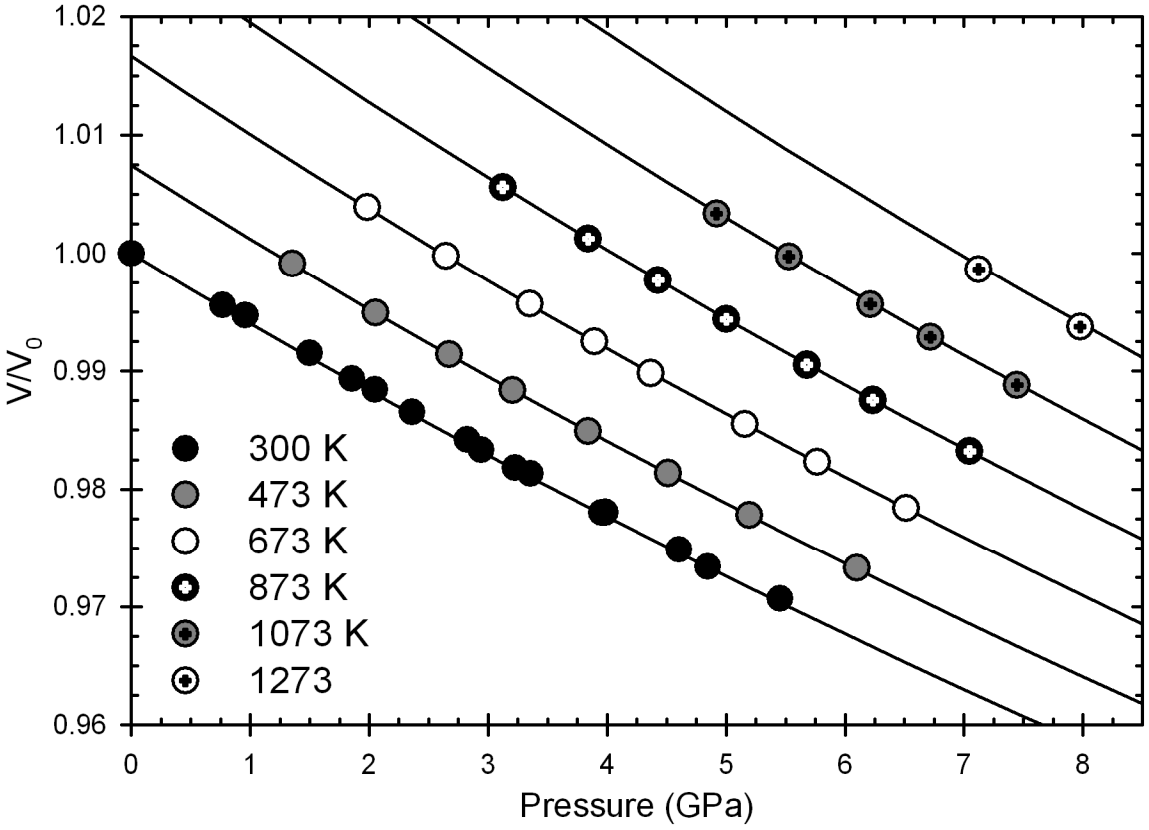

Figure 4.5.6. Variation of unit-cell volumes of ε-FeSi as a function of pressure and temperature from the ultrasonic measurements and X-ray data to 8 GPa and 1273 K. Data symbols are coded by temperature as shown in the legend. Lines represent compression curves calculated based on fitted parameters.

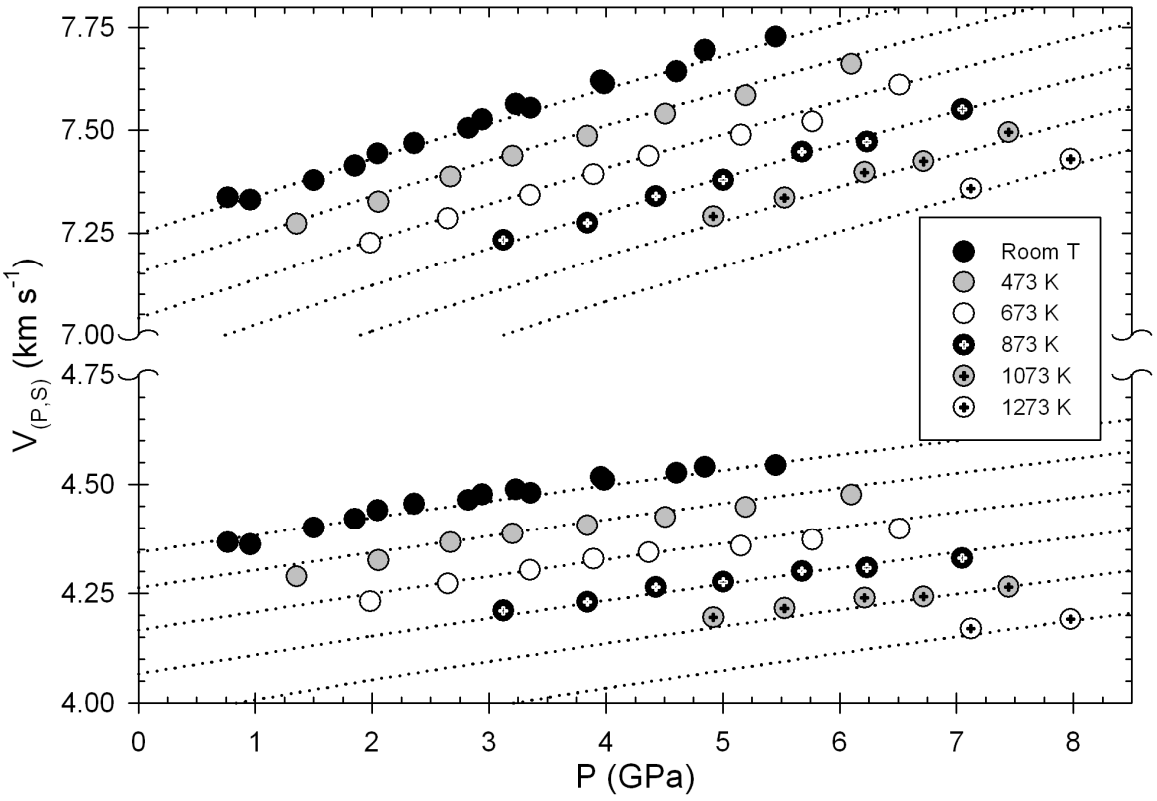

Figure 4.5.7. Variation of elastic compressional (V_P) and shear (V_S) wave velocities for ε-FeSi as a function of pressure and temperature from the ultrasonic measurements and X-ray data to 8 GPa and 1273 K. Data above the break are P-wave velocities, and data below the break are S-wave velocities. Data symbols are coded by temperature as shown in the legend; velocities obtained from the finite-strain fitting of the thermoelastic data are shown as dashed lines.

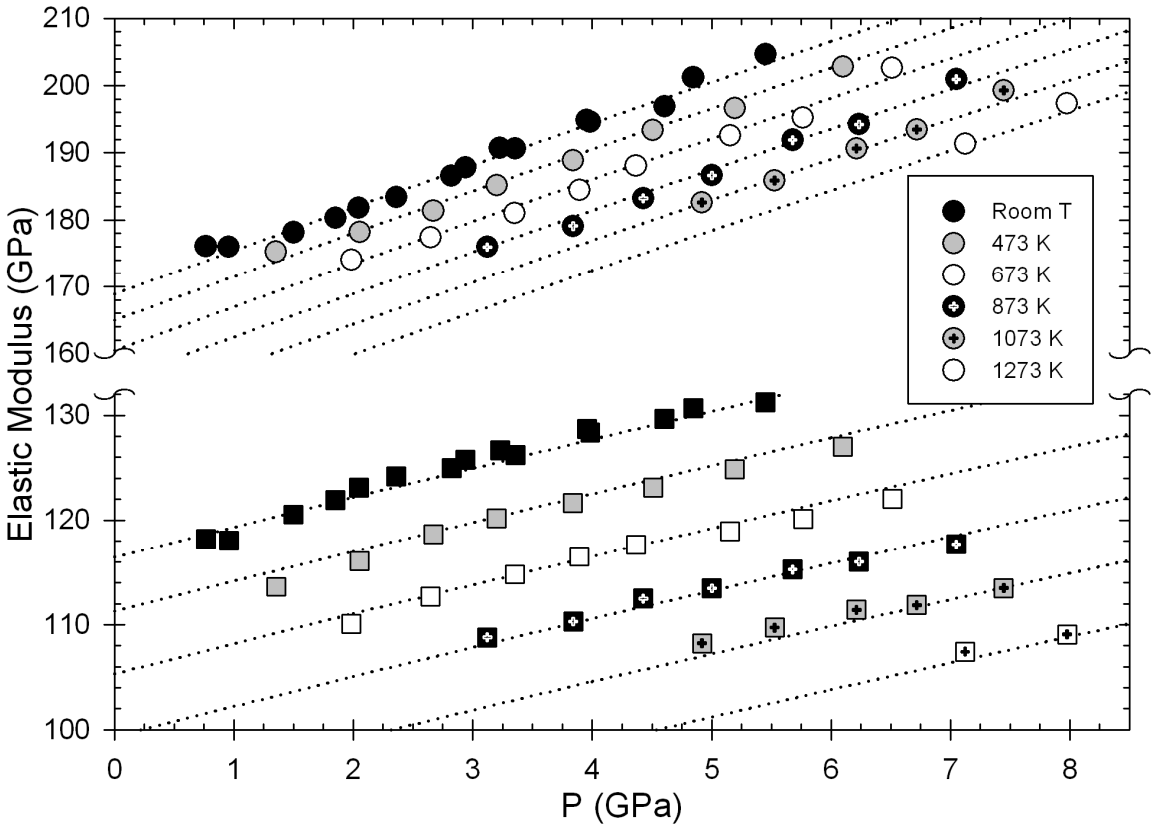

Figure 4.5.8. Variation of experimental measurements of elastic bulk (K_S) and shear (G) moduli as a function of pressure. Circles are adiabatic bulk modulus measurements, squares are shear modulus values; symbols are coded by temperature, using the same coding for both elastic moduli. The third-order finite-strain fits of these experimental data are shown as dashed lines.

Table 4.1. Experimental ultrasonic and X-ray results on FeS_2 at Room T

P (GPa)[a]	ρ (g cm^{-3})	2tp (ms)	2ts (ms)	L (mm)	V (Å^3)	V_P (km s^{-1})	V_S (km s^{-1})	K_S (GPa)	G (GPa)
0.00	5.012	-	-	0.6100	159.01(3)	-	-	-	-
1.88	5.078	0.1558	0.2518	0.6060	156.94(4)	7.78	4.81	150.7	117.5
3.20	5.122	0.1528	0.2480	0.6043	155.58(5)	7.91	4.87	158.5	121.5
4.28	5.157	0.1508	0.2452	0.6032	154.54(4)	8.00	4.92	163.6	124.8
5.22	5.186	0.1488	0.2426	0.6023	153.66(4)	8.10	4.97	169.5	128.1
6.15	5.215	0.1474	0.2410	0.6010	152.82(4)	8.15	4.99	173.5	129.8
6.81	5.234	0.1464	0.2398	0.6002	152.25(4)	8.20	5.01	176.8	131.4
7.54	5.256	0.1450	0.2380	0.5995	151.63(4)	8.27	5.04	181.4	133.5
8.24	5.276	0.1438	0.2366	0.5991	151.05(4)	8.33	5.06	185.9	135.1
8.88	5.294	0.1428	0.2354	0.5987	150.54(4)	8.39	5.09	189.7	137.2
9.57	5.313	0.1418	0.2342	0.5983	149.99(5)	8.44	5.11	193.5	138.7
MAC Experiment 1 - X-ray Only									
P (GPa)[b]	ρ (g cm^{-3})	2tp (ms)	2ts (ms)	L (mm)	V (Å^3)	V_P (km s^{-1})	V_S (km s^{-1})	K_S (GPa)	G (GPa)
0.00	5.020	-	-	-	158.75(4)	-	-	-	-
1.89	5.087	-	-	-	156.66(5)	-	-	-	-
3.40	5.138	-	-	-	155.11(5)	-	-	-	-
4.55	5.176	-	-	-	153.97(6)	-	-	-	-
5.54	5.207	-	-	-	153.05(9)	-	-	-	-
6.62	5.240	-	-	-	152.07(5)	-	-	-	-
7.36	5.263	-	-	-	151.43(7)	-	-	-	-
8.17	5.287	-	-	-	150.74(8)	-	-	-	-
8.94	5.309	-	-	-	150.10(5)	-	-	-	-
9.70	5.331	-	-	-	149.49(4)	-	-	-	-
10.45	5.352	-	-	-	148.89(5)	-	-	-	-
MAC Experiment 2 - X-ray Only									
P (GPa)[b]	ρ (g cm^{-3})	2tp (ms)	2ts (ms)	L (mm)	V (Å^3)	V_P (km s^{-1})	V_S (km s^{-1})	K_S (GPa)	G (GPa)
0.00	5.019	-	-	-	158.78(5)	-	-	-	-
1.70	5.080	-	-	-	156.87(5)	-	-	-	-
3.29	5.134	-	-	-	155.21(9)	-	-	-	-
4.44	5.172	-	-	-	154.09(4)	-	-	-	-
5.52	5.206	-	-	-	153.07(5)	-	-	-	-
6.81	5.246	-	-	-	151.91(4)	-	-	-	-
7.56	5.270	-	-	-	151.23(5)	-	-	-	-
8.55	5.297	-	-	-	150.45(6)	-	-	-	-
9.53	5.327	-	-	-	149.59(9)	-	-	-	-

[a]Pressures were calculated using Equation 3.1. [b]Pressures measured by X-ray diffraction of NaCl standard. Values in parentheses are 1s error in the last digits. Two-way travel times have 1s of ~0.4 ns for *S* waves and ~0.2 ns for *P* waves. The precision of image measurement of sample length is 0.2-0.4%. Uncertainties in velocities are less than 0.3% , and less than 1.0% for the derived elastic moduli. The densities at high pressures are calculated using unit-cell volumes obtained from X-ray data and the theoretical density.

Table 4.2. Comparison of elastic properties of FeS_2 with previous studies

Ref.	Method	P Range (GPa)	V_0 (Å^3)	K_{S0} (GPa)	K_{S0}'	K_{T0} (GPa)	K_{T0}'	G_0 (GPa)	G_0'
1	**Ultrasonics w/ X-Ray**	**10**	**159.01(3)**	**138.9(7)**	**6.0(1)**	**137.5**	**6.0**	**112.3(3)**	**3.0(<1)**
1	XRD-MAC	10	159.01(3)	-	-	137.51(1)	6.01(1)	-	-
2	XRD-MAC	9.5	158.78(5)	-	-	136.7(9)	5.3(3)	-	-
3	XRD-MAC	10.5	158.75(3)	-	-	137.6(5)	5.3(1)	-	-
4	XRD-DAC	13.2	159.14(5)	-	-	143.1(10)	5.0(2)	-	-
5	Linear Compression	0.3	-	-	-	148	-	-	-
6	Diffuse X-Ray	0	158.34	-	-	143.3	-	123.8	-
7	Ultrasonic	0	158.87	-	-	145.9	-	129.8	-
8	Shockwave	180	-	162(9)	4.7(3)	-	-	-	-
9	Radial XRD in DAC	50	159.04	-	-	133.5(52)	5.73(58)	-	-
10	Calculation	Calc. 44 GPa	157.33	157.5	-	154.5	-	-	-
11	Calculation	Calc. 150 GPa	158.87	-	-	176.21	4.65	-	-
12	Calculation	Calc. 135 GPa	159.035	-	-	150	4.56	131	1.85

1. This Study; 2. This Study; 3. This Study; 4. This Study; 5. Bridgman (1949); 6. Prasad & Wooster (1956); 7. Simmons & Birch (1963); 8. Ahrens & Jeanloz (1987); 9. Merkel et al (2002); 10. Sithole et al (2003); 11. Blanchard et al (2005); 12. LePage & Rodgers (2005)

XRD = X-Ray Diffraction; MAC = Multi-Anvil Cell; DAC = Diamond Anvil Cell

Table 4.3. Unit cell parameters as determined by X-ray diffraction for FeS-I, II, and III at high pressure

FeS-I (Hexagonal)								
P (GPa)	T (K)	a (Å)	b (Å)	c (Å)	β (°)	V (Å^3)	V_m (cm^3 mol^{-1})	ρ (g cm^{-3})
0.00	300	5.972(2)	5.972(2)	11.722(6)	120.0000	362.1(3)	18.17(3)	4.838
0.43	300	5.962(3)	5.962(3)	11.701(6)	120.0000	360.2(5)	18.08(4)	4.864
1.47	300	5.935(5)	5.935(5)	11.646(8)	120.0000	355.3(5)	17.83(4)	4.930
2.45	300	5.908(4)	5.908(4)	11.590(7)	120.0000	350.3(3)	17.58(3)	5.001
3.11	300	5.889(6)	5.889(6)	11.552(9)	120.0000	346.9(3)	17.41(3)	5.050
3.67	300	5.872(4)	5.872(4)	11.512(7)	120.0000	343.8(5)	17.25(4)	5.096
4.31	***300***	***5.849(3)***	***5.849(3)***	***11.461(7)***	***120.0000***	***339.6(6)***	***17.04(5)***	***5.159***
0.64	302	5.959(4)	5.959(4)	11.689(6)	120.0000	359.4(5)	18.03(4)	4.875
FeS-II (Orthorhombic)								
P (GPa)	T (K)	a (Å)	b (Å)	c (Å)	β (°)	V (Å^3)	V_m (cm^3 mol^{-1})	ρ (g cm^{-3})
4.31	***300***	***5.711(3)***	***3.352(2)***	***5.778(4)***	***90.0000***	***110.59(9)***	***16.65(2)***	***5.272***
4.86	300	5.693(3)	3.341(2)	5.755(4)	90.0000	109.44(8)	16.48(2)	5.336
5.18	300	5.678(3)	3.336(2)	5.743(4)	90.0000	108.78(9)	16.38(2)	5.368
5.69	300	5.661(2)	3.327(2)	5.721(4)	90.0000	107.76(9)	16.22(2)	5.419
6.29	300	5.641(4)	3.317(2)	5.699(3)	90.0000	106.63(9)	16.05(2)	5.476
6.76	***300***	***5.625(3)***	***3.309(2)***	***5.686(4)***	***90.0000***	***105.82(8)***	***15.93(2)***	***5.518***
FeS-III (Monoclinic)								
P (GPa)	T (K)	a (Å)	b (Å)	c (Å)	β (°)	V (Å^3)	V_m (cm^3 mol^{-1})	ρ (g cm^{-3})
6.76	***300***	***8.159(6)***	***5.687(8)***	***6.487(6)***	***93.45(5)***	***299.9(2)***	***15.05(2)***	***5.841***
7.11	300	8.139(6)	5.678(7)	6.482(7)	93.39(6)	298.7(3)	14.99(3)	5.864
7.49	300	8.136(7)	5.663(8)	6.475(6)	93.42(6)	297.4(2)	14.93(2)	5.890
8.06	300	8.111(6)	5.659(9)	6.465(9)	93.32(9)	296.1(5)	14.86(4)	5.917
8.46	300	8.099(8)	5.645(8)	6.460(7)	93.28(7)	294.8(4)	14.79(3)	5.943
8.89	300	8.077(6)	5.635(7)	6.453(6)	93.18(5)	293.5(2)	14.73(2)	5.970
9.14	300	8.059(7)	5.624(7)	6.451(7)	93.20(6)	292.1(3)	14.66(3)	5.997
9.51	300	8.033(6)	5.621(8)	6.442(7)	93.11(7)	290.9(3)	14.60(2)	6.022
9.91	300	8.036(8)	5.609(9)	6.438(8)	93.22(7)	289.8(4)	14.54(3)	6.046
10.34	300	8.020(7)	5.601(8)	6.435(7)	93.22(6)	288.7(2)	14.49(2)	6.067

Pressures were measured by X-ray diffraction of NaCl standard. Values in parentheses are 1σ error in the last digits. The densities at high pressures are calculated using unit-cell volumes obtained from X-ray data and the theoretical density. Bold italicized lines are data collected for coexisting phases.

Table 4.4. Experimental ultrasonic and X-ray results on FeS during cold compression

P (GPa)	*T* (K)	Phase	2*tp* (ms)	2*ts* (ms)	*L* (mm)	*V* (Å^3)	*V* (cm^3 mol^{-1})	ρ (g cm^{-3})	V_S (km s^{-1})	*G* (GPa)	V_{Pcal} (km s^{-1})	K_{Scal} (GPa)
0.00	300	I	-	-	-	362.1(3)	18.17(3)	4.838	-	-	-	-
0.43	300	I	0.3290	0.5690	0.8159	360.2(5)	18.08(4)	4.864	2.87	40.1	5.27	81.6
1.47	300	I	0.3344	0.5590	0.8122	355.3(5)	17.83(4)	4.930	2.91	41.8	5.16	75.6
2.45	300	I	0.3330	0.5524	0.8086	350.3(3)	17.58(3)	5.001	2.93	42.9	5.05	70.3
3.11	300	I	0.3336	0.5466	0.8067	346.9(3)	17.41(3)	5.050	2.95	44.0	4.97	66.1
3.67	300	I	0.3378	0.5414	0.8025	343.8(5)	17.25(4)	5.096	2.96	44.7	4.90	62.8
4.31	***300***	***I***	***0.3480***	***0.5296***	***0.7967***	***339.6(6)***	***17.04(5)***	***5.159***	***3.01***	***46.7***	***4.79***	***56.0***
4.31	***300***	***II***	***0.3480***	***0.5296***	***0.7967***	***110.59(9)***	***16.65(2)***	***5.272***	***3.01***	***47.8***	***4.69***	***52.3***
4.86	300	II	0.3556	0.5252	0.7913	109.44(8)	16.48(2)	5.336	3.01	48.3	4.72	54.4
5.18	300	II	0.3602	0.5236	0.7884	108.78(9)	16.38(2)	5.368	3.01	48.6	4.74	55.8
5.69	300	II	0.3620	0.5216	0.7840	107.76(9)	16.22(2)	5.419	3.01	49.1	4.76	57.3
6.29	300	II	0.3618	0.5188	0.7778	106.63(9)	16.05(2)	5.476	3.00	49.3	4.80	60.5
6.76	***300***	***II***	***0.3868***	***0.5210***	***0.7755***	***105.82(8)***	***15.93(2)***	***5.518***	***2.98***	***49.0***	***4.82***	***62.9***
6.76	***300***	***III***	***0.3868***	***0.5210***	***0.7755***	***299.9(2)***	***15.05(2)***	***5.841***	***2.98***	***51.9***	***5.15***	***85.8***
7.11	300	III	0.3476	0.5196	0.7733	298.7(3)	14.99(3)	5.864	2.98	52.1	5.17	87.3
7.49	300	III	0.3398	0.5168	0.7706	297.4(2)	14.93(2)	5.890	2.98	52.3	5.20	89.5
8.06	300	III	0.3316	0.5146	0.7671	296.1(5)	14.86(4)	5.917	2.98	52.6	5.22	91.2
8.46	300	III	0.3252	0.5118	0.7644	294.8(4)	14.79(3)	5.943	2.99	53.1	5.25	93.0
8.89	300	III	0.3184	0.5098	0.7634	293.5(2)	14.73(2)	5.970	2.99	53.4	5.27	94.6
9.14	300	III	0.3122	0.5086	0.7620	292.1(3)	14.66(3)	5.997	3.00	54.0	5.30	96.5
9.51	300	III	0.3058	0.5070	0.7601	290.9(3)	14.60(2)	6.022	3.00	54.2	5.32	98.2
9.91	300	III	0.2994	0.5054	0.7583	289.8(4)	14.54(3)	6.046	3.00	54.4	5.34	99.9
10.34	300	III	0.2920	0.5034	0.7553	288.7(2)	14.49(2)	6.067	3.00	54.6	5.36	101.5

Pressures were measured by X-ray diffraction of NaCl standard. Values in parentheses are 1σ error in the last digits. Two-way travel times have 1σ of ~0.4 ns for *S* waves. The precision of image measurement of sample length is 0.2-0.4%. Uncertainties in velocities are less than 0.3% , and less than 1.0% for the derived shear moduli. The densities at high pressures are calculated using unit-cell volumes obtained from X-ray data and the theoretical density. V_P and K_S were calculated based on fitted values of K_0 and K_0' from P-V EoS (Eq. 3.1). Bold italicized lines are data collected for coexisting phases.

Table 4.5. Comparison of elastic properties of FeS-I, FeS-II, and FeS-III with previous studies

FeS-I										
Ref.	Method	P Range (GPa)	Fit Conditions	V_0 (cm^3 mol^{-1})	K_{S0} (GPa)	K_{S0}'	K_{T0} (GPa)	K_{T0}'	G_0 (GPa)	G_0'
1	**Ultrasonics w/ X-Ray**	**4.3**	**0 GPa, 300K**	**18.170(17)**	**83.2**	**-4.3**	**-**	**-**	**39.6(4)**	**1.1(2)**
1	XRD-MAC	4.3	0 GPa, 300K	18.170(17)	-	-	81.2(6)	-4.3(2)	-	-
2	XRD-DAC	3	0 GPa, 300K	18.163(16)	-	-	89.2(6)	-4.2(3)	-	-
3	XRD-DAC	3.4	0 GPa, 300K	18.162(54)	-	-	82(7)	-5(4)	-	-
4	XRD-MAC	3	0 GPa, 300K	18.191(20)	-	-	73(3)	4 (fixed)	-	-
5	Calculation	Calc. ~5 GPa	0 GPa, 300K	17.500(12)	-	-	75.6(7)	-0.9(2)	-	-
6	Calculation	Calc. 0-2.3 GPa	0 GPa, 17K	18.181	-	-	257(4)	4 (fixed)	-	-
6	Calculation	Calc. 2.3-5 GPa	0 GPa, 17K	18.181	-	-	109(3)	4 (fixed)	-	-
FeS-II										
Ref.	Method	P Range (GPa)	Fit Conditions	V_0 (cm^3 mol^{-1})	K_{S0} (GPa)	K_{S0}'	K_{T0} (GPa)	K_{T0}'	G_0 (GPa)	G_0'
1	**Ultrasonics w/ X-Ray**	**4.3 - 6.8**	**0 GPa, 300K**	**18.553(1)**	**32.13**	**4.78**	**-**	**-**	**44.5(3)**	**1.1(2)**
1	XRD-MAC	4.3 - 6.8	0 GPa, 300K	18.553(1)	-	-	30.73(1)	4.78(1)	-	-
2	XRD-DAC	4 - 6.6	0 GPa, 300K	18.337(52)	-	-	35.8(20)	4.4(4)	-	-
3	XRD-DAC	3.6 - 6.4	0 GPa, 300K	18.44(4)	-	-	35(4)	5(2)	-	-
4	XRD-MAC	3.0 - 7.0	?* GPa, 300K	-	-	-	44(3)	4 (fixed)	-	-
5	Calculation	Calc. 0-9 GPa	-	16.765(6)	-	-	76.8(3)	2.20(9)	-	-
6	Calculation	Calc. 5-7 GPa	?* GPa, 17K	-	-	-	67(5)	4 (fixed)	-	-
FeS-III										
Ref.	Method	P Range (GPa)	Fit Conditions	V_0 (cm^3 mol^{-1})	K_{S0} (GPa)	K_{S0}'	K_{T0} (GPa)	K_{T0}'	G_0 (GPa)	G_0'
1	**Ultrasonics w/ X-Ray**	**6.8 - 10.4**	**0 GPa, 300K**	**16.756(1)**	**51.553**	**5.239**	**-**	**-**	**43.9(3)**	**1.3(2)**
1	XRD-MAC	6.8 - 10.4	0 GPa, 300K	16.756(1)	-	-	48.402(1)	5.239(1)	-	-
2	XRD-DAC	7.9 - 11.6	0 GPa, 300K	16.738(1)	-	-	47.777(3)	5.898(9)	-	-
4	XRD-MAC	7 - 14.5	10.3 GPa, 300K	14.555	-	-	49(2)	4 (fixed)	-	-
5	Calculation	Calc. 0-25 GPa	-	14.844(18)	-	-	157.7(8)	4.72(3)	-	-
6	Calculation	Calc. 8-28 GPa	?* GPa, 17K	-	-	-	153(3)	4 (fixed)	-	-

1. This Study; 2. This Study; 3. King & Prewitt (1982); 4. Kusaba et al (1997); 5. Martin et al (2001); 6. Kobayashi et al (2005)

*Reference pressure of fitting not given by authors. XRD = X-Ray Diffraction; MAC = Multi-Anvil Cell; DAC = Diamond Anvil Cell

Table 4.6. Unit cell parameters as determined by X-ray diffraction for FeS-IV and V at high P and T

FeS-IV (Hexagonal)								
P (GPa)	T (K)	a (Å)	b (Å)	c (Å)	β (°)	V (Å^3)	V_m (cm^3 mol^{-1})	ρ (g cm^{-3})
6.68	673	6.666(2)	6.666(2)	5.515(3)	120.0000	212.2(1)	15.97(1)	5.504
6.34	473	6.610(3)	6.610(3)	5.515(4)	120.0000	208.7(2)	15.71(1)	5.597
6.08	306	6.539(2)	6.539(2)	5.533(3)	120.0000	204.9(2)	15.42(1)	5.701
5.96	673	6.705(2)	6.705(2)	5.555(3)	120.0000	216.3(1)	16.28(1)	5.400
5.59	473	6.637(3)	6.637(3)	5.5723)	120.0000	212.6(4)	16.00(3)	5.494
5.21	308	6.576(2)	6.576(2)	5.576(4)	120.0000	208.8(1)	15.72(1)	5.594
5.11	***673***	***6.771(2)***	***6.771(2)***	***5.606(3)***	***120.0000***	***222.6(1)***	***16.76(2)***	***5.246***
4.58	473	6.688(2)	6.688(2)	5.625(4)	120.0000	217.9(2)	16.40(1)	5.360
4.17	305	6.632(2)	6.632(2)	5.619(3)	120.0000	214.0(2)	16.11(1)	5.458
3.55	473	6.739(3)	6.739(3)	5.682(4)	120.0000	223.5(2)	16.83(1)	5.225
3.10	306	6.683(2)	6.683(2)	5.674(4)	120.0000	219.5(2)	16.52(2)	5.320
3.01	473	6.775(2)	6.775(2)	5.701(3)	120.0000	226.6(2)	17.06(2)	5.154
2.48	304	6.714(2)	6.714(2)	5.704(3)	120.0000	222.7(1)	16.77(1)	5.243
2.22	473	6.824(4)	6.824(4)	5.732(5)	120.0000	231.2(5)	17.40(4)	5.051
1.65	303	6.760(2)	6.760(2)	5.744(3)	120.0000	227.3(1)	17.11(1)	5.139
1.06	302	6.792(3)	6.792(3)	5.778(3)	120.0000	230.8(2)	17.37(2)	5.061
FeS-V (Hexagonal)								
P (GPa)	T (K)	a (Å)	b (Å)	c (Å)	β (°)	V (Å^3)	V_m (cm^3 mol^{-1})	ρ (g cm^{-3})
8.31	1073	3.367(1)	3.367(1)	5.547(1)	120.0000	54.46(3)	16.397(2)	5.361
7.45	873	3.358(1)	3.358(1)	5.517(1)	120.0000	53.87(2)	16.220(2)	5.420
7.47	1073	3.387(1)	3.387(1)	5.578(1)	120.0000	55.41(3)	16.684(2)	5.269
6.70	873	3.376(1)	3.376(1)	5.555(1)	120.0000	54.83(5)	16.510(4)	5.325
6.22	1073	3.419(1)	3.419(1)	5.624(1)	120.0000	56.93(3)	17.142(3)	5.128
5.59	873	3.408(1)	3.408(1)	5.607(1)	120.0000	56.39(3)	16.978(2)	5.178
5.11	***673***	***3.388(1)***	***3.388(1)***	***5.598(1)***	***120.0000***	***55.65(3)***	***16.76(2)***	***5.247***
5.10	1073	3.451(1)	3.451(1)	5.688(1)	120.0000	58.67(2)	17.666(2)	4.976
4.44	873	3.439(1)	3.439(1)	5.669(1)	120.0000	58.05(2)	17.479(2)	5.030
4.01	673	3.423(1)	3.423(1)	5.660(1)	120.0000	57.44(2)	17.295(1)	5.083
3.87	873	3.457(1)	3.457(1)	5.692(1)	120.0000	58.92(2)	17.741(1)	4.955
3.44	673	3.440(1)	3.440(1)	5.686(1)	120.0000	58.27(2)	17.546(2)	5.010
2.61	673	3.464(1)	3.464(1)	5.715(1)	120.0000	59.37(3)	17.876(2)	4.918

Pressures were measured by X-ray diffraction of NaCl standard. Values in parentheses are 1σ error in the last digits. The densities at high pressures are calculated using unit-cell volumes obtained from X-ray data and the theoretical density. Bold italicized lines are data collected for coexisting phases.

Table 4.7. Experimental ultrasonic and X-ray results on FeS at high P and T

P (GPa)	*T* (K)	Phase	2*tp* (ms)	2*ts* (ms)	*L* (mm)	*V* (Å^3)	*V* (cm^3 mol^{-1})	ρ (g cm^{-3})	V_S (km s^{-1})	*G* (GPa)	V_{Pcal} (km s^{-1})	K_{Scal} (GPa)
8.31	1073	V	0.3082	0.5538	0.7307	54.46(3)	16.397(2)	5.361	2.64	37.4	4.36	52.0
7.45	873	V	0.3088	0.5290	0.7257	53.87(2)	16.220(2)	5.420	2.74	40.7	4.42	51.6
7.47	1073	V	0.3114	0.5556	0.7275	55.41(3)	16.684(2)	5.269	2.61	35.9	4.32	50.5
6.70	873	V	0.3144	0.5326	0.7235	54.83(5)	16.510(4)	5.325	2.72	39.4	4.37	49.2
6.22	1073	V	0.3138	0.5572	0.7159	56.93(3)	17.142(3)	5.128	2.57	33.9	4.25	47.4
5.59	873	V	0.3166	0.5336	0.7145	56.39(3)	16.978(2)	5.178	2.68	37.2	4.30	46.1
5.11	***673***	***V***	***0.3264***	***0.5160***	***0.7118***	***55.65(3)***	***16.76(2)***	***5.247***	***2.76***	***40.0***	-	-
5.10	1073	V	0.3144	0.5630	0.7107	58.67(2)	17.666(2)	4.976	2.52	31.6	4.17	44.4
4.44	873	V	0.3146	0.5374	0.7065	58.05(2)	17.479(2)	5.030	2.63	34.8	4.23	43.6
4.01	673	V	0.3196	0.5152	0.7040	57.44(2)	17.295(1)	5.083	2.73	37.9	4.29	43.0
3.87	873	V	0.3168	0.5448	0.7112	58.92(2)	17.741(1)	4.955	2.61	33.8	4.20	42.3
3.44	673	V	0.3180	0.5228	0.7090	58.27(2)	17.546(2)	5.010	2.71	36.8	4.25	41.4
2.61	673	V	0.3166	0.5324	0.7154	59.37(3)	17.876(2)	4.918	2.69	35.6	4.21	39.7
6.68	673	IV	0.3262	0.5058	0.7185	212.2(1)	15.97(1)	5.504	2.84	44.4	4.47	50.8
6.34	473	IV	0.3196	0.4836	0.7151	208.7(2)	15.71(1)	5.597	2.96	49.0	4.57	51.6
6.08	306	IV	0.3106	0.4676	0.7139	204.9(2)	15.42(1)	5.701	3.05	53.0	4.65	52.6
5.96	673	IV	0.3206	0.5082	0.7166	216.3(1)	16.28(1)	5.400	2.82	42.9	4.44	49.3
5.59	473	IV	0.3178	0.4834	0.7117	212.6(4)	16.00(3)	5.494	2.94	47.5	4.55	50.4
5.21	308	IV	0.3106	0.4684	0.7115	208.8(1)	15.72(1)	5.594	3.04	51.7	4.62	50.5
5.11	***673***	***IV***	***0.3264***	***0.5160***	***0.7118***	***222.6(1)***	***16.76(2)***	***5.246***	***2.76***	***40.0***	-	-
4.58	473	IV	0.3134	0.4850	0.7075	217.9(2)	16.40(1)	5.360	2.92	45.7	4.51	48.1
4.17	305	IV	0.3088	0.4676	0.7045	214.0(2)	16.11(1)	5.458	3.01	49.5	4.59	49.1
3.55	473	IV	0.3022	0.4842	0.7009	223.5(2)	16.83(1)	5.225	2.89	43.6	4.47	46.3
3.10	306	IV	0.2960	0.4686	0.6999	219.5(2)	16.52(2)	5.320	2.99	47.6	4.55	46.7
3.01	473	IV	0.3026	0.4900	0.7058	226.6(2)	17.06(2)	5.154	2.88	42.7	4.45	45.1
2.48	304	IV	0.2906	0.4722	0.7023	222.7(1)	16.77(1)	5.243	2.97	46.2	4.53	46.0
2.22	473	IV	0.3000	0.4980	0.7123	231.2(5)	17.40(4)	5.051	2.86	41.3	4.42	43.6
1.65	303	IV	0.2892	0.4796	0.7087	227.3(1)	17.11(1)	5.139	2.96	45.0	4.50	44.1
1.06	302	IV	0.2900	0.4836	0.7115	230.8(2)	17.37(2)	5.061	2.94	43.7	4.48	43.3
0.64	302	I	0.2904	0.4986	0.7137	359.4(5)	18.03(4)	4.875	2.86	39.9	-	-

Pressures were measured by X-ray diffraction of NaCl standard. Values in parentheses are 1σ error in the last digits. Two-way travel times have 1σ of ~0.4 ns for *S* waves. The precision of image measurement of sample length is 0.2-0.4%. Uncertainties in velocities are less than 0.3% , and less than 1.0% for the derived shear moduli. The densities at high pressures are calculated using unit-cell volumes obtained from X-ray data and the theoretical density. V_P and K_S were calculated based on fitted values of K_0 and K_0' from P-V EoS (Eq. 3.1). Bold italicized lines are data collected for coexisting phases.

Table 4.8. Comparison of thermoelastic properties of FeS-IV and FeS-V with previous studies

FeS-IV											
Ref.	Method	P-T Range	Fit Conditions	V_0 (cm^3 mol^{-1})	α (K^{-1})	K_0 (GPa)	K_0'	$\partial K_0/\partial T$ (GPa K^{-1})	G_0 (GPa)	G_0'	$\partial G/\partial T$ (GPa K^{-1})
1[a]	**Ultrasonics w/ X-Ray**	**1-7 GPa, 300-673K**	**0 GPa, 300K**	**17.848(8)**	**2.16 x 10^{-4}**	**39.96**	**1.772**	**-0.009**	**40.8(3)**	**1.82(1)**	**-0.0259(8)**
1[b]	XRD-MAC	1-7 GPa, 300-673K	0 GPa, 300K	17.848(8)	2.16 x 10^{-4}	37.08(9)	1.800(5)	-0.0172(2)	-	-	-
2[b]	XRD-DAC	25 GPa, 800 K	0 GPa, 800K	17.80(5)	-	54(6)	4 (fixed)	-	-	-	-
3[b]	XRD-MAC	15 GPa, 873K	7.5 GPa, 473K	-	-	48(5)	4 (fixed)	-	-	-	-
3[b]	XRD-MAC	15 GPa, 873K	7.5 GPa, 573K	-	-	49(2)	4 (fixed)	-	-	-	-
4[b]	XRD-MAC	20 GPa, 1200K	0 GPa, 600K	17.164(31)	8.98 x 10^{-5}	62.5(9)	4 (fixed)	-0.0208(28)	-	-	-
FeS-V											
Ref.	Method	P & T Range	Fit Conditions	V_0 (cm^3 mol^{-1})	α (K^{-1})	K_0 (GPa)	K_0'	$\partial K_0/\partial T$ (GPa K^{-1})	G_0 (GPa)	G_0'	$\partial G/\partial T$ (GPa K^{-1})
1[a]	**Ultrasonics w/ X-Ray**	**2.7-7.8 GPa, 673-1073K**	**0 GPa, 300K**	**18.385(6)**	**1.42 x 10^{-4}**	**35.09**	**2.412**	**-0.0023**	**38.1(2)**	**2.13(2)**	**-0.0199(9)**
1[b]	XRD-MAC	1-7 GPa, 300-673K	0 GPa, 300K	18.385(6)	1.42 x 10^{-4}	33.42(8)	2.372(6)	-0.0075(2)	-	-	-
3[b]	XRD-MAC	11 GPa, 923 K	0 GPa, 573K	-	-	43(3)	4 (fixed)	-	-	-	-
4[b]	XRD-MAC	22 GPa, 1600K	0 GPa, 1000K	18.042(45)	1.042 x 10^{-4}	54.3(10)	4 (fixed)	-0.0117(15)	-	-	-

1. This Study; 2. Fei et al (1995); 3. Kusaba et al (1998); 4. Urakawa et al (2004)

[a]Adiabatic; [b]Isothermal; XRD = X-Ray Diffraction; MAC = Multi-Anvil Cell; DAC = Diamond Anvil Cell

Table 4.9. Experimental ultrasonic and X-ray results on ε-FeSi at Room T

P (GPa)[a]	ρ (g cm^{-3})	2tp (μs)	2ts (μs)	L (mm)	V (Å^3)	V_P (km s^{-1})	V_S (km s^{-1})	K_S (GPa)	G (GPa)
2.01	6.246	0.2578	0.4304	0.9380	89.36(4)	7.28	4.36	172.7	118.7
3.35	6.293	0.2512	0.4246	0.9352	88.69(4)	7.45	4.41	186.1	122.4
4.65	6.338	0.2472	0.4202	0.9346	88.06(3)	7.56	4.45	194.9	125.5
5.79	6.376	0.2440	0.4162	0.9328	87.53(3)	7.65	4.48	202.5	128.0
6.75	6.407	0.2412	0.4122	0.9312	87.11(3)	7.72	4.52	207.3	130.9
7.72	6.438	0.2390	0.4088	0.9293	86.69(5)	7.78	4.55	212.0	133.3
8.51	6.463	0.2370	0.4056	0.9273	86.36(7)	7.83	4.57	216.3	135.0
9.42	6.490	0.2352	0.4026	0.9256	85.99(4)	7.87	4.60	218.9	137.3
10.53	6.524	0.2334	0.3998	0.9238	85.55(4)	7.92	4.62	223.6	139.3
11.40	6.549	0.2316	0.3964	0.9236	85.22(7)	7.98	4.66	227.4	142.2
11.88	6.563	0.2300	0.3950	0.9230	85.04(3)	8.03	4.67	232.3	143.1
12.02	6.567	0.2288	0.3944	0.9214	84.99(3)	8.05	4.67	234.6	143.2
5.34	6.357	0.2292	0.3898	0.8856	87.80(3)	7.73	4.54	205.1	131.0
4.80	6.339	0.2302	0.3902	0.8857	88.04(3)	7.70	4.54	201.6	130.7
4.51	6.330	0.2306	0.3894	0.8813	88.18(4)	7.64	4.53	196.3	129.9
3.91	6.310	0.2316	0.3908	0.8825	88.46(5)	7.62	4.52	194.5	128.9
3.90	6.309	0.2320	0.3916	0.8832	88.46(3)	7.61	4.51	194.3	128.3
3.18	6.285	0.2336	0.3936	0.8835	88.80(3)	7.56	4.49	190.3	126.7
3.28	6.288	0.2340	0.3946	0.8840	88.76(3)	7.56	4.48	191.1	126.2
2.90	6.275	0.2352	0.3954	0.8851	88.94(4)	7.53	4.48	187.9	125.9
2.75	6.270	0.2358	0.3964	0.8849	89.02(4)	7.51	4.46	187.3	124.7
2.32	6.255	0.2372	0.3976	0.8858	89.23(5)	7.47	4.46	183.1	124.4
1.98	6.243	0.2378	0.3986	0.8851	89.40(4)	7.44	4.44	181.5	123.1
1.82	6.237	0.2390	0.4008	0.8860	89.48(4)	7.41	4.42	180.0	121.8
1.44	6.224	0.2400	0.4024	0.8855	89.68(3)	7.38	4.40	178.3	120.5
0.74	6.198	0.2420	0.4066	0.8877	90.05(5)	7.34	4.37	176.1	118.4
0.89	6.204	0.2422	0.4070	0.8877	89.97(4)	7.33	4.36	176.1	117.9

[a]Pressures were calculated using third-order finite-strain EoS. Values in parentheses are 1σ error in the last digits. Two-way travel times have 1σ of ~0.4 ns for *S* waves and ~0.2 ns for *P* waves. The precision of image measurement of sample length is 0.2-0.4%. Uncertainties in velocities are less than 0.3% , and less than 1.0% for the derived elastic moduli. The densities at high pressures are calculated using unit-cell volumes obtained from X-ray data and the theoretical density. Top portion of data collected during cold compression (above line), bottom portion collected during decompression after heating.

Table 4.10. Comparison of elastic properties of ε-FeSi with previous studies

Ref.	Method	P Range (GPa)	V_0 (Å^3)	K_{S0} (GPa)	K_{S0}'	K_{T0} (GPa)	K_{T0}'	G_0 (GPa)	G_0'
1	Ultrasonics w/ X-Ray	12	90.45(3)	165.3(17)	6.0(3)	160.5	6	113.1(8)	2.7(1)
2	**Ultrasonics w/ X-Ray**	**5.5**	**90.45(3)**	**169.3(8)**	**6.5(3)**	**164.4**	**6.5**	**116.3(4)**	**3.0(1)**
1	XRD-MAC	12	90.45(3)	-	-	160.5(1)	6.0(1)	-	-
2	XRD-MAC	5.5	90.45(3)	-	-	164.6(1)	6.5(1)	-	-
3	XRD-DAC	15	90.40(3)	-	-	169.4(64)	6.7(14)	-	-
4	Resonant Ultrasonics	0	-	173*	-	-	-	116*	-
5	XRD-DAC	50	89.015	-	-	209	3.5	-	-
6	Neutron	9	90.21(2)	-	-	160	4 (fixed)	-	-
7	XRD-DAC	8.25	90.39(4)	-	-	172	4 (fixed)	-	-
8	XRD-DAC	50.7	90.193	-	-	184.7	4.75	-	-
9	Calculation	Calculated	88.896	227 (0K)	3.9	227	3.9	-	-
10	Calculation (LDA)	Calculated	84.09	-	-	255	4.143	-	-
10	Calculation (GGA)	Calculated	90.174	-	-	221	4.175	-	-

1. This Study, Cold Compression; 2. This Study, After Heating; 3. This Study, DAC; 4. Sarrao et al (1994); 5. Knittle & Williams (1995); 6. Wood et al (1995); 7. Guyot et al (1997); 8. Lin et al (2003); 9. Vocadlo et al (1999); 10. Caracas & Wentzcovitch (2004)
*Estimates based on graphical data

Table 4.11. Experimental ultrasonic and X-ray results on ε-FeSi at high P and T

P (GPa)	T (K)	$2tp$ (μs)	$2ts$ (μs)	L (mm)	V (Å^3)	ρ (g cm^{-3})	V_P (km s^{-1})	V_S (km s^{-1})	K_S (GPa)	G (GPa)
7.98	1273	0.2428	0.4304	0.9020	89.89(3)	6.210	7.43	4.19	197.5	109.0
7.45	1073	0.2384	0.4190	0.8934	89.44(4)	6.241	7.50	4.26	200.0	113.3
7.05	873	0.2356	0.4108	0.8895	88.93(3)	6.276	7.55	4.33	200.9	117.7
6.51	673	0.2336	0.4042	0.8889	88.50(3)	6.307	7.61	4.40	202.4	122.1
6.10	473	0.2316	0.3964	0.8872	88.03(3)	6.340	7.66	4.48	202.3	127.2
5.45	308	0.2292	0.3898	0.8856	87.80(3)	6.357	7.73	4.54	205.1	131.0
4.85	300	0.2302	0.3902	0.8857	88.05(3)	6.339	7.70	4.54	201.6	130.7
7.12	1273	0.2430	0.4288	0.8940	90.33(3)	6.179	7.36	4.17	191.5	107.4
6.72	1073	0.2392	0.4186	0.8880	89.81(3)	6.215	7.42	4.24	193.2	111.7
6.23	873	0.2370	0.4110	0.8854	89.32(4)	6.249	7.47	4.31	193.9	116.1
5.77	673	0.2350	0.4042	0.8838	88.85(4)	6.282	7.52	4.37	195.3	120.0
5.19	473	0.2328	0.3970	0.8829	88.44(4)	6.311	7.58	4.45	196.0	125.0
4.60	308	0.2306	0.3894	0.8813	88.18(4)	6.330	7.64	4.53	196.3	129.9
3.95	303	0.2316	0.3908	0.8825	88.46(5)	6.310	7.62	4.52	194.5	128.9
6.21	1073	0.2406	0.4198	0.8900	90.06(3)	6.198	7.40	4.24	190.8	111.4
5.68	873	0.2384	0.4128	0.8878	89.60(4)	6.230	7.45	4.30	192.2	115.2
5.15	673	0.2364	0.4062	0.8852	89.14(3)	6.262	7.49	4.36	192.6	119.0
4.51	473	0.2344	0.3994	0.8837	88.77(3)	6.288	7.54	4.43	192.9	123.4
3.98	308	0.2320	0.3916	0.8832	88.47(3)	6.309	7.61	4.51	194.3	128.3
3.23	304	0.2336	0.3936	0.8835	88.81(3)	6.285	7.56	4.49	190.3	126.7
5.53	1073	0.2430	0.4228	0.8913	90.43(3)	6.172	7.34	4.22	186.0	109.9
5.00	873	0.2406	0.4152	0.8877	89.94(4)	6.206	7.38	4.28	186.4	113.7
4.37	673	0.2384	0.4082	0.8866	89.53(4)	6.234	7.44	4.34	188.5	117.4
3.84	473	0.2364	0.4016	0.8848	89.09(3)	6.265	7.49	4.41	189.0	121.8
3.36	308	0.2340	0.3946	0.8840	88.76(3)	6.288	7.56	4.48	191.1	126.2
2.94	303	0.2352	0.3954	0.8851	88.95(4)	6.275	7.53	4.48	187.9	125.9
4.92	1073	0.2450	0.4258	0.8931	90.76(4)	6.150	7.29	4.20	182.2	108.5
4.43	873	0.2424	0.4172	0.8896	90.25(5)	6.185	7.34	4.26	183.6	112.2
3.89	673	0.2402	0.4102	0.8878	89.77(4)	6.217	7.39	4.33	184.1	116.6
3.20	473	0.2382	0.4038	0.8859	89.40(3)	6.243	7.44	4.39	185.2	120.3
2.82	308	0.2358	0.3964	0.8849	89.02(4)	6.270	7.51	4.46	187.3	124.7
2.36	303	0.2372	0.3976	0.8858	89.23(5)	6.255	7.47	4.46	183.1	124.4
3.84	873	0.2446	0.4206	0.8897	90.56(5)	6.163	7.27	4.23	178.7	110.3
3.35	673	0.2422	0.4132	0.8891	90.06(4)	6.198	7.34	4.30	181.1	114.6
2.67	473	0.2400	0.4060	0.8864	89.68(3)	6.224	7.39	4.37	181.4	118.9
2.05	308	0.2378	0.3986	0.8851	89.41(4)	6.243	7.44	4.44	181.5	123.1
1.85	303	0.2390	0.4008	0.8860	89.49(4)	6.237	7.41	4.42	180.0	121.8
3.12	873	0.2466	0.4236	0.8918	90.96(4)	6.136	7.23	4.21	175.7	108.8
2.65	673	0.2442	0.4164	0.8896	90.43(3)	6.172	7.29	4.27	178.0	112.5
2.06	473	0.2422	0.4102	0.8872	89.99(3)	6.202	7.33	4.33	178.2	116.3
1.50	308	0.2400	0.4024	0.8855	89.68(3)	6.224	7.38	4.40	178.3	120.5
0.77	303	0.2420	0.4066	0.8877	90.05(5)	6.198	7.34	4.37	176.1	118.4
1.98	673	0.2466	0.4210	0.8909	90.80(5)	6.147	7.23	4.23	174.7	110.0
1.35	473	0.2446	0.4148	0.8895	90.37(5)	6.176	7.27	4.29	174.8	113.7
0.96	308	0.2422	0.4070	0.8877	89.97(4)	6.204	7.33	4.36	176.1	117.9

Pressure on sample calculated using Eq. 14. Values in parentheses are 1σ error in the last digits. Two-way travel times have 1σ of ~0.4 ns for *S* waves and ~0.2 ns for *P* waves. The precision of image measurement of sample length is 0.2-0.4%. Uncertainties in velocities are less than 0.3%, and less than 1.0% for the derived elastic moduli. The densities at high pressures are calculated using unit-cell volumes obtained from X-ray diffraction.

Table 4.12. Comparison of thermoelastic properties of ε-FeSi

Ref.	V_0 ($Å^3$)	$\alpha = a + bT$ a (K^{-1})	b (K^{-1})	K (GPa)	K'	$\partial K/\partial T$ (GPa K^{-1})	G (GPa)	G'	$\partial G/\partial T$ (GPa K^{-1})	Notes
1*	**90.45(3)**	**3.75 x 10^{-5}**	**1.40 x 10^{-8}**	**168.9(7)**	**6.6(2)**	**-0.023(1)**	**116.5(3)**	**2.9(1)**	**-0.030(1)**	**UI-X; 8 GPa, 1273 K**
2*	90.45(3)	-	-	169.3(8)	6.5(3)	-	116.3(4)	3.0(1)	-	UI-X; 12 GPa, 300 K
3*	-	-	-	173‡	-	-	116‡	-	-	RUS; 50-380 K
4†	89.015	-	-	209	3.5	-	-	-	-	EoS; 50 GPa, RT
5†	90.21(2)	-	-	160	4§	-	-	-	-	NToF EoS; 9 GPa, RT
6†	90.39(4)	-	-	172	4§	-0.043	-	-	-	EoS; 8.25 GPa, RT
7†	90.193	-	-	184.7	4.75	-	-	-	-	EoS; 50.7 GPa, RT
8a	88.896	-	-	227	3.9	-	-	-	-	Calc.; 0 K
9	84.09	-	-	255	4.143	-	-	-	-	Calc.; LDA
9	90.174	-	-	221	4.175	-	-	-	-	Calc.; GGA

UI-X, ultrasonic interferometry w/ X-Ray; RUS, resonant ultrasonic spectroscopy; EoS, equation of state (static compression); NToF, neutron time-of-flight; RT, Room Temperature.

*Adiabatic values. †Isothermal values. ‡Estimates based on graphical data. §Assumed value.

References: 1. This Study; 2. Whitaker et al. (2008); 3. Sarrao et al. (1994); 4. Knittle and Williams (1995); 5. Wood et al. (1995); 6. Guyot et al. (1997); 7. Lin et al. (2003); 8. Vocadlo et al. (1999); 9. Caracas and Wentzcovitch (2004).

CHAPTER 5. IMPLICATIONS AND CONCLUSIONS

In previous chapters, exciting new results on iron/light-element alloy phases have been presented that have helped to increase the database of available information on these materials, and in some cases have also helped to dispel some of the controversy regarding these phases. Now, with these results in hand, comparisons can be drawn between the different samples studied here, and extrapolations of these datasets can be used to compare with seismic profiles of Earth's deep interior, specifically the solid inner core. These comparisons are the focus of this final chapter of this dissertation.

5.1 – Sample Comparison

The results obtained from the various fittings of the datasets for each of the materials examined in this study are tabulated in Table 5.1. Figure 5.1.1 shows a comparison of the room temperature compression behavior of all the iron/light-element alloy (ILEA) phases studied in the DAC experiments. The top panel shows data points and calculated compression curves, while the bottom panel shows only the curves for clarity. It can clearly be seen in this diagram that the three phases of FeS are significantly more compressible than the other phases studied. Even FeS-III, which is the so-called high pressure phase of FeS (Kusaba et al., 1997; Urakawa et al., 2004), is more than twice as compressible as the other materials within the pressure range explored. This large compressibility would lead to abnormally high compression factors ($V_0/V > 2.25$) at the very high pressures of the Earth's inner core, which indicates that these phases are unlikely to exist under such conditions. This has been shown to in fact be the case, as recent studies have found higher-pressure polymorphs of FeS (Ohfuji et al., 2007; Ono and Kikegawa, 2006; Sata et al., 2008).

Of the remaining three materials, pyrite is the most compressible, while ε-FeSi is the least compressible. Fe_3P, as described previously, shows a possible change in the slope of the compression curve at ~8 GPa, and its compressibility is between that of pyrite and fersilicite within the pressure range shown in Figure 5.1.1. The phase transition in this material that occurs at pressures above 20 GPa makes further extrapolation of the "high pressure" portion of the compression curve obsolete. Since no data exist on the physical properties of this high pressure phase of schreibersite (Scott et al., 2008), its compressibility cannot be assessed here. If the entire Fe_3P dataset is fit as a whole, its compression curve follows that of pyrite closely at low pressures, then moves steadily toward that of fersilicite with increasing pressure. With increasing pressure, the incompressibility of this material quickly surpasses that of ε-FeSi, owing to its relatively large K_T' value.

Figure 5.1.2 shows a comparison of the room temperature compression behavior of all the phases studied in the MAC experiments. The top panel shows data points and calculated compression curves, while the bottom panel shows only the curves for clarity. FeS-IV and FeS-V are also shown on this diagram, and they exhibit even higher

compressibility than the other phases of FeS. For all of the other phases, the same trends exhibited in Figure 5.1.1 are also seen here, and comparison between these two diagrams emphasizes the remarkable similarity in the datasets collected in the DAC and MAC experiments.

The observed trends in compressibility may be related to structure and chemistry. More data need to be collected on additional ILEA phases before this link can be fully assessed. It is interesting to note, however, that to a first approximation this trend in compressibility is inversely related to the density of the material. The FeS phases all have lower density than pyrite, which is lower than fersilicite, and schreibersite has the highest density. Examining the dataset in closer detail shows that the trends are in fact related to atomic spacing rather than density. The parameter $(M_0/\rho)^{1/3}$, where M_0 is the mean atomic weight and ρ is the density, can be used as a measure of the average interatomic spacing (i.e., Duffy and Anderson, 1989).

Figure 5.1.3 a) shows the adiabatic bulk modulus as a function of the average interatomic spacing. The phase represented by each data point is indicated on the diagram. The values used for Fe_3P were the isothermal parameters obtained from the P-V fitting presented in Chapter 3. Insufficient data exist for converting these isothermal parameters to adiabatic, and since the conversion would lead to a change of only ~1-3% at room T, these values were left unchanged and plotted for comparison. This figure shows a clear trend toward decreasing bulk modulus as average interatomic spacing increases. FeS-I is an outlier in this diagram, but it should be recalled that this phase also had a negative K_S'; if K_S were fixed at a similar value to the other FeS room T phases, the K would decrease significantly, and therefore plot in the same region as the other FeS phases on this diagram.

Figure 5.1.3 b) shows the adiabatic bulk modulus as a function of the product of the bulk modulus and the average interatomic spacing. Data points are labeled as in part a). The trendline is a linear regression of all data points. This diagram shows that there is a strong linear relationship between the bulk modulus and its product with average interatomic spacing, with a clear inverse relationship between the bulk modulus and average interatomic spacing. The more tightly packed the crystal structure is, the less compressible it will be, while a more open structure will lead to a greater compressibility. Figure 5.1.4 shows the same relationships for the shear modulus of the ILEA phases studied here. The same trends are exhibited in both the rigidity and compressibility of the materials, indicating that to a first order, both the bulk modulus and the shear modulus are directly related to the average interatomic spacing of the crystal structure of these ILEA phases.

One interesting note to make here is regarding the existence of the FeS-II vs. FeS-IV phase. Previous studies have noted that FeS-II is found during cold compression of the material, but when coming down from high temperature, the sample does not transform back into FeS-II, but rather remains in the FeS-IV phase (King and Prewitt, 1982; Urakawa et al., 2004). This is consistent with the results presented here. However, no explanation as to why this is the case has been offered. It is suggested here that the reason for the lack of back-transformation is caused by the volume difference between the two phases; for a given pressure, the room T volume of FeS-IV is significantly less than that of FeS-II. In order to back-transform from FeS-IV to FeS-II, the material must undergo a significant volume increase. Since this transformation is not observed experimentally,

this indicates that the change in internal energy between these two phases is not sufficient to overcome this volume change, which results in the FeS-IV phase being more stable under pressure.

One of the overarching goals of this study was to determine whether or not the differences commonly seen between results in DAC and MAC experiments could be reconciled. The two major hypotheses for the source of these discrepancies going into this study were differences in pressure range of the experiments and inter-laboratory differences, since very rarely do the same workers conduct both DAC and MAC experiments. In the experiments conducted in this study, the results of the two different types of experiments are markedly similar; in fact the results are a much closer match than has been seen between these two types of experiments on these materials before. The volume vs. pressure plots in Chapter 4 show that there is remarkably good agreement between the results of experiments that were conducted in Diamond Anvil Cells and those conducted in the Multi-Anvil Apparatus. This is also evidenced in the close match of the parameters obtained from the various fittings of the datasets for each material as tabulated in Table 5.1. Also, the striking similarity between the datasets presented in Figure 5.1.1 and 5.1.2 reinforce how good the agreement between the results of the two types of experiments is.

This lends credence to the possibility of the discrepancy being caused by the introduction of inter-laboratory error (i.e., slight differences in sample composition, preparation, etc.). However, the pressure ranges explored in the two types of experiments were purposely kept similar, so the effect of an expanded pressure range cannot be ruled out. Future DAC experiments on these materials at higher pressures are required to answer this question more definitively.

5.2 – Implications for Earth's Core

Seismic wave propagation and normal mode oscillations are the tools that are available to directly probe the Earth's core remotely. These data can be used to determine the velocity and density structure of the deep interior of the Earth, as was done in the PREM model (Dziewonski and Anderson, 1981). Birch (1952) proposed on the basis of shockwave experiments that the Earth's core was not dense enough to be composed solely of Fe according to seismic profiles. Several studies that followed reinforced this idea that there must be some lighter elements in the bulk core, and specifically the solid inner core, to drive the density down from that of pure Fe (i.e., Fiquet et al., 2001; Jephcoat and Olson, 1987; Mao et al., 1998).

There have been a plethora of experimental studies conducted on iron and its alloys at high pressures and temperatures that have been aimed at understanding their physical properties under extreme conditions to begin to elucidate possible candidate light elements in the Earth's core (see Figure 5.2.1). Extensive studies on pure Fe have been conducted in both shockwave experiments (i.e., Ahrens et al., 2002; Brown and McQueen, 1986), and under static conditions (i.e., Badro et al., 2007; Fiquet et al., 2001; Lin et al., 2005; Mao et al., 1998; Mao et al., 2001; Mao et al., 2008; Uchida et al., 2001). Studies have also been conducted on several different ILEA compositions, such as iron silicides (Badro et al., 2007; Lin et al., 2003b), iron hydride (Mao et al., 2004), iron sulfides (Badro et al., 2007; Lin et al., 2004a), and iron carbides (Fiquet et al., 2009; Gao

et al., 2008). Figure 5.2.1 is a density vs. pressure diagram showing a host of data from these previous experimental studies on pure Fe and various ILEAs.

Experimental investigations of these materials suffer from the handicap that it is extremely difficult to attain the pressures and temperatures necessary to replicate the conditions found in the Earth's core. While the experiments conducted in this work are limited to much lower pressures than those found in the core region, they provide information on a material's physical properties at elevated pressures and temperatures that cannot be attained in other ways. The same equations that are used for fitting the datasets can then be used to extrapolate these parameters to higher pressures and temperatures, thereby modeling how these materials would behave under conditions representative of those found in the Earth's core.

The initial intent of this work was to do a straightforward extrapolation of the parameters obtained in the high temperature ultrasonic experiments to core conditions and compare these extrapolations with existing results on pure Fe and other ILEA compositions. In conducting these extrapolations, however, it was discovered that the lack of higher-order terms in the finite-strain equations led to the material's density increasing with increasing temperature at pressures above 150 to 200 GPa. This is caused by the small magnitude of the thermal expansion term being swamped out by the relatively larger ($\partial K/\partial T$) which effectively increases the compressibility of a material with increasing temperature. At the extremely high pressures associated with the Earth's core, these higher-order terms contribute significantly to any extrapolations using these finite-strain equations. Since these higher-order terms were not available, a calculation was instead conducted that isothermally compressed the sample material at 300 K to the pressure of the Inner Core-Outer Core Boundary (IOB) and beyond (see Figure 5.2.2).

Some important determinations can be made qualitatively simply by looking at Figure 5.2.2. The 300 K extrapolations of the ILEA data, along with the 300 K isotherm for hcp Fe, are plotted here over the reference data and compared to the PREM model. The black hashed-lined area shows the density of hcp Fe at 4500 K (upper bound) and 6500 K (lower bound). First thing to note is that the density of Fe is greater than that of PREM at inner core pressures regardless of temperature. Though the high temperature behavior of the ILEA compounds cannot be shown here, there are some important observations that can be made.

FeS-I does not extend beyond 5 GPa, as the extrapolation fails due to the negative K' value. FeS-II cannot be extrapolated above 189 GPa because, as will be shown in a later diagram, the S-wave velocity drops to zero. FeS-IV and FeS-V are both even denser than Fe, and unless their thermal expansivities are even greater at core pressures than they are at ambient conditions, then they must be rejected as possible inner core constituents because they would create an even bigger density offset from PREM. FeS-III, while falling below the PREM density at core pressures, has sufficient density that an inordinate amount of this phase would be required in the core to satisfy the density constraints of PREM. Based on density alone, FeSi and FeS_2 are more likely candidates to be found in the inner core. Based on these observations, all five phases of FeS examined in this study are not possible inner core constituents; however the results on these phases are included in the following figures and discussion for comparison purposes. This of course is in keeping with the discovery of new high pressure phases of

FeS (Ohfuji et al., 2007; Ono and Kikegawa, 2006). These initial observations can now be tested by developing a numerical model to test possible inner core compositions.

5.2.1 – 300 K Model. The extrapolations conducted at 300 K can be used to compare to the Earth's core by assuming that the acoustic velocity in a material is dependent solely on the density of the material, and that the temperature has a negligible effect ("Birch's Law"). Strong correlations between low and high temperature datasets from both static and dynamic experiments on pure Fe have been used to suggest that Birch's Law is valid under extreme pressures (Badro et al., 2007; Brown and McQueen, 1986; Fiquet et al., 2001; Jephcoat and Olson, 1987; Mao et al., 1998; Mao et al., 2001).

Recent work has shown, however, that Birch's Law is violated in pure Fe at intermediate pressures (Lin et al., 2005). Similar behavior is observed in the samples studied here under the relatively low-pressure conditions in which the experiments were conducted. However, despite this deviation from perfect Birch's Law behavior, the same study proposed that the intrinsic effect that temperature would have on compressional wave velocities in a material would become marginal, and the relationship between density and velocity should be restored (Lin et al., 2005). Since Birch's Law behavior was presumed to return at the conditions of the Earth's inner core, and because several previous investigations were conducted under the assumption that this relationship held true, a numerical model was constructed as in previous studies (Badro et al., 2007; Fiquet et al., 2009) to determine possible compositions of the solid inner core under the assumption that Birch's Law is maintained under core conditions.

By fitting all of the available velocity and density data on pure Fe, a Birch's Law equation whereby velocity is a function of density is obtained. By using the thermal equation of state (TEOS) given by Uchida et al (2001) for hcp Fe, the density of hcp Fe under the conditions of the Earth's inner core can be determined, and that density can be used to obtain a velocity using the Birch's Law relation. With this information in hand, density-velocity-composition models of the Earth's inner core as a mixture of pure Fe and a single light element can be calculated. Average ρ and velocity of a two-component ideal solid system are given by the following relationships:

$$\rho_{av} = x\rho_1 + (1-x)\rho_2 \tag{5.1}$$

$$V_{av} = \frac{V_1 \cdot V_2}{(1-x)V_1 + xV_2} \tag{5.2}$$

where x is the volume fraction of component 1.

By setting the average density and velocity to the values given by PREM, and using the density of hcp iron (ρ_2) calculated using the TEOS of Uchida et al (2001) and the assumption that velocity is a function of density for both materials, these two equations can be solved analytically to give unique solutions for x (volume fraction of the alloying ILEA) and the density of the ILEA (ρ_1). For these models, the density of Fe was calculated at pressures ranging from the IOB to the center of the core at temperatures from 4500 to 6500 K.

Figure 5.2.3 a) shows the P-wave velocities as a function of density from previous experimental studies; the symbols are the same as those used in Figure 5.2.1. The gray

dashed lines are calculated using the Birch's Law relationship for various compounds given in Badro et al (2007) and Fiquet et al (2009); the Birch's Law line for Fe was calculated using the relationship derived from the fitting done in this study. Figure 5.3.2 b) shows the 300 K extrapolations of the ILEA phases from this study. Again, it is clear the FeS phases can be immediately eliminated as possible constituents of the inner core. The 300 K extrapolation for FeS-IV is drastically different than that determined previously (the Birch Law line just above the PREM values) by Badro et al (2007). However, their study also eliminated FeS-IV, which is the only phase of troilite they investigated, as a possible inner core constituent based on the unusually high amount of S it would require to be present in the core (9.7 wt. %), and the unreasonably high compression factor required to fit the PREM model ($V_0/V = 2.49$).

Figure 5.2.4 a) shows the variation in bulk sound speed as a function of density, and Figure 5.2.4 b) shows the variation in adiabatic bulk modulus with density. Similar trends are observed for these parameters that were seen in the P-wave velocities. First, all of the FeS phases can again be ruled out as possibilities. FeS_2 and FeSi again become the two primary candidate phases based on visual analysis of these diagrams.

Figure 5.2.5 a) and b) shows the variation in V_S and G, respectively, with density. It can be seen here that all of the previous experimental data on pure Fe and various ILEA compounds yield values significantly greater than the PREM model for V_S and G. Interestingly, FeS-III is the only phase that would bring down the V_S from pure Fe toward the PREM model values, but it would be required that the dominant phase in the core be FeS, and that Fe would alloy sparsely into that phase, which is certainly not the case. The available S-wave velocity data are very sparse, so it is difficult to make any solid predictions or statements based on them. However, even from the minimal data that are available, it can be clearly seen that any combination Fe and ILEA compounds that have been studied to date cannot satisfy the S-wave velocity constraints of the PREM model. Assuming that Birch's Law holds true for these materials under inner core conditions, this discrepancy is likely caused by attenuation and dispersion of S-waves (i.e., Faul et al., 2004; Jackson et al., 2000).

The simple mixing model outlined above was conducted using V_P under the assumption that Birch's Law would be valid using both pyrite and fersilicite as possible core constituents to directly compare with the results of Badro et al. (2007). The 300 K extrapolation of FeS_2 (Figure 5.3.2 b) deviates fairly significantly from the Birch's Law line for this phase determined by Badro et al (2007), as do the results of the model calculations. The model presented here suggests that if FeS_2 is a possible constituent of the Earth's inner core, 2.2-2.6 wt. % S would be expected in the solid phase depending on the temperature and pressure. This is within the range determined by Chen et al. (2007, 1.3-3.7 wt. %), but significantly different than the value of 3.6 wt. % obtained by Badro et al (2007), who also determined that this is not a likely candidate phase because the compression factor would have to be the same as at ambient pressure ($V_0/V = 1.0$). The compression factor obtained here for this phase ranges from 1.27-1.50, which is a large range. According to Badro et al. (2007), values of ~1.3 are considered in good agreement with EOS studies and core models, though it is unclear why they state this. In addition, this amount of S is higher than that estimated to be in the bulk core based on cosmochemical constraints (~1.90 wt. %, i.e., McDonough, 2004). It has also been suggested that even less than 1 wt. % S may be present in the core based on volatilization

temperatures of sulfur (Badro et al., 2007). Keeping these constraints in mind, it seems unlikely that sulfur would be the dominant light element in the core, despite the relatively good agreement of the V_P-density-composition model for FeS_2 presented here with the PREM model.

The 300 K extrapolations of the ε-FeSi data, while still notably different from the Birch's Law line of Badro et al (2007), is in much better agreement than the results of any of the other phases investigated in both studies. The model presented here suggests that the presence of 2.2-2.4 wt. % Si as ε-FeSi in the solid inner core with a compression factor of 1.28-1.34 would satisfy both the density and velocity requirements of the PREM model. This is well within the broad range of 1.3-5.1 wt. % Si suggested as an upper limit by Chen et al. (2007). These results also agree very well with those of Badro et al. (2007), who obtained 2.3 wt. % Si with a compression factor of 1.28 in their model. It should be noted here that the temperature(s) at which the density of pure Fe was calculated was not given in their study, nor was the exact pressure(s) under which their calculations were conducted. The results of this model for e-FeSi match the results of Badro et al. (2007) extremely well, including compression factors obtained over the entire range of P and T explored.

The aforementioned mixing models were conducted using P-wave velocities. The same type of model was attempted using bulk sound speed, but the results were very conflicting. It is not possible to fit these data in the same manner as the P-wave velocities and get consistent results. Bulk sound speed is directly obtained from the density and bulk modulus ($V_\Phi = (K_S/\rho)^{0.5}$), and is related to the V_S and V_P. If the model can satisfy the constraints of both V_P and V_Φ, it should be able to also satisfy the constraints of V_S since all three velocities are related, and as mentioned previously, all available data on Fe and ILEA compounds have shear wave velocities that are faster than those found in the inner core according to PREM. Therefore, these simple models utilizing the Birch's Law assumption cannot account for the seismic observations of the inner core.

Lin et al. (2005) also determined that, though it is possible that Birch's Law behavior in pure Fe may return at core conditions insofar as V_P is concerned, V_S would still deviate from this simple velocity-density relationship, and temperature would still have an effect. Therefore, it is the conclusion of this author that it is not possible to create a compositional model for the inner core that complies with Birch's Law and can satisfy the constraints of S-wave velocities because of this unique high-temperature behavior of materials and the experimental difficulty in replicating such conditions on the proper frequency scale.

5.2.2 – High Temperature Model. The model presented in the last section depends upon the assumption that Birch's Law is adhered to by the materials in question under the extreme conditions of pressure and temperature found in the Earth's inner core. This is a tenuous assumption to make regarding these materials, as there is some evidence that their behavior does not in fact conform to Birch's Law. The data presented in this dissertation on ε-FeSi, which is the most complete dataset collected and presented, suggest that Birch's Law does not hold for this material. Figure 5.2.6 shows the variation in acoustic velocities and elastic bulk and shear moduli as a function of density. These diagrams clearly show that for a given density, the velocities and elasticity of this material are not independent of temperature.

In addition, a previous nuclear resonant inelastic X-ray scattering study on hcp-Fe at high pressures and temperatures found that there was a significant temperature effect on the compressional and shear wave velocities, showing that Birch's Law was violated at intermediate pressures (Lin et al., 2005). However, this study also suggested that at the higher pressures present in the Earth's inner core, Birch's Law behavior would return for compressional waves only, while shear waves would still deviate from Birch's Law. Theoretical studies have also led to conflicting results as some have found that Birch's Law behavior is observed in iron and several ILEA compounds at high pressures and temperatures (i.e., Vocadlo, 2007), while others have found the opposite to be true (i.e., Steinle-Neumann et al., 2001).

Since the behavior of ILEA phases and pure Fe under conditions corresponding to those found in the Earth's inner core cannot currently be directly studied, extrapolations of data collected at lower pressures and temperatures must be relied upon in order to draw comparisons to seismic profiles. These extrapolations are highly dependent upon the assumptions under which they are conducted, and the current experimental evidence suggests that the assumption of Birch's Law behavior at core pressures for these iron minerals, while convenient for constructing compositional models, may be invalid. Therefore, it may be more appropriate to construct a model that attempts to account for the deviation of these materials from perfect Birch's Law behavior.

For the dataset on ε-FeSi, the deviations of V_P , V_Φ, and V_S from perfect Birch's Law behavior were determined as a function of both density and temperature. These deviations were then applied to the extrapolated values calculated at 300 K in the previous section for temperatures of 4500, 5500, and 6500 K. The same was then done using K_S and G to check for consistency, and the results obtained matched perfectly. The other phases examined in this dissertation were not able to be compared in this way due to insufficient data. The data presented in Lin et al. (2005) on pure hcp Fe were also analyzed in this way to determine the deviation from Birch's Law behavior as a function of temperature. Since there were a very limited number of datapoints in this study, an average $(\partial K_S/\partial T)_V$ and $(\partial G/\partial T)_V$ was calculated for the entire dataset, and then assumed constant for extrapolation. These deviations were then applied to the values obtained in the previous section at 4500, 5500, and 6500 K using the densities given by the thermal equation of state of Uchida et al. (2001).

Figures 5.2.7 – 5.2.9 show the results of these new calculations. All 4500 K data are in red while 5500 K data are in green, and 6500 K data are in blue. Examination of these diagrams shows that though there are deviations from the 300 K line in all of these parameters at low densities, at higher densities (increasing pressure) there is very little deviation from the 300 K line in V_Φ (Figure 5.2.8a) and K_S (Figure 5.2.9a). This is consistent with the findings of Lin et al. (2005) who determined that at intermediate and high pressures, V_Φ (and therefore K_S) followed Birch's Law, while V_P and V_S (and therefore G) did not. One very interesting thing to note is that the V_S and G of the pure Fe falls below the PREM values for the inner core. These parameters have consistently been problematic in previous models trying to match experimental data to PREM because both Fe and the ILEA phases had shear velocities that were too high. By treating the existing data on Fe differently than has been done before and taking away the Birch's Law assumption, this simple model has shown a decrease in shear velocities of pure iron below those of PREM.

A new compositional model for the inner core was conducted using the same calculations as presented in the previous section. However, instead of only fitting one parameter at a time, the model was minimized against V_P and V_Φ simultaneously to obtain a single volume fraction and density for ε-FeSi. V_S was not included as a parameter for minimization in this model because the three velocities are interrelated, and fitting for V_P and V_Φ fixes the value of V_S. This mixing model was carried out for the 4500, 5500, and 6500 K extrapolations shown in Figures 5.2.7 – 5.2.9. The results of this model are plotted on these diagrams; 4500 K results are shown as red X's, green X's are the 5500 K model, and the 6500 K model is represented by the blue X's.

Looking at the P wave velocity model (Figure 5.2.7b), a few observations can be made. First, the density of the iron silicide required for the 5500 K and 6500 K models are higher than that calculated at 400 GPa and 300 K, which is the rightmost extent of the model lines. The density of iron silicide in the 4500 K model is much more reasonable, and less than that calculated for this phase at 300 K under inner core pressures, which would be expected due to some amount of thermal expansion. The model velocity-density results plot almost directly on top of the PREM values for all three temperatures, though the higher temperatures are slightly shifted to lower densities; the 4500 K model appears to give the best fit.

The model of the bulk sound speed (Figure 5.2.8a) again shows that the ε-FeSi densities obtained at 5500 and 6500 K are too high while the results of the 4500 K model are reasonable, which is also clear on all subsequent figures. The model bulk sound speed-density results for all three temperatures again match PREM values quite well, with the 4500 K model yielding the closest match. The same trends are observed in the K_S-ρ systematics (Figure 5.2.9a), as is expected. Based on the compressional velocities and bulk sound speed, which are the parameters against which the model was minimized, the 4500 K model yields the most reasonable results for the density of the e-FeSi ILEA phase, and most closely matches the velocities (and bulk modulus) given by PREM for the inner core.

This model also led to some very interesting results for the shear wave velocities (Figure 5.2.8b). There is a remarkably good match for the PREM data at 4500 K. The model results at 5500 and 6500 K are not nearly as close, however. These same trends are seen in the shear modulus as well (Figure 5.2.9b). The difference in slope between the PREM values and the model results in these figures is simply an artifact of the linear mixing calculations and is not physically meaningful. These results are very striking because no model has come close to matching the PREM values for shear modulus or velocities before. Simply by treating the existing data on pure iron differently than has been done in the past, we have been able to account for the PREM signature of the inner core. Of the three temperatures chosen for this study, the 4500 K model matches PREM most closely for V_P, V_Φ, V_S, K_S, and G. This is at the lower end of the estimated range of temperatures at the IOB, which will be addressed later.

The 4500 K model presented here suggests that the presence of 4.0-5.1 wt. % Si as ε-FeSi in the solid inner core with a compression factor of 1.58-1.60 would satisfy both the density and velocity requirements of the PREM model. This amount of Si is at the higher end of the broad range of 1.3-5.1 wt. % Si suggested as an upper limit by Chen et al. (2007), and significantly higher than the results of Badro et al. (2007), who obtained 2.3 wt. % Si with a compression factor of 1.28 in their model. Though Badro et al. (2007)

stated that a compression factor of ~1.3 was reasonable for materials under conditions of the inner core according to equation of state studies, they did not say what they meant by this. This would only be a reasonable compression factor if the thermal expansion at pressures found in the inner core was the same as at ambient pressure, which is highly unlikely. The value of ~1.6 obtained here is very similar to the compression factor of Fe under these conditions (1.64-1.67).

The Earth's core, though predominantly made up of Fe, also contains a significant amount of Ni. Lin et al (2003b) showed that nickel alloying with iron has little effect on the sound velocities obtained, and the slope of the velocities as a function of density is parallel to that of pure iron. The effect of up to 15 wt. % Ni on both the types and amounts of light elements that can alloy with Fe has been shown to be negligible. Because of this, a linear relation can be calculated for any Ni concentration in the Fe-Ni alloy compared to pure Fe by adjusting the density to that of the alloy. Assuming a full 15 wt. % Ni is present in the inner core as an extreme upper bound, this 4500 K model adjusts to give results of 4.1-5.2 wt. % Si in the inner core.

Solubility and partitioning data found in other studies can be used to estimate the composition of the outer core based on the constraints on inner core composition provided by the results of the model. Previous studies have focused on determining the partitioning behavior of light elements between metallic iron liquid and solid, and partition coefficients, which are the ratio of the amount of an element found in the liquid phase to the amount found in the solid phase ($D_x^{Liq/Sol}$), have been derived from their results. The weight converted partition coefficient for silicon between liquid and solid iron phases has been shown to be 1.2 (Alfe et al., 2002; Badro et al., 2007). Using the values of 4.0 wt. % Si as the minimum amount in the inner core and 5.2 wt. % as the maximum amount (coexisting with 15 wt. % Ni), a range of 4.8-6.12 wt. % Si is obtained for the outer core. This is significantly below the upper limit estimated by thermal expansion studies (11-19 wt. %, Chen et al., 2007), but nearly a perfect match to the amount of Si predicted to be in the core based on isotopic and geochemical-cosmochemical constraints (~5-6 wt. %, i.e., Georg et al., 2007; McDonough, 2004; McDonough and Sun, 1995)

The presence of Si alone in the outer core in these abundances does not account for the discrepancy in density from pure Fe found in the PREM model. However the presence of an element such as oxygen, which has a very high liquid to solid partition coefficient in iron ($D^{liq/sol} = 400$) would help to account for the density deficit in the outer core without having a very significant impact on the composition of the inner core. Experimental studies on the solubility of O in iron that is in equilibrium with perovskite at 97 GPa found that 5.3 wt. % O was quenched in the liquid metal (Takafuji et al., 2005). Using this experimental value of 5.3 wt. % O, which would give ~0.1 wt. % in the solid inner core, combined with 4.8-6.12 wt. % Si in the outer core would account almost entirely for the density discrepancy.

Interesting to note, however, is that a previous study sought to discount Si as a possible element in the Earth's core based upon the constraint of the K' value of Fe-Si ILEA compounds (Williams and Knittle, 1997). This study determined that materials with a K' of around 4 or less would not be suitable candidates for core materials, and at the time the value of K' they used for FeSi was 3.5 (Knittle and Williams, 1995).

However, if the value of K' reported in this work is used, then FeSi becomes a prime candidate for a core material, as does pyrite, reinforcing the findings of this investigation.

The model that yielded the closest match to PREM in this study was the 4500 K model. While this temperature falls at the lower end of the broad range of IOB temperatures that have been suggested (~4500-7600 K), it is lower than the current best estimates of the temperature at the IOB (~5200-5300 +/- 400 K, Ahrens et al., 2002; Boehler, 2000; Hemley and Mao, 2001) which are based on the melting temperature of pure Fe at that pressure. However, it is important to note that these experimental studies on the melting of pure Fe were conducted at lower pressures, and the melting curve was extrapolated up to inner core pressures. It is also worth noting that there is a large shift toward higher melting temperatures in shockwave experiments at high pressures (see Dubrovinsky and Lin, 2009) which have yielded temperatures as high as 7600 K (Jeanloz, 1990).

There are also previous studies which have suggested significantly lower temperatures for the IOB. One study called for an IOB temperature of 4400 K using DFT calculations (Sherman, 1997), which agrees very well with the model results presented here. A possible IOB temperature of 4700 K has been estimated using the example of S as the light element in the inner core (Jeanloz, 1990; Williams and Jeanloz, 1990). In addition, the presence of Ni in the Fe alloy is expected to decrease the melting temperature by ~200 K (Jeanloz, 1990). A temperature of 4500 K may therefore not be unreasonable if one considers the large uncertainty in temperature in the experimental results, combined with the presence of both nickel and a significant amount of light elements in the system, which will further depress the melting point of the alloy.

A previous theoretical study found that under any conditions of temperature relevant to the Earth's inner core, no combination of pure Fe and ILEA phases could account for the shear velocities of PREM because all of the phases studied had shear velocities that were too high (Vocadlo, 2007). This led the author to the conclusion that in order to account for the low shear velocities of PREM, there must be ~8 % melt in the inner core. However, it is important to note that theoretical studies cannot account for such things as attenuation, as mentioned in the previous section. Also, the results of Vocadlo (2007) found that these materials obeyed Birch's Law, which other theoretical studies (Steinle-Neumann et al., 2001) as well as the results presented here indicate may not be the case.

Currently, determining the amount of a given light element in the core is largely model-dependent. Assumptions must be made and extrapolation of data to higher pressures and temperatures is required. Small changes in any of these assumptions or extrapolations can bring about large changes in the results of these models. However, until sufficient data is acquired on Fe and candidate ILEA compositions at P-T conditions relevant to the Earth's core, these models are the best approximation that can be made. Based on the experimental partitioning results discussed above and the results of the models presented here, a compositional model of the Earth's inner core containing 4.0-5.2 wt. % Si and ~0.1 wt. % O is obtained, which corresponds to an outer core containing 4.8-6.12 wt. % Si and 5.3 wt. % O. This compositional model is consistent with geochemical and isotopic estimates of the amount of these elements in the core (Georg et al., 2007; McDonough, 2004; McDonough and Sun, 1995), and can also account for the PREM velocity and density profile of the inner core as well as the density discrepancy that PREM shows from pure Fe in the outer core.

5.3 – Conclusions

Understanding the composition of the Earth's core is integral to answering many questions in the Earth Sciences, including the mechanisms and timing of core formation and the conditions under which the core formed. It also has important implications for the composition of the Earth's mantle. Because of the remote nature of the core, seismic profiles of the Earth's interior must be relied upon to determine the velocity and density structure of the deep Earth, and these profiles must then be compared with experimental data on candidate core phases at extreme conditions. Though the experimental database on these relevant phases is constantly growing as new materials are studied and new techniques are developed, it is still lacking in many areas. Until the experimental database on Fe and iron/light-element alloy (ILEA) compounds is sufficiently expanded to P-T conditions relevant to the Earth's core, the data available must be used to construct models that attempt to satisfy these seismic observations.

The work presented in this dissertation was designed to study the physical properties of several ILEA compounds at high pressures and temperatures in order to quantify their behavior under extreme conditions. Four such materials (Fe_3P, FeS_2, FeS and ε-FeSi) were studied in this investigation using a combination of synchrotron-based static compression experiments in Diamond Anvil Cells (DAC) and combined ultrasonic interferometry and synchrotron X-radiation in a Multi-Anvil Cell (MAC). The results of these two different types of experiments showed much better agreement than has ever before been seen between MAC and DAC experiments on these types of materials. The results of these experiments have provided an important benchmark for future studies on these materials and have resolved some of the controversy regarding the physical properties of these phases under extreme conditions.

The results of the ultrasonic experiments were extrapolated to pressures and temperatures relevant to the Earth's inner core, and a compositional-density-velocity model was constructed for the solid portion of the core by accommodating for the evidence that these iron materials may not obey Birch's Law under the conditions found in the inner core. By treating the existing data on pure Fe differently than previous studies and accounting for this non-Birch's Law behavior, a model accounting for all aspects of PREM in the inner core, including the shear velocities, has been generated. The best-fit result of this model yielded an inner core containing 4.0-5.2 wt. % Si at 4500 K, which corresponds to 4.8-6.12 wt. % Si in the liquid outer core. These values are entirely consistent with geochemical and isotopic estimates. With ~0.1 wt. % O in the inner core, and 5.3 wt. % O in the outer core, geochemical models can be satisfied by these results, as well as the density deficit in the outer core prescribed by PREM.

While there is no attempt here to make such a bold statement as, "The core has been solved," the excellent fit of the experimental data and the models presented here to seismic profiles is certainly noteworthy. There are many assumptions that have gone into these models, some of which may be more valid than others. However, the results presented in this study are the best approximations that can be made with the methods and data available. It is clear from these results, however, that the assumption that Birch's Law is valid for these materials under core conditions is tenuous at best, and likely not correct. Further experimental studies on these and other ILEA compounds to more extreme conditions of pressure and temperature are required in order to further constrain the possible composition of the Earth's core.

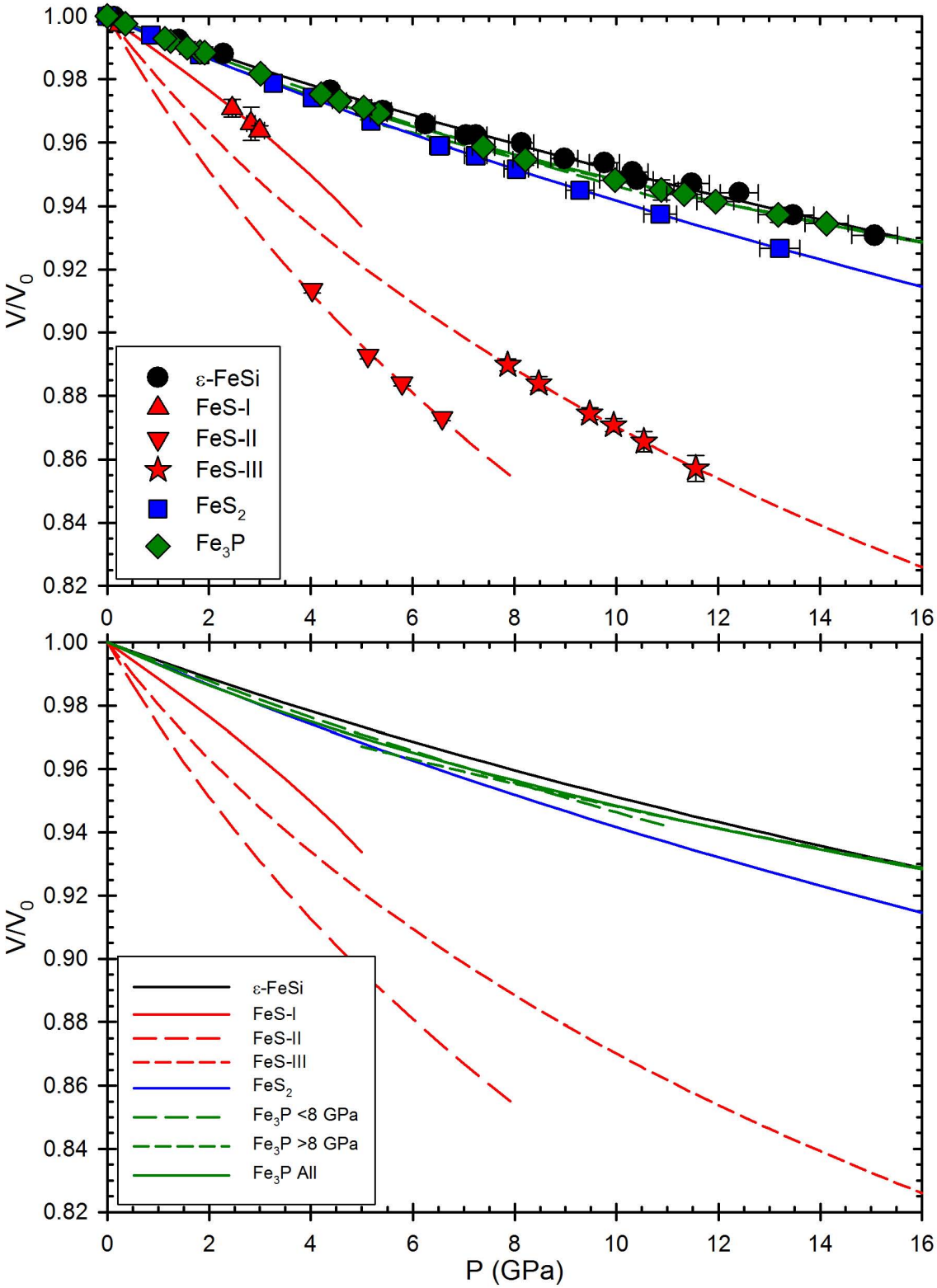

Figure 5.1.1. Comparison of room temperature compression behavior of all materials studied in the Diamond Anvil Cell (DAC) experiments. Top panel shows data for each phase studied along with calculated compression curves from the BM-3 fitting of each dataset. Bottom panel shows only curves for clarity.

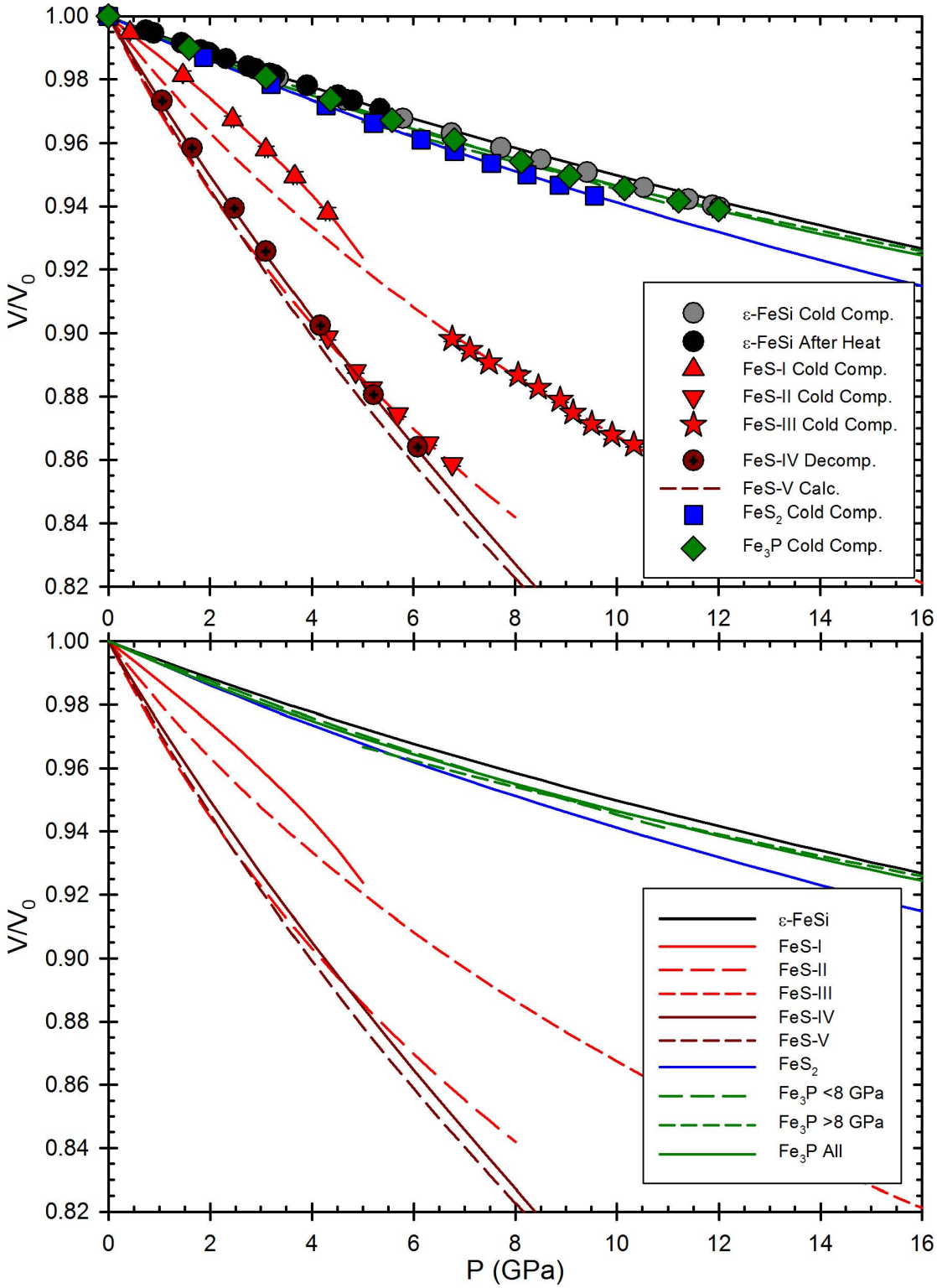

Figure 5.1.2. Comparison of room temperature compression behavior of all materials studied in the Multi-Anvil Cell (MAC) experiments. Top panel shows data for each phase studied along with calculated compression curves from the BM-3 fitting of each dataset. Note that FeS-V does not exist at room T, so only the calculated curve is shown. Bottom panel shows only curves for clarity.

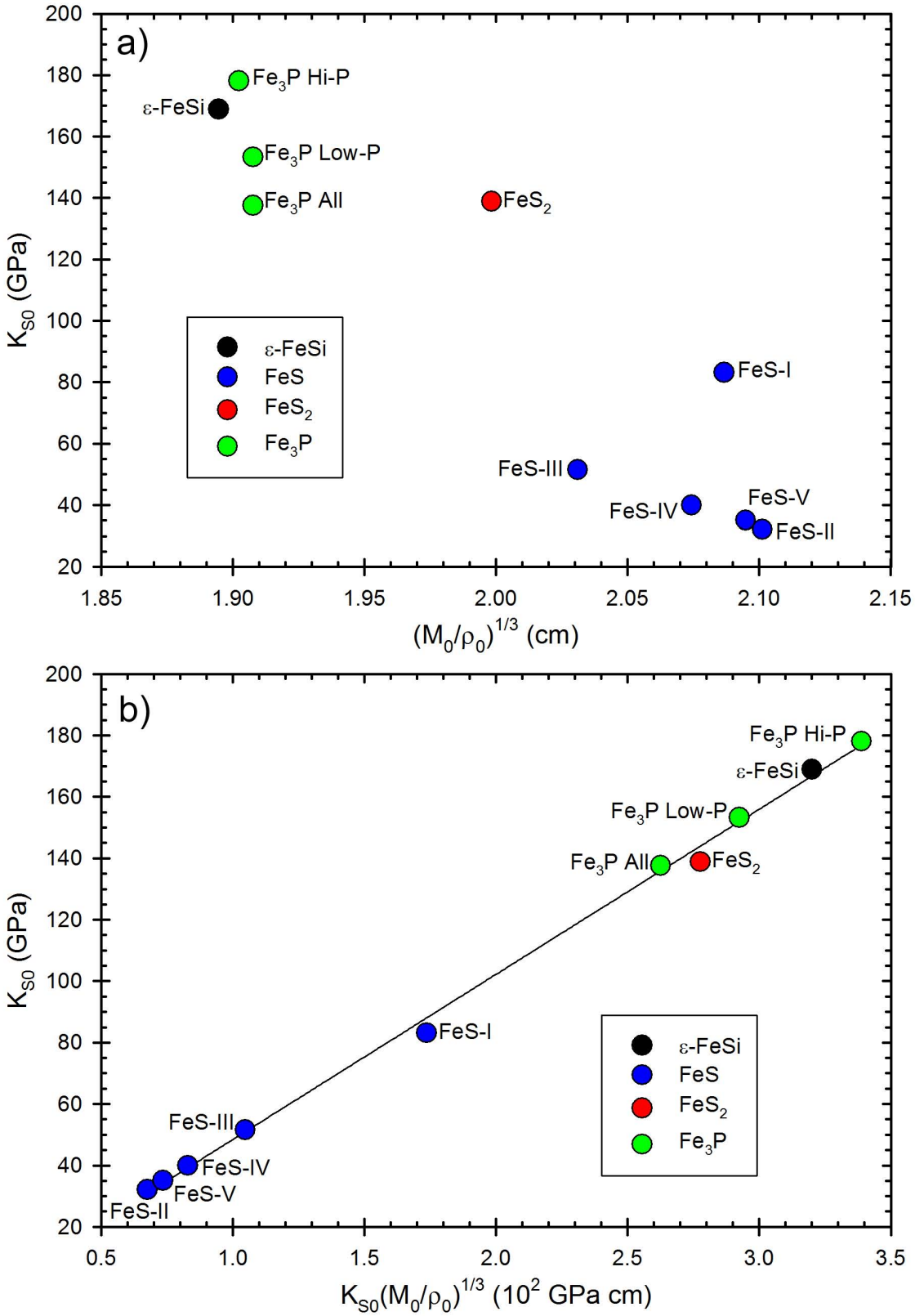

Figure. 5.1.3. Plot of adiabatic bulk modulus vs. a) average interatomic spacing and b) the product of the bulk modulus and average interatomic spacing. Data points are labeled for each phase studied. Trendline is obtained via linear regression of all data points.

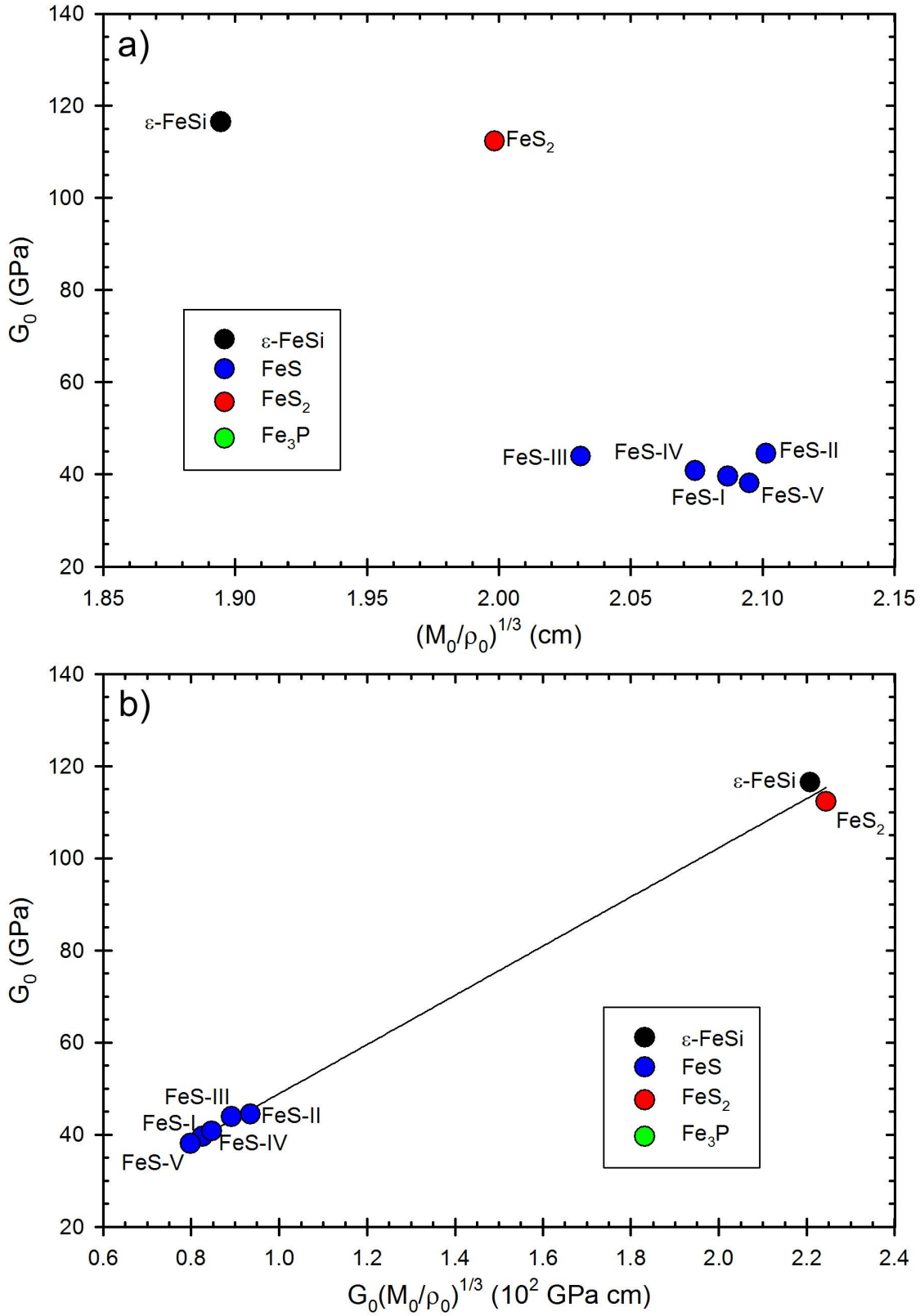

Figure. 5.1.4. Plot of shear modulus vs. a) average interatomic spacing and b) the product of the shear modulus and average interatomic spacing. Data points are labeled for each phase studied. Trendline is obtained via linear regression of all data points.

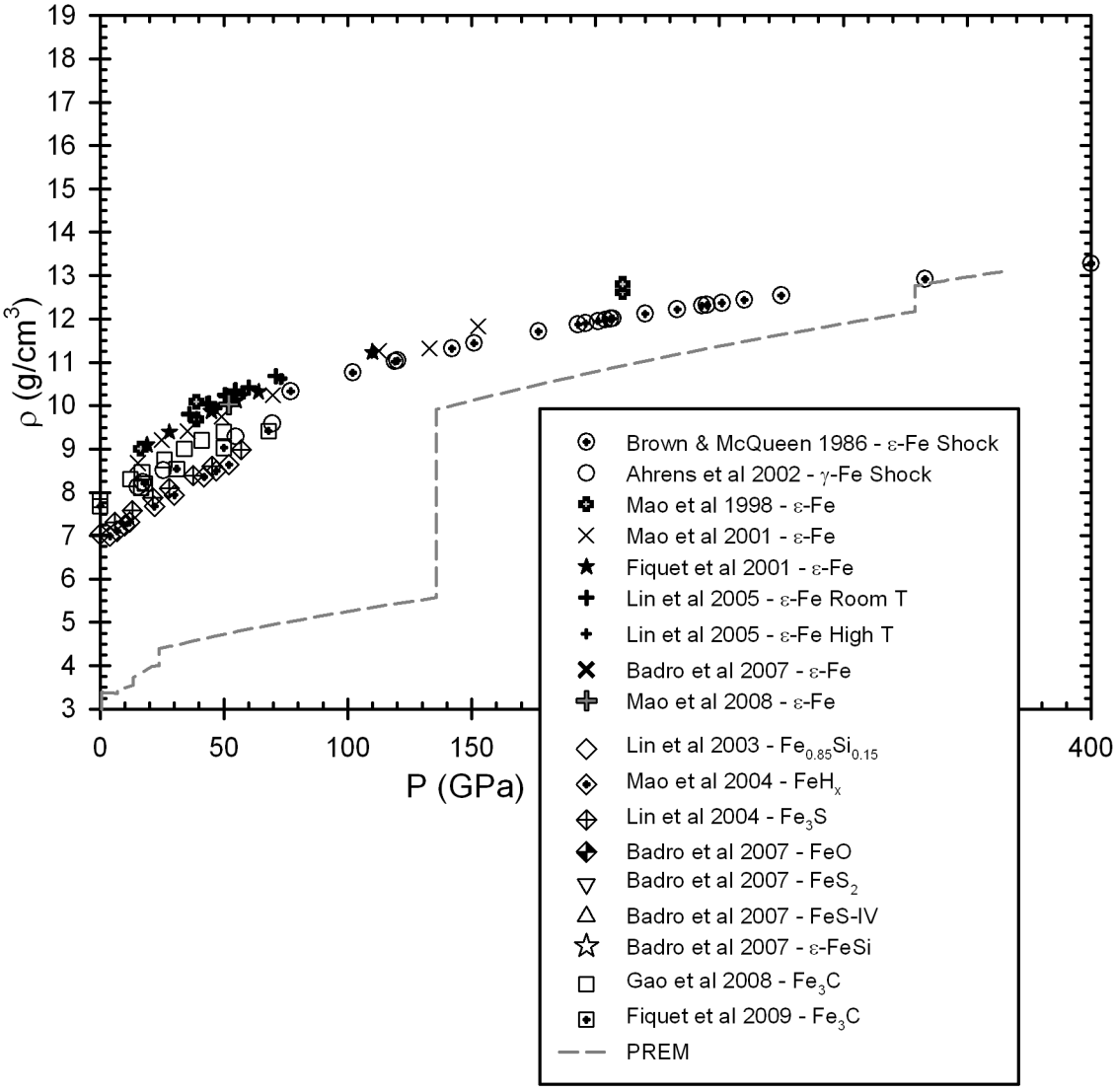

Figure 5.2.1. Density vs. pressure diagram showing data from previous studies on various materials with comparison to PREM (Dziewonski and Anderson, 1981). Several materials are shown on this diagram, including pure Fe (Ahrens et al., 2002; Badro et al., 2007; Brown and McQueen, 1986; Fiquet et al., 2001; Lin et al., 2005; Mao et al., 1998; Mao et al., 2001; Mao et al., 2008), iron silicides (Badro et al., 2007; Lin et al., 2003b), iron hydride (Mao et al., 2004), iron sulfides (Badro et al., 2007; Lin et al., 2004a), and iron carbides (Fiquet et al., 2009; Gao et al., 2008). Symbols used in this figure will be used to represent the same data in all subsequent diagrams.

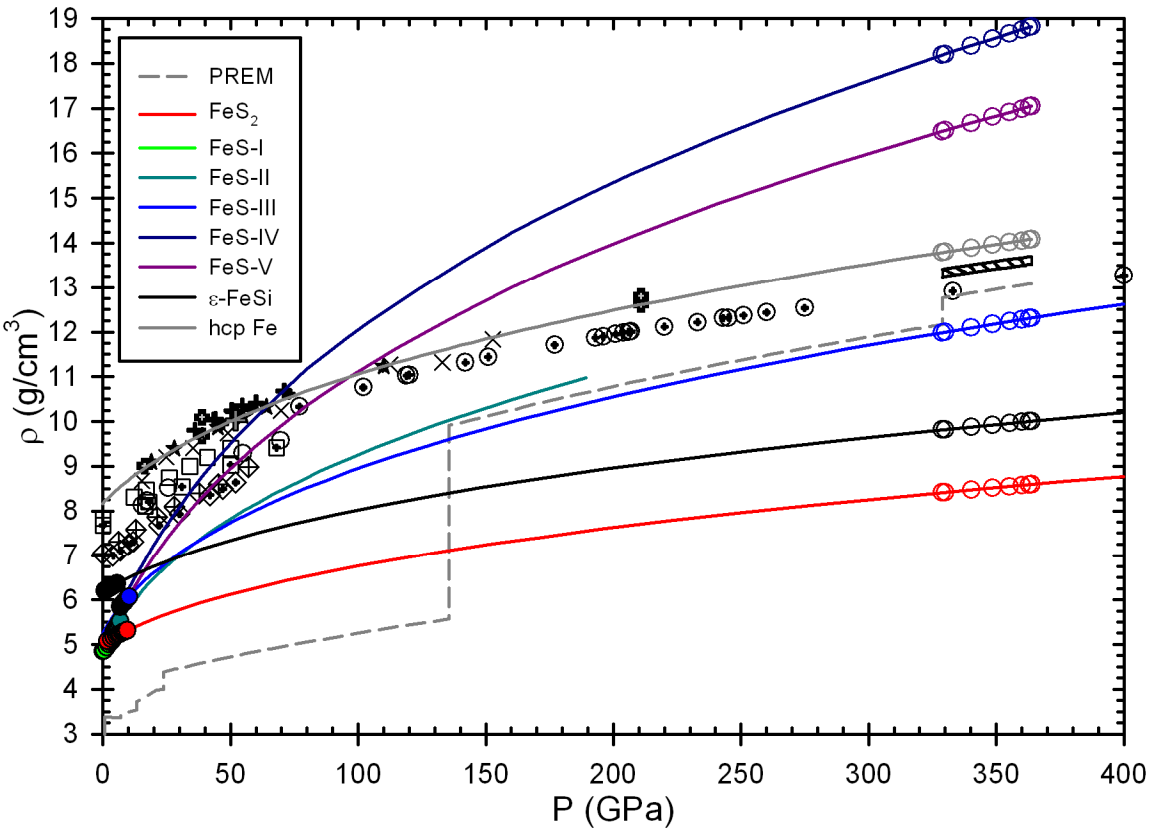

Figure 5.2.2. Density vs. pressure diagram showing 300 K extrapolation of data from this study to inner core pressures compared with previous studies on various materials and PREM. Data are color coded according to phase. Filled circles represent actual data collected in the experiment, and open circles represent the calculated density at various levels within the inner core according to PREM. Gray line and open circles represent hcp Fe at 300 K from the thermal equation of state given by Uchida et al (2001). The black hashed-lined area shows the density of hcp Fe at 4500 K (upper bound) and 6500 K (lower bound). The same color and symbol scheme is used in all subsequent diagrams for consistency.

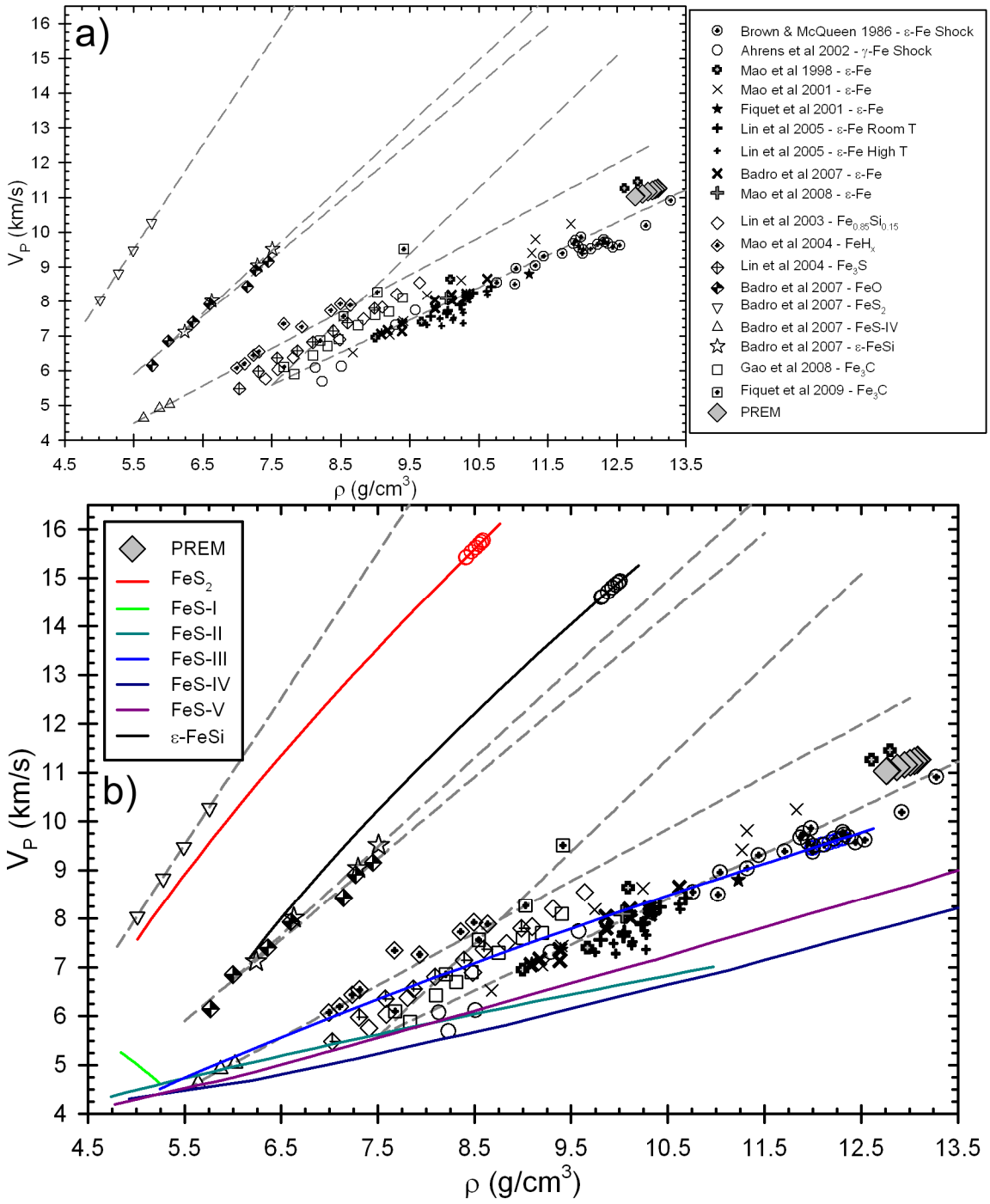

Figure 5.2.3. P-wave velocity vs. density diagrams. a) Data from previous studies shown again for clarity using the same symbols as in Figure 5.2.1. The gray dashed lines are calculated using the Birch's Law equations given by Badro et al (2007) and Fiquet at al (2009). b) 300 K extrapolation of data from this study compared with previous data and the PREM model.

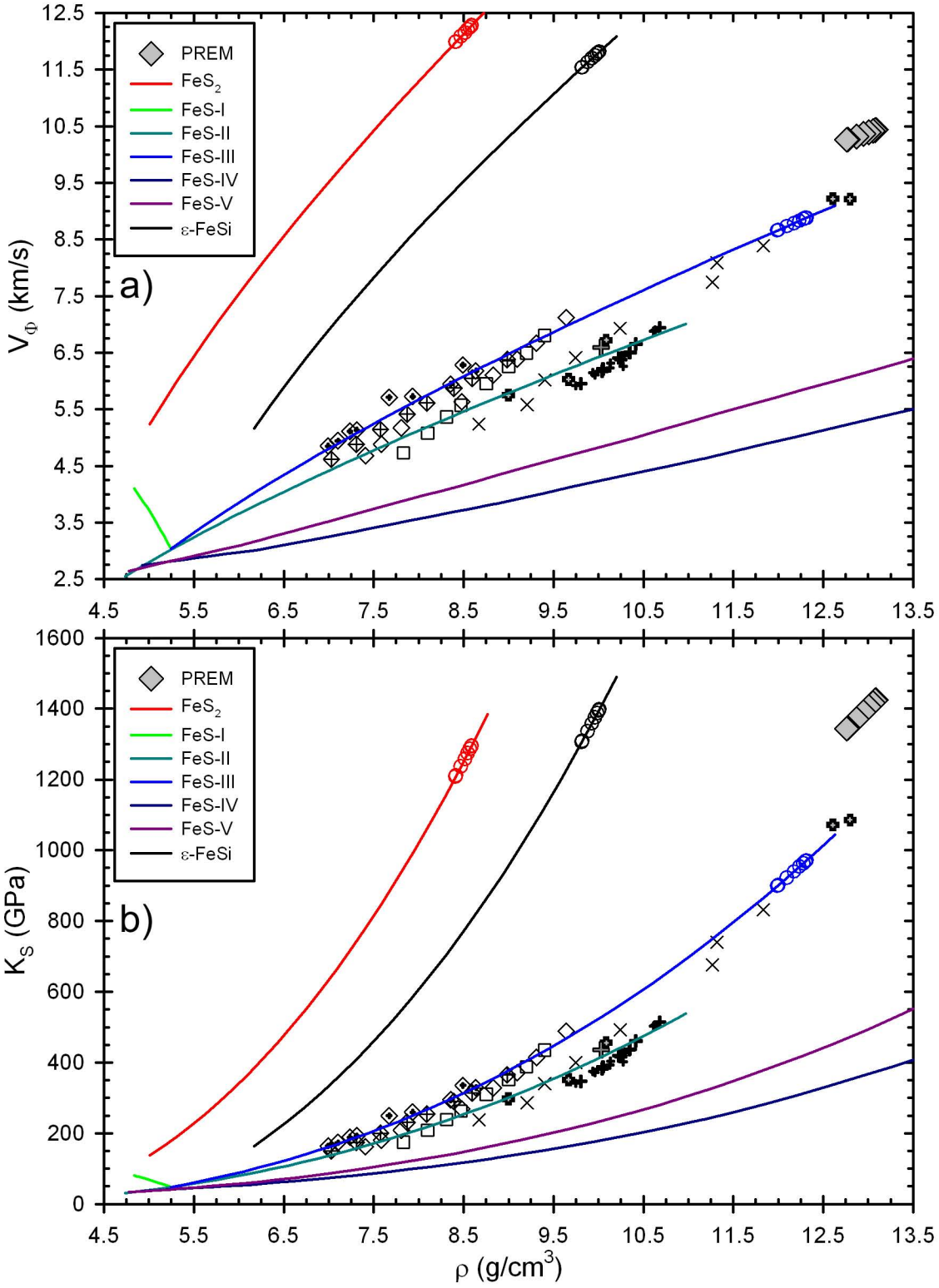

Figure 5.2.4. a) Bulk sound speed vs. density. b) Elastic bulk modulus vs. density. Data are coded as in previous figures.

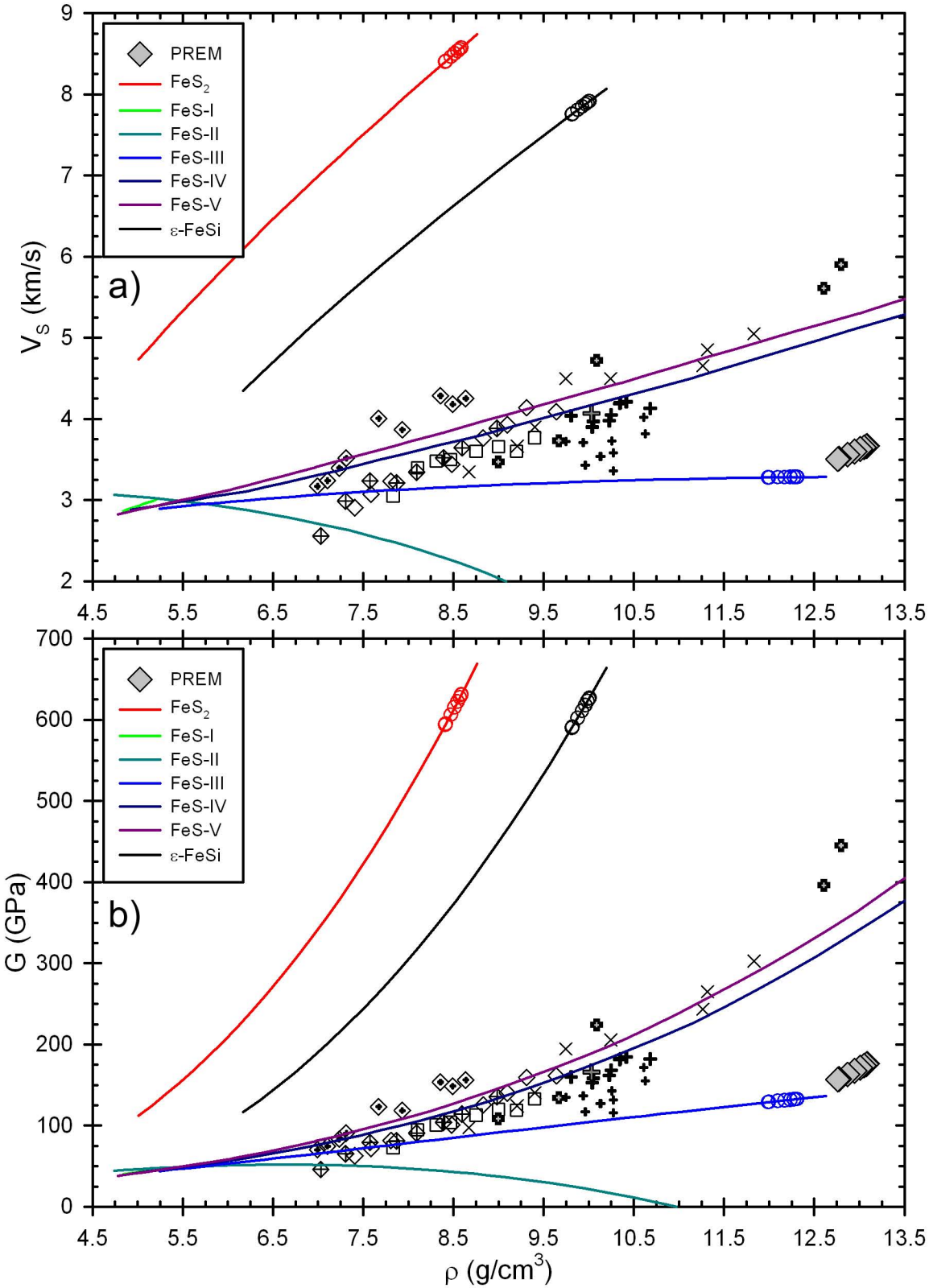

Figure 5.2.5. a) S-wave velocity vs. density. b) Elastic shear modulus vs. density. Data are coded as in previous figures.

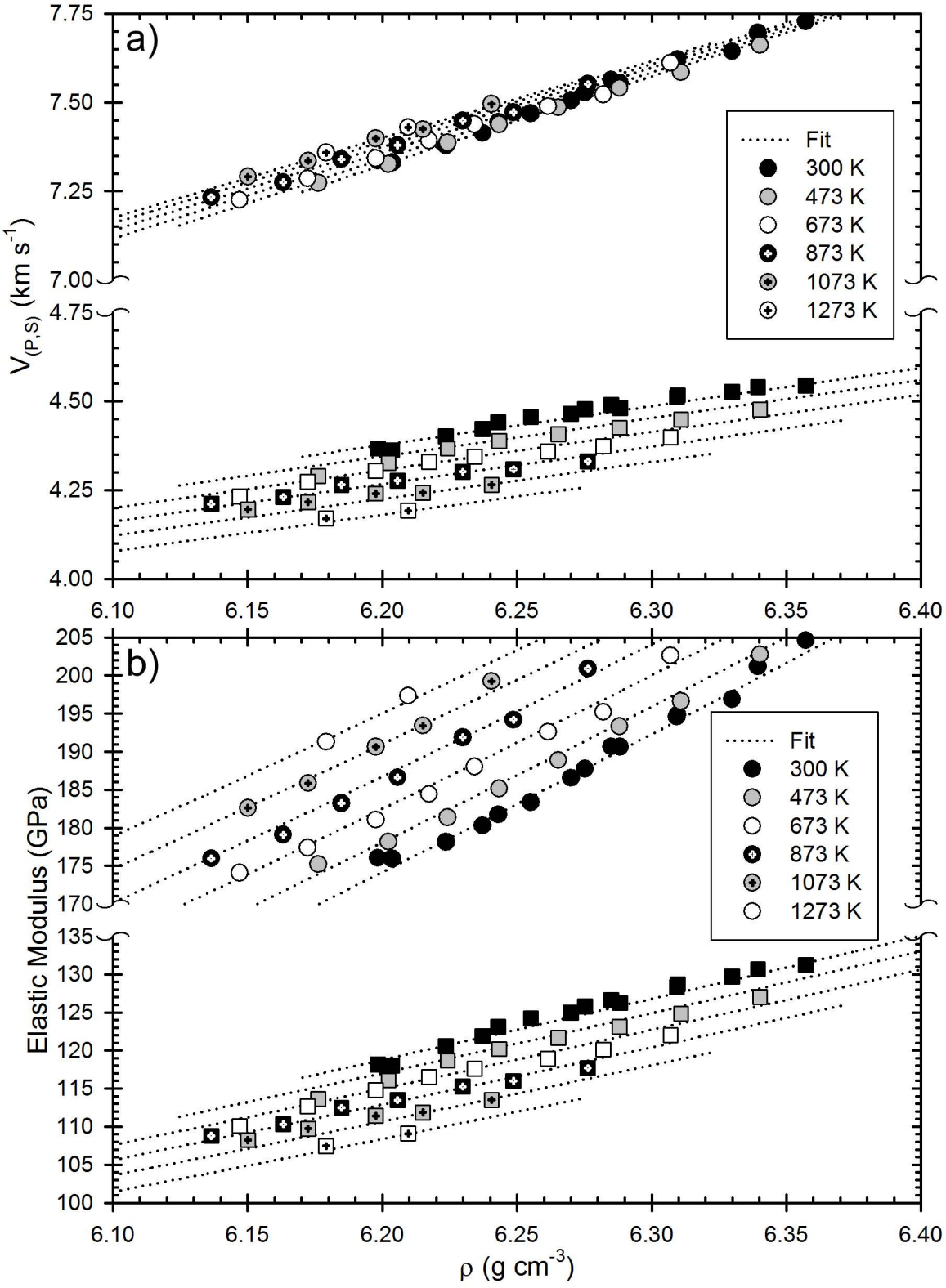

Figure 5.2.6. a) Acoustic velocities and b) elastic modulus as a function of density for e-FeSi at high P and T. It is clear from these diagrams that Birch's Law does not hold for this material under these conditions.

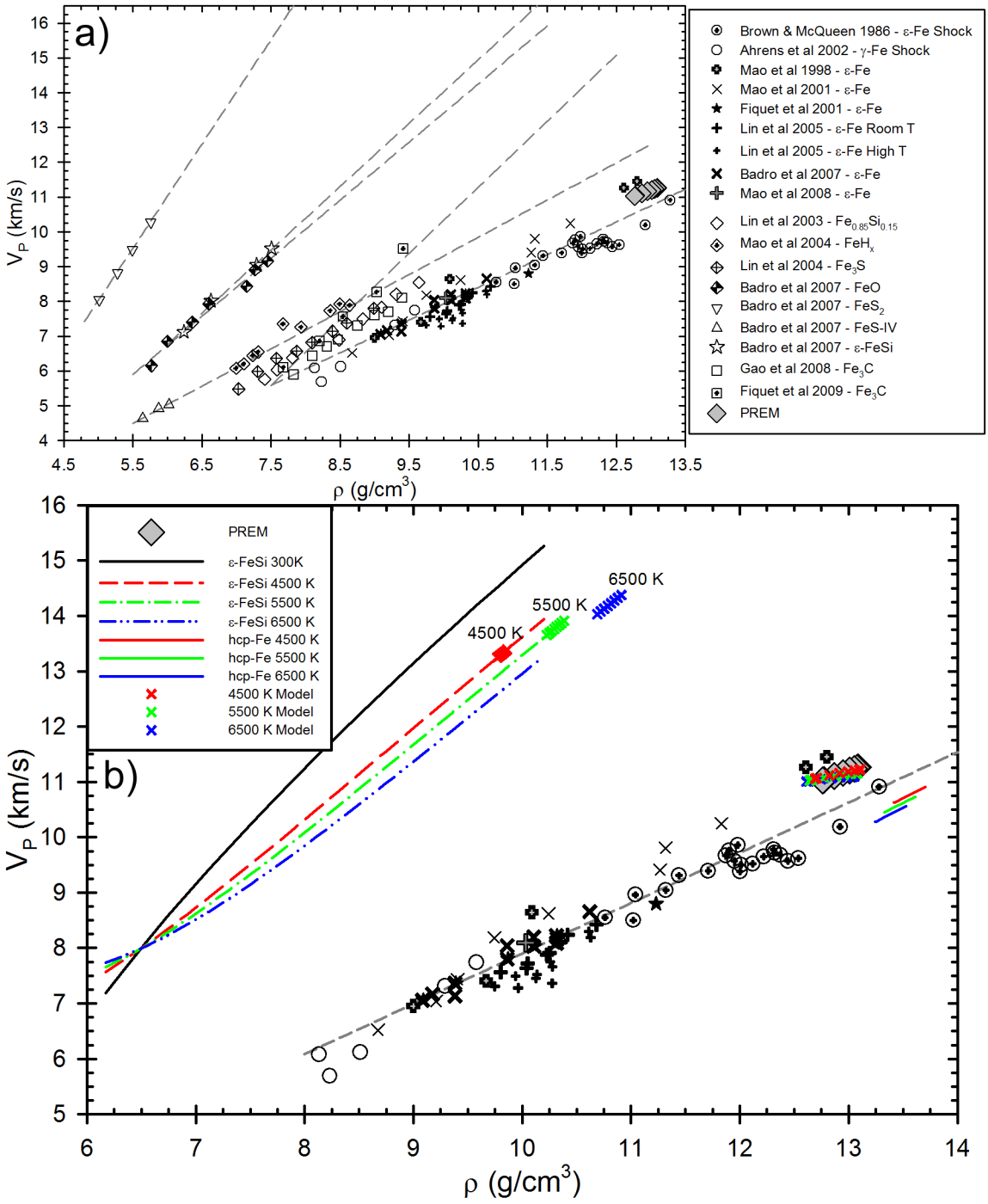

Figure 5.2.7. P-wave velocity vs. density diagrams. a) Data from previous studies shown again for clarity using the same symbols as in Figure 5.2.1. The gray dashed lines are calculated using the Birch's Law equations given by Badro et al (2007) and Fiquet at al (2009). b) 300 K extrapolation of ε-FeSi data from this study, along with calculated Birch's Law deviations at 4500 K (all red data), 5500 K (all green data), and 6500 K (all blue data). These deviations were also calculated for Fe using the data of Lin et al. (2005). Model calculated as for 300 K data in previous section; model results are shown on the diagram as x's.

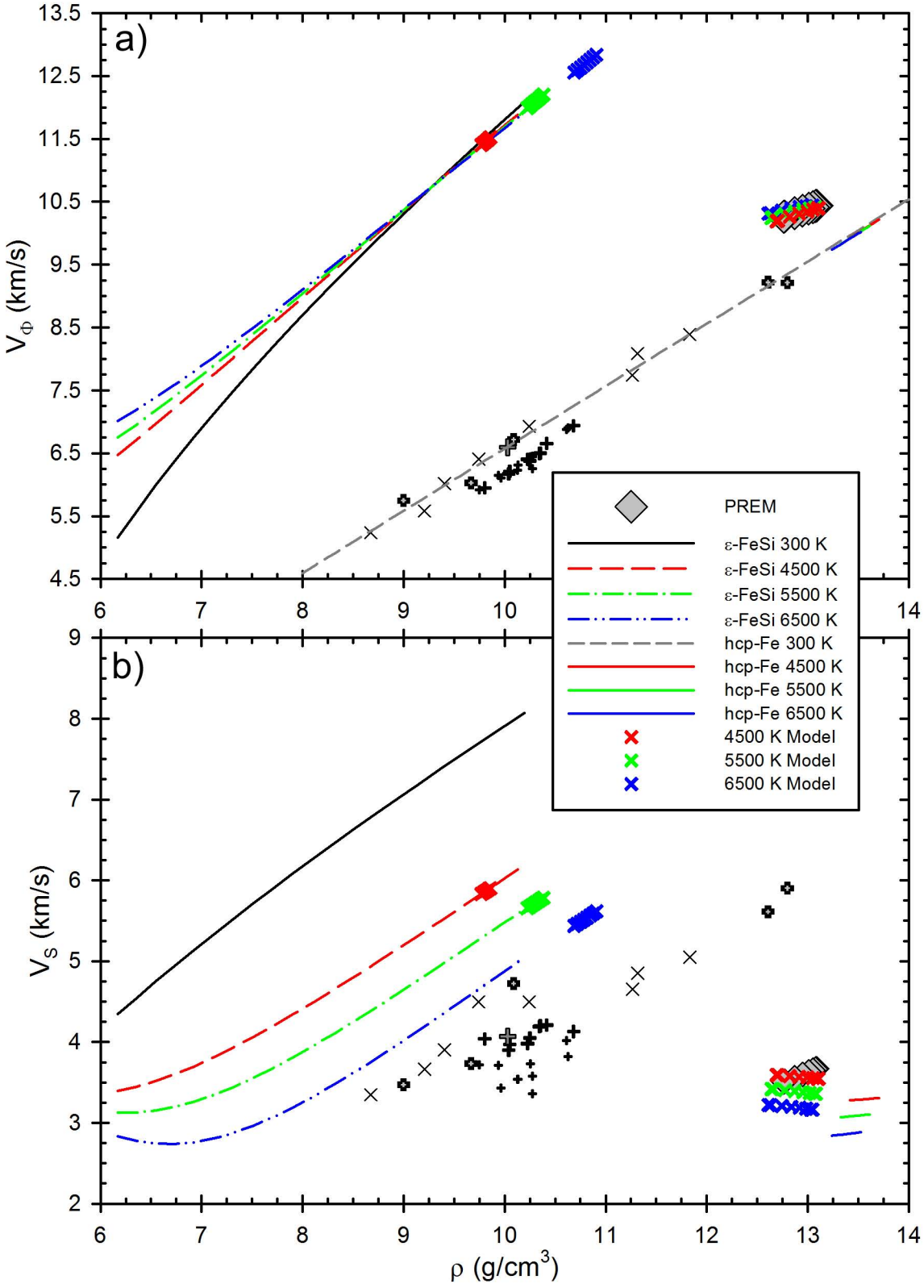

Figure 5.2.8. a) Bulk sound speed and b) shear wave velocities as a function of density. Results of high temperature extrapolations and modeling are shown.

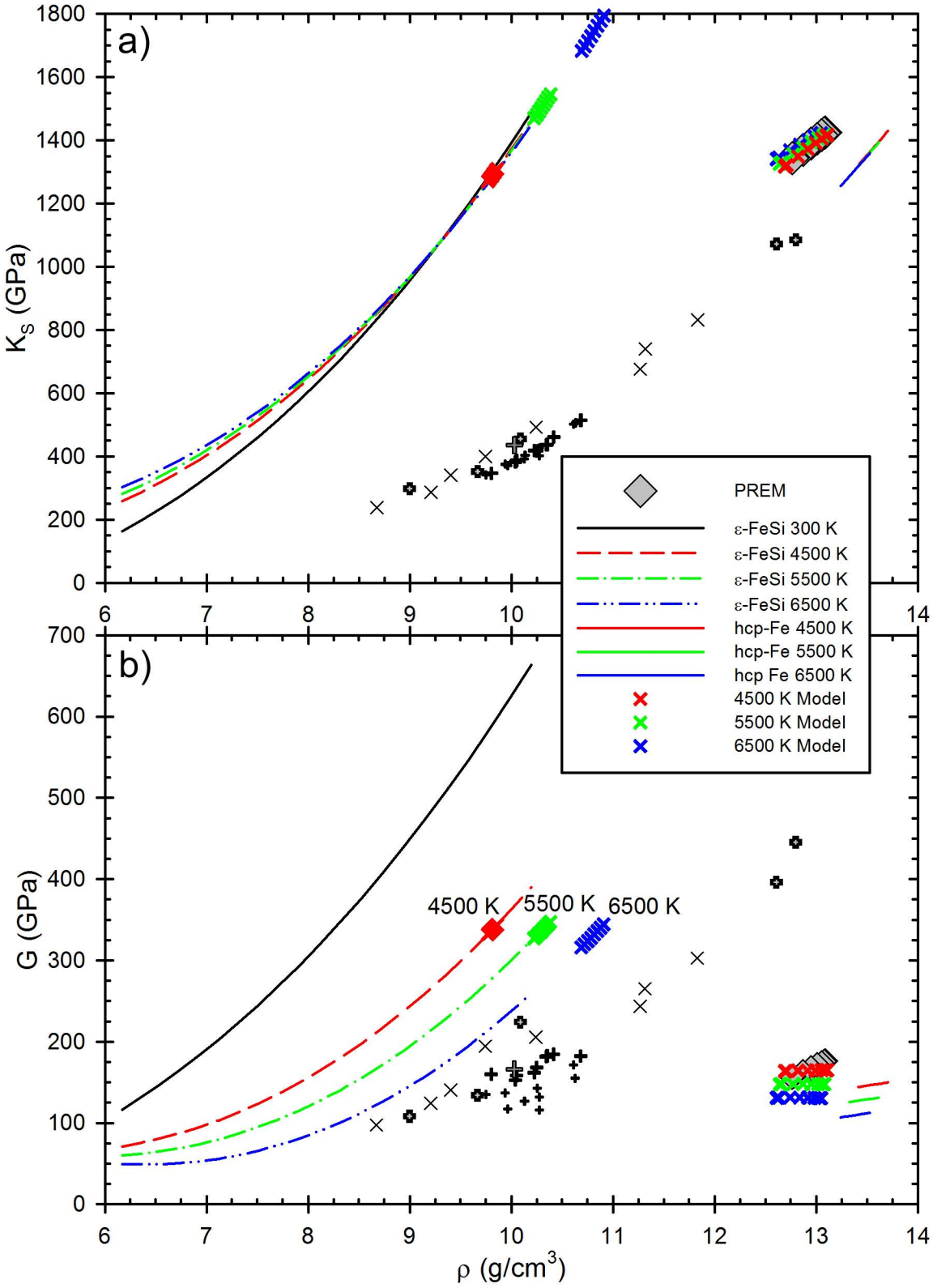

Figure 5.2.9. a) Adiabatic bulk and b) shear modulus as a function of density. Results of high temperature extrapolations and modeling are shown.

Table 5.1. Comparison of results on all materials studied in this investigation

Material	Method	P (GPa)	V_0 (Å^3)	K_0 (GPa)	K_0'	$\partial K_0/\partial T$ (GPa K^{-1})	G_0 (GPa)	G_0'	$\partial G_0/\partial T$ (GPa K^{-1})
ε-FeSi[a]	Ultrasonics & X-ray	8 (300-1273 K)	90.45(3)	168.9(7)	6.6(2)	-0.023(1)	116.5(3)	2.9(1)	-0.030(1)
FeS-I[a]	Ultrasonics w/ P-V	4.3 (300 K)	362.07(35)	83.2	-4.3	-	39.6(4)	1.1(2)	-
FeS-II[a]	Ultrasonics w/ P-V	4.3-6.8 (300 K)	123.24(1)	32.13	4.78	-	44.5(3)	1.1(2)	-
FeS-III[a]	Ultrasonics w/ P-V	6.8-10.4 (300 K)	333.541(4)	51.553	5.239	-	43.9(3)	1.3(2)	-
FeS-IV[a]	Ultrasonics w/ P-V-T	1-7 (300-673 K)	237.11(4)	39.96	1.772	-0.0090	40.8(3)	1.82(1)	-0.0259(8)
FeS-V[a]	Ultrasonics w/ P-V-T	2.7-7.8 (673-1073 K)	61.061(3)	35.09	2.412	-0.0023	38.1(2)	2.13(2)	-0.0199(9)
FeS_2[a]	Ultrasonics & X-ray	10 (300 K)	159.01(3)	138.9(7)	6.0(1)	-	112.3(3)	3.0(<1)	-
ε-FeSi[b]	MAC P-V-T	8 (300-1273 K)	90.45(3)	164.6(1)	6.5(1)	-0.039(1)	-	-	-
FeS-I[b]	MAC P-V	4.3 (300 K)	362.07(35)	81.2(6)	-4.3(2)	-	-	-	-
FeS-II[b]	MAC P-V	4.3-6.8 (300 K)	123.24(1)	30.73(1)	4.78(1)	-	-	-	-
FeS-III[b]	MAC P-V	6.8-10.4 (300 K)	333.541(4)	48.402(1)	5.239(1)	-	-	-	-
FeS-IV[b]	MAC P-V-T	1-7 (300-673 K)	237.11(4)	37.08(9)	1.800(5)	-0.0172(2)	-	-	-
FeS-V[b]	MAC P-V-T	2.7-7.8 (673-1073 K)	61.061(3)	33.42(8)	2.372(6)	-0.0075(2)	-	-	-
FeS_2[b]	MAC P-V	10 (300 K)	159.01(3)	137.51(1)	6.01(1)	-	-	-	-
Fe_3P[b]	MAC P-V	8 (300 K)	368.9(5)	153.3(9)	5.3(2)	-	-	-	-
ε-FeSi[b]	DAC P-V	15 (300 K)	90.40(3)	169.4(64)	6.7(14)	-	-	-	-
FeS-I[b]	DAC P-V	3 (300 K)	361.94(32)	89.2(6)	-4.2(3)	-	-	-	-
FeS-II[b]	DAC P-V	4-6.6 (300 K)	121.80(34)	35.8(20)	4.4(4)	-	-	-	-
FeS-III[b]	DAC P-V	7.9-11.6 (300 K)	333.8940(1)	47.777(3)	5.898(9)	-	-	-	-
FeS_2[b]	DAC P-V	13.2 (300 K)	159.14(5)	143.1(10)	5.0(2)	-	-	-	-
Fe_3P[b]	DAC P-V	8 (300K)	369.2(6)	156.8(11)	5.3(3)	-	-	-	-

[a]Adiabatic values; [b]Isothermal values

REFERENCES

Ahrens, T.J., Holland, K.G., and Chen, G.Q. (2002) Phase diagram of iron, revised-core temperatures. Geophysical Research Letters, 29(7), 4.

Ahrens, T.J., and Jeanloz, R. (1987) Pyrite - Shock Compression, Isentropic Release, and Composition of the Earth's Core. Journal of Geophysical Research-Solid Earth and Planets, 92(B10), 10363-10375.

Al-Sharif, A.I., Abu-Jafar, M., and Qteish, A. (2001) Structural and electronic structure properties of FeSi: the driving force behind the stability of the B20 phase. Journal of Physics-Condensed Matter, 13(12), 2807-2815.

Alfe, D., Gillan, M.J., and Price, G.D. (2002) Composition and temperature of the Earth's core constrained by combining ab initio calculations and seismic data. Earth and Planetary Science Letters, 195(1-2), 91-98.

Anders, E., and Ebihara, M. (1982) Solar System Abundances of the Elements. Geochimica Et Cosmochimica Acta, 46(11), 2363-2380.

Anderson, W.W., and Ahrens, T.J. (1996) Shock temperature and melting in iron sulfides at core pressures. Journal of Geophysical Research-Solid Earth, 101(B3), 5627-5642.

Badro, J., Fiquet, G., Guyot, F., Gregoryanz, E., Occelli, F., Antonangeli, D., and d'Astuto, M. (2007) Effect of light elements on the sound velocities in solid iron: Implications for the composition of Earth's core. Earth and Planetary Science Letters, 254(1-2), 233-238.

Birch, F. (1947) Finite Elastic Strain of Cubic Crystals. Physical Review, 71(11), 809-824.

-. (1952) Elasticity and Constitution of the Earth Interior. Journal of Geophysical Research, 57(2), 227-286.

-. (1964) Density and Composition of the Mantle and Core. Journal of Geophysical Research, 69(20), 4377-4388.

Blanchard, M., Alfredsson, M., Brodholt, J., Price, G.D., Wright, K., and Catlow, C.R.A. (2005) Electronic structure study of the high-pressure vibrational spectrum of FeS2 pyrite. Journal of Physical Chemistry B, 109(46), 22067-22073.

Boehler, R. (2000) High-pressure experiments and the phase diagram of lower mantle and core materials. Reviews of Geophysics, 38(2), 221-245.

Bridgman, P.W. (1949) Linear Compressions to 30,000 kg/cm^2, Including Relatively Incompressible Substances. Proceedings of the American Academy of Arts and Sciences, 77(6), 189-234.

Brown, J.M., Ahrens, T.J., and Shampine, D.L. (1984) Hugoniot Data For Pyrrhotite and the Earth's Core. Journal of Geophysical Research, 89(NB7), 6041-6048.

Brown, J.M., and McQueen, R.G. (1986) Phase Transitions, Gruneisen Parameter, and Elasticity for Shocked Iron Between 77 GPa and 400 GPa. Journal of Geophysical Research-Solid Earth and Planets, 91(B7), 7485-7494.

Caracas, R., and Wentzcovitch, R. (2004) Equation of state and elasticity of FeSi. Geophysical Research Letters, 31(20), 4.

Chen, B., Gao, L.L., Funakoshi, K., and Li, J. (2007) Thermal expansion of iron-rich alloys and implications for the Earth's core. Proceedings of the National Academy of Sciences of the United States of America, 104(22), 9162-9167.

Chrystal, R.S.B. (1965) Thermal Expansion of Iron Pyrites. Transactions of the Faraday Society, 61(512P), 1811.

Davies, G.F., and Dziewonski, A.M. (1975) Homogeneity and Constitution of Earths Lower Mantle and Outer Core. Physics of the Earth and Planetary Interiors, 10(4), 336-343.

Dobson, D.P., Crichton, W.A., Bouvier, P., Vocadlo, L., and Wood, I.G. (2003) The equation of state of CsCl-structured FeSi to 40 GPa: Implications for silicon in the Earth's core. Geophysical Research Letters, 30(1), 4.

Dobson, D.P., Vocadlo, L., and Wood, I.G. (2002) A new high-pressure phase of FeSi. American Mineralogist, 87(5-6), 784-787.

Dreibus, G., and Palme, H. (1996) Cosmochemical constraints on the sulfur content in the Earth's core. Geochimica Et Cosmochimica Acta, 60(7), 1125-1130.

Dubrovinsky, L.S., and Lin, J.F. (2009) Mineral Physics Quest to the Earth's Core. EOS, Transactions, American Geophysical Union, 90(3), 21-22.

Duffy, T.S., and Anderson, D.L. (1989) Seismic Velocities in Mantle Minerals and the Mineralogy of the Upper Mantle. Journal of Geophysical Research-Solid Earth and Planets, 94(B2), 1895-1912.

Dziewonski, A.M., and Anderson, D.L. (1981) Preliminary Reference Earth Model. Physics of the Earth and Planetary Interiors, 25(4), 297-356.

Dziewonski, A.M., and Gilbert, F. (1971) Solidity of the Inner Core of the Earth Inferred From Normal Mode Observations. Nature, 234(5330), 465-466.

Fasiska, E.J., and Zwell, L. (1967) Thermal Expansion of Fe_3P. Transactions of the Metallurgical Society of America, 239(6), 924.

Faul, U.H., Gerald, J.D.F., and Jackson, I. (2004) Shear wave attenuation and dispersion in melt-bearing olivine polycrystals: 2. Microstructural interpretation and seismological implications. Journal of Geophysical Research-Solid Earth, 109(B6), 20.

Fei, Y.W., Li, J., Bertka, C.M., and Prewitt, C.T. (2000) Structure type and bulk modulus of Fe3S, a new iron-sulfur compound. American Mineralogist, 85(11-12), 1830-1833.

Fiquet, G., Badro, J., Gregoryanz, E., Fei, Y.W., and Occelli, F. (2009) Sound velocity in iron carbide (Fe3C) at high pressure: Implications for the carbon content of the Earth's inner core. Physics of the Earth and Planetary Interiors, 172(1-2), 125-129.

Fiquet, G., Badro, J., Guyot, F., Requardt, H., and Krisch, M. (2001) Sound velocities in iron to 110 gigapascals. Science, 291(5503), 468-471.

Gao, L.L., Chen, B., Wang, J.Y., Alp, E.E., Zhao, J.Y., Lerche, M., Sturhahn, W., Scott, H.P., Huang, F., Ding, Y., Sinogeikin, S.V., Lundstrom, C.C., Bass, J.D., and Li, J. (2008) Pressure-induced magnetic transition and sound velocities of Fe3C: Implications for carbon in the Earth's inner core. Geophysical Research Letters, 35(17).

Georg, R.B., Halliday, A.N., Schauble, E.A., and Reynolds, B.C. (2007) Silicon in the Earth's core. Nature, 447(7148), 1102-1106.

Guyot, F., Zhang, J.H., Martinez, I., Matas, J., Ricard, Y., and Javoy, M. (1997) P-V-T measurements of iron silicide (epsilon-FeSi). Implications for silicate-metal interactions in the early Earth. European Journal of Mineralogy, 9(2), 277-285.

Gwanmesia, G.D., Li, B.S., and Liebermann, R.C. (1993) Hot-Pressing of Polycrystals of High-Pressure Phases of Mantle Minerals in Multi-Anvil Apparatus. Pure and Applied Geophysics, 141(2-4), 467-484.

Gwanmesia, G.D., Liebermann, R.C., and Guyot, F. (1990) Hot-Pressing and Characterization of Polycrystals of Beta-Mg2SiO4 for Acoustic Velocity Measurements. Geophysical Research Letters, 17(9), 1331-1334.

Hammersley, A.P., Svensson, S.O., Hanfland, M., Fitch, A.N., and Hausermann, D. (1996) Two-dimensional detector software: From real detector to idealised image or two-theta scan. High Pressure Research, 14(4-6), 235-248.

Hemley, R.J., and Mao, H.K. (2001) In situ studies of iron under pressure: New windows on the Earth's core. International Geology Review, 43(1), 1-30.

Hirao, N., Kondo, T., Ohtani, E., Takemura, K., and Kikegawa, T. (2004) Compression of iron hydride to 80 GPa and hydrogen in the Earth's inner core. Geophysical Research Letters, 31(6), 4.

Hofmeister, A.M., and Mao, H.K. (2003) Pressure derivatives of shear and bulk moduli from the thermal Gruneisen parameter and volume-pressure data. Geochimica Et Cosmochimica Acta, 67(6), 1207-1227.

Jackson, I., Fitz Gerald, J.D., and Kokkonen, H. (2000) High-temperature viscoelastic relaxation in iron and its implications for the shear modulus and attenuation of the Earth's inner core. Journal of Geophysical Research-Solid Earth, 105(B10), 23605-23634.

Jacobs, J.A. (1987) The Earth's Core. 304 pp. p. New York Academic.

Jeanloz, R. (1979) Properties of Iron at High Pressures and the State of the Core. Journal of Geophysical Research, 84(NB11), 6059-6069.

-. (1990) The Nature of the Earth's Core. Annual Review of Earth and Planetary Sciences, 18, 357-386.

Jephcoat, A., and Olson, P. (1987) Is the Inner Core of the Earth Pure Iron. Nature, 325(6102), 332-335.

King, H.E., and Prewitt, C.T. (1982) High-Pressure and High-Temperature Polymorphism of Iron Sulfide (FeS). Acta Crystallographica Section B-Structural Science, 38(JUL), 1877-1887.

Kleppe, A.K., and Jephcoat, A.P. (2004) High-pressure Raman spectroscopic studies of FeS2 pyrite. Mineralogical Magazine, 68(3), 433-441.

Knittle, E., and Jeanloz, R. (1991) The High-Pressure Phase-Diagram of Fe0.94o - a Possible Constituent of the Earths Core. Journal of Geophysical Research-Solid Earth, 96(B10), 16169-16180.

Knittle, E., and Williams, Q. (1995) Static Compression of Epsilon-FeSi and an Evaluation of Reduced Silicon as a Deep Earth Constituent. Geophysical Research Letters, 22(4), 445-448.

Kobayashi, H., Kamimura, T., Ohishi, Y., Takeshita, N., and Mori, N. (2005) Structural and electrical properties of stoichiometric FeS compounds under high pressure at low temperature. Physical Review B, 71(1), 7.

Kusaba, K., Syono, Y., Kikegawa, T., and Shimomura, O. (1997) Structure of FeS under high pressure. Journal of Physics and Chemistry of Solids, 58(2), 241-246.

-. (1998) High pressure and temperature behavior of FeS. Journal of Physics and Chemistry of Solids, 59(6-7), 945-950.

Le Page, Y., and Rodgers, J.R. (2005) Ab initio elasticity of FeS2 pyrite from 0 to 135 GPa. Physics and Chemistry of Minerals, 32(8-9), 564-567.

Li, B.S., Chen, K., Kung, J., Liebermann, R.C., and Weidner, D.J. (2002) Sound velocity measurement using transfer function method. Journal of Physics-Condensed Matter, 14(44), 11337-11342.

Li, B.S., Kung, J., and Liebermann, R.C. (2004) Modem techniques in measuring elasticity of Earth materials at high pressure and high temperature using ultrasonic interferometry in conjunction with synchrotron X-radiation in multi-anvil apparatus. Physics of the Earth and Planetary Interiors, 143-44, 559-574.

Li, B.S., Woody, K., and Kung, J. (2006) Elasticity of MgO to 11 GPa with an independent absolute pressure scale: Implications for pressure calibration. Journal of Geophysical Research-Solid Earth, 111(B11), 10.

Li, B.S., and Zhang, J.Z. (2005) Pressure and temperature dependence of elastic wave velocity of MgSiO3 perovskite and the composition of the lower. Physics of the Earth and Planetary Interiors, 151(1-2), 143-154.

Li, J., and Agee, C.B. (2001) Element partitioning constraints on the light element composition of the Earth's core. Geophysical Research Letters, 28(1), 81-84.

Li, J., Fei, Y., Mao, H.K., Hirose, K., and Shieh, S.R. (2001) Sulfur in the Earth's inner core. Earth and Planetary Science Letters, 193(3-4), 509-514.

Lin, J.F., Campbell, A.J., Heinz, D.L., and Shen, G.Y. (2003a) Static compression of iron-silicon alloys: Implications for silicon in the Earth's core. Journal of Geophysical Research-Solid Earth, 108(B1), 12.

Lin, J.F., Fei, Y.W., Sturhahn, W., Zhao, J.Y., Mao, H.K., and Hemley, R.J. (2004a) Magnetic transition and sound velocities of Fe3S at high pressure: implications for Earth and planetary cores. Earth and Planetary Science Letters, 226(1-2), 33-40.

Lin, J.F., Struzhkin, V.V., Mao, H.K., Hemley, R.J., Chow, P., Hu, M.Y., and Li, J. (2004b) Magnetic transition in compressed Fe3C from x-ray emission spectroscopy. Physical Review B, 70(21), 4.

Lin, J.F., Struzhkin, V.V., Sturhahn, W., Huang, E., Zhao, J.Y., Hu, M.Y., Alp, E.E., Mao, H.K., Boctor, N., and Hemley, R.J. (2003b) Sound velocities of iron-nickel and iron-silicon alloys at high pressures. Geophysical Research Letters, 30(21), 4.

Lin, J.F., Sturhahn, W., Zhao, J.Y., Shen, G.Y., Mao, H.K., and Hemley, R.J. (2005) Sound velocities of hot dense iron: Birch's law revisited. Science, 308(5730), 1892-1894.

Liu, W., Kung, J., and Li, B.S. (2005) Elasticity of San Carlos olivine to 8 GPa and 1073 K. Geophysical Research Letters, 32(16), 4.

Mao, H.K., Bell, P.M., Shaner, J.W., and Steinberg, D.J. (1978) Specific Volume Measurements of Cu, Mo, Pd, and Ag and Calibration of Ruby R1 Fluorescence Pressure Gauge From 0.06 to 1 Mbar. Journal of Applied Physics, 49(6), 3276-3283.

Mao, H.K., and Hemley, R.J. (1996) Experimental studies of Earth's deep interior: Accuracy and versatility of diamond-anvil cells. Philosophical Transactions of the Royal Society of London Series a-Mathematical Physical and Engineering Sciences, 354(1711), 1315-1332.

Mao, H.K., Shu, J.F., Shen, G.Y., Hemley, R.J., Li, B.S., and Singh, A.K. (1998) Elasticity and rheology of iron above 220 GPa and the nature of the Earth's inner core. Nature, 396(6713), 741-743.

Mao, H.K., Xu, J., Struzhkin, V.V., Shu, J., Hemley, R.J., Sturhahn, W., Hu, M.Y., Alp, E.E., Vocadlo, L., Alfe, D., Price, G.D., Gillan, M.J., Schwoerer-Bohning, M., Hausermann, D., Eng, P., Shen, G., Giefers, H., Lubbers, R., and Wortmann, G. (2001) Phonon density of states of iron up to 153 gigapascals. Science, 292(5518), 914-916.

Mao, W.L., Struzhkin, V.V., Baron, A.Q.R., Tsutsui, S., Tommaseo, C.E., Wenk, H.R., Hu, M.Y., Chow, P., Sturhahn, W., Shu, J.F., Hemley, R.J., Heinz, D.L., and Mao, H.K. (2008) Experimental determination of the elasticity of iron at high pressure. Journal of Geophysical Research-Solid Earth, 113(B9), 14.

Mao, W.L., Sturhahn, W., Heinz, D.L., Mao, H.K., Shu, J.F., and Hemley, R.J. (2004) Nuclear resonant x-ray scattering of iron hydride at high pressure. Geophysical Research Letters, 31(15), 4.

Marshall, W.G., Nelmes, R.J., Loveday, J.S., Klotz, S., Besson, J.M., Hamel, G., and Parise, J.B. (2000) High-pressure neutron-diffraction study of FeS. Physical Review B, 61(17), 11201-11204.

Martin, P., Price, G.D., and Vocadlo, L. (2001) An ab initio study of the relative stabilities and equations of state of FeS polymorphs. Mineralogical Magazine, 65(2), 181-191.

McDonough, W.F. (2004) Compositional model for the Earth's core. In R.W. Carlson, H.D. Holland, and K.K. Turekian, Eds. Elsevier, Oxford.

McDonough, W.F., and Sun, S.S. (1995) The Composition of the Earth. Chemical Geology, 120(3-4), 223-253.

McQueen, R.G., and Marsh, S.P. (1966) Shockwave Compression of Iron-Nickel Alloys and the Earth's Core. Journal of Geophysical Research, 71(6), 1751-1756.

Merkel, S., Jephcoat, A.P., Shu, J., Mao, H.K., Gillet, P., and Hemley, R.J. (2002) Equation of state, elasticity, and shear strength of pyrite under high pressure. Physics and Chemistry of Minerals, 29(1), 1-9.

Nelmes, R.J., McMahon, M.I., Belmonte, S.A., and Parise, J.B. (1999) Structure of the high-pressure phase III of iron sulfide. Physical Review B, 59(14), 9048-9052.

Ohfuji, H., Sata, N., Kobayashi, H., Ohishi, Y., Hirose, K., and Irifune, T. (2007) A new high-pressure and high-temperature polymorph of FeS. Physics and Chemistry of Minerals, 34(5), 335-343.

Oldham, R.D. (1906) Constitution of the Interior of the Earth as Revealed by Earthquakes. Quarterly Journal of the Geological Society, 62, 456-475.

Ono, S., and Kikegawa, T. (2006) High-pressure study of FeS, between 20 and 120 GPa, using synchrotron X-ray powder diffraction. American Mineralogist, 91(11-12), 1941-1944.

Ono, S., Kikegawa, T., and Ohishi, Y. (2007) Equation of state of the high-pressure polymorph of FeSi to 67 GPa. European Journal of Mineralogy, 19(2), 183-187.

Pauling, L., and Soldate, A.M. (1948) The Nature of the Bonds in the Iron Silicide FeSi and Related Crystals. Acta Crystallographica, 1(1-6), 212-216.

Prasad, S.C., and Wooster, W.A. (1956) The Elasticity of Iron Pyrites, FeS_2. Acta Crystallographica, 9(2), 169-173.

Sarrao, J.L., Mandrus, D., Migliori, A., Fisk, Z., and Bucher, E. (1994) Elastic Properties of FeSi. Physica B, 199, 478-479.
Sata, N., Ohfuji, H., Hirose, K., Kobayashi, H., Ohishi, Y., and Hirao, N. (2008) New high-pressure B2 phase of FeS above 180 GPa. American Mineralogist, 93(2-3), 492-494.
Scott, H.P., Huggins, S., Frank, M.R., Maglio, S.J., Martin, C.D., Meng, Y., Santillan, J., and Williams, Q. (2007) Equation of state and high-pressure stability of Fe3P-schreibersite: Implications for phosphorus storage in planetary cores. Geophysical Research Letters, 34(6), 5.
Scott, H.P., Kiefer, B., Martin, C.D., Boateng, N., Frank, M.R., and Meng, Y. (2008) P-V equation of state for Fe2P and pressure-induced phase transition in Fe3P. High Pressure Research, 28(3), 375-384.
Scott, H.P., Williams, Q., and Knittle, E. (2001) Stability and equation of state of Fe3C to 73 GPa: Implications for carbon in the Earth's core. Geophysical Research Letters, 28(9), 1875-1878.
Sherman, D.M. (1997) The composition of the Earth's core: constraints on S and Si vs. temperature. Earth and Planetary Science Letters, 153(3-4), 149-155.
Simmons, G., and Birch, F. (1963) Elastic Constants of Pyrite. Journal of Applied Physics, 34(9), 2736-&.
Sithole, H.M., Ngoepe, P.E., and Wright, K. (2003) Atomistic simulation of the structure and elastic properties of pyrite (FeS2) as a function of pressure. Physics and Chemistry of Minerals, 30(10), 615-619.
Skinner, B.J. (1966) Thermal Expansion. In S.P.J. Clark, Ed. Handbook of Physical Constants, p. 75-95. Geological Society of America, Boulder, CO.
Smith, F.G. (1942) Variation in the properties of pyrite. American Mineralogist, 27(1), 1-19.
Steinle-Neumann, G., Stixrude, L., Cohen, R.E., and Gulseren, O. (2001) Elasticity of iron at the temperature of the Earth's inner core. Nature, 413(6851), 57-60.
Takafuji, N., Hirose, K., Mitome, M., and Bando, Y. (2005) Solubilities of O and Si in liquid iron in equilibrium with (Mg,Fe)SiO3 perovskite and the light elements in the core. Geophysical Research Letters, 32(6), 4.
Tenailleau, C., Etschmann, B., Wang, H., Pring, A., Grguric, B.A., and Studer, A. (2005) Thermal expansion of troilite and pyrrhotite determined by in situ cooling (873 to 373 K) neutron powder diffraction measurements. Mineralogical Magazine, 69(2), 205-216.
Uchida, T., Wang, Y.B., Rivers, M.L., and Sutton, S.R. (2001) Stability field and thermal equation of state of epsilon-iron determined by synchrotron X-ray diffraction in a multianvil apparatus. Journal of Geophysical Research-Solid Earth, 106(B10), 21799-21810.
Urakawa, S., Hasegawa, M., Yamakawa, Y., Funakoshi, K.I., and Utsumi, W. (2002) High-pressure phase relationships for FeS. High Pressure Research, 22(2), 491-494.
Urakawa, S., Someya, K., Terasaki, H., Katsura, T., Yokoshi, S., Funakoshi, K.I., Utsumi, W., Katayama, Y., Sueda, Y.I., and Irifune, T. (2004) Phase relationships and equations of state for FeS at high pressures and temperatures and implications

for the internal structure of Mars. Physics of the Earth and Planetary Interiors, 143, 469-479.

Vocadlo, L. (2007) Ab initio calculations of the elasticity of iron and iron alloys at inner core conditions: Evidence for a partially molten inner core? Earth and Planetary Science Letters, 254(1-2), 227-232.

Vocadlo, L., Knight, K.S., Price, G.D., and Wood, I.G. (2002) Thermal expansion and crystal structure of FeSi between 4 and 1173 K determined by time-of-flight neutron powder diffraction. Physics and Chemistry of Minerals, 29(2), 132-139.

Vocadlo, L., Price, G.D., and Wood, I.G. (1999) Crystal structure, compressibility and possible phase transitions in epsilon-FeSi studied by first-principles pseudopotential calculations. Acta Crystallographica Section B-Structural Science, 55, 484-493.

Vorobyev, Y.N., and Yelsukov, Y.P. (1998) On hyperfine interaction parameters in Fe3P 25 years later. Physica Status Solidi B-Basic Research, 205(2), R13-R14.

Whitaker, M.L., Liu, W., Liu, Q., Wang, L., and Li, B. (2008) Combined *in situ* synchrotron X-ray diffraction and ultrasonic interferometry study of ε-FeSi at high pressure. High Pressure Research, 28(3), 385-395.

-. (2009) Thermoelasticity of ε-FeSi to 8 GPa and 1273 K. American Mineralogist, 94(7), 1039-1044.

Williams, Q., and Jeanloz, R. (1990) Melting Relations in the Iron-Sulfur System at Ultra-High Pressures - Implications for the Thermal State of the Earth. Journal of Geophysical Research-Solid Earth and Planets, 95(B12), 19299-19310.

Williams, Q., and Knittle, E. (1997) Constraints on core chemistry from the pressure dependence of the bulk modulus. Physics of the Earth and Planetary Interiors, 100(1-4), 49-59.

Wood, I.G., Chaplin, T.D., David, W.I.F., Hull, S., Price, G.D., and Street, J.N. (1995) Compressibility of FeSi between 0 and 9 Gpa, Determined by High-Pressure Time-of-Flight Neutron Powder Diffraction. Journal of Physics-Condensed Matter, 7(36), L475-L479.

Wood, I.G., David, W.I.F., Hull, S., and Price, G.D. (1996) A high-pressure study of epsilon-FeSi, between 0 and 8.5 GPa, by time-of-flight neutron powder diffraction. Journal of Applied Crystallography, 29, 215-218.

Yagi, T., and Hishinuma, T. (1995) Iron Hydride Formed by the Reaction of Iron, Silicate, and Water - Implications for the Light-Element of the Earths Core. Geophysical Research Letters, 22(14), 1933-1936.

Zaitsev, A.I., Dobrokhotova, Z.V., and Mogutnov, B.M. (1995) Thermodynamics of Iron Phosphides. High Temperature and Materials Science, 34(1-3), 173-185.